ABSTRACT

Title of Document: DEVELOPMENT OF A SNUBBER TYPE MAGNETORHEOLOGICAL FLUID ELASTOMERIC LAG DAMPER FOR HELICOPTER STABILITY AUGMENTATION

Grum T. Ngatu, Doctor of Philosophy, 2009

Directed By: Professor Norman M. Wereley
Department of Aerospace Engineering

Most advanced helicopter rotors are typically fitted with lag dampers, such as elastomeric or hybrid fluid-elastomeric (FE) lag dampers, which have lower parts counts, are lighter in weight, easier to maintain, and more reliable than conventional hydraulic dampers. However, the damping and stiffness properties of elastomeric and fluid elastomeric lag dampers are non-linear functions of lag/rev frequency, dynamic lag amplitude, and operating temperature. It has been shown that elastomeric damping and stiffness levels diminish markedly as amplitude of damper motion increases. Further, passive dampers tend to present severe damping losses as damper operating temperature increases either due to in-service self-heating or hot atmospheric conditions. Magnetorheological (MR) dampers have also been

considered for application to helicopter rotor lag dampers to mitigate amplitude and frequency dependent damping behaviors. MR dampers present a controllable damping with little or no stiffness. Conventional MR dampers are similar in configuration to linear stroke hydraulic type dampers, which are heavier, occupy a larger space envelope, and are unidirectional. Hydraulic type dampers require dynamic seal to prevent leakage, and consequently, frequent inspections and maintenance are necessary to ensure the reliability of these dampers. Thus, to evaluate the potential of combining the simplicity and reliability of FE and smart MR technologies in augmenting helicopter lag mode stability, an adaptive magnetorheological fluid-elastomeric (MRFE) lag damper is developed in this thesis as a retrofit to an actual fluid-elastomeric (FE) lag damper. Consistent with the loading condition of a helicopter rotor system, single frequency (lag/rev) and dual frequency (lag/rev at 1/rev) sinusoidal loading were applied to the MRFE damper at varying temperature conditions. The complex modulus method was employed to linearly characterize and compare the performance of the MRFE damper with the baseline FE damper performance. Based on experimental measurements, it is shown in the research that at all test temperatures, a significant damping control range, extending beyond the baseline FE damper, can be provided by the MRFE damper with the application of varying magnetic fields. This controllable damping range can be programmed to potentially provide the required damping augmentation as a function of different flight conditions. The added benefits of employing smart MR fluids in MRFE lag dampers are to produce adequate damping at critical flight

conditions while concurrently reducing periodic hub loads at other flight conditions and to compensate damping losses associated with temperature.

The other main objective of the present research is to develop and formulate a comprehensive analytical model that can accurately describe the non-linear hysteretic behavior that is demonstrated by the MRFE lag damper. Thus, a hydromechanical model, which can delineate the physical flow motion of the system and accurately describe the non-linear hysteretic behavior of the MRFE damper is proposed. The hydromechanical model explored in this study is a design-based model which describes the damper system with a series of lumped hydraulic, mechanical and magnetorheological components. The model employs physical parameters such as inertia, damping, yield force and compliances that are dependent on damper geometry and material properties of components and which can potentially be approximated *a priori*. Further, temperature variation will mainly cause material properties to change. Once model parameters have been established, the model is shown to simulate accurately the measured hysteretic force-displacement history under single and dual frequency excitations, and varying temperatures.

DEVELOPMENT OF A SNUBBER TYPE MAGNETORHEOLOGICAL FLUID ELASTOMERIC LAG DAMPER FOR HELICOPTER STABILITY AUGMENTATION.

By

Grum T. Ngatu

Thesis submitted to the Faculty of the Graduate School of the
University of Maryland, College Park, in partial fulfillment
of the requirements for the degree of
Doctor of Philosophy
2009

Advisory Committee:
Professor Norman M. Wereley, Chair/Advisor
Professor Amr Baz (Dean's Representative)
Professor Darryll Pines
Professor Alison Flatau
Professor Sung Lee

Dedication

To my parents, Sihin and Tamrat

Acknowledgements

I would like to extend my deepest and sincere gratitude to my advisor, Professor Norman Wereley, for being such a wonderful advisor and mentor throughout my years at Maryland. He gave a chance to a part-time student, who had to work long hours every week to make ends meet and stay enrolled. I am candidly grateful to him for believing in me and giving me the opportunity to pursue my graduate studies under his guidance. His knowledge, understanding and support have provided a solid foundation for my research work. His confidence in my ideas and constant encouragements are immensely appreciated. Further, I would like to thank Professor Amr Baz, Professor Darryll Pines, Professor Alison Flatau and Professor Sung Lee for agreeing to serve on my dissertation committee. I am very fortunate to have such a distinguished committee who took an interest and provided insightful critiques of my work.

I would also like to thank Dr. Mary Bowden for all her support, especially in my early years at Maryland. When I first met her, I was an immigrant from a far-off place, working at a low-paying hourly job, with a big dream of pursuing my education. From the time I met her, she always had faith in my success, and facilitated my joining UMD as an advanced special graduate student. Her help and support along the way, and her motherly attitude are of a great value to me.

During the length of my research work, I have collaborated with many colleagues to whom I am wholeheartedly grateful. A special thanks to Dr. Peter Hu for his unparalleled support on this project. The contribution of Dr. Curt Kothera on this project was crucial in its successful completion. Many thanks to Dr. Young-Tai Choi

for his valuable insights and suggestions. I am very grateful to Michael Perna for his help in machining the retrofit damper components.

Next, I would like to thank all my friends at UMD CORE Lab, TSi and else where for all their moral and technical support through out the years. I want to especially thank Yosef Hussein for his help and friendship that stretches back a decade and half and for many more to come. A special thanks to my friend Ben for his assistance above and beyond the call of duty.

This work was supported by a DARPA Phase II SBIR project, contract number W31P4Q06C0400, with technical monitor Daniel Newman. Technical guidance from LORD Corp. on MR Fluid and damper details is gratefully acknowledged. I am also thankful to Dr. Peter Chen and Techno-Sciences, Inc., for all the support provided. I would also like to humbly acknowledge fellowship support from the Alfred P. Sloan Foundation.

Most importantly, my family has given me their unconditional love, support and devotion throughout my life. I could never thank you guys enough. This dissertation is dedicated to my parents who have always believed in me, and longed patiently to see me successfully complete this challenging task. I hope I have made them proud, and I hope that made the long wait to see me finish worthwhile.

Table of Contents

List of Tables

List of Figures

Chapter 1: Introduction

1.1 Motivation and Objectives

The susceptibility of helicopter rotor systems to aeromechanical instabilities is a well established phenomenon. These aeromechanical instabilities are non-linear phenomena which involve complex interactions of aerodynamic, elastic and inertial forces [1]. Particularly, mechanical instabilities, such as ground resonance and air resonance, are violent instabilities which could result in a catastrophic failure in soft-in-plane rotor systems. Soft-in-plane implies that the first lag mode lag/rev frequency is less than the 1/rev rotor frequency. Ground resonance is a dynamic helicopter instability which occurs as a result of the coupling between the blade lead-lag motion and the hub in-plane motion. This instability takes place when the helicopter is on the ground and the regressive lag/rev frequency coalesces with the support mode while the helicopter is spinning up to its operational 1/rev frequency. Air resonance is caused by the coupling of the low frequency blade flap and lag modes and rigid body modes. This instability occurs during specific flight regimes and aerodynamic forces are needed to determine the instability. Air resonance is primarily a problem of hingeless and bearingless rotor systems. Ground and air resonances are the primary rationale soft-in-plane helicopter rotor systems are equipped with lead-lag damper. In conventional articulated rotors, ground resonance is mitigated by employing hydraulic and elastomeric lag dampers. Modern helicopters are tending towards hingeless and bearingless rotor designs due to their reduced cost and maintenance,

improved hub design and better handling quality [1]. Due to stress and weight considerations, these rotor systems are soft-in-plane, and they are typically fitted with lag dampers made of passive materials, such as elastomers, to provide the required damping [2-6]. Compared to conventional hydraulic lag dampers, elastomeric lag dampers have a simple design, lower parts count, and are lighter in weight. They do not introduce moving parts, thus they have no sliding seals of hydraulic dampers to wear out and leak. They show gradual wear and tear which is visually detectable, and thus are easier to maintain, and more reliable. Unlike hydraulic dampers, elastomeric dampers do not produce extremely high damping forces at high lead-lag velocities [6]. In order to provide the required damping, a highly hysteretic filled elastomeric material is utilized. Typically, elastomeric lag dampers have been designed in three configurations (Figure 1.1): a flat plate or double lap shear type, where elastomer is bonded between metallic plates, a tubular type, where an elastomeric ring is bonded between two concentric cylinders, and a snubber or round-stacked type, which is made from a laminated stack of alternating elastomeric-metallic rings [2]. Under dynamic lag motions, the elastomer is sheared and provides damping through energy dissipation. In addition, the elastomer introduces stiffness into the system that can be used as a design parameter to change the natural frequency of the lag mode to avoid resonances [6, 7]. However, these highly damped elastomers exhibit a non-linear hysteretic response to dynamic loading. Furthermore, the damping and stiffness properties of elastomeric dampers are non-linear functions of the lag/rev frequency, dynamic lag amplitude, and operating temperature. It has been shown that elastomeric damping and stiffness levels diminish markedly as amplitude of damper motion

increases [2-7]. In addition, there is a reduction in damping as the excitation frequency is increased. At small lead-lag displacements, these elastomeric dampers have exhibited low loss factors and high stiffness, resulting in unfavorable limit cycle instabilities [4]. In forward flight conditions, the blade lead-lag motion in helicopters occurs at two frequencies, the lag/rev frequency and 1/rev frequency, and as the 1/rev amplitude is increased, it substantially reduces damping at lower lag/rev amplitudes, thus causing undesirable limit cycle oscillations [4, 6].

In order to address these undesirable effects of elastomeric dampers, a fluid-elastomeric (FE) lag damper, combining viscous fluid damping with an elastomeric material, was designed by Lord Corporation. Such a damper is also referred to as a Fluidlastic® lag damper [2, 4, 8, 9]. Fluid-elastomeric (FE) lag dampers alleviate the undesirable effects of elastomeric dampers' non-linear behavior by minimizing the dependence of the lag mode damping and stiffness on amplitude and frequency, resulting in a predominantly linear performance. In addition, these types of dampers require smaller space envelopes, accommodate multi-axis motions and provide longer service life than elastomeric dampers [2]. In this damper arrangement, the elastomer body is utilized both as a seal and to pump fluid between chambers to induce viscous damping. Thus, similar to elastomeric dampers, they still have no moving parts and dynamic seals, have simple design feature and low parts count. Since the majority of damping is supplied through viscous damping, the elastomeric material employed need not be selected based on its damping property, but rather on its stiffness and shear fatigue properties [8]. Even though FE lag dampers provide a substantially improved performance over elastomeric dampers, they are limited to providing fixed

or passive damping. Since damping augmentation is only required over certain flight regimes where there is a potential for instabilities to occur [10], a passive damper providing a fixed damping could produce unfavorably large periodic loads on the rotor hub. Further, passive dampers tend to present severe damping losses as temperature increases either due to in-service self-heating or hot operating conditions. Under these circumstances, elastomer softening and/or fluid thinning occurs which adversely affects damper performance [2-4, 11, 12]. Thus, an adaptive damper, which can produce the desired amount of damping without a corresponding increase in periodic loads and can be adjusted to compensate for performance losses at extreme environmental conditions, would be of considerable value.

A promising alternative is to make use of smart or controllable fluids, such as Magnetorheological (MR) fluids, to offer adaptive capability in which damping can be controlled in an optimal manner. Magnetorheological fluids typically consist of spherical micron-sized ferromagnetic particles (microspheres) suspended in a fluid medium such as silicone or hydraulic oil. Their rheological properties, thus their viscosity and yield stress, can continuously be varied and controlled in an optimal fashion by applying a varying magnetic field. The potential benefits of employing smart MR fluids are: 1) to produce adequate damping at critical flight conditions while concurrently reducing periodic hub loads at other flight conditions, 2) to compensate and/or provide required damping at different extreme ambient atmospheric conditions associated with desert, high-altitude or severe cold weather operations, 3) to compensate damping losses due to large damper temperatures arising from in-service self-heating, and 4) to balance the difference in damping among

individual lag dampers utilized in a rotor and help minimize the impact on rotor tracking conditions.

There are two fundamental configurations of elastomeric and fluid-elastomeric (FE) lag dampers that are well suited for introducing an adaptable material, such as MR fluids, to develop a hybrid magnetorheological fluid-elastomeric (MRFE) lag dampers. The first configuration is the tubular configuration, where an elastomeric material is bonded and sheared between two concentric circles that move relative to each other to construct an elastomeric lag damper, while a viscous fluid is included in the inner cylinder for the case of a tubular FE damper. The second configuration is the round-stacked or snubber type configuration, where a snubber type elastomeric damper is built from a laminated stack of alternating elastomeric-metallic rings with an elastomeric center wall running along the diameter. In the case of a snubber type FE damper, the elastomeric body of the damper is filled with viscous fluid to induce viscous damping. The elastomeric lag dampers in both tubular and snubber configurations are typically made of highly-damped, filled elastomers to provide the required damping. They exhibit a non-linear hysteretic behavior under dynamic loading. In the case of FE dampers, the elastomer, in both configurations, is not primarily employed to generate damping, thus its design is based on enhanced fatigue life and greater modulus range [2]. To supply the required damping, the viscosity of the enclosed fluid and the orifice geometries are optimized. By introducing a smart MR fluid in elastomeric lag dampers or replacing the viscous fluid with MR fluids in FE dampers as the working fluid inside the elastomeric bearing or snubber, and an electromagnetic coil to activate the MR fluid, the damping capacity of these passive

lag dampers can be significantly enhanced. Deformation or flexing of the elastomeric body results in relative motion between damper body and a retrofitted magnetorheological (MR) valve, forcing MR fluid to flow through the valve, where it can be activated in real time. The basic advantage of such an approach is that there are no sliding seals involved like in hydraulic dampers, thus, their susceptibility to external or environmental leakage and associated damping losses are minimized. They also require less maintenance as there are no sliding seals exposed to wear and tear, which involve frequent inspection, overhaul and replacement. Further, while the stiffness of the elastomeric material can be utilized as an additional rotor hub design parameter and the total damping is provided by the combination of the elastomer (minimal in FE damper case) and MR fluid, the hybrid magnetorheological fluid and elastomeric (MRFE) lag damper can actively and selectively augment damping over critical frequency ranges and operating conditions, and enhance stability of the helicopter. Last but not least, the passive damping, in both the elastomer and MR damping components, can potentially provide a fail-safe damping in the event of reduced or no-power operation where control of the field dependant MR damping is partially or totally lost.

Corresponding to the two basic elastomeric and FE lag damper configurations, there are two MRFE damper designs that can be developed from these types of lag dampers. The first one is the linear stroke MRFE lag damper which is developed from a tubular configured elastomeric or FE damper. Schematics of this tubular (also known as concentric bearing) type MRFE damper is shown in Figure 1.2a. This type of MRFE damper has been developed at UMD recently from a concentric or tubular

type elastomeric damper [13, 14], and a brief discussion is outlined here. The linear stroke MRFE damper consists of an elastomeric layer between concentric cylinders and an MR reservoir enclosed with in the inner tube. The nominal overall length of the original elastomeric damper is 150 mm, the thickness of the elastomeric layer is 6.5 mm and the inner diameter of the inner tube is 45 mm. To provide adaptive and active damping, an MR valve compatible in size with the inner tube and contained in a piston is retrofitted or seated in the inner chamber. The relative motion between the outer cylinder to which the rod and piston are attached, and the inner tube leads to a shear deformation of the elastomer along the damper body length, and forces the MR fluid to flow through the field activated gaps in the piston and the passive gap between the inner cylinder or tube and the piston outer diameter. The elastomeric body and the MR damping in this configuration are assumed to be decoupled systems, since each component responds to dynamic loading independent of the other. The total damping of the system can be estimated by the linear superposition of the damping from its components. Note that this MRFE damper has the same over all dimensions as the original damper, which should make it a direct replacement for the existing elastomeric damper. The original elastomeric lag damper has a total weight of 0.54 kg, while after the introduction of the MR valve and piston, and MR fluid, the MRFE weighs about 1.30 kg.

The second MRFE damper configuration, which is proposed in this research, is a snubber type MRFE damper, which is developed from a round-stacked or snubber type FE damper. Schematics of this snubber type MRFE damper is shown in Figure 1.2b. For a small penalty of design complexity, the existing snubber type FE lag

damper offers a compact size, light weight, multi-axis operation, and longer service or fatigue life than elastomeric lag dampers. The MRFE lag damper is also intended to maintain these properties. The elastomeric body of the FE damper is used to seal and pump fluid between chambers to create the required damping. Fluid performance is tailored somewhat like a hydraulic damper, while the elastomer is formulated for high endurance life to minimize the space envelope [2]. The cylindrical body of the snubber type MRFE damper consists of a multiple lamination of metallic and elastomeric ring layers, with an outer circumferential metal plate midway along body height. The nominal overall height of the original elastomeric damper is 4.2 in (106 mm) and diameter of 4.65 in (118 mm). Elastomeric deformation forces fluid to flow through a vertical, elastomeric center wall that contains two flow ports. This wall essentially separates the internal damper cavity into two fluid reservoirs. Note that the baseline FE damper (Bell 430 damper) is assembled as a molded unit, so there is no possibility for fluid to be exchanged from one reservoir to the other without passing through one of the flow ports. This behavior can potentially be maintained in developing the MRFE damper. This will completely avoid the use of internal dynamic seals to prevent unnecessary passive flow passages between the fluid chambers. To provide adaptive or active damping, up to four MR valves compatible in size with the chamber dimensions can be introduced at the two port holes, two on each side of the center wall. The relative motion between the MRFE damper mid plate and the outer (top and bottom) plates deforms or flexes the elastomeric body, and forces the MR fluid to flow through the field activated gaps in the MR valves. Thus, by varying the applied magnetic field, the MR damping component of the

MRFE damper can be controlled and optimized as required. In addition, the MRFE damper developed would occupy the same space envelope as the original FE damper, making it interchangeable with the existing FE lag damper on the helicopter rotor system. Since the damper development replaces the existing viscous fluid with MR fluid and only introduces two additional MR valves, the weight penalty could be kept to the minimum.

The snubber type MRFE damper includes damping and stiffness effects from its elastomeric body and damping from MR component, and an appropriate analytical model is necessary to describe the behavior of the damper. First of, the behaviors of these materials is very complex. Constitutive behaviors and characteristics of both elastomers and MR fluids are non-linear and dependent on amplitude and frequency of loading motion. In addition, material properties of elastomers and MR fluid are affected by temperature. The elastomer in this MRFE configuration is not only exposed to shear deformation, but also to volumetric expansion, which introduce additional stiffness and damping in the system. Since the elastomeric body in this design acts as an accumulator and a pump, the two systems, i.e. the elastomer and the MR components in this configuration are completely coupled systems, so that the dynamics are more complex. These behaviors will make characterization, modeling and design of the MRFE lag damper a very challenging endeavor. The fundamental requirement for an accurate damper characterization and modeling can be viewed from two perspectives: 1) to design and predict damper performance *a priori*, such that requirements are met before development and production, and 2) damper performance strongly influences the dynamics and aeromechanical stability properties

of the helicopter rotor, thus accurate damper model will help in attempts to predict these stability characteristics.

Thus, the objective of the current research can be summarized as: 1) developing a snubber type MR fluid-elastomeric (MRFE) lag damper, 2) evaluating its controllable damping performance under different loading conditions encountered by a helicopter lag damper, 3) evaluating MRFE damper characteristics under varying operating temperature conditions and asses its damping compensation associated with temperature, 4) developing an MRFE damper model to accurately describe MRFE damper dynamic behavior, and 5) evaluation of the temperature compensating behavior of the MRFE damper employing different control schemes.

1.2 Smart MR Fluids: A Material Review

MR fluids belong to a special class of fluids that change their rheological properties on the application of a magnetic field. Conventional MR fluids are composed of micron-sized ferromagnetic spherical particles suspended in a hydrocarbon, silicone, or aqueous carrier fluid. The size of the particles is usually on the order of 1 to 10 microns. Upon application of a magnetic field (on-state), the particles acquire a magnetic polarization and attract one another, forming a chain-like structure that join to form fibrils parallel to the applied field. This initially viscous liquid/particle suspension (~0.1 – 0.3 Pa s) without an applied magnetic field (off-state) is converted to a semi-solid in the presence of a field with an extremely high change in viscosity (~10^5 – 10^6 times) and a substantial field-induced yield stress of up to 100 kPa is required to break the chains and shear the material [15, 16]. The ideal Bingham behavior of MR fluids is represented in Figure 1.3, which depicts the

off-state and on-state variation of the applied shear stress in the MR fluid with shear strain rate. At off-state condition, the MR fluid behaves basically as a Newtonian fluid, with a constant viscosity, given by the slope of the line. Upon the application of a magnetic field, the fluid initially behaves as a rigid material. But as the applied shear stress increases and reaches the yield stress τ_y, the fluid yields and induces fluid flow. Thereafter, a finite fluid flow can be maintained by the applied shear, and the MR fluid behaves as a Newtonian fluid in this post-yield condition. The slope of the curve in the post-yield region is assumed to be equal to the zero field viscosity of the fluid. The fast response (in milli-second) and controllability of MR fluids have made them very attractive for implementation in semi-active smart vibration-absorption systems [17], primary vehicle suspension systems [18, 19], landing gear for aircraft [20-22], adaptive crew seats for vibration [23-25] and shock isolation [26-27].

The field dependent shear strength of MR fluids depends on several factors including the size, composition, and volume fraction of the particles, the strength of the applied magnetic field, and the particle geometry. Increasing the volume fraction of particles in the suspension results in an increase in the achievable yield strength, but also results in an increase in the off-state viscosity. Commercial MR fluids are generally composed of 30 to 40 vol. % of particles within the suspensions. As the applied magnetic field is increased, the shear strength of the fluid increases until the magnetization saturation of the particles is reached [28]. Increasing the size of the particles increases the shear strength of the fluid [16]; however, spherical particles larger than about 10 μm tend to settle rapidly even with the addition of special additives. Particles in the nanometer regime tend to settle more slowly (if not

indefinitely suspended by Brownian motion), but greatly reduce the yield strength of the MR fluid [29-32]. Within the ideal size range of 1-10 μm diameter particles, sedimentation still occurs due to the inherent density difference between the particles and the carrier fluid. Once settled, the spherical particles tend to form tightly packed sediments caused by remnant magnetization and are not easily re-dispersed [33]. Since the yield stress of MR fluids is directly related to the volume fraction of particles in the suspension, the behavior of the fluid is less predictable during this remixing period. Problems associated with settling and tightly packed sediment formation have been partially reduced by the addition of special additives, such as surfactants, nanoparticles and other non-spherical particles [31, 32, 34-36]. Sedimentation of the particles in conventional MR fluids is a key hurdle to overcome before more diverse applications can be realized [34].

Previous studies suggest that MR fluids utilizing non-spherical iron particles exhibit enhanced rheological properties as well as greater stability [16, 37]. MR fluids composed strictly of nanowires have displayed better performance in terms of magnetoreology and stability than corresponding fluids containing only spherical particles at similar volume fractions [16]. This sedimentation stability has been demonstrated for MR suspensions that contain 6 vol. % of iron nanowires only, which produced fluids that did not settle even after 2 months [16]. However, these studies were limited to low particle volume fractions of 10 vol. % (48 wt. %) or less, thus producing small yield stresses that are largely insufficient for most dynamic applications. Thus, by replacing part of the microsphere particles of a high vol. % MR fluid with nanowires similar to those used in Ref. 16, it was possible to produce a

novel MR fluid, called dimorphic MR fluid. These fluids were created at UMD CORE research lab with the aim of improving the settling properties of MR fluids while maintaining a higher vol. % of ferromagnetic particles and, thus, a greater workable yield stress than fluids using strictly nanowires. These substitutions significantly reduced the rate of particle settling, enabling the MR fluid to maintain a uniform dispersion without marked sedimentation for an extended period of time. In addition, at the level of nanowire concentration and geometry studied, it was possible to maintain the high level of yield stress observed in conventional microsphere-based MR fluids. A detail description and results of this study is given in Appendix A.

The dependence of MR fluid property on temperature is a crucial aspect that needs to be addressed in the design of MR devices such as dampers. Both the viscosity and yield strength of MR fluids decreases with increasing temperature. The viscosity of MR fluid decreases rapidly with temperature, thus decreasing the off-state and the post-yield viscosities. However, the yield stress property of MR fluids shows a stable behavior over a wide range of temperature. They exhibit a relatively small yield strength reduction (~10%) over a temperature range of -40^{o}C to 150^{o}C [38].

1.3 Literature Survey

1.3.1 Elastomeric Lag Dampers

Elastomeric dampers employing filled elastomeric material technology have been established to be sufficient in providing damping augmentation in helicopter rotor systems. In order to provide the required damping, a highly-damped elastomeric material is utilized, which exhibits a viscoelastic-like behavior under dynamic

conditions. The main advantage is their simple design, light weight and few components. They do not also employ dynamic seals, they show gradual wear and tear which is visually detectable, and thus are easier to maintain, more reliable, and have longer service life. These elastomeric lag dampers have been used widely in both articulated and hingeless/bearingless helicopter rotor system to provide required damping.

Ideal viscoelastic materials under sinusoidal excitation can effectively be characterized using the complex modulus method. In this model, the energy stored in the system is the measure of the storage modulus and the energy dissipated is the measure of the loss modulus, and can equivalently be represented by a Kelvin model. The behavior of a viscoelastic material represented by the Kelvin model consists of a Newtonian damper and a Hookean elastic spring in parallel, and the resulting hysteresis loop is elliptical in shape. For a constant test condition (constant amplitude, frequency, pre-load and temperature conditions) many elastomeric or rubber materials (for example Lord SPE17 elastomer) show this kind of behavior under dynamic applications. In these kind of materials, non-linear behaviors arise from variations in excitation amplitude, frequency, pre-load and temperature conditions. The elastomer is excited harmonically over a spectrum of amplitude, frequency, temperature and pre-load, and its corresponding complex moduli are then computed from the test results. These frequency domain complex modulus can then be introduced in time domain as a Hookean stiffness and Newtonian damping of the Kelvin model to reconstruct the elliptical hysteretic behavior of the elastomer with good accuracy.

The model parameters can then be either compiled into an easily accessible "look-up table" or expressed as a series of functions that are fitted to the computed parameters.

On the other hand, almost all elastomeric lag dampers are highly damped, filled elastomers (Lord BTR and SPE I elastomers) and exhibit a non-linear hysteretic behavior that is also dependent on displacement and velocity, resulting in a non-elliptical force-vs-displacement curve when undergoing harmonic excitation [3-5, 39]. This non-linear behavior is mostly based on the interaction between fillers and rubber compound inside the filled elastomeric material [13, 40]. Before a large deformation of the filled elastomeric lag damper occurs, an intact filler structure displays a large stiffness and small loss factor for small amplitudes. As the input displacement increases, the filler structure starts to break resulting in a corresponding loss in stiffness. The breaking of the filler structure is similar to that of frictional behavior. The continuous breaking of the filler structure increases the loss factor, thus increasing also available damping from the damper. As the input displacement increases further, the frictional effect is fully released, and both stiffness and loss factor drop to lower levels, which then are maintained relatively constant by the remaining polymer chain [13]. The linear complex modulus method, while useful in evaluating the general damper performance, does not fully capture the non-linearities arising in filled elastomers. To account for the non-linear behavior, Felkner *et al* [6] proposed a non-linear complex modulus model, where stiffness and damping are non-linear functions of displacement. Even though this approach was useful in describing the displacement dependent complex modulus and in dual frequency studies, the model can highly over predict the actual damping force [3, 39]. Tarzanin *et al* [41]

and Panda *et al* [4] modified the Kelvin model by replacing the dashpot with a variable friction damping element. The model is shown to correlate well with the experimental data over the range of frequency and amplitude tested. Krishnan [42] developed a model by adding a cubic spring in parallel to the Kelvin chain. Snyder *et al* [3] improved this model by adding an elasto-slide element in series with the cubic spring. Both models were shown to capture the non-linear elastomeric damper hysteresis. Behavior of a viscoelastic solid can be represented by a standard linear solid model or sometimes known as the Zener model, which basically is a Kelvin model with a leading spring in series. Gandhi and Chopra [43] utilized this analogy and developed a non-linear viscoelastic model by employing a non-linear leading spring. In this study, the model parameters were identified using complex modulus data published by McGuire. Thus, the fidelity of the model in capturing the non-linear hysteresis is not assured. Lesieutre and Bianchini [44] developed the anelastic displacement field (ADF) model to characterize the dynamic performance of a linear viscoelastic material. The development of the ADF model is based the notion of scalar internal variables or "augmenting thermodynamic fields" (ATF) that described the interaction of the displacement fields with irreversible processes occurring at the material level. Instead of the thermodynamic processes themselves, the ADF approach focuses on the effects of such processes on displacement fields which combine elastic and anelastic fields. Although no explicit physical interpretation is given [13], the anelastic part might consist of numerous sub-systems which considers the effects of multiple relaxation processes. But, a single ADF model is mechanical analogous to a Zener model. In order to address the non-linear viscoelastic material

behavior, Govindswamy *et al* [45] developed a non-linear ADF model which has a similar mechanical analogy as the linear version but employs non-linear springs and dashpot. The model was able to show at room temperature the variation of the complex modulus with amplitude, and capture and match the stress-strain hysteresis at a fixed frequency (4Hz). However, it was unable to capture both the frequency and amplitude dependence simultaneously [46]. To further improve performance, different functional forms of the ADF system have been proposed. Brackbill *et al* [46] added a discrete friction damping and linear spring elements in parallel with the nonlinear ADF model in order to capture the rate-independent nonlinear dissipative behavior of elastomer due to the presence of filler materials which adds in parallel to the rate-dependent (viscous) damping of the rubber. The introduced parameters result from amplitude dependent-relaxation. Including more friction-spring pairs, at the expense of adding more model parameters, results in a more accurate curve-fit over a broad frequency and amplitude range. As many as sixteen parameters were used to construct the model and the parameter determination process was complicated by the fact that some parameters were chosen by empirical observation. Ramrakhyani *et al* [47] replaced the discrete friction–spring elements with a continuously yielding element and the multiple linear elastic ADF elements with a linear fractional derivative element and was able to reduce the number of model parameters to eight. However, it did not improve the hysteresis loop prediction and model parameter determination remained complicated. Recently, Hu *et al* [5] developed the rate-dependent elastoslide model based on the triboelastic theory [48, 49] that combined a constant linear spring in parallel with a series of rate-dependent elasto-slide elements

with a yield-distribution function to account for yield force. The theory of triboelasticity stated that the behavior of a filled elastomer can be represented by a large or infinite number of alternate springs and frictional slides in series, and each slide has a constant yield force and each spring has a constant stiffness [5, 13]. Coveney *et al* [48] developed a three-parameters standard triboelastic solid (STS) based on theory of triboelasticity and further developed a four-parameter rate-dependent triboelastic (RT) model. These models gave a satisfactory representation of material behavior. However, since the yield force is fixed along different slides, these models show less flexibility to represent the amplitude dependent behavior for different filled-level materials. The rate-dependent elastoslide model consists of a large number of rate-dependent elastoslide elements with different yield levels and a parallel linear spring element. The elastoslide element is used to simulate the frictional behavior of the filler structure in the elastomer, and the linear spring represents the remaining material stiffness. The model is shown to predict well damper response within the range of amplitudes and frequencies investigated.

Characterization of elastomeric lag dampers under varying operating temperature conditions is of significant importance in assessing damper performance. In a typical damping device, there are two main sources of temperature variation in the system: (1) ambient atmospheric temperature conditions which tend to decrease or increase damper operating temperature; and (2) in-service self-heating which is associated with internal energy dissipation. Elastomeric dampers are shown to exhibit thermoviscoelastic behavior, where the damper's complex modulus changes non-linearly with variation in operating temperature [4, 50]. Elastomeric dampers present

a temperature dependent softening and stiffening at low and high temperatures respectively [3, 50] which can have an adverse effect on damper performance. When exposed to low temperatures, elastomeric materials tend to become hard and firm. Its elasticity decreases and damping is increased [51]. Hausmann and Gergely [50] conducted temperature tests to characterize the effects of operating temperature and self-heating on damper performance. The hysteresis plots clearly showed the decrease in dissipated energy as elastomer temperature is increased. Experimental results have also shown a significant reduction in linearized in-phase and quadrature modulus in elastomeric lag dampers with increasing temperature [3, 50, 52]. Some proposed models have tried to incorporate the effects of temperature in predicting dynamic behavior of elastomeric lag damper. Based on the complex modulus method, Hausmann and Gergely [50] developed a series of shift functions to characterize the thermoviscoelastic behavior of elastomeric lag dampers. The amplitude dependence of the complex modulus is introduced through one fit-function, while temperature effects are addressed through another, which is then coupled to the frequency fit-function. The procedure was able to accurately capture the storage and loss modulus. Snyder *et al* [3] introduced a linearized saturation-decay-rate equation to capture the trend of the parameters of the Kelvin chain with cubic spring and elasto-slide element model. Although, at each test temperature, the fit-function coefficients were evaluated at every frequency and amplitude combination, the model was able to capture the non-linearity in the elastomeric lag damper. Temperature effects were also examined using initially a single non-linear amplitude dependent ADF model and later a linear multi-ADF model by introducing a classical Arrhenius relationship [52]. The former

model was able to predict fairly well the high-temperature performance of the elastomeric damper at a frequency of 10 Hz. Having a multi-ADF system in the later model are shown to improve temperature behavior over a broad frequency range, with limited accuracy. Since additional ADF fields increase the number of degree of freedom in the system, the complexity of the model is also increased in parallel.

1.3.2 Fluid-elastomeric (FE) Lag Dampers

Elastomeric lag dampers demonstrate damping and stiffness losses as amplitude of input excitation and frequency is increased. The large reduction in damping as the amplitude of loading motion increases leads to excessive size and weight of dampers in order to accommodate all operating conditions [7]. At small lead-lag displacements, these elastomeric dampers show low loss factors and high stiffness, resulting in unfavorable limit cycle instabilities. In forward flight conditions, the blade lead-lag motion in helicopters occurs at two frequencies, the lag/rev frequency and 1/rev frequency, and as the 1/rev amplitude is increased, it substantially reduces damping at lower lag/rev amplitudes, thus causing undesirable limit cycle oscillations. In order to address these undesirable effects of elastomeric dampers, a fluid-elastomeric (FE) lag damper, also known as Fluidlastic® lag damper, which combines viscous fluid damping and elastomeric material, was designed by Lord Corporation [2, 4, 8, 9]. These fluid-elastomeric (FE) lag dampers employ bonded elastomeric technology which is used to seal and pump a non-toxic viscous fluid to provide damping. Some of their advantages include simplicity, lightweight, small space envelope, multi-axis capability, energy storage and fatigue properties, reliability and a broader range of dynamic capability. They also do not require

dynamic or sliding seals, extremely close tolerances, plated surfaces and polished finishes on components [2, 8]. Since they are hermetically sealed, they are not subjected to leakage and are designed to be maintenance-free. They show gradual deterioration which is visually detectable before the dynamic characteristics are degraded. The majority of damping is supplied through viscous damping, and the elastomeric material employed need not be selected based on its damping property, but rather on its stiffness and shear fatigue properties. Recent dynamic tests have demonstrated that FE dampers show less dependency of elastic stiffness on the input amplitude and higher loss factor than elastomeric dampers.

The complex modulus method is usually employed to characterize the over all FE damper behavior. It gives a relatively accurate performance of the damper system in terms of the stored energy (storage modulus) and dissipated energy (loss modulus) when excited under sinusoidal excitation. However, the complex modulus linearization technique does not identify the inherent hydraulic behavior of the FE damper under sinusoidal excitation. The model does not describe adequately the actual physical flow phenomenon or flow dynamics in fluid based FE dampers. It treats the damper as a bulk body or a 'black box,' and tries to depict the over all performance of the system by relating the output to the input though the complex modulus or Kelvin model. Parameter identifications are also based on test results. However, the snubber type FE damper, which is the damper of interest in this research, has its body or chambers made of elastomeric material into which fluid is contained resulting in two completely coupled systems (hydraulic and mechanical). Consequently, it is difficult to differentiate the contribution from system components

and adequately explain the inherent coupling effect. Since the complex modulus model is insufficient to describe the dynamics of the snubber type FE device, it becomes very difficult: 1) to design and predict damper performance *a priori*, before development and production, and 2) to be applied in dynamics and aeromechanical stability analysis of the helicopter rotor. Few models based on lumped parameter approaches have been proposed to model the hysteretic behavior of a snubber type FE lag damper [2, 53, 54]. These models are shown to give good correlation between measured data and model results for the range of test performed. Even though the models try to distinguish the contributions from system components, they fall short in accurately describing the flow dynamics of the hydraulic system [53, 54]. All model parameters are estimated and optimized without enough discussion of their physical interpretations and reasoning, and their associated derivations. The shear and bulge stiffness of the FE damper are given as non-linear functions of displacement and velocity. The model results have shown the shear stiffness to be more dominant than bulge stiffness; however, in-house test results have suggested otherwise. The damping from elastomer shear and bulging, and plus the hydraulic or viscous damping are all given as a non-linear functions of velocity. Again, the model damping from shear deformation is significant, but in-house testing have shown that minimal damping is gained from elastomer in shear, and majority of the damping from the FE device is due to flow resistance or viscous flow (70% - 80%). The reasoning behind the fluid inertial effect and fluid mass amplification outlined in the models were not clearly explained. The models, which are formulated and validated at room temperature, utilize as many as fourteen parameters [53, 54].

Characterization of fluid-elastomeric lag dampers under varying operating temperature conditions is of significant importance in damper performance. In a typical damping device, there are two main sources of temperature variation in the system: (1) ambient atmospheric temperature conditions which tend to decrease or increase damper operating temperature; and (2) in-service self-heating which is associated with internal energy dissipation. Temperature effects on elastomeric dampers behavior were discussed previously (see section *1.3.1*). In typical fluid or hydraulic dampers, the dependence of liquid viscosity with temperature is a trend where liquid viscosity decreases with increasing temperature. Generally, viscosity decreases rapidly with temperature [55]. The damping force of a hydraulic damper system is directly proportional to viscosity of the enclosed fluid. Thus, as the fluid temperature increases, fluid viscosity tends to decline, resulting in lower damping forces. Furthermore, fluid-elastomeric lag dampers present additional complexity as they are coupled devices of elastomeric and hydraulic systems. Once again, the complex modulus method is usually employed to characterize the over all FE damper behavior at varying temperatures. It gives a relatively accurate performance of the damper system in terms of the stored energy (storage modulus) and dissipated energy (loss modulus) when excited under sinusoidal excitation at different temperatures. In the lumped parameter modeling discussed in the previous paragraph [53, 54], temperature effects are accounted by introducing a non-linear ADF (Anelastic Displacement Field) and slider elements [56] in parallel with the room temperature model [54]. This modification further introduces eight parameters, which makes parameter identification a difficult task. In addition, the ADF based model only

accounted the temperature dependent behavior of the FE damper elastomeric body, and the temperature characterization of the hydraulic system was not addressed.

1.3.3 Semi-active Lag Damping: MR and MRFE Lag Dampers

Magnetorheological fluids typically consist of spherical micron-sized magnetic particles (microspheres) suspended in a liquid medium such as silicone or hydraulic oil [57, 58]. Their rheological properties, and thus their yield stresses and viscosities, can be rapidly and continuously controlled by varying the applied magnetic field. Conventional MR fluids utilize spherical micron-sized iron particles at high weight fractions and are shown to exhibit high yield stresses, up to 100 KPa [15, 16]. The fast response and controllability of MR fluids have made them very attractive for implementation in semi-active smart vibration-absorption systems [17], primary vehicle suspension systems [18, 19], landing gear for aircraft [20-22], adaptive crew seats for vibration [23-25] and shock isolation [26-27]. Because the yield stress of the MR fluid exhibits a substantial controllable range when a magnetic field is applied, many MR fluid based devices were designed such that their damping level can be controlled in feedback by applying a magnetic field [59, 60].

The study of semi-active damper technology in helicopter rotor systems dates back to the 1990's when the Commanche helicopter was reported to be encountering a significant air resonance due to the non-linearity of the elastomeric damper [9, 13]. One key research topic that resulted was improving the performance of the lead-lag damper. To this effect, a significant progress was the development of the hybrid fluid-elastomeric (FE) lag damper exclusively designed and manufactured by Lord Corp. (see *section 1.3.2*). However, both elastomeric and FE dampers are passive dampers,

and their damping properties will vary due to excitation displacement and velocity, ambient temperature variations and in-service self-heating, resulting in uncertainties in lag damper performances. MR fluids have been found very attractive in their feasibility to enhance helicopter rotor lag damping systems. The potential application of hydraulic type or linear stroke MR dampers in mitigating ground resonance instabilities has been explored [61]. Even though there are a number of control schemes developed in controlling smart fluid based dampers [62-66], there only has been limited work explored in helicopter lag damping control scheme development using MR dampers. Marathe *et al* [59] combined an MR damper model into a rotor aeromechanical model and investigated the effects of two different control schemes on rotor stability. The two control schemes were the On-Off scheme and the Feedback Linearization scheme, and they were compared for lag transient responses in ground resonance and their ability to reduce periodic damper loads in forward flight. The results implied that using a shear mode MR damper of size comparable to an elastomeric lag damper can provide sufficient damping for ground resonance stabilization and can significantly reduce periodic damper loads with a judicious choice of operation scheme. The On-Off scheme is simple and easy to apply, but it is not optimal in reducing hub loads. Feedback linearization control was more versatile, however it was recognized that since such algorithm is developed based on the MR damper model, its performance is sensitive to model error or uncertainties [67]. Gandhi *et al* [67] explored the effects of MR fluid damper model uncertainties on helicopter rotor system stability when feedback control law was utilized. The study showed that by increasing control gain, hence increasing the prescribed damping

ratio, to a sufficiently high value, limit cycle instability can eventually be eliminated, for given uncertainty bound. However, large prescribed damping ratios would result in high periodic damper loads in forward flight. The study suggested that the periodic damper loads can be substantially reduced, while maintaining stability, if a band-rejecting filter is used which eliminates the 1/rev periodic component of velocity and leaves only the perturbation velocity in the feedback signal. Zhao *et al* [60] developed a different linearization feedback control strategy to integrate the MR damper into classic linear ground resonance analysis, and be applied to the ground resonance problem to stabilize an unstable rotor system assuming an isotropic rotor hub (all damper and blades similar), and to control undamaged dampers to recover rotor stability in case of an anisotropic rotor hub due to damper damage and/or degradation. The study showed that using MR dampers and a semi-active controller can stabilize an unstable rotor and maintain the design stability margin in the rotor system. In addition, the robustness study showed that MR dampers, actuated with a properly designed controller, can recover stability when the rotor system loses stability due to damper degradation, except in the case where 100% damping was lost on one blade.

Magnetorheological (MR) lag dampers can experience a large temperature variation as a result of extreme atmospheric weather conditions or due to heating caused by self-heating and magnetic circuit. So far, very limited studies have dealt with the effects of temperature and heat transfer in MR lag dampers, while some work has been done on generic MR dampers. Gordaninejad and Breese [68] and Dorgruoz et al [69] presented theoretical analysis for temperature increase in different sizes of MR dampers and demonstrated a good correlation between theoretical and

experimental results. The results exhibited a significant reduction in peak force with rising temperatures, and this was attributed to the reduced viscosity of the fluid. As the MR fluid's temperature rises, the viscosity decreases and consequently the damping force decreases. However, since the variation in yield stress of MR fluid between room temperature and 150°C was not more than 5%, it was assumed to be independent of the temperature and a function of the applied field only [69]. Thus, MR dampers have the potential to compensate damping degradation due to a rise in temperature by increasing the applied magnetic field until the required damping is attained. The above results did not consider the effects of a control scheme. Liu *et al* [70] formulated a skyhook controller that is temperature dependent for a vehicle suspension employing MR damper. The results indicated that the compensated skyhook control system offers improved overall performance as compared to the uncompensated skyhook control system at the operating temperature range of an off-road MR damper application. The effectiveness of the temperature feedback increased with increasing temperature. Since the plastic viscosity of the MR fluid increased exponentially with decreasing temperature, at lower temperatures the uncontrollable viscous damping force becomes the dominant one, and the effect of temperature compensation diminishes. Batterbee and Sims [71] examined temperature dependent dynamic behavior and investigated various control strategies of an MR vibration isolation system. The study showed that there is a limited reduction in yield force with increasing temperatures, which was attributed to a reduction in the MR fluid's yield stress. Secondly, the slope of the post-yield force-velocity response decreases with increasing temperature, which was associated with a

reduction in fluid viscosity. Finally, the size of the force-velocity hysteresis loop reduces which was attributed to the change in damper stiffness caused by the rising accumulator pressure with increasing temperature. Various controllers were also compared in order to assess their relative robustness against temperature uncertainty. These were proportional, PID, gain scheduling, and on/off control. Each system was configured to implement a semi-active skyhook control law. Control system experiments were performed at different temperatures using the hardware-in-the-loop simulation method. All control schemes were shown to be equally sensitive to temperature. A numerical control sensitivity analysis showed that viscosity variation have the most significant effect on stability, while damper stiffness has a notable influence and the change in yield has a negligible impact. Even though all the investigations mentioned above discussed temperature effects on some MR devices, they do not address particular application in helicopter rotor and corresponding lag damping applications. Future works on MR lag dampers should address these issues since MR lag dampers offer an opportunity to enhance stability augmentation strategies over passive elastomeric dampers.

Recent work has been done to evaluate the feasibility and capabilities of employing MR dampers in conjunction with elastomeric materials in helicopter lead-lag damping applications. Kamath *et al.* [10, 72] modified a pair of 1/6th Froude-scale Comanche helicopter fluid-elastomeric lag dampers to a pair of hybrid elastomeric-MR dampers and demonstrated their capability for lag mode damping applications. Hu *et al.* [7] also conducted analytical and experimental studies on a parallel arrangement of an elastomeric lag damper and two conventional MR

dampers. In this preliminary MRFE damper test set up, there were two distinct damping components: 1) an elastomeric damping component, and 2) a magneto-rheological damping component. The elastomeric damper was a double lap shear, high loss factor filled elastomer, while the MR damping component was comprised of two linear stroke MR dampers. In this parallel configuration, the damping contribution from each damping component were found to be additive, so that the MR and elastomer damper can be characterized independently [7, 13]. This experimental feasibility study demonstrated a significant controllable damping dynamic range that was provided by the MR component of the damper assembly. Recently, a full-scale linear stroke tubular magnetorheological fluid-elastomeric (MRFE) lag damper, which can be fully integrated into an actual helicopter rotor system, has been developed [14]. The linear stroke MRFE lag damper was developed as a retrofit to an existing tubular configured elastomeric lag damper. The elastomeric damper modified has an elastomeric material bonded between two concentric cylinders, into which a piston, an MR valve and MR fluid were introduced. Similar to the preliminary study in Ref. [7], the elastomer and MR component of this MRFE lag damper are in a parallel combination, and they are assumed to be decoupled, such that their individual contribution can be linearly superposed to give the total MRFE damper performance. The study has shown that at field-off condition, the MRFE damper behaves as a passive FE lag damper. As field is applied to the MR valve, the damping of the MRFE device can be varied substantially, and thus, has the potential to augment damping over critical frequency range of the helicopter rotor. However, similar to elastomeric, FE and MR lag dampers, the performance of an MRFE lag damper is

substantially affected by temperature. The variation in temperature arise mainly from atmospheric conditions and self-heating, and results in an interdependent and complex temperature effect since the MRFE damper is a hybrid of elastomeric and MR fluid damping systems. However, to date, to the author's knowledge, there has not been any recorded study on the effects of temperature on MRFE lag dampers. Further, MRFE damper temperature compensating control schemes should also be outlined or investigated in their application in mitigating helicopter rotor instabilities.

Classic Bingham-Plastic and Herschel-Bulkley based models have been utilized to model the non-linear hysteresis of ER and MR devices [73-76]. The classic Bingham-plastic model, which is modeled as a parallel combination of a dashpot and a Coulomb friction element, accounts well the post-yield behavior of ER and MR fluids, while it assumes a rigid fluid behavior in the pre-yield region. Thus, it is unable to capture the pre-yield hysteresis behavior. The Biviscous model [77], which is an extension of the Bingham-plastic model, utilizes piecewise continuous functions to represent pre- and post-yield damping, but the model fails to capture the force-velocity hysteresis. Further, physically motivated phenomenological and mechanism based models have been developed to characterize MR dampers. An extension of the biviscous model, the hysteretic biviscous model formulated by Pang *et al* [76] combines a series of piecewise continuous functions to capture the pre-yield hysteresis. Gamota and Filisko [78] developed an expansion of the Bingham model by introducing a Zener element in series to capture the pre- and post-yield behavior. Kamath *et al* [10, 72] presented a mechanism based nonlinear piecewise smooth viscoelastic-plastic model. The model employs a preyield viscoelastic and post-yield

viscous models with a series of switching functions to describe the smooth transition between the pre-yield and post-yield regions. Phenomenological models employing mathematical functions have also been proposed. Choi *et al* [79] employed a polynomial fit to capture the force-velocity hysteresis of an MR damper. Ma *et al* [80] and Wang *et al* [81] developed a model based on generalized symmetric Sigmoid functions to characterize MR behavior. The Bouc-Wen [82, 83] model is a phenomenological model which has been well suited in numerical modeling of hysteretic systems. The model combines the Bouc-Wen element in parallel with a spring and a viscous dashpot. The modified Bou-Wen [83] model introduces additional viscous dashpot in series and a spring element in parallel to better predict the force-velocity hysteresis. Part of the multi-parametric Bouc-Wen element parameters are strong functions of applied field while others are applied to control the smooth transition from pre-yield to post-yield regions. A hydromechanical model was also developed [84-86] to address the non-linear behavior of MR dampers. The hydromechanical model consists of physically motivated hydraulic and mechanical lumped parameters to represent fluid inertia, resistance, yield force and compliances associated with MR dampers. The model was able to account for the pre-yield hysteretic behavior of an MR damper. Recently, Hu *et al* [87] formulated the rate-dependent elasto-slide model, which uses a rate-dependent slide in series with a spring for pre-yield stiffness. The rate dependent elasto-slide is then combined in parallel to a viscous damper to emulate the post-yield behavior of the MR fluid, and a stiff spring to represent accumulator and dynamic rod seals. The model has few parameters which are amplitude and frequency independent. The model was able to

capture and reconstruct the non-linear dynamic hysteresis behavior of elastomeric and MR dampers for the tested amplitude and frequency ranges.

Limited work has been done in modeling hybrid magnetorheological fluid-elastomeric lag dampers. In the feasibility study carried out on the $1/6^{th}$ Froude scale MRFE damper by Kamath *et al* [10, 72], the device was decoupled into two components combined in parallel: a passive component comprising of elastomer and zero-field MR fluid responses and an active components related to the MR effect. The MR effect caused by magnetic field application is extracted form the system by subtracting the field-off damping force from the field-on force, both measured at the same frequency and amplitude. The passive contribution is then modeled with the complex modulus method while the active part is modeled with the non-linear viscoelastic-plastic model. In feasibility study presented by Hu *et al* [7] and the full-scale tubular type MRFE lag damper also developed by Hu *et al* [14], the elastomeric and the hydraulic part are inherently decoupled systems. Thus, each system is independently modeled using the distributed rate-dependent elasto-slide model for the elastomer and the rate-dependent elasto-slide model for the MR fluid. The total effect is a linear summation of the individual contributions.

In addition, these parametric models are based on the physical phenomena of the system whereby a series of mechanisms and/or mathematical functions are formulated to relate the input to the output. There are two main shortcomings in applying these models to the snubber type MRFE lag damper under study:

1) These models do not describe adequately the actual physical flow phenomenon or flow dynamics in fluid based MR dampers. They do not

present the interaction between mechanical, hydraulic and magnetorheological systems, which is an inherent feature of hydraulic based MRFE dampers.

2) Most models are not sufficient to design and predict damper performance *a priori*, before development and production.

3) The snubber type MRFE device has a completely coupled elastomeric, hydraulic and magnetorheological system which the aforementioned models do not address. The snubber type MRFE damper has its body or chambers made of elastomeric material into which fluid is contained. However, previous models are formulated independently for elastomeric or MR damper and do not consider a situation in which the two systems are coupled.

4) Consequently, it is difficult to employ such models to describe the dynamics of the snubber type MRFE device, and to be applied in dynamics and aeromechanical stability analysis of the helicopter rotor system.

Hydromechanical modeling has been applied in passive engine mount systems [88, 89] and active ER and MR damper systems [84-86], but there only have been limited studies in their application in helicopter damping systems and specifically in snubber type MRFE lag dampers The hydromechanical approach concentrates matter and energy into discrete "lumps," which lead to ordinary differential equations. In contrast, a more complex approach would be to consider a "continuous" distribution of matter, which always leads to complex partial differential equations [90]. The hydromechanical model, thus, is less complex, and deals with time-varying behavior

of connected components or lumps of a system, assuming no span-wise variation within each component or lump. The model is a design based model which describes the damper system with a series of lumped hydraulic and mechanical components. The model employs physical parameters such as inertia, damping, yield force and compliances that are dependent on damper geometry and material properties of components, which can potentially be approximated *a priori*.

1.4 Scope of Current Research

A semi-active snubber type Magnetorheological Fluid-Elastomeric (MRFE) lag damper technology is developed in this research to mitigate amplitude and temperature dependent damping loss issues associated with passive elastomeric and fluid-elastomeric (FE) lag dampers and to provide adaptable lag damping for varying lag damping requirements at different flight conditions. The enhanced and controllable energy dissipative behavior, and thus the associated damping, of smart MR and MRFE lag dampers have been proven to be potentially effective in helicopter rotor stability augmentation. These semi-active damping devices could be a cost-effective alternatives to existing passive dampers, which can provide adaptive, selective and individual damping augmentation of the rotor. They can also be designed without changing the existing volume envelope of elastomeric or FE lag dampers, paving the way for their smooth integration into the rotor systems. Due to MR and MRFE lag dampers low power requirements, power input from neighboring systems (for example, powered through existing de-icing slip-ring) can be tapped to supply the required current to activate these adaptive systems.

The current research effort is based on the process of developing and modeling a novel snubber type MRFE lag damper. The dissertation is thus organized in 6 chapters:

- Chapter 2: The performance of a baseline snubber (also known as round-stacked) type FE lag damper (Lord Corp. Bell-430 Fluidlastic® lag damper) is investigated. Characterization and performance of the FE damper under varying single and dual frequency excitation are examined. Further, effects of temperature on damper performance were also characterized. To describe the dynamic behavior of the FE lag damper, a hydromechanical model was developed to describe the damper hysteretic behaviors over a broad amplitude and temperature conditions, and the modeling results were correlated with the experimental data using measured and optimized model parameters. The analysis combines lumped mechanical and hydraulic parameters that can describe flow resistance and inertance, and chamber compliances. The model effectively describes the contribution from each system component and the inherent coupling effect between chamber compliance and viscous damping. Extensive FE damper experiments including single and dual frequency at varying temperatures were conducted, and the model was validated at all test conditions.
- Chapter 3: The development of a snubber type MRFE lag damper is described. The MRFE damper is characterized and its damping performance under varying single and dual frequency excitation are evaluated. The MRFE damper performance is also compared with the baseline FE damper. The

hydromechanical model from chapter 2 was re-developed to describe the non-linear, hysteretic behavior of the MRFE damper over a broad amplitude range, under single and dual frequencies. The modeling results were correlated with the experimental data using measured and optimized model parameters. The analysis combines lumped magnetorheological, mechanical and hydraulic parameters that can describe yield strength, flow resistance and inertance, and chamber compliances. The model effectively describes the contribution from each system component and the inherent coupling effect between chamber compliance and viscous damping.

- Chapter 4: The effects of temperature on performance of the MRFE damper are evaluated. Its potential in compensating temperature effects is examined. Since hydromechanical model parameters are fundamentally functions of damper geometry and material property, temperature effects will only cause the latter to change. Thus, material properties at each temperature are initially estimated, which later are reasonably scaled as necessary to accurately simulate the measured hysteretic force-displacement and force-velocity histories of the MRFE damper under single and dual frequency excitations. Thus, all except one parameter are estimated using valve geometry and material properties.
- Chapter 5: A feasibility study of applying the MRFE damper in temperature compensating control schemes is presented. Using experimental database and the hydromechanical model of the MRFE damper, control systems were designed to track a reference damping profile, which is a function of

amplitude only, in the presence of measured amplitude and temperature variations at the rotor lag/rev frequency (3.8 Hz). Both gain scheduled (interpolating look-up table) and closed-loop (proportional-integral and gain scheduling) techniques were employed in simulations and experiments.

- Chapter 6: Conclusions of the present work and original contributions are summarized and some recommendations for future work are discussed.

(a) Flat plate or double lap shear type

(b) Tubular or concentric type

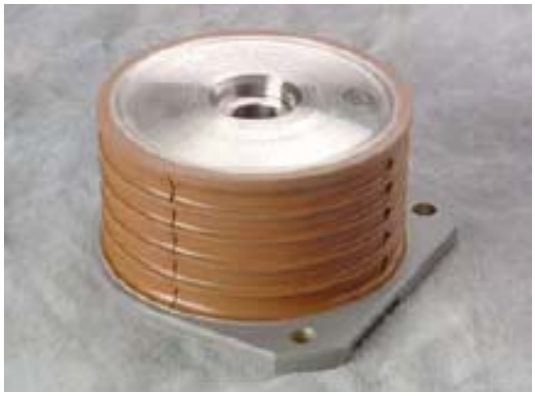

(c) Snubber or round-stacked type

Figure 1.1: Types of elastomeric lag dampers

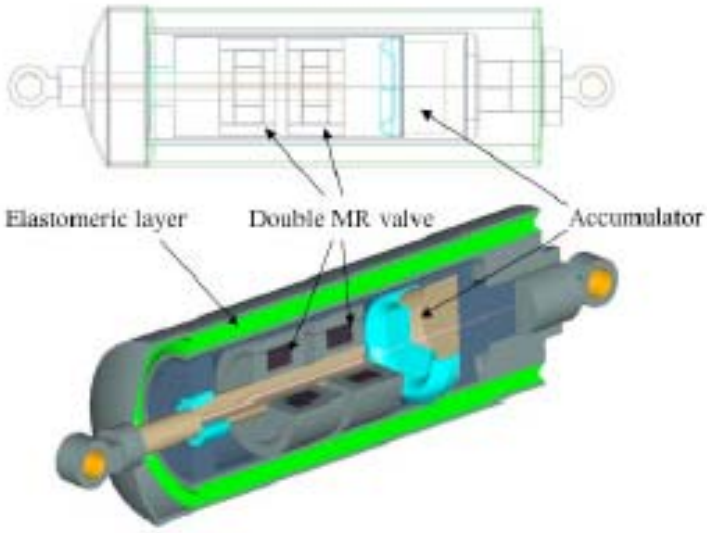

(a) Tubular type, linear stroke MRFE lag damper configuration

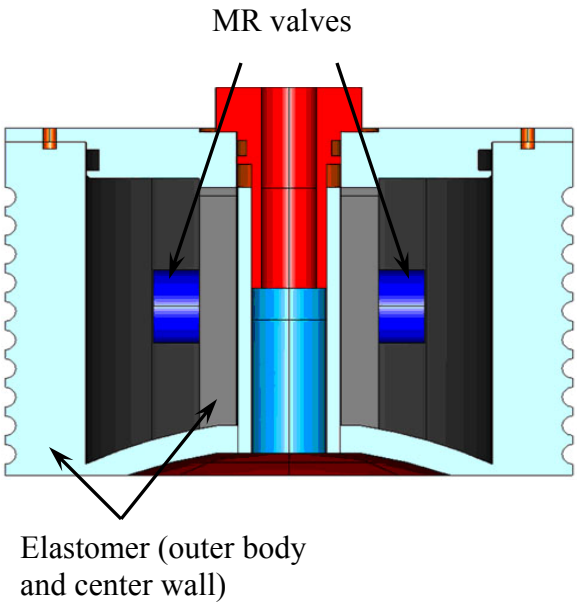

(b) Snubber type MRFE lag damper configuration

Figure 1.2: Potential MRFE lag damper design configuration schemes

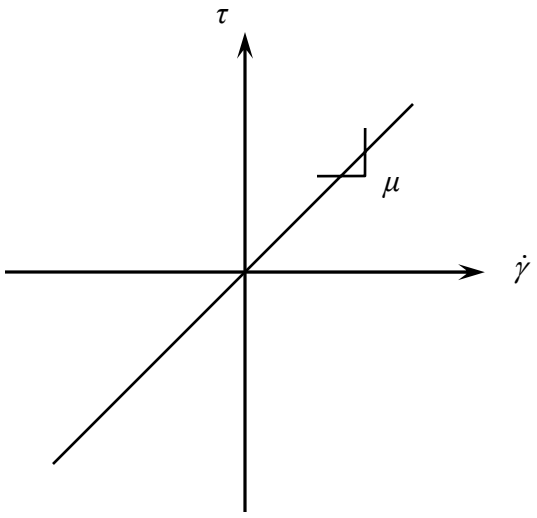

(b) Off-state

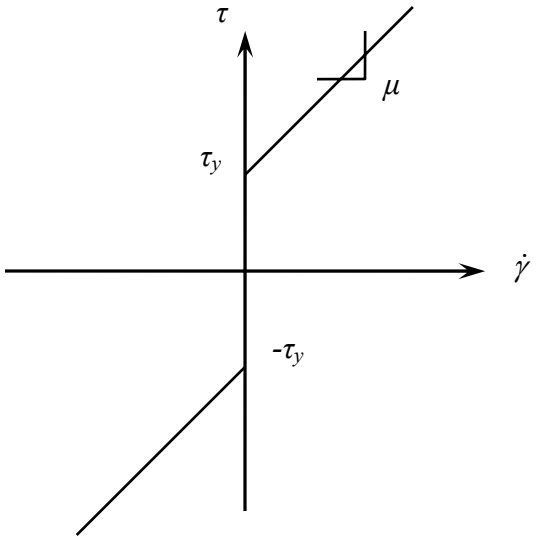

(b) On-state

Figure 1.3: Simplified Bingham yield behavior of MR fluids

Chapter 2: Hydromechanical Analysis of a Snubber Type Fluid-Elastomeric Lag Damper Incorporating Temperature Effects

2.1 Introduction

Most modern hingeless/bearingless helicopter main rotors are equipped with lead-lag dampers to alleviate aeromechanical instabilities such as air and ground resonance resulting from the interaction of the poorly damped regressing lag mode of the rotor blades with body support modes. These types of rotors are typically fitted with lag dampers made of passive materials, such as elastomers, to dissipate energy. A typical elastomeric damper is made of elastomer sandwiched between three parallel attachment plates [8]. Another type has a tubular configuration where an elastomeric ring is bonded between two concentric cylinders [14]. Compared to conventional hydraulic lag dampers, elastomeric lag dampers have lower parts count, are lighter in weight, easier to maintain, and more reliable [4, 6]. Unlike hydraulic dampers, elastomeric dampers do not produce extremely high damping forces at high lead-lag velocities [6]. In order to provide the required damping, a highly hysteretic elastomeric material is utilized. Under dynamic lag motions, the elastomer is sheared and provides damping through energy dissipation. In addition, the elastomer introduces stiffness into the system that can be used as a design parameter to change the natural frequency of the lag mode to avoid resonances [6, 7].

These highly damped elastomeric dampers exhibit a non-linear hysteretic response to dynamic loading. Further, the damping and stiffness properties of elastomeric dampers are non-linear functions of the lag/rev frequency, dynamic lag amplitude, and operating temperature. It has been shown that elastomeric damping and stiffness levels diminish markedly as amplitude of damper motion increases [2-8]. In addition, there is a reduction in dimensional damping as the excitation frequency is increased. At small lead-lag displacements, these elastomeric dampers have exhibited low loss factor and high stiffness, resulting in unfavorable limit cycle instabilities [4]. In forward flight conditions, the blade lead-lag motion in helicopters occurs at two frequencies, the lag/rev frequency and 1/rev frequency, and as the 1/rev amplitude is increased, it substantially reduces damping at lower lag/rev amplitudes, thus causing undesirable limit cycle oscillations [4, 6]. Hence, it is of great value to build a lead-lag damper having as simple a design as elastomeric lag dampers, but with stiffness and damping characteristics being as independent of the excitation frequency and amplitude as possible. This kind of arrangement will broaden the operational range over which the designed damping is most effective. To this effect, a fluid-elastomeric (FE) lead-lag damper, a combined system of viscous fluid damping and elastomeric material, was uniquely designed by Lord Corporation, and is also referred to as Fluidlastic® lag damper [2, 4, 8, 9]. FE lag dampers exhibit a much stable stiffness and loss factor characteristics that are less dependent on excitation amplitude than elastomeric dampers [2, 4, 8]. In this kind of damper arrangement, the majority of damping is supplied through viscous damping, thus the elastomeric material employed need not be selected based on its damping property, but rather on

its stiffness and shear fatigue properties [8]. Selection of elastomeric material based on fatigue performance will also help reduce the overall damper size. In addition, FE dampers are able to provide higher motions and longer service life [2]. Further, fluid performance parameters can be optimized to maximize damping by adjusting orifice geometries and fluid viscosity, and lowering elastic stiffness by utilizing elastomers with improved fatigue life and greater modulus range [2]. This will help the lag damper to maintain a steady performance over a wider range of operating spectrum. FE lag dampers show a relatively modest dependence of in-phase and quadrature stiffness on excitation frequency [8].

Characterization of fluid-elastomeric lag dampers under varying operating temperature conditions is of significant importance in damper performance. In a typical damping device, there are two main sources of temperature variation in the system: (1) ambient atmospheric temperature conditions which tend to decrease or increase damper operating temperature; and (2) in-service self-heating which is associated with internal energy dissipation. Elastomeric dampers are shown to exhibit thermoviscoelastic behavior, where the damper's complex modulus changes non-linearly with variation in operating temperature [4, 11]. Elastomeric dampers present a temperature dependent softening and stiffening at low and high temperatures respectively [3, 11] which can have an adverse effect on damper performance. When exposed to low temperatures, elastomeric materials tend to become hard and firm. Their elasticity decreases and damping is increased [51]. Hausmann and Gergely [11] conducted temperature tests to characterize the effects of test temperature and self-heating on damper performance. The hysteresis plots clearly showed the decrease in

dissipated energy as elastomer temperature is increased. Experimental results have also shown a significant reduction in the linearized in-phase and quadrature moduli in elastomeric lag dampers with decreasing temperature [3, 11, 52]. In typical fluid or hydraulic dampers, the dependence of liquid viscosity with temperature is a trend where liquid viscosity decreases with increasing temperature. Generally, viscosity decreases rapidly with temperature [55]. The damping force of a hydraulic damper system is directly proportional to viscosity of the enclosed fluid. Thus, as the fluid temperature increases, fluid viscosity tends to decline, resulting in lower damping forces. Furthermore, snubber type fluid-elastomeric lag dampers present additional complexity as they are coupled devices of elastomeric and hydraulic systems.

In the present study, the performance and characteristics of a full scale snubber type round-stacked FE lead-lag damper, also known as Fluidlastic® (LORD Corp.) lead-lag damper, is investigated at varying operating temperature conditions. Due to the kinematical complexity in modern hingeless helicopter main rotors, snubber type FE lag dampers are usually made from a laminated stack of alternating elastomeric-metallic rings, and damping fluids are included in the flexible body to increase dynamic range of the FE damper [9]. For this type of damper, the elastomer body which contains fluid acts as a seal and as a pump to force viscous fluid between chambers to create damping. Consistent with the loading conditions for a helicopter lag damper, the FE damper and the FE damper elastomeric body were tested under single frequency (lag/rev) and dual frequency (lag/rev and 1/rev) sinusoidal excitation at temperatures varying from 10°C to 50°C (50°F to 122°F), which are within the ambient operating range. These experiments were conducted by placing the damper in

an environmental chamber and adjusting the ambient temperature surrounding the damper. At each of the set points, the temperature was held constant for up to 60 minutes prior to beginning the tests, which were performed beginning at temperature closest to the ambient and with each successive test moving farther from the starting point (colder/hotter than the previous).

The complex modulus method is employed to characterize the FE damper performance as the operating temperature is varied. It is shown that the equivalent damping of the FE damper decreases with increasing temperature. In addition, the in-phase stiffness of the damper tends to decrease with increasing temperature. However, the complex modulus linearization technique does not identify and describe the inherent hydraulic behavior of the FE damper under sinusoidal excitation. The model does not describe adequately the actual physical flow phenomenon or flow dynamics in the fluid based FE dampers. It treats the damper as a bulk body or a 'black box,' and tries to depict the over all performance of the system by relating the output to the input though the complex modulus. Parameter identifications are also based on test results. However, the snubber type FE damper has its body or chambers made of elastomeric material into which fluid is contained resulting in two completely coupled systems (hydraulic and mechanical). Consequently, it is difficult to apply such a model to describe the dynamics of the snubber type FE device. It does not present the interaction between mechanical and hydraulic systems, which is an inherent feature of hydraulic based FE damper.

To account for the hysteretic behavior and accurately predict the damping force of the FE lead-lag damper, a design motivated hydromechanical model, based on

lumped parameters, is formulated. Few models based on lumped parameter approaches have been proposed to model the hysteretic behavior of FE lag damper [2 53, 54]. These models are shown to give good correlation between measured data and model results. However, these models do not describe well the flow dynamics of the hydraulic system. The physical interpretation of the analogous mechanical system and the logic behind are not well explained. All model parameters are estimated and optimized to simulate dynamic damper performance. The shear and bulge stiffness of the FE damper are given as non-linear functions of displacement and velocity. The model results have shown the shear stiffness to be more dominant than bulge stiffness, however test results have suggested otherwise. The damping from elastomer shear and bulging, and plus the hydraulic or viscous damping are all assumed to be a non-linear functions of velocity. Again, the model damping from shear deformation is significant, but in-house testing have shown that minimal damping is gained from elastomer in shear, and majority of the damping from the FE device is due to flow resistance or viscous flow (up to 80%). The reasoning behind the fluid inertial effect and fluid mass amplification outlined in the models were not clearly explained. The models, which are formulated and validated at room temperature, utilize as many as fourteen parameters [53, 54]. To account for temperature effects, a non-linear ADF (Anelastic Displacement Field) and slider elements [46] are added in parallel with the room temperature model [54]. This modification further introduces eight parameters. In addition, the ADF based model only accounted the temperature dependent behavior of the FE damper elastomeric body, and the temperature characterization of the hydraulic system was not addressed.

The proposed hydromechanical model was formulated to model the dynamic behavior of a snubber type fluid-elastomeric lag damper. Although hydromechanical modeling has been applied in passive systems [88, 89], there only have been limited studies in their application in helicopter damping systems and specifically in snubber type FE lag dampers, which are coupled systems of hydraulic and elastomeric material. The hydromechanical model is a design based model which describes the time-varying behavior of a series of lumped hydraulic and mechanical components of a damper system. The model describes the physical flow dynamics of the system and takes into account chamber compliance, fluid inertance and resistance. Thus, model parameters can potentially be determined from damper geometry and material properties. Model parameters at different test temperatures basically vary depending on damper material behaviors at the specified temperatures. Once model parameters have been established at each test temperature, the model is shown to reconstruct quite accurately the measured hysteretic force-displacement, force-velocity and force-time histories under single and dual frequency excitations.

2.2 Temperature Testing of FE Lag damper

A pictorial and section view of the baseline FE damper is shown in Figures 2.1a and 2.1b. The flexible body of the damper is made of metallic shims interspersed with elastomeric layers, or a multiple lamination of metallic and elastomeric ring layers. These laminates are bonded to metallic plates at both ends. At center height, a circumferential middle plate is attached to the elastomeric cylinder wall. A flexible center wall is placed in the middle of the cavity of the snubber body. This flexible center wall made of rubber runs along the diameter of the flexible cylinder,

completely molded at both ends to the elastomeric damper body. This creates two distinct volume chambers into which a viscous fluid is poured and completely sealed. Note that this baseline FE damper (Bell 430 damper) is factory assembled as a molded unit, so there is no possibility for fluid to be exchanged from one reservoir to the other without passing through one of the flow ports located in the center wall. There are four threaded holes for filling and draining fluid, two on each side of the damper. Once fluid is poured into the chambers, the holes are bolted and a compression bolt is mounted through the center hole of the damper assembly, which creates a positive internal pressure. This damper has a compact size with a height of about 106. 68 mm (4.20) in and diameter of 118.11 mm (4.65 in). In the current helicopter rotor system as shown in Figure 2.2, each blade is equipped with a pair of FE lag dampers. The lag dampers, which are housed in the pitch horn adapter assembly, are attached to the inboard side of the blade cuff or torque tube, which in turn is attached to the blade and flexure at its outboard end. The paired lag dampers are interconnected by a shear restraint that is installed in the composite yoke flexure. The relative motion of the flexure yoke and the torque tube, which constitutes the lead-lag motion, deforms the paired lag dampers. The flow ports are located in the middle of the flexible center wall, and the deformation of the snubber body can force the fluid to flow between chambers through these port holes, providing the required blade lead-lag damping.

To begin evaluating the FE damper performance, its dynamics are first studied. For small displacement applied at the center of the damper, the FE damper is assumed to deform as shown in Figure 3.3. In the actual rotor blade setting, the lag damper is

intended to accommodate both radial and translational lead-lag motions of the blades. However, for small displacement, approximation of the actual lead-lag motion of the rotor blades with translational motion is assumed to be acceptable. The forcing function is applied at the damper mid-plate which creates a triangular damper deformation with the upper and lower plates. This causes the volume of one of the elastomeric chambers to decrease, forcing the fluid to flow through the flow ports into the other chamber as the other chamber volume increases to compensate for the in-flow. Due to the absence of a well defined piston and the complex damper features, the input displacement excitation is not uniform throughout the damper height. It varies from zero at damper extremities to maximum at damper center, which is the input displacement from the MTS machine. However, all damper analysis is evaluated based on the input excitation at damper mid-plate.

To mimic the lead-lag motion of helicopter blades as applied to the FE lag damper, a test fixture was fabricated to hold dampers in a 24.5 kN MTS servo-hydraulic testing machine. Figure 3.3a shows the baseline FE lag damper test set-up where the mid-plate is connected to the load cell by means of the test jig via an extension rod. The lower mounting bracket is attached to the lag damper through a mounting rod that is slotted in at the mounting hole, located at the lag damper center, passing through the center wall. The lower mounting bracket is attached to the MTS actuator through an extension rod. The center wall is oriented horizontally such that the motion of the MTS actuator connected to the lower bracket forces fluid to flow from one chamber to the other, by deforming the elastomeric outer wall, and emulating the lead-lag motion. The displacement and force were measured by the

LVDT sensor and load cell of the MTS machine. The frequencies of excitations were chosen to be 3.8 Hz and 5.8 Hz, which correspond to an actual rotor system lag/rev and 1/rev or rotor RPM frequency. Damper testing was carried out with varying excitation amplitudes. The excitation amplitudes ranged from 0.762 mm (30 mil) to 3.81 mm (150 mil) in increments of 0.50 mm (20 mil) at both lag/rev and 1/rev frequencies.

To evaluate FE damper performance at varying temperatures, the damper was place in an ATS environmental heating chamber or test oven as shown in Figure 3.3b. This test oven is capable of generating temperatures as high as 425°C. It is also designed for cryogenic cooling, and liquid nitrogen (LN2) tanks were used for lower temperature tests (10 and 20ºC). The oven is designed to be mounted on the MTS machine (Figure 2.3a) using mounting brackets. The environmental heating chamber is equipped with a temperature control system, which regulates and maintains the desired temperature as measured by the control thermocouple. These experiments were conducted by placing the damper in the environmental chamber and adjusting the ambient temperature surrounding the damper. Because the temperature tests were performed on a factory sealed FE damper, it was not possible to access inner damper body and the enclosed fluid to measure and control their temperature. Thus, based on our experience with a similar but modified damper with accessible fluid chambers, in the current FE damper, at each test temperature, the ambient chamber temperature was held constant between 45 to 60 minutes prior to the beginning of each test. It is assumed within this time range, the damper inner and outer temperatures are the same as the ambient chamber temperature.

For single frequency evaluation, sinusoidal displacement tests were carried out with varying excitation amplitudes. The excitation amplitudes ranged from 0.762 mm (0.03 in) to 3.81 mm (0.15 in) in increments of 0.50 mm (.02 in) at both lag/rev and 1/rev frequencies. The single frequency force-displacement and force-velocity data were utilized to estimate the hydromechanical model parameters and evaluate model dependability. For dual frequency tests, a dual frequency combination of 3.8 Hz/5.8 Hz was used to evaluate the fidelity of the model in multi-frequency loading scenarios.

During each test, the sampling frequencies were 1024 Hz and 512 Hz for the single and dual frequency tests respectively, which are considerably higher than the required Nyquist frequency. Nominally, ten cycles of force and displacement data were collected at each test set up. To reduce the noise of the input sinusoidal displacement signal, a Fourier series was used to reconstruct the input displacement. The reconstructed displacement signal was then differentiated to obtain the velocity signal. The Fourier series expansion of the input displacement signal is given by:

$$x(t) = \frac{x_o}{2} + \sum_{k=1}^{\infty} \left(X_{c,k} \cos(k\omega t) + X_{s,k} \sin(k\omega t) \right) \tag{2.1}$$

where

$$X_{c,k} = \frac{\omega}{\pi k} \int_0^{\frac{2\pi}{k\omega}} x(t) \cos(k\omega t) dt$$

$$X_{s,k} = \frac{\omega}{\pi k} \int_0^{\frac{2\pi}{k\omega}} x(t) \sin(k\omega t) dt \tag{2.2}$$

Any bias and higher harmonics at single frequency tests were filtered, so as only the frequencies of interest, i.e. $\omega = \omega_{lag}$ and $\omega = \omega_{pri}$, remained. Then the displacement and velocity data were reconstructed using the first harmonics only as

$$x(t) = X_s \sin(\omega t) + X_c \cos(\omega t)$$
$$\dot{x}(t) = \omega X_s \cos(\omega t) - \omega X_c \sin(\omega t) \tag{2.3}$$

For dual frequency evaluation, the HP8904A function generator was used to create and sum the two sinusoidal signals in order to attain an accurate dual frequency excitation. The general equation for the input dual displacement signal is expressed as:

$$x(t) = X_{lag} \sin(\omega_{lag} t) + X_{pri} \sin(\omega_{pri} t) \tag{2.4}$$

where ω_{lag} and X_{lag} represent the lag/rev (lag mode) frequency and the corresponding input amplitude while ω_{pri} and X_{pri} represent the 1/rev (rotor) frequency and the corresponding amplitude. The signal is periodic with a period equal to the frequency corresponding to the highest common factor of the two harmonics, which is 0.2 Hz. Thus, the displacement input signal was filtered using the Fourier expansion at 0.2 Hz as the base frequency. The first twenty-nine harmonics were required to reconstruct the dual frequency displacement signal. The measured force data at all frequencies and temperatures were not filtered and were used in the developed model as recorded.

At selected amplitude of 2.286 mm, Figures 2.4a and 2.4b show the force versus displacement plots of the FE damper at lag/rev and 1/rev frequencies and at varying temperatures ranging from 10°C to 50°C. In each force-displacement plot, the area enclosed by the hysteresis cycle is proportional to the amount of energy dissipated per cycle. The damping available is in turn proportional to the energy dissipated per

cycle. It is observed that as damper temperature increased, the area enclosed per cycle, and thus dissipated energy per cycle, decreased. Thus, for both frequencies, maximum damping was attained at the lowest temperature (10°C), and minimum damping at the highest temperature (50°C).

2.3 Linearized Characterization of FE Lag Damper

A typical approach for characterization of damper performance is the complex modulus method. It is a linear characterization technique of damper properties which treats the complex stiffness k^* as a combination of the in-phase stiffness k' and the loss stiffness k'', given as:

$$k^* = k' + ik'' = k'(1 + i\eta) \tag{2.5}$$

where the loss factor η is defined as the ratio of the loss stiffness to the in-phase stiffness. The damper force is estimated by the first Fourier sine and cosine components at the excitation frequency:

$$F(t) = F_s \sin(\omega t) + F_c \cos(\omega t) = k'x(t) + \frac{k''}{\omega}\dot{x}(t) \tag{2.6}$$

The stiffness k' and k'' are determined by substituting the displacement function and its derivative from equation 2.3 into the force equation above:

$$k' = \frac{F_c X_c + F_s X_s}{X_c^2 + X_s^2} \tag{2.7}$$

$$k'' = \frac{F_c X_s - F_s X_c}{X_c^2 + X_s^2} \tag{2.8}$$

The equivalent damping C_{eq} is approximated by:

$$C_{eq} \cong \frac{k''}{\omega} \tag{2.9}$$

This linearization technique is an approximation because the complex stiffness assumes steady state harmonics at the excitation frequency. However, it gives an acceptable representation of the linearized in-phase stiffness and equivalent damping of the FE damper for comparing overall damping performances under different loading conditions and temperature variations.

The in-phase stiffness k' and equivalent damping C_{eq} of the FE damper at lag/rev and 1/rev frequencies for different test temperatures are shown in Figures 2.5 and 2.6. For all frequency cases, the equivalent damping and in-phase stiffness of the FE damper is temperature dependent, decreasing in magnitude as operating temperature increases. The damping losses with temperature increment are more pronounced than the stiffness losses, where as high as a 50% damping loss is observed at lag/rev frequency as the temperature varied from 10°C to 50°C. Further, the equivalent damping of the device is moderately dependent on amplitude. In addition, for both lag/rev and 1/rev frequencies, similar damping behaviors are observed at all temperatures. The in-phase stiffness variation of the FE damper is fairly small at all dynamic amplitudes tested at both frequencies. However, the stiffness does show a temperature dependent behavior for the range of test temperatures. The in-phase stiffness of the damper decreases noticeably as the test temperature is increased from 10°C to 50°C. However, this loss is not as severe as the damping loss that occurred with increasing temperature.

Helicopter lag dampers encounter multi-frequency excitation, especially in forward flight, where the forced lag motion occurs at the 1/rev rotor frequency. Under such circumstances, the complex modulus of an elastomeric damper at Lag/rev

frequency decreases significantly, especially at lower amplitudes. However, in the case of the fluid-elastomeric lag damper, the lag/rev damping available at dual frequency is higher than the damping at single frequency. This is shown at 10°C and 50°C in Figures 2.7 and 2.8 respectively. This can be attributed to the increase in flow rate, resulting in a rise in viscous losses, as damper stroke is increased. Note that majority of the damping is provided through viscous flow. This issue will be addressed in *Section 2.5*. However, the in-phase stiffness of the FE damper remains relatively constant at both temperatures.

2.4 Hydromechanical Modeling of FE Damper

The aforementioned complex modulus linearized characterization of the FE damper is a system or mechanism based model for prediction of the dynamic amplitude and temperature dependent damping and stiffness. It, however, does not describe the flow dynamics within the FE damper, which is an inherent characteristic in a hydraulic based damper system. The model treats the damper as a 'black box,' and fits the Kelvin model to the over all damper behavior relating output to input. It does not describe the inherent hydromechanical coupling phenomenon of the system and does not distinguish between the contributions of the elastomeric material and the hydraulic system. To better understand the behavior of such a passive device, a hydromechanical model based on lumped fluid and mechanical systems is proposed.

The proposed lumped parameter control volumes are shown in Figure 2.9. For clarity, the two flow ports or valves are identified with subscripts *a* and *b*. There are two volume chambers (1 and 5) which are lumped into fluid pressures P_1 and P_5 and compliances S_1 and S_5. Both S_1 and S_5 represent the compliances of the fluid and the

chamber. Control volumes *a2, a3, a4, b2, b3* and *b4* are lumped into fluid inertances I_{a2}, I_{a3}, I_{a4}, I_{b2}, I_{b3} and Ib_4 and passive flow resistances R_{a2}, R_{a3}, R_{a4}, R_{b2}, R_{b3} and R_{b4}. A one-dimensional fluid flow is assumed such that the velocity and pressure of a control volume are span wise constant. However, they do vary time wise. In addition, an incompressible and laminar flow is also assumed.

The model is first formulated for a general case where the two flow ports and two chambers are assumed to be different. The Kelvin model is assumed for the FE damper elastomeric body in shear deformation, where it is modeled as a linear spring and linear dashpot combination. The two elastomeric chambers are broken into two semi-circular wall connected at the center, and they are assigned masses m_{r1} and m_{r5}. The shear mode in-phase stiffness and equivalent damping of the FE damper elastomeric body from the complex modulus method are utilized as the spring constants k_{r1} and k_{r5} and damping coefficients C_{r1} and C_{r5}. These values are estimated by pouring out the viscous fluid from the FE device and testing the FE damper elastomeric body (i.e. empty FE damper) at varying temperatures.

The proposed lumped parameter model includes three lumped masses (m_A, m_B and m_r) and three dynamic degrees of freedom ($x(t)$, $x_A(t)$ and $x_B(t)$), as will be shown later. The governing equation of motion of the elastomer is given by:

$$F(t)-(k_{r1}+k_{r5})x(t)-(C_{r1}+C_{r5})\dot{x}(t) - A_p(P_5(t)-P_1(1))=(m_{r1}+m_{r5})\ddot{x}(t) \tag{2.10}$$

Similar to an elastomer deformed in shear, bulging of an elastomer due to volumetric expansion exhibits damping. Colgate *et al* [91] recommend that some improvement could be attained in modeling by considering bulge damping. This

compliant damping is captured by introducing a resistant parameter [89] on the net flow into the compliant chambers resulting in the volumetric expansion. Thus, applying the continuity argument to the volume chambers 1 and 5, we get:

$$A_p\dot{x}(t) - q_a(t) - q_b(t) = S_5(\dot{P}_5(t) - R_5(A_p\ddot{x}(t) - \dot{q}_a(t) - \dot{q}_b(t))) \tag{2.11}$$

$$-A_p\dot{x}(t) + q_a(t) + q_b(t) = S_1(\dot{P}_1(t) - R_1(-A_p\ddot{x}(t) + \dot{q}_a(t) + \dot{q}_b(t))) \tag{2.12}$$

where R_1 and R_5 are the elastomeric resistances. The flow rates through flow ports *a*, and *b*, in terms of the fluid inertance displacements x_a and x_b are given by:

$$q_a(t) = A_{a2}\dot{x}_{a2}(t) = A_{a3}\dot{x}_{a3}(t) = A_{a4}\dot{x}_{a4}(t) \tag{2.13}$$

$$q_b(t) = A_{b2}\dot{x}_{b2}(t) = A_{b3}\dot{x}_{b3}(t) = A_{b4}\dot{x}_{b4}(t) \tag{2.14}$$

where A_{ai} and x_{ai} are the cross sectional area and fluid inertance displacement of the i^{th} lump in flow port *a*, and similarly for flow port *b*. The combined compliances of the fluid chambers for control volume 1 and 5 are given by:

$$S_1 = \frac{A_p^2}{k_{c1}}, \qquad S_5 = \frac{A_p^2}{k_{c5}} \tag{2.15}$$

Here, k_{c1} and k_{c5} represent the bulge stiffness effects of the two volume chambers, which are dominated by the elastomer bulge stiffness contribution. Due to the complexity of the damper design, deformation and the absence of a well defined piston, an equivalent piston area, A_p, is formulated to account for the total displaced fluid volume.

Also from the hydraulic model shown in Figure 2.9, the total pressure drop in the two flow ports or valves (control volumes 2 to 4) due to fluid flow is given by:

$$(P_5(t) - P_1(t)) = I_a\dot{q}_a(t) + R_a q_a(t) \tag{2.16}$$

$$(P_5(t) - P_1(t)) = I_b\dot{q}_b(t) + R_b q_b(t) \tag{2.17}$$

The terms I_a and R_a are given by:

$$I_a = \rho \sum_{i=2}^{4} \frac{l_{ai}}{A_{ai}} \tag{2.18}$$

$$R_a = \frac{128\mu(T)}{\pi} \sum_{i=2}^{4} \left(\frac{l_{ai}}{D_{ai}^4} \right) + R_{min\,orlosses} \tag{2.19}$$

where ρ is fluid density and l_{ai} and D_{ai} are length and diameter of the i^{th} lump in flow port a. The equation for the resistance is derived from laminar flow analysis. The above equations holds true for the second flow port by replacing the subscript a with b. As shown in the above equation, the viscosity μ is a function of temperature, and it was estimated at each test temperature using a rheometer. Due to laminar flow assumption with low Reynolds number, the minor losses are ignored.

By eliminating the internal variables P_1 and P_5 from equations 2.10 – 2.12 and 2.16 – 2.17, we obtain the following three equations in terms of time varying variables:

$$\begin{aligned}&(m_{r1} + m_{r5})\ddot{x}(t) + (C_{r1} + C_{r2})\dot{x}(t) + (k_{r1} + k_{r2})x(t) \\ &+ (C_{c1} + C_{c5})\left(\dot{x}(t) - \dot{x}_A(t) - \dot{x}_B(t)\right) + (k_{c1} + k_{c5})\left(x(t) - x_A(t) - x_B(t)\right) = F(t)\end{aligned} \tag{2.20}$$

$$\begin{aligned}&m_A\ddot{x}_A(t) + C_A\dot{x}_A(t) - (C_{c1} + C_{c5})\left(\dot{x}(t) - \dot{x}_A(t) - \dot{x}_B(t)\right) \\ &- (k_{c1} + k_{c5})\left(x(t) - x_A(t) - x_B(t)\right) = 0\end{aligned} \tag{2.21}$$

$$\begin{aligned}&m_B\ddot{x}_B(t) + C_B\dot{x}_B(t) - (C_{c1} + C_{c5})\left(\dot{x}(t) - \dot{x}_A(t) - \dot{x}_B(t)\right) \\ &- (k_{c1} + k_{c5})\left(x(t) - x_A(t) - x_B(t)\right) = 0\end{aligned} \tag{2.22}$$

The generalized inertance displacement x_A and mass m_A, and the viscous damping C_A for valve a and the bulge damping C_{c1} and C_{c5} are expressed as:

$$x_A = (A_{a4}/A_p)x_{a4}, \qquad m_A = I_a A_p^2, \qquad C_A = R_a A_p^2,$$
$$C_{c1} = R_1 A_p^2, \qquad C_{c5} = R_5 A_p^2 \tag{2.23}$$

This holds true for the second flow path by replacing the subscript *a* with *b*. Equations 2.20 – 2.22 are the basic equations of the hydromechanical model describing the FE damper system. However, it is still difficult to formulate a mechanism and associated equations of motions to describe the system. This is primarily due to the fact that the input displacement *x*, the generalized inertance displacements x_A and x_B are all coupled to each other through the bulge stiffness and bulge damping components. This coupling arises from the fact that both flow ports experience the same pressure drop (equation 2.16 & 17). In addition, in dissimilar valves, which is the initial assumption, there is unequal flow rate in the two valves arising from differences in head losses. We can define a transfer function relation of the flow rates from equations 2.16 and 2.17 as:

$$q_a(i\omega) = \frac{(P_5 - P_1)}{\frac{I_a}{R_a} i\omega + 1} \tag{2.24}$$

$$q_b(i\omega) = \frac{(P_5 - P_1)}{\frac{I_b}{R_b} i\omega + 1} \tag{2.25}$$

Combining the above equations with the generalized inertance displacements from equation 2.23, we get the following relation:

$$\frac{x_A}{x_B}(i\omega) = \psi(i\omega) \tag{2.26}$$

where the valve factor $\psi(i\omega)$ is given by:

$$\psi(i\omega) = \frac{m_B i\omega + C_B}{m_A i\omega + C_A} \tag{2.27}$$

By plugging equation 2.27 in equations 2.20 – 2.22, we get the following 4 equations of motions:

$$\begin{aligned}&(m_{r1} + m_{r5})\ddot{x}(t) + (C_{r1} + C_{r5})\dot{x}(t) + (k_{r1} + k_{r5})x(t) \\ &+ (C_{c1} + C_{c5})\left(\dot{x}(t) - (1+\psi)\dot{x}_A(t)\right) + (k_{c1} + k_{c5})\left(x(t) - (1+\psi)x_A(t)\right) = F(t)\end{aligned} \tag{2.28}$$

$$\begin{aligned}&m_A\ddot{x}_A(t) + C_A\dot{x}_A(t) - (C_{c1} + C_{c5})\left(\dot{x}(t) - (1+\psi)\dot{x}_A(t)\right) \\ &- (k_{c1} + k_{c5})\left(x(t) - (1+\psi)x_A(t)\right) = 0\end{aligned} \tag{2.29}$$

$$\begin{aligned}&(m_{r1} + m_{r5})\ddot{x}(t) + (C_{r1} + C_{r5})\dot{x}(t) + (k_{r1} + k_{r5})x(t) \\ &+ (C_{c1} + C_{c5})\left(\dot{x}(t) - (1+\psi^{-1})\dot{x}_B(t)\right) + (k_{c1} + k_{c5})\left(x(t) - (1+\psi^{-1})x_B(t)\right) = F(t)\end{aligned} \tag{2.30}$$

$$\begin{aligned}&m_B\ddot{x}_B(t) + C_B\dot{x}_B(t) - (C_{c1} + C_{c5})\left(\dot{x}(t) - (1+\psi^{-1})\dot{x}_B(t)\right) \\ &- (k_{c1} + k_{c5})\left(x(t) - (1+\psi^{-1})x_B(t)\right) = 0\end{aligned} \tag{2.31}$$

Equations 2.28 – 2.29 describe damper dynamics in terms of generalized inertance variable x_A and equations 2.30 – 2.31 describe in terms of generalized inertance variable x_B. However, these sets of equations are coupled through the valve factor function ψ. The valve factor ψ which relates the generalized inertance variables, theoretically varies from zero (no flow in flow valve *b*) to infinity (no flow in flow valve *a*). The valve factor is a function of the head losses encountered in the flow ports as shown in equation 2.27. C_{c1} and C_{c5} represent the damping contribution of the elastomeric body due to volumetric flexing of volume chambers.

Figures 2.10 and 2.11 give the mechanism of the proposed hydromechanical model in terms of generalized inertance variables x_A and x_B respectively. Both

systems are composed of parallel and series combinations of linear springs and dashpots elements. The analogous mechanical systems (Figures 2.10 and 2.11) and associated governing equations 2.28 – 2.31 show that the hydromechanical coupling behaviors are evident in the chamber compliance effects (C_{c1}, C_{c5}, k_{c1}, k_{c5}). The generalized inertance masses (m_A, m_B) and viscous damping (C_A, C_B) terms represent contributions from the hydraulic component of the device.

In our present design, since there are two identical flow ports and elastomeric chambers, the following assumptions will hold true: $k_{c1} = k_{c5} = k_c$, $C_{c1} = C_{c5} = C_c$, $m_{r1} = m_{r5} = m_r$, $k_{r1} = k_{r5} = k_r$, $C_{r1} = C_{r5} = C_r$ and $\psi = 1$. Thus, the equations of motion from equation 2.28 – 2.29 will further reduce to:

$$2m_r\ddot{x}(t) + 2C_r\dot{x}(t) + 2k_r x(t) + 2C_c\left(\dot{x}(t) - 2\dot{x}_A(t)\right) + 2k_c\left(x(t) - 2x_A(t)\right) = F(t) \tag{2.32}$$

$$m_A\ddot{x}_A(t) + C_A\dot{x}_A(t) - 2C_c\left(\dot{x}(t) - 2\dot{x}_A(t)\right) - 2k_c\left(x(t) - 2x_A(t)\right) = 0 \tag{2.33}$$

2.5 Parameter Identification and Model Performance

To begin the optimization procedure to accurately simulate measured damper dynamics, some of the parameters were determined initially to lower the number of model optimized parameters. Table 2.1 outlines the measured and model estimated and dependent parameters. The dependent variables are functions of both the measured and estimated parameters. In order to minimize the squared mean error between the measured and predicted damping forces of the FE damper at each test temperature, a constrained least-mean-squared (LMS) error minimization technique was employed to estimate and optimize the equivalent piston area A_p, the bulge

stiffness k_c and the bulge damping C_c. The rubber mass is neglected in this optimization. The error function for the hydromechanical model is expressed as:

$$E(A_p, k_c, C_c) = \sum_{j=1}^{N} \left(F(t_j) - F^*(t_j) \right)^2 \tag{2.34}$$

where $F(t_j)$ is the actual measured force, $F^*(t_j)$ is the calculated force from the hydromechanical modeling, t_j is the time at which the j^{th} sample was measured and N is the number of data points per cycle.

Neglecting the small density variation with temperature, the inertance was assumed to remain constant at all temperatures. The viscosity of the viscous fluid enclosed is measured at each test temperature using an Anton Paar Physica MCR300 parallel disc rheometer. Using the measured viscosity value, the resistance in the port holes is estimated. These results are plotted for both lag/rev and 1/rev frequencies in Figure 2.12. As expected, the resistance decreases significantly with decreasing temperature. Figures 2.13a and 2.13b show the optimized equivalent piston areas obtained from the error minimization procedure at different amplitudes and frequencies. At all temperatures, the equivalent area increases as the stroke amplitude is increased. In addition, there is a small increase in slope as the operating temperature is increased from 20ºC to 30ºC. Figures 2.14a and 2.14b show the inertance mass at lag/rev and 1/rev. They show the same trend as the equivalent piston area since inertance is constant at all temperatures. The stiffness contributions from shear deformation of the FE damper elastomeric body (FE damper without fluid) and volumetric deformation or bulging of the elastomeric volume chamber at lag/rev and 1/rev are given in Figures 2.15a and 2.15b respectively. At both frequencies and all temperatures, the bulge stiffness is much higher than the shear

stiffness of the elastomer. Both stiffness values decrease with increasing temperature, while they remain relatively constant with varying amplitudes. The damping contributions from the hydraulic and mechanical components are given in Figures 2.16a and 2.16b. The plots show that majority of the FE device damping is provided through viscous damping, while elastomeric shear deformation contributes minimal damping. The viscous damping, which is proportional to the square of the equivalent piston area, increases with increasing input stroke or amplitude. This is why the total damping rises with amplitude, as was shown earlier (*Section 2.3*). The viscous damping is notably affected by temperature, exhibiting a reduction by more than half as temperature is varied from 10°C to 50°C.

The damping force versus velocity cycles at lag/rev and 1/rev frequencies and two different operating temperatures are given in Figures 2.17a and 2.17b respectively. The plots show that the hydromechanical model closely estimates the actual hysteretic damping force behavior of the FE damper from experimental measurements. To measure the performance of the hydromechanical model, the average error between the measured and estimated force time histories were calculated. The relative root mean squared (rms) force error per cycle is given by:

$$E_{rms} = \left[\frac{\sum_{j=1}^{N} \left(F(t_j) - F^*(t_j) \right)^2}{\sum_{j=1}^{N} F(t_j)^2} \right]^{1/2} X\ 100\% \qquad (2.35)$$

By determining these force errors, we can quantify the measure of how well the model captures the FE damper response. As Figures 2.18a and 2.18b show, the

maximum error in damping force between the estimated and measured force is about 5% at lag/rev excitation frequency and 7.7% at 1/rev frequency.

To predict the response of the FE damper under dual frequency excitation, it was subjected to various combinations of lag/rev and 1/rev frequency amplitudes under various temperatures, and the force-time history is used to evaluate the model performance. The dual frequency test matrix at all temperatures is given in Table 2.2. Utilizing optimized model parameters, the FE damper dual frequency response was predicted by linear superposition of the estimated damper performance at each excitation frequency. The modeling results for a combination of the lag/rev and 1/rev frequencies at two different temperature conditions are given in Figure 2.19. In the figures, X_{lag} represent the amplitude of the harmonic input at the lag/rev frequency while X_{pri} represents the amplitude at 1/rev frequency. The results show that the hydromechanical model was able to predict FE damper dual frequency performance reasonably well over the amplitude and frequency spectrum investigated.

2.6 Conclusion

This investigation demonstrates the behavior of a snubber type fluid-elastomeric (FE), also known as Fluidlastic® (Lord Corp.), lag damper under dynamic load applications at different operating temperatures ranging from 10°C to 50°C. The FE lag damper is employed in helicopter rotor system to ensure helicopter stability in alleviating air and ground resonances. Unlike elastomeric lag dampers, FE dampers provide damping and stiffness that does not diminish with excitation amplitude. At 10°C and 50°C respectively, the lag mode damping showed a nearly 20% and a 40% increment as the amplitude was increased from 0.762 mm (0.03 in) to 3.38 mm (0.15

in), while the stiffness showed a less than 10% variation. However, damper performance is substantially affected by ambient operating temperature conditions. For instance, at constant amplitudes of 0.762 mm (0.03 in) and 3.38 mm (0.15 in) respectively, the lag mode damping showed a nearly 50% and 40% drops as the temperature was increased from 10°C to 50°C, while the stiffness was reduced by about 20% for both cases.

The complex modulus method does not describe the flow dynamics that is involved in the system. It treats the damper as a bulk body or 'black box,' and compares the total system performance by relating the output to the input. It does not delineate the contributions from the different components of the damper. Hence, to better understand the hydraulic characteristics of the FE damper and predict the damping force, a hydromechanical model was proposed and formulated. The model uses the lumped parameter approach which takes into account the mechanical and hydraulic physical phenomena taking place within the damper. The hydromechanical model is a semi-empirical model where parameters are fundamentally dependent on damper geometry and material properties at a given test condition, which can potentially be known *a priori* or be identified using simple experiments. These parameters included fluid viscosity, density, elastomer shear stiffness and damping, and damper geometry. These also lead to the identification of dependent parameters which are viscous damping and inertance mass effects. Three model parameters were estimated from measured damper data. These parameters, which are bulge stiffness and bulge damping, and the equivalent piston area, were optimized to accurately simulate damper hysteresis utilizing the model. The analogous mechanical system

and corresponding equations of motion are shown to illustrate the flow behavior, as well as the coupling between the mechanical and hydraulic systems of the FE damper. The model is observed to have good correlation with the measured hysteresis of the FE damper for the range of amplitudes, frequencies and temperatures tested and will be useful for future design and performance studies.

Table 2.1 Measured, model estimated and dependent model parameters

Measured Parameters	Model Estimated Parameters	Dependent Parameters
Viscosity, μ	Eqv. Piston area, A_p	Mass, m_A
Resistance, R	Bulge stiffness, k_c	Viscous damping, C_A
Density, ρ	Bulge damping, C_c	
Inertance, I		
Shear stiffness, k_r		
Shear damping, C_r		

Table 2.2 Dual frequency test matrix

$X_{lag/rev}$ [in]	$X_{1/rev}$ [in]	0.03	0.05	0.07	0.09	0.10	0.13
0.03		X	X	X	X	X	X
0.05		X	X	X	X	X	
0.07		X	X	X	X		
0.09		X	X	X			
0.10		X	X				
0.13		X					

(a) Factory-sealed FE (a.k.a. Fluidlastic®) Damper

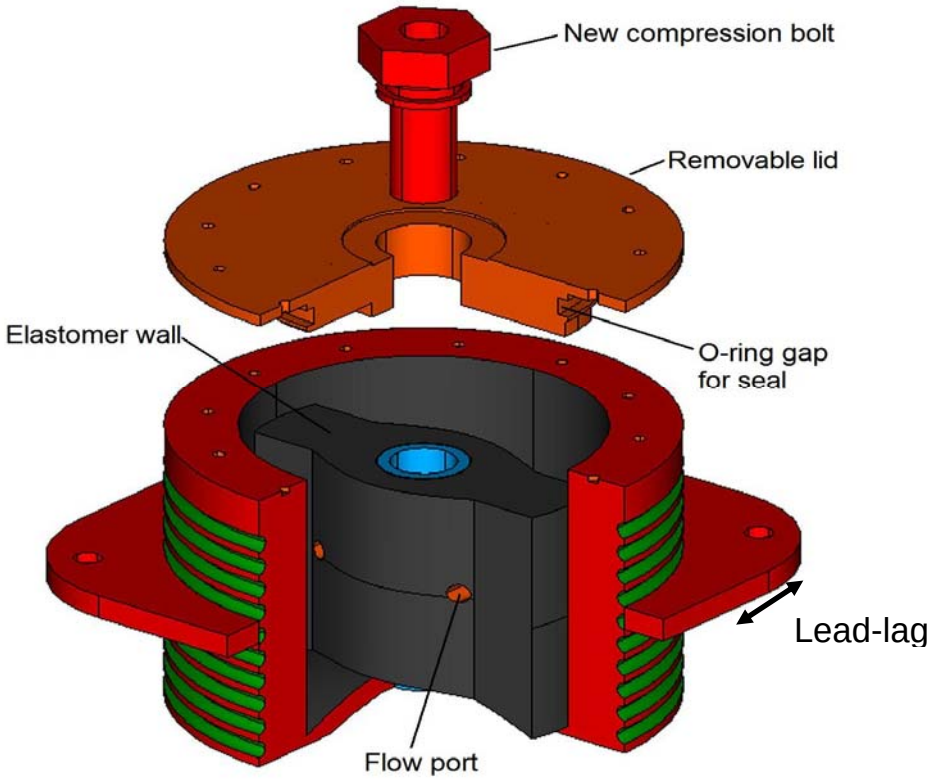

(b) Simplified Isometric View of the FE Damper

Fig. 2.1: Pictorial and isometric view of the baseline FE lag damper

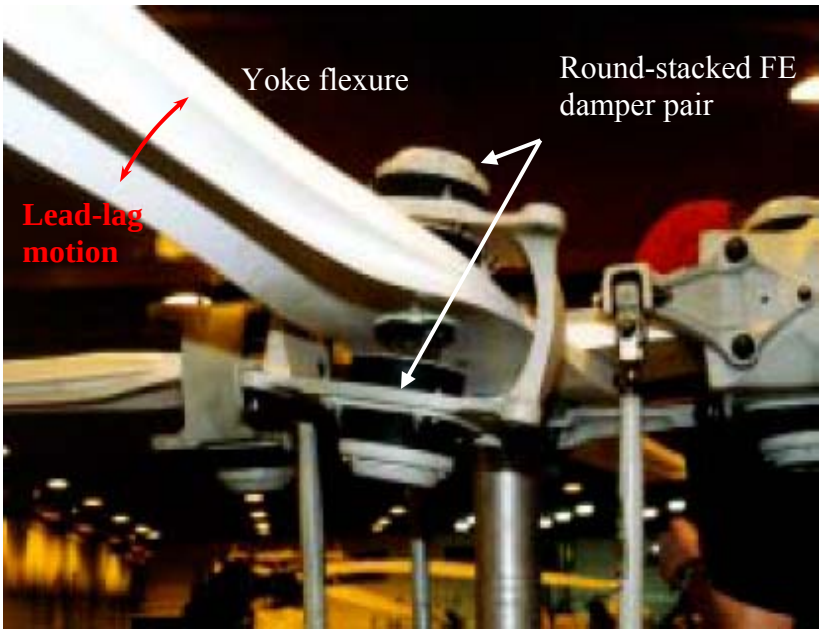

Figure 2.2: Schematic of main rotor blade with paired FE lag dampers (Courtesy of Bell Helicopter)

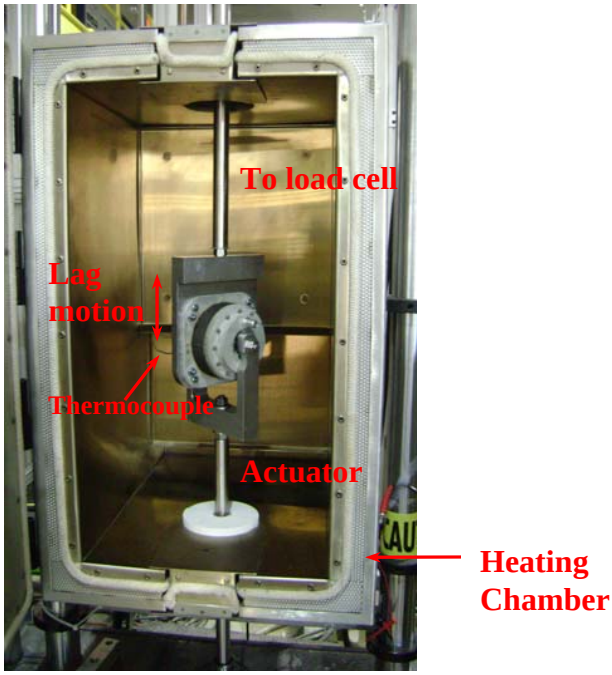

(a) FE lag damper test set-up on MTS testing machine

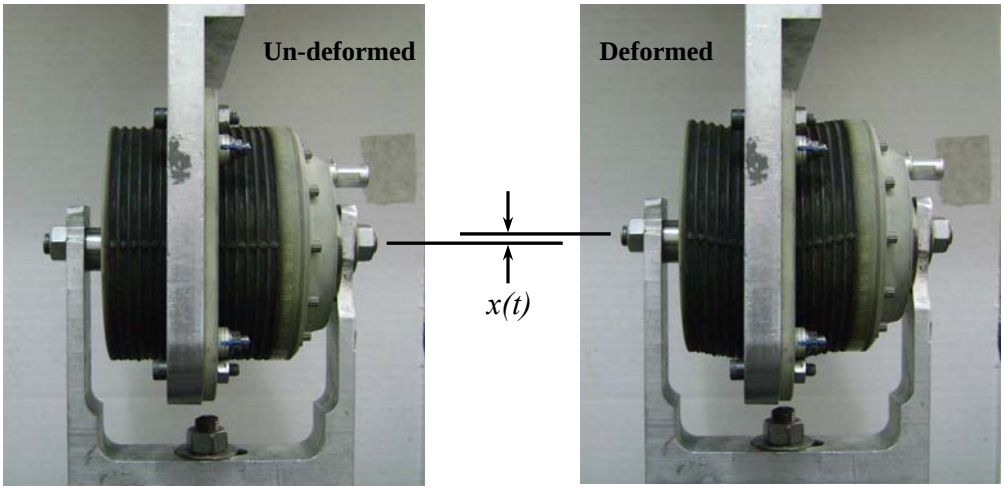

(b) Deformation of FE lag damper on MTS testing machine

Figure 2.3: FE lag damper test set-up on MTS testing machine

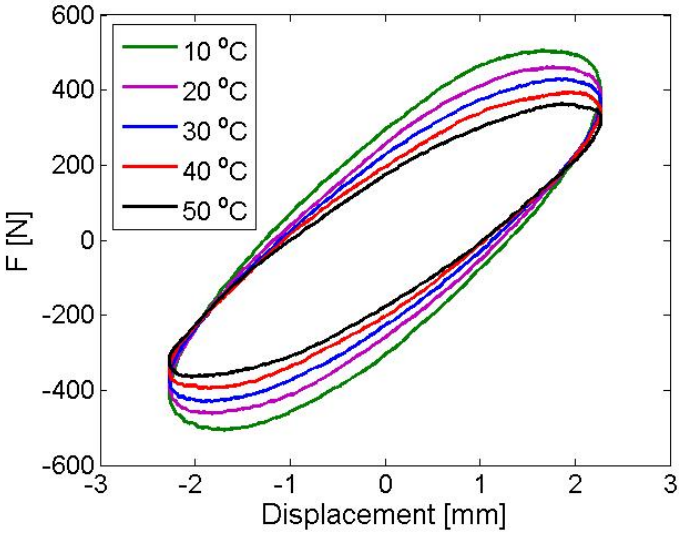

(a) lag/rev results

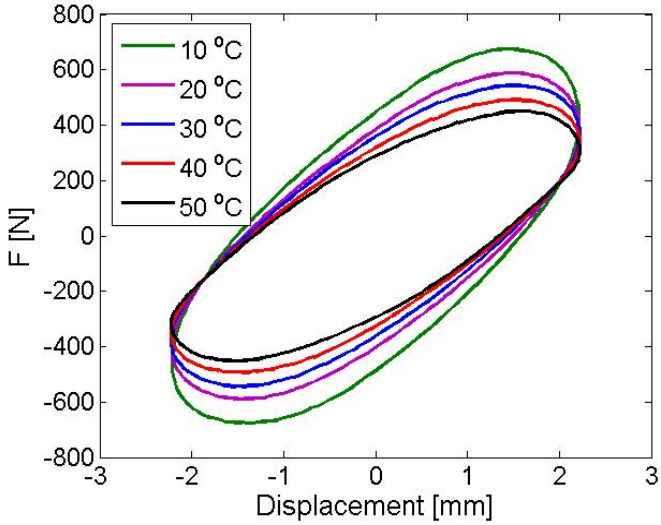

(b) 1/rev results

Figure 2.4: Typical force-displacement hysteresis results at single frequency

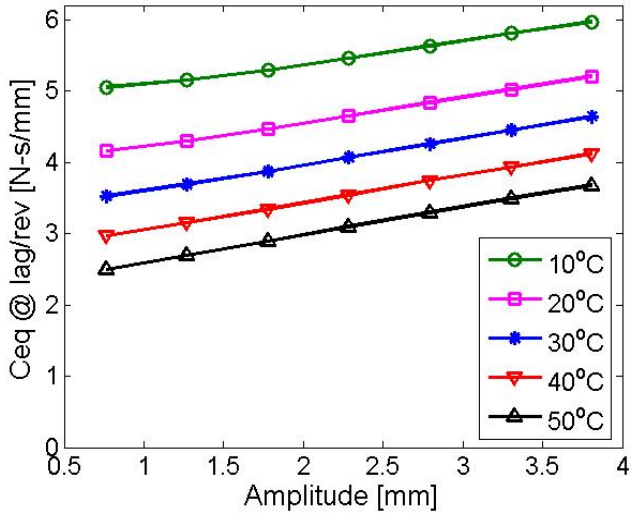

(a) Equivalent damping

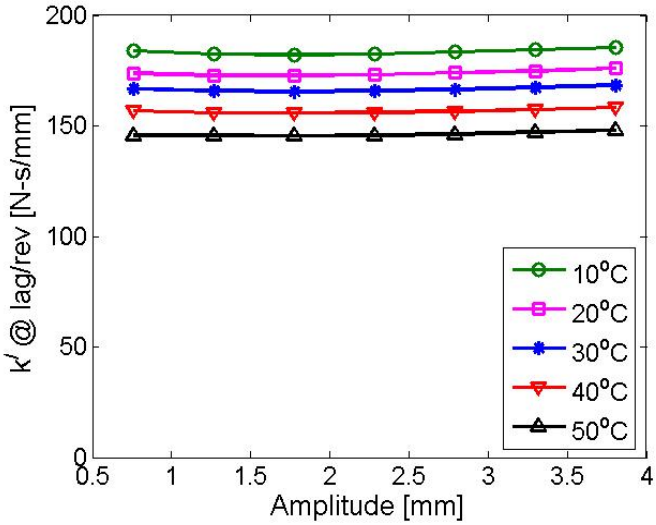

(b) In-phase stiffness

Figure 2.5: Single frequency test results at lag/rev frequency

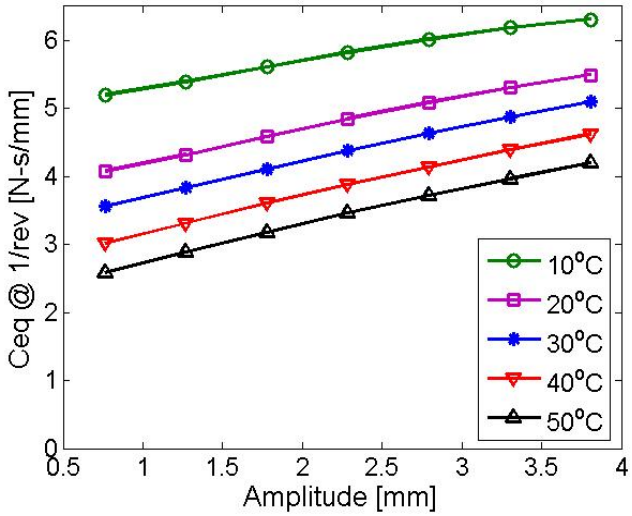

(a) Equivalent damping

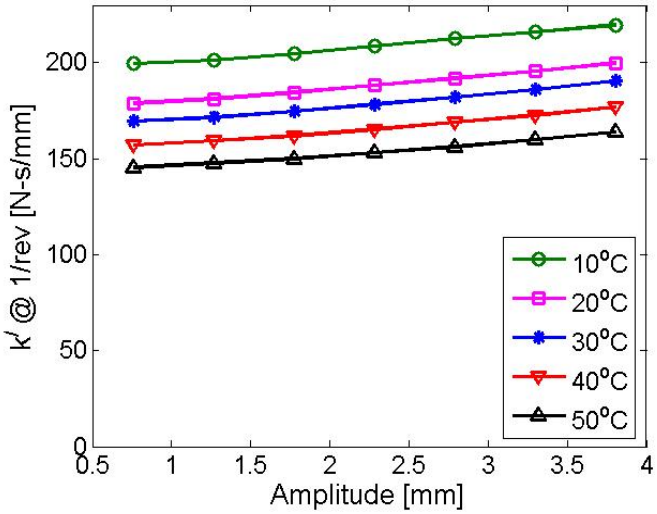

(b) In-phase stiffness

Figure 2.6: Single frequency test results at 1/rev frequency

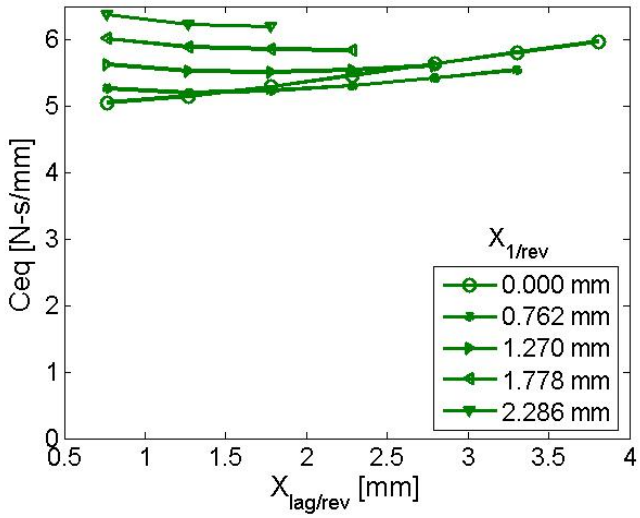

(a) Equivalent damping @ lag/rev

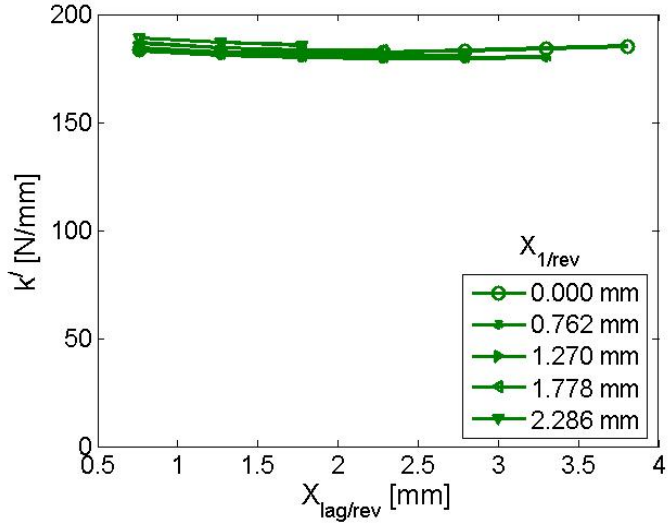

(b) In-phase stiffness @ lag/rev

Figure 2.7: Dual frequency test results at lag/rev, T = 10°C

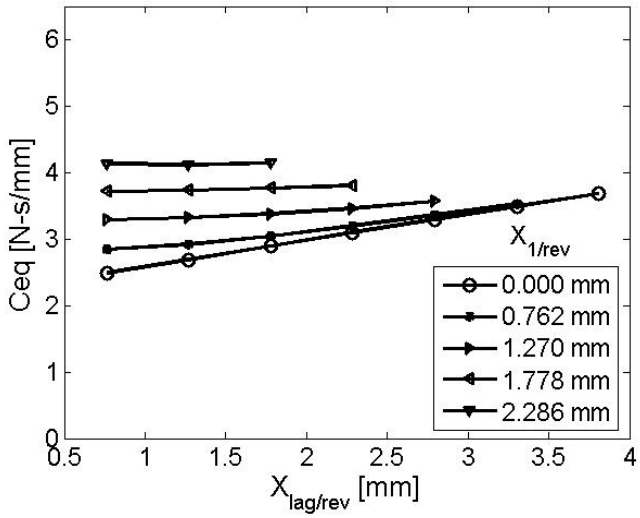

(a) Equivalent damping @ lag/rev

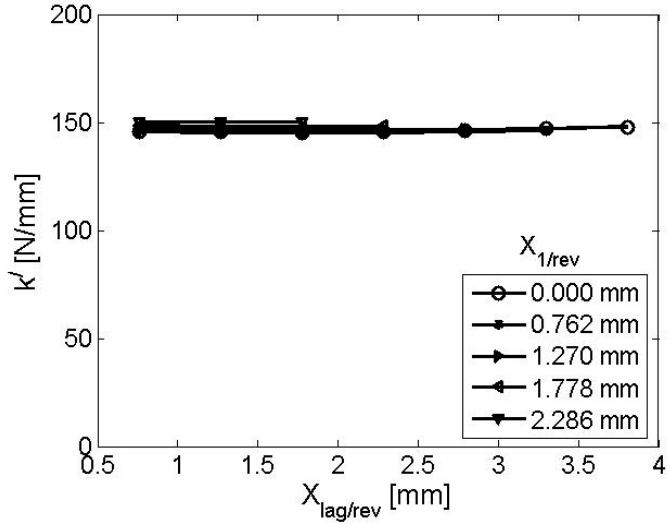

(b) In-phase stiffness @ lag/rev

Figure 2.8: Dual frequency test results at lag/rev, T = 50°C

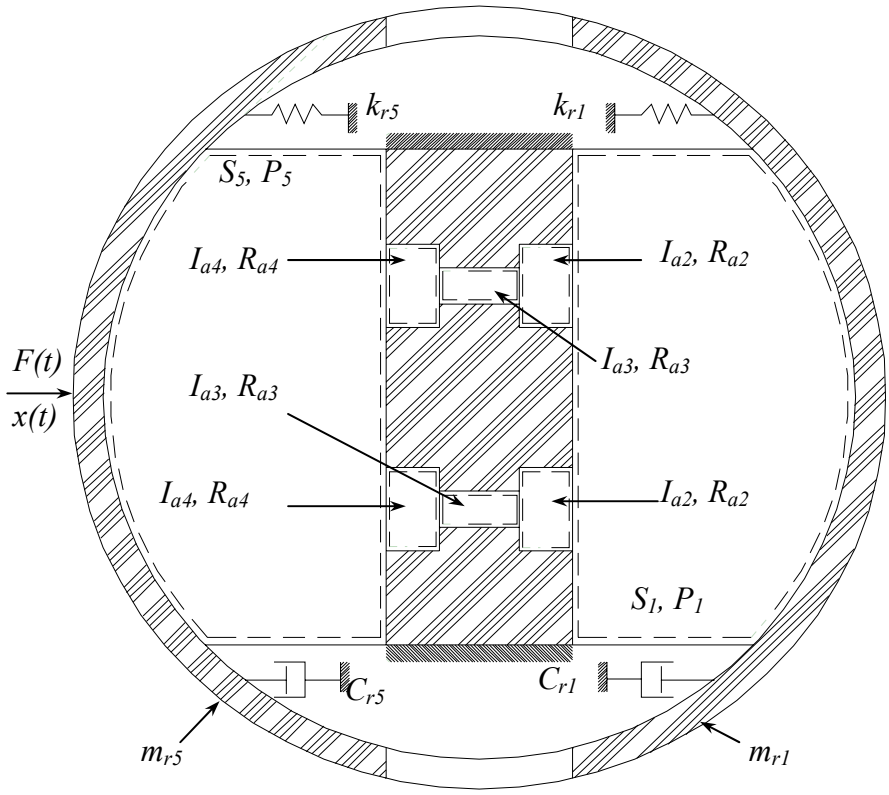

Figure 2.9: Section view of proposed hydromechanical model of FE damper

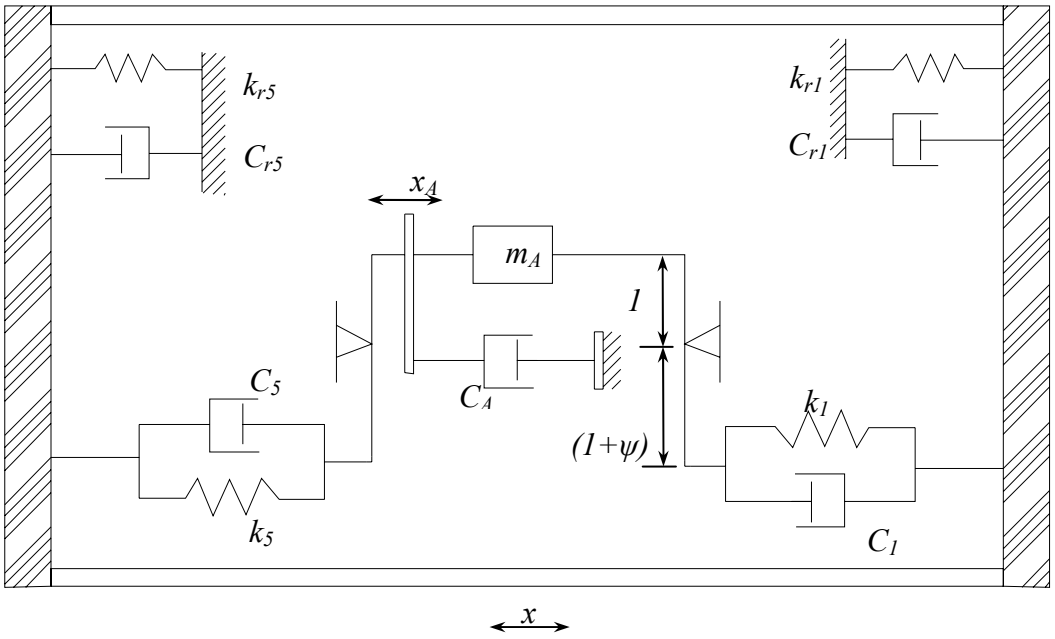

Figure 2.10: Analogous mechanical system of the hydromechanical model in terms of x_A (valve a)

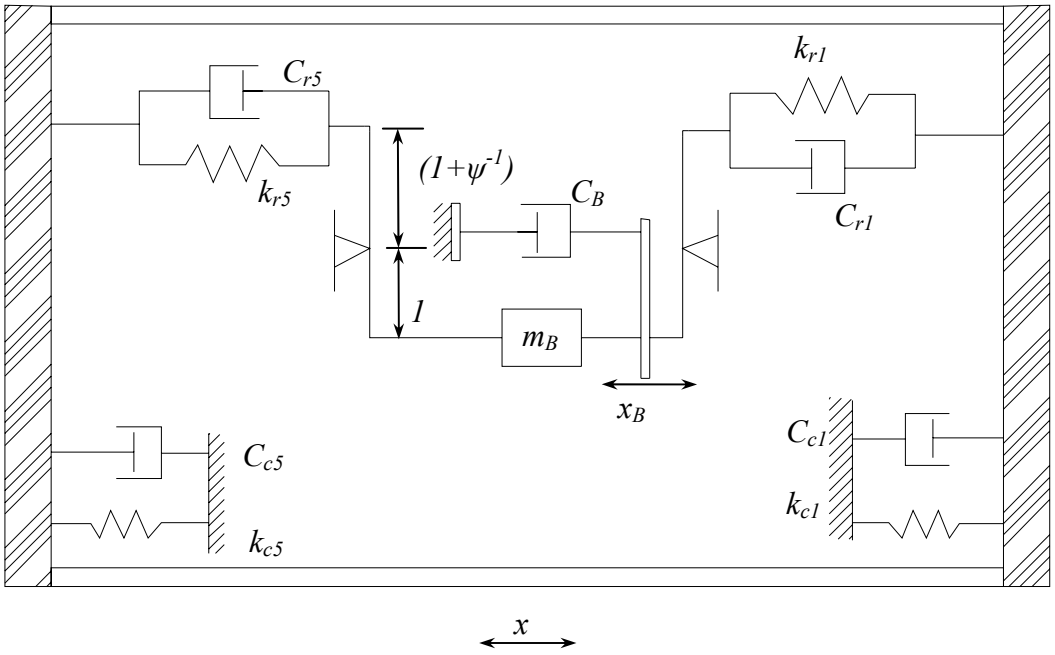

Figure 2.11: Analogous mechanical system of the hydromechanical model in terms of x_B (valve *b*)

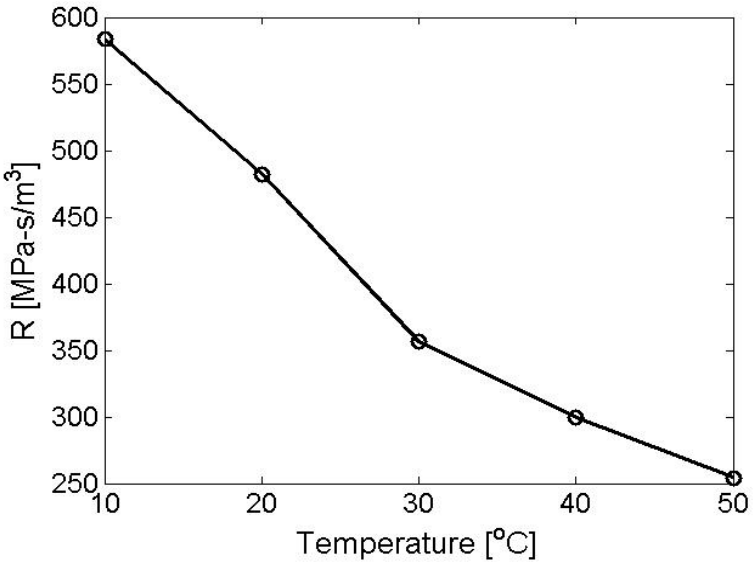

Figure 2.12: Resistance due to viscous flow in port holes

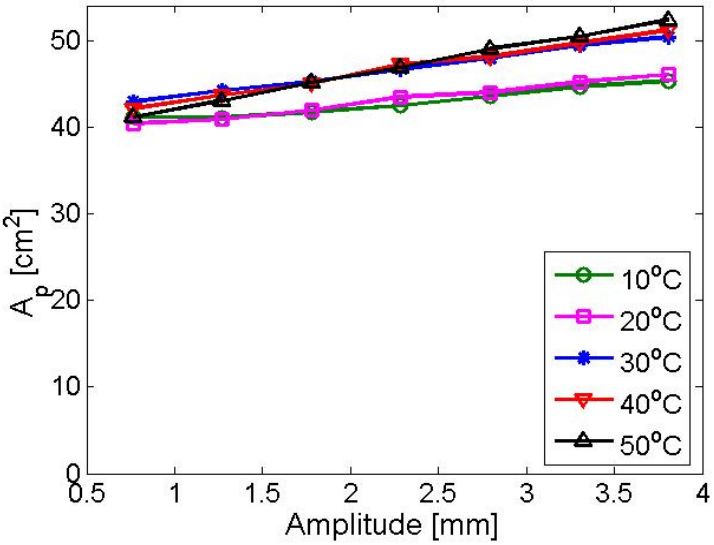

(a) Equivalent piston area A_p at lag/rev

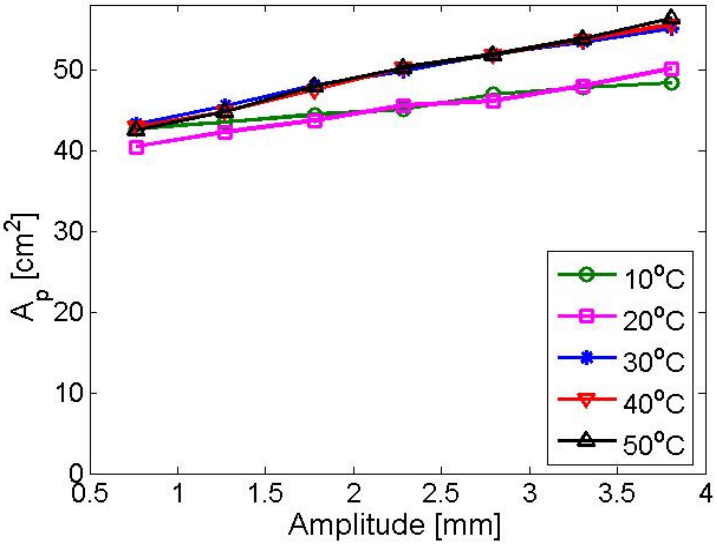

(b) Equivalent piston area A_p at

Figure 2.13: Optimized equivalent piston area A_p

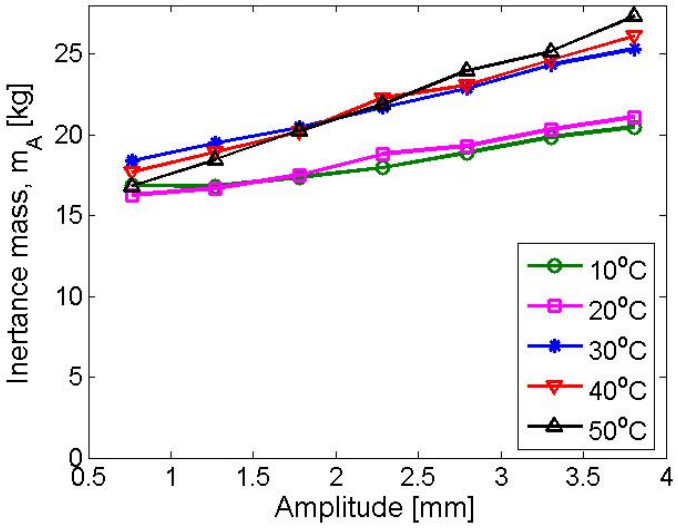

(a) Inertance mass m_A @ lag/rev

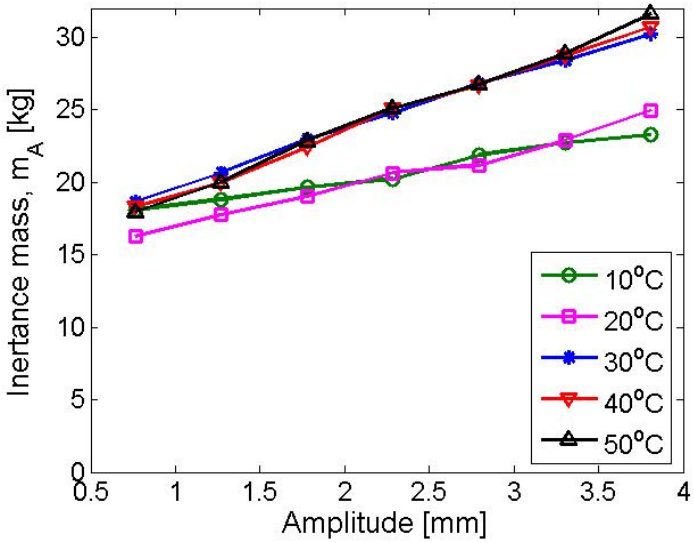

(b) Inertance mass m_A @ 1/rev

Figure 2.14: Inertance mass m_A

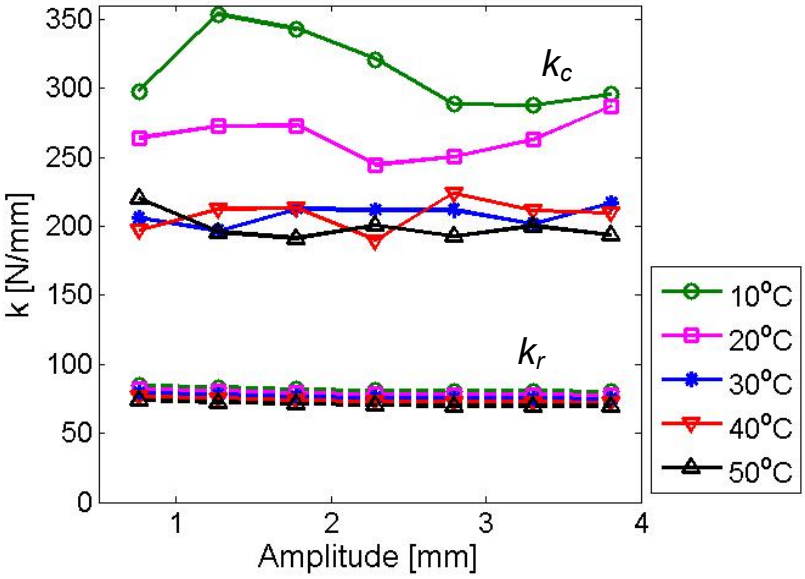

(a) Stiffness @ lag/rev

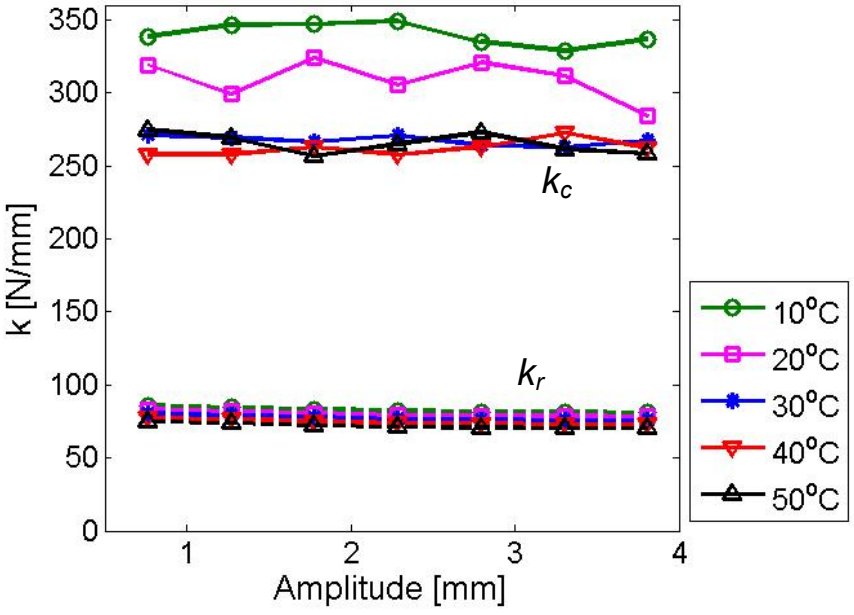

(b) Stiffness @ 1/rev

Figure 2.15: Bulge and shear stiffness of FE damper

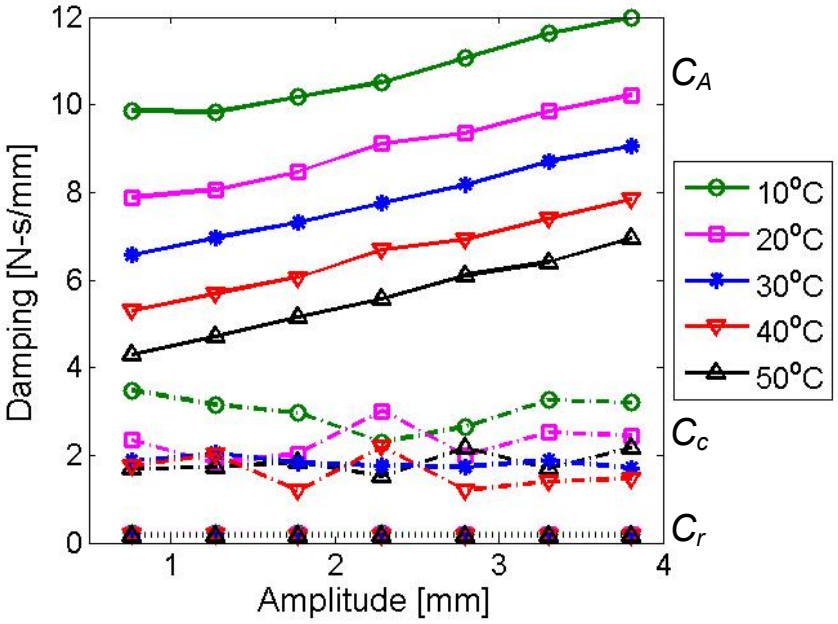

(a) Damping contributions @ lag/rev

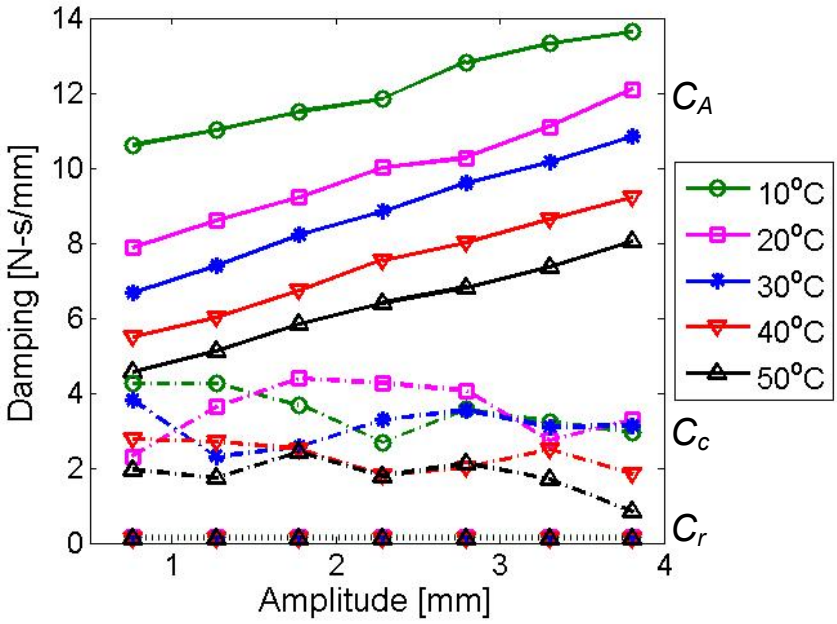

(b) Damping contributions @ 1/rev

Figure 2.16: Damping contribution from FE damper components

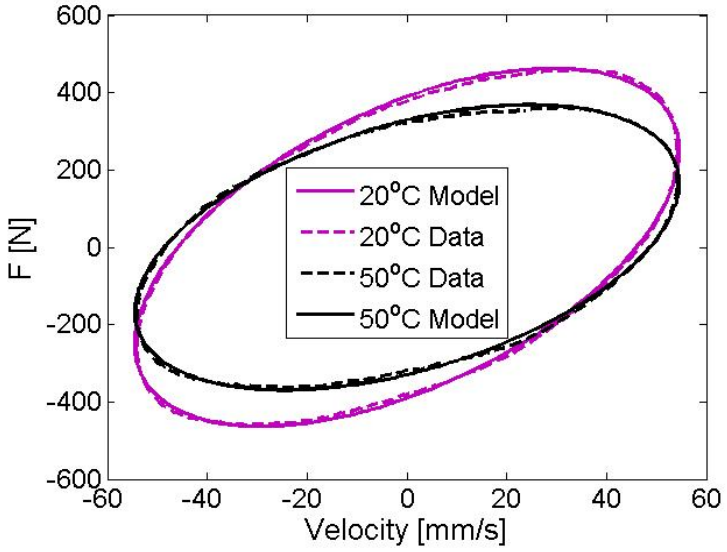

(a) Model performance @ lag/rev

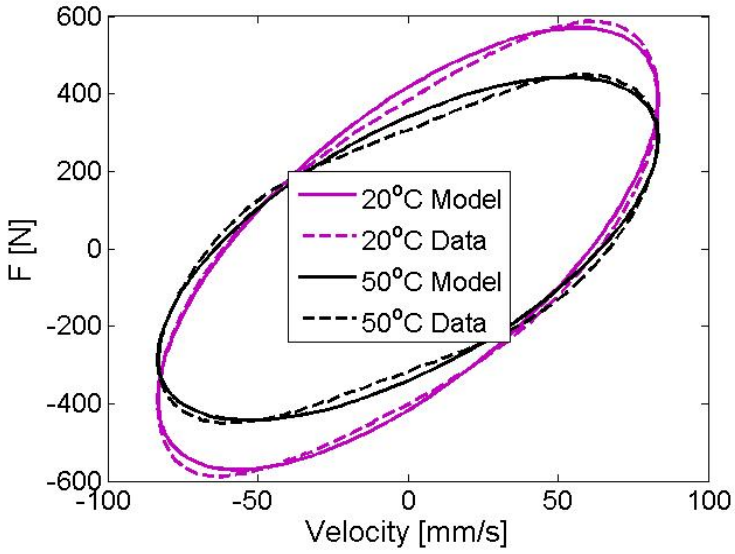

(b) Model performance @ 1/rev

Figure 2.17: Single frequency comparison between measured and predicted damper forces

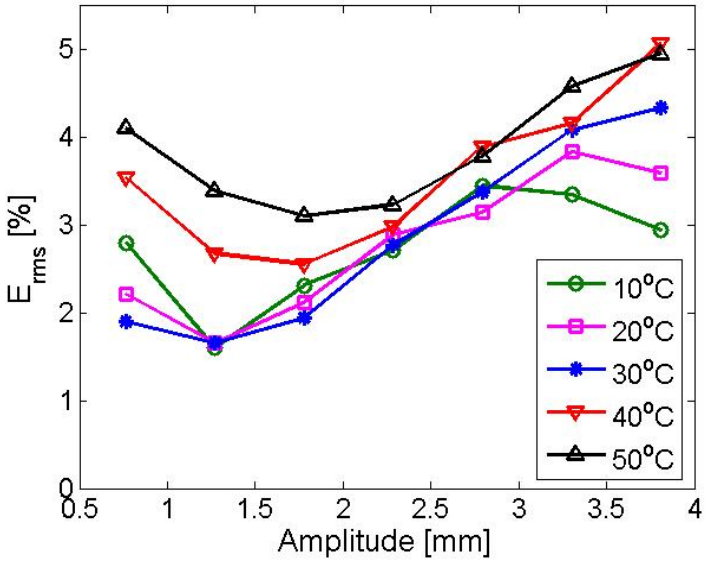

(a) Model error @ lag/rev

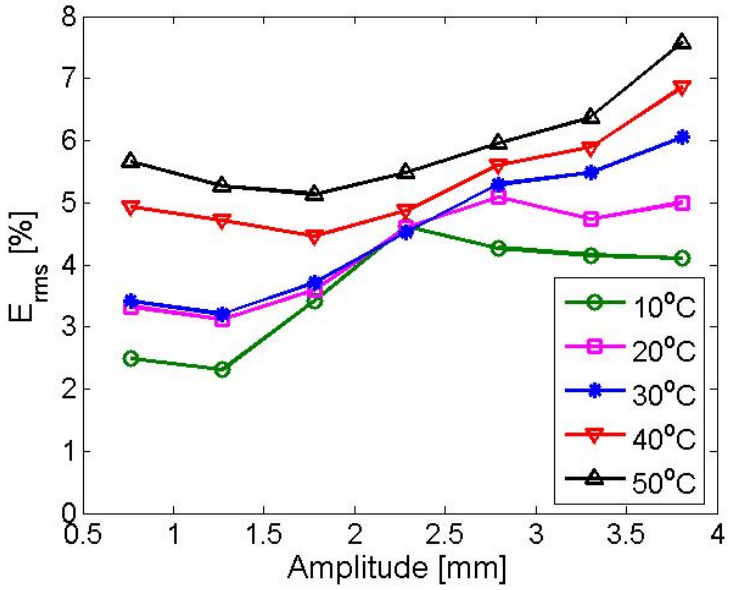

(b) Model error @ 1/rev

Figure 2.18: Single frequency model error estimation

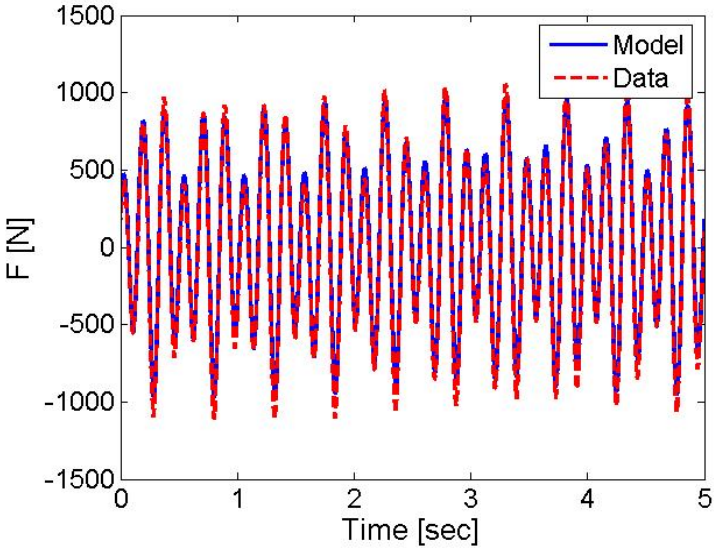

(a) T = 20°C, X_{lag} = 1.27 mm, $X_{1/rev}$ = 2.79 mm

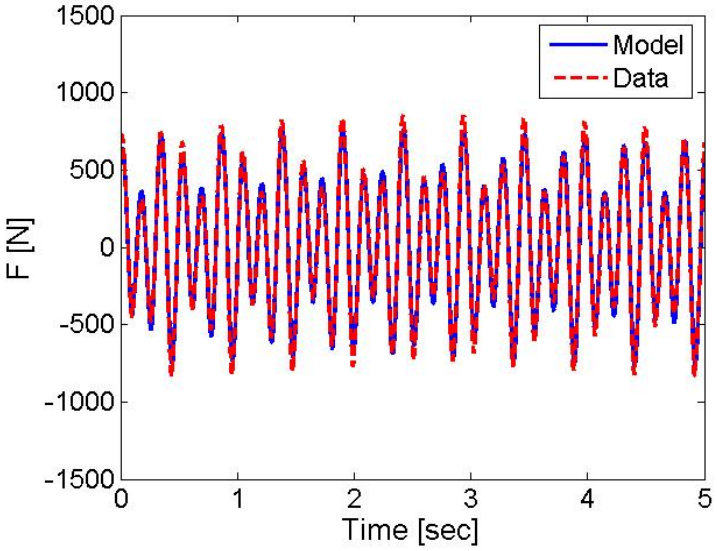

(a) T = 50°C, X_{lag} = 1.27 mm, $X_{1/rev}$ = 2.79 mm

Figure 2.19: Dual frequency comparison between measured and predicted damper forces

Chapter 3: Development, Characterization and Modeling of a Snubber Type MRFE Lag Damper

3.1 Introduction

Magnetorheological fluids typically consist of spherical micron-sized magnetic particles (microspheres) suspended in a liquid medium such as silicone or hydraulic oil [57, 58]. Their rheological properties, and thus their yield stresses and viscosities, can be rapidly and continuously controlled by varying the applied magnetic field. Conventional MR fluids utilize spherical micron-sized iron particles at high weight fractions and are shown to exhibit high yield stresses, up to 100 kPa [15, 16]. The fast response and controllability of MR fluids have made them very attractive for implementation in semi-active smart vibration-absorption systems [17–27]. Magnetorheological fluids have also been considered for application to helicopter rotor lag dampers [7, 10, 14, 72]. Much of this work has been done to evaluate the feasibility and capabilities of employing MR dampers in conjunction with elastomeric materials in helicopter lead-lag damping applications. Kamath *et al* [10, 72] modified a pair of 1/6th Froude-scale Comanche helicopter fluid-elastomeric lag dampers to a pair of hybrid elastomeric-MR dampers and demonstrated their capability in lag mode damping applications. Hu *et al* [7] also conducted analytical and experimental studies on a parallel arrangement of an elastomeric lag damper and two conventional MR dampers, and demonstrated a significant controllable damping dynamic range. Recently, a full-scale linear stroke tubular magnetorheological fluid-elastomeric

(MRFE) lag damper, which can be fully integrated into an actual helicopter rotor system, was developed [14]. The study has shown that at the field-off condition, the MRFE damper behaves as the baseline FE damper. As field is applied to the MR valve, the damping of the MRFE device can be varied substantially, and thus, has the potential to augment damping over critical frequency range of the helicopter rotor.

In the present study, a full scale MR fluid-elastomeric (MRFE) lag damper is developed by incorporating two MR valves into a snubber type round-stacked FE, also known as Fluidlastic® (LORD Corp.), lead-lag damper. The device was experimentally evaluated for its controllable damping capability and dynamic range under sinusoidal excitation, consistent with helicopter lead-lag damper loading conditions. Due to kinematical complexity in modern hingeless helicopter main rotors, a snubber type FE lag damper is usually made from a laminated stack of alternating elastomeric-metallic rings, and damping fluids are included in the flexible body to increase dynamic range of the FE damper [9]. In the present FE lag damper, a multiple lamination of elastomeric and metallic rings forms the cylindrical damper body with two chambers. The flexing of the elastomer forces fluid to flow from one chamber in to the other through flow ports, thus providing the required damping. This FE damper has an advantage over conventional linear stroke hydraulic dampers, as it does not include any moving parts, thus avoiding the issue of wear and leakage. Although the elastomer introduces a significant stiffness to the system, its damping contribution is minimal compared to the viscous damping generated. The MRFE damper utilizes the existing flexible damper body and the flexible center wall of the FE damper, with the two port holes in the center wall retrofitted with one MR valve

each. The MRFE damper can provide controllable damping and can potentially augment damping over critical frequency ranges and adverse operating conditions, and increase stability of a helicopter rotor. Further, the MRFE damping components can still provide fail-safe passive damping in the event of reduced or no-power operation. The MRFE retrofit shares a similarity with the baseline FE damper as it does not introduce any moving component.

The complex modulus method is employed to characterize the MRFE damper performance and compare it with the baseline FE damper. It is shown that the field-off damping of the MRFE damper is smaller than the baseline FE damper, and a significant damping control range, extending beyond the baseline FE damper, can be provided by the MRFE damper with the application of varying magnetic fields. However, the complex modulus linearization technique does not identify and describe the non-linear behavior of the MRFE damper under sinusoidal excitation, which is a consequence of the magnetorheological effect. Various models based on lumped parameter approaches have been proposed to model the non-linear hysteretic behavior of elastomeric lag dampers [3-6, 41-47], MR dampers [10, 73-87], and hybrid elastomeric-MR and MRFE lag dampers [7, 10, 14, 72] under harmonic excitations. These models were able to capture and reconstruct the non-linear dynamic hysteresis behavior of elastomeric and MR dampers for the tested amplitude and frequency ranges. A review of some of the elastomer, FE and MRFE modeling schemes and their features, along with the model developed in this paper, are summarized in Table 3.1. All of these parametric models are based on the physical phenomena of the system where by a series of mechanisms and/or mathematical functions are

formulated to relate the input to the output. There are two main shortcomings in applying these models to the snubber type MRFE lag damper under study:

1) These models do not describe adequately the actual physical flow phenomenon or flow dynamics in fluid based MR dampers. They do not present the interaction between mechanical, hydraulic and magnetorheological systems, which is an inherent feature of hydraulic based MRFE dampers.
2) Most models are based on parameter identification using test data. Thus, they are not sufficient to design and predict damper performance *a priori*, before development and production.
3) The snubber type MRFE device has a completely coupled elastomeric, hydraulic and magnetorheological system which the aforementioned models do not address. The snubber type MRFE damper has its body made of elastomeric material in which fluid is contained. However, previous models are formulated independently for elastomeric or MR damper and do not consider a situation in which the two systems are coupled.
4) Consequently, it is difficult to employ such models to describe the dynamics of the snubber type MRFE device, and to be applied in dynamics and aeromechanical stability analysis of the helicopter rotor system.

Thus, a hydromechanical model, which can delineate the physical flow dynamics of the system and accurately describe the non-linear hysteretic behavior of the MRFE damper is proposed. The hydromechanical model explored in this study is a predictive or design-oriented model which describes the damper system with a series

of lumped hydraulic, mechanical and magnetorheological components. The model employs physical parameters such as inertia, damping, yield force and compliances that are dependent on damper geometry and material properties of components and which can potentially be approximated *a priori*. Previous MRFE dampers have decoupled systems, which are basically modeled as a parallel combination of elastomeric and MR damper elements [7, 14]. In the current MRFE lag damper, the hydromechanical model is able to account for the coupling between the elastomeric and MR systems, which is manifested through chamber compliances. Once model parameters have been established, the model is shown to simulate accurately the measured force-displacement history under single and dual frequency excitations.

3.2 Development of the MRFE Lag Damper

A section and schematic view of the baseline snubber type fluid-elastomeric (FE) lag damper (Lord Corp. Fluidlastic® lag damper) is shown in Figure 2.1. A discussion of the FE damper and its integration in a helicopter rotor system are shown in Figure 2.2 and discussed in *Section 2.2*. The design of the MRFE damper requires the development and retrofit of two MR valves inside the existing baseline FE damper body and exchanging the existing passive, hydraulic fluid with field-controllable, MR fluid (provided by LORD Corp.). The development of the MR valves involves fitting the existing two port holes located in the center wall with two flow mode MR valves. The development of the MR valves inside the existing lag damper center wall is shown in Figure 3.1. These internal MR valves are placed at the two existing flow ports located in the center wall, one in each hole on each side of the fluid chambers. Figure 3.1a shows the top view (top plate removed), and Figure 3.2b shows a section

side view of the lag damper with MR valves installed. The new MR retrofit design introduces only the MR valves. Thus, the MRFE still maintains the wear and tear, and leakage free feature of the baseline FE damper. In addition, this helps minimize the weight penalty incurred due to addition of MR components. The baseline FE damper was found to weigh about 2.14 kg, while the prototype MRFE damper weighed about 2.75 kg. This shows a 28% increment in damper weight. Figure 3.2a shows the orientation and Figure 3.2b the detailed sketch of one of the incorporated MR valves with its basic components. The MR valve includes a bobbin with coil and a flux return, which in this case is designed in the shape of a stepped hollow tube, with the larger diameter tube accommodating the bobbin, and the smaller tube to be threaded into the flow ports. The diameter of the flow port was made as large as possible in order to reduce viscous losses in the passive length of the ME valve. Magnetic field is provided by an electromagnet enclosed in the valve such that the MR fluid flowing through the flow valve can be activated. Feed-troughs were incorporated into the new top plate of the MRFE damper to access the enclosed electromagnet wires to supply current.

Figure 3.2b also shows the flow path of the MR fluid in the valve. The electromagnetic coil in the MR valve is wound around the bobbin, which is inserted into the flux return. Initial MR valves were designed using a Herschel-Bulkley model [74] with flow index of $n=1$, i.e., Bingham-Plastic model. The annular gap thickness d can be varied by changing the radius of the bobbin r, changing the inner diameter of the flux return ring, or changing both at the same time. The active valve length L_c can be adjusted to increase or decrease the magnetic flux that activates the MR fluid, as

well. Overall, the maximum size of the valve, specified by the flux return outer diameter D_o and the valve length L_p determine whether the valve satisfies two key design imposed by a retrofit to the baseline FE damper body, that is, the required stroke of the damper is the same as the baseline damper and the MR valves avoid contact with the outer cylindrical wall. Figure 3.2b also depicts the path of the magnetic flux, which is initiated upon application of a current. In addition to imposing constraints on valve sizing, the current MR retrofit package creates unfavorable passive viscous losses due to unavoidable fluid flow through small diameter passage ways and 90° turns, resulting from the existing FE lag damper design feature. Thus, MR valves were further adjusted empirically based on test data until acceptable performance was attained. Future designs can avoid these unfavorable conditions by designing an MR valve that can be fully imbedded within the center wall of the baseline FE damper, while maintaining straight flow passages.

Figure 3.3 gives a picture of the components and assembly of the MR valve, which includes the bobbin, coil and flux return. Once the coil is wound on the bobbin, it is attached to the flux return using screws. The damper is assembled as a sealed unit, so that minimal possibility exists for the fluid to pass from one chamber to the other without traveling through the flow port of the MR valve. The original FE damper was factory assembled as a molded unit. However, in order to design and fit the MR valves, the upper surface of the elastomeric center wall was damaged during the disassembly process, as the top plate had to be cut to be removed. A rubber repair kit was used to rebuild the wall and provide a smooth surface for sealing with the new top plate. Refer to Figure 3.4a. The new top plate and compression bolt were

machined in-house, which are shown in Figure 3.4b. The original baseline FE damper is preloaded in compression once the viscous fluid inside the chambers is sealed, creating a positive pressure inside damper. However, during assembly of the prototype parts, once the MR fluid was injected into the damper and sealed, the elastomer was approximately pre-compressed by 18% to create positive inner pressure, which was slightly less than the approximately 20% pre-compression of the baseline FE damper.

3.3 Experimental Evaluation MRFE Lag Damper

The baseline FE damper dynamics discussed in section 2.3 is repeated here for convenience. For small displacement applied at the center of the damper, the interior of the MRFE damper is assumed to deform in a similar way as the baseline FE damper as shown in Figure 2.3b. In the actual rotor blade setting, the FE and MRFE lag dampers are intended to accommodate both radial and translational lead-lag motions of the blades. However, for small displacement, approximation of the actual lead-lag motion of the rotor blades with translational motion is assumed to be acceptable. The forcing function is applied at the damper mid-plate which creates a triangular damper deformation with the upper and lower plates. This causes the volume of one of the elastomeric chambers to decrease, forcing the fluid to flow through the flow ports into the other chamber as the other chamber volume increases to compensate for the in-flow. Due to the absence of a well defined piston and the complex damper features, the input displacement excitation is not uniform throughout the damper height. It varies from zero at damper extremities to maximum, which

equals the input displacement excitation, at damper center. However, all damper analysis is evaluated based on the input excitation at damper mid-plate.

To mimic the lead-lag motion of helicopter blades as applied to the baseline FE lag damper and the MRFE damper, a test fixture was fabricated to hold dampers in a 24.5 kN MTS servo-hydraulic testing machine. Figure 3.5 shows the baseline FE lag damper test set-up where the mid-plate is connected to the load cell by means of the test jig. The lower mounting bracket is attached to the lag damper through a mounting rod that is slotted in at the mounting hole, located at the lag damper center, through the center wall. The center wall is oriented horizontally such that the motion of the MTS actuator connected to the lower bracket forces fluid to flow from one chamber to the other, by deforming the elastomeric outer wall, and emulating the lead-lag motion. The displacement and force were measured by the LVDT sensor and load cell of the MTS machine. The frequencies of excitations were chosen to be 3.8 Hz and 5.8 Hz, which correspond to an actual rotor system lag/rev and 1/rev or rotor RPM frequencies. For the MRFE damper, a DC power supply was employed to provide a controlled current input to the MR valve during testing. The applied current varied from 0 – 1 A, in increments of 0.25 A. An HP 8904A multi-function synthesizer was employed to generate and the sinusoidal signals for the dual frequency tests. All test evaluations conducted on the MTS machine were at an ambient temperature of about 27.5°C, and with no temperature control during testing.

The steady-state dynamic tests were carried out for three cases: baseline FE lag damper, FE damper elastomeric body (FE damper without fluid), and the MRFE damper. For single frequency evaluation, sinusoidal displacement tests were carried

out with varying excitation amplitudes. The excitation amplitudes ranged from 0.762 mm (0.03 in) to 3.81 mm (0.15 in) in increments of 0.50 mm (.02 in) at both lag/rev and 1/rev frequencies. At each excitation amplitude and frequency, a DC current varying from 0 to 1 A was supplied to the MRFE damper. The single frequency force-displacement and force-velocity data were utilized to estimate the hydromechanical model parameters and evaluate model dependability. For dual frequency tests, a dual frequency combination of 3.8 Hz/5.8 Hz was used to evaluate the fidelity of the model in multi-frequency loading scenarios. The dual frequency test matrix is shown in Table 3.2.

During each test, the sampling frequencies were 1024 Hz and 512 Hz for the single and dual frequency tests respectively, which are considerably higher the required Nyquist frequency. Nominally, ten cycles of force and displacement data were collected at each test set up. To reduce the noise of the input sinusoidal displacement signal, a Fourier series was used to reconstruct the input displacement. The reconstructed displacement signal was then differentiated to obtain the velocity signal. The Fourier series expansion of the input displacement signal is given by:

$$x(t) = \frac{x_o}{2} + \sum_{k=1}^{\infty} \left(X_{c,k} \cos(k\omega t) + X_{s,k} \sin(k\omega t) \right) \tag{3.1}$$

where

$$X_{c,k} = \frac{\omega}{\pi k} \int_0^{\frac{2\pi}{k\omega}} x(t) \cos(k\omega t) dt$$

$$X_{s,k} = \frac{\omega}{\pi k} \int_0^{\frac{2\pi}{k\omega}} x(t) \sin(k\omega t) dt \tag{3.2}$$

Any bias and higher harmonics at single frequency tests were filtered, so as only the frequencies of interest, i.e. $\omega = \omega_{lag}$ and $\omega = \omega_{pri}$, remained. Then the displacement and velocity data were reconstructed using the first harmonics only as

$$\begin{aligned} x(t) &= X_s \sin(\omega t) + X_c \cos(\omega t) \\ \dot{x}(t) &= \omega X_s \cos(\omega t) - \omega X_c \sin(\omega t) \end{aligned} \tag{3.3}$$

For dual frequency evaluation, the HP8904A function generator was used to create and sum the two sinusoidal signals in order to attain an accurate dual frequency excitation. The general equation for the input dual displacement signal is expressed as:

$$x(t) = X_{lag} \sin(\omega_{lag} t) + X_{pri} \sin(\omega_{pri} t) \tag{3.4}$$

where ω_{lag} and X_{lag} represent the lag/rev (lag) frequency and its corresponding input amplitude while ω_{pri} and X_{pri} represent the 1/rev (rotor) frequency and its corresponding amplitude. The signal is periodic with a period equal to the frequency corresponding to the highest common factor of the two harmonics, which is 0.2 Hz. Thus, the displacement input signal was filtered using the Fourier expansion at 0.2 Hz as the base frequency. The first twenty-nine harmonics were required to reconstruct the dual frequency displacement signal. Since the MRFE damper force has a non-linear behavior, the measured force data at all frequencies was not filtered and was used in the developed hydromechanical model as recorded.

Figure 3.6a shows the lag/rev frequency force versus displacement plots of the baseline FE damper, the FE damper elastomeric body (empty FE damper) body, and Figure 3.6b for the MRFE damper at current values varying from 0 A to 1 A at a constant amplitude of 2.286 mm. In each force-displacement plot, the area enclosed

by the hysteresis loop is proportional to the amount of energy dissipated per cycle. The damping available is in turn proportional to the energy dissipated per cycle. Referring to Figure 3.6a, it is observed that the force displacement curves of the baseline FE damper and its elastomeric body show fixed damping. The shapes of hysteretic force-displacement curves for the FE damper and the FE damper elastomeric body dampers are also elliptical in shape, and tilted at a fairly constant angle. When the FE damper elastomeric body is periodically excited, the elastomer deforms in shear mode, and the relatively small enclosed loop area of the hysteretic elastomer plot implies that in the shear mode, it contributes a small fraction of the total damping to the baseline FE damper performance. However, its stiffness contribution is quite significant. A majority of the baseline FE damping is contributed through viscous damping and chamber bulge damping, which is a consequence of elastomer-fluid interaction during excitation, resulting in a volumetric expansion of the elastomer. Later in the hydromechanical modeling section, it will be shown that the primary source of damping is due to viscous flow. From Figure 3.6b, the MRFE damper at zero applied magnetic field behaves in a manner similar to the FE damper and the FE damper elastomeric body, having an elliptical force-displacement plot. Under the application of a magnetic field, the MRFE damper behavior transforms substantially, exhibiting significant non-linearity, reflected in the non-elliptical force-displacement loops. This property, demonstrated in the figure, shows the hysteretic behavior of the MRFE damper under varying input currents. As control current is applied, the dissipated energy per cycle, thus the available damping in the MRFE device, increases significantly. This is due to the additional controllable damping

contribution from the MR effect, on top of the viscous and bulge damping. Further, as current is applied to the MRFE damper, there is a large jump in the near zero velocity force response (corresponding to maximum displacement), which enlarges the enclosed hysteretic loop area. This indicates that the controllable damping behavior of the MRFE damper is achieved through the yield stress of the MR fluid in the MR valves.

3.4 Linear Characterization

A typical approach to characterize damper performance quantitatively is the complex modulus method. It is a linear characterization technique of damper properties which treats the complex stiffness k^* as a combination of the in-phase stiffness k' and the loss stiffness k'', given as:

$$k^* = k' + ik'' = k'(1 + i\eta) \tag{3.5}$$

where the loss factor η is defined as the ratio of the loss stiffness to the in-phase stiffness. This technique has been extensively used in characterizing elastomeric, fluid-elastomeric and MRFE dampers. The damper force is estimated by the first Fourier sine and cosine components at the excitation frequency:

$$\begin{aligned} F(t) &= F_s \sin(\omega t) + F_c \cos(\omega t) \\ &= k'x(t) + \frac{k''}{\omega}\dot{x}(t) \end{aligned} \tag{3.6}$$

The stiffness k' and k'' are determined by substituting the displacement function and its derivative from equation 3.3 into the force equation:

$$k' = \frac{F_c X_c + F_s X_s}{X_c^2 + X_s^2} \tag{3.7}$$

$$k'' = \frac{F_c X_s - F_s X_c}{X_c^2 + X_s^2} \tag{3.8}$$

The equivalent damping C_{eq} is approximated by:

$$C_{eq} \cong \frac{k''}{\omega} \tag{3.9}$$

This linearization technique is an approximation method in non-linear systems because the complex stiffness assumes steady state harmonics at the excitation frequency. However, it gives an acceptable representation of the linearized in-phase stiffness and equivalent damping of the FE damper, the FE damper elastomeric body and the MRFE damper for comparing overall damping performances under different loading conditions.

The in-phase stiffness k' and equivalent damping C_{eq} of the FE damper and the FE damper elastomeric body (i.e. empty FE damper) at lag/rev and 1/rev frequencies are shown in Figure 3.7. We observe that C_{eq} of the baseline FE damper shows moderate amplitude dependence at both frequencies, while it remains fairly constant for the FE damper elastomeric body. The equivalent damping C_{eq} of both the baseline FE damper and the FE damper elastomeric body show a weak dependence on excitation frequency. Further, the majority of the energy dissipation (damping) is contributed by the viscous and compliant components (volumetric expansion of elastomer), with a very small contribution from the shear deformation of the elastomer. However, this method can not show the individual damping contributions of the viscous and compliance components. The in-phase stiffness also shows a fairly weak dependence on amplitude, with a maximum increment of about 12% in the case of the baseline FE damper at 1/rev frequency.

The complex modulus and equivalent damping of the MRFE and baseline FE dampers at lag/rev and 1/rev frequencies are shown in Figures 3.8 and 3.9 respectively. Loss factor is a key characterization parameter to describe the behavior of a spring-damper system, which is a ratio between loss stiffness and in-phase stiffness. Figure 3.8a gives the loss factor of the MRFE damper at lag/rev frequency. The loss factor shown as in dotted line is obtained from the FE damper. The field-off loss factor of the MRFE damper is at least 35% higher than the baseline FE damper. The loss factor of the MRFE is higher than the baseline FE damper at all times, indicating greater available damping. As the applied current initially increases, the loss factor of the MRFE damper generally increases, and then shows a reduction at lower amplitudes. As shown in Figure 3.8a, the in-phase stiffness of the MRFE damper is higher at low displacements and high fields, resulting in a relatively lower loss factor. Notably, the loss factor decreases with decreasing amplitude as the applied current is over 0.5 A. Note that the off-state in-phase stiffness of the MRFE dampers in much lower than the baseline FE damper, which is attributed to the damaged elastomeric center wall, which occurred during retrofitting, as mentioned in the previous section. Figure 3.8b shows the equivalent damping of the FE and MRFE dampers at the lag/rev frequency as a function of lag motion for different constant applied currents. The dotted line in Figure 3.8b is the equivalent damping of the baseline FE damper. The passive damping component of the MRFE damper has additional viscous losses due to the retrofit components. However, since the viscosity of the MR fluid in the MRFE device is lower than the silicon fluid used in the baseline FE damper, the field-off (0A) equivalent damping of the MRFE damper is

still lower than that of the baseline FE damper, which was a goal of this study. This is a potential benefit for reducing helicopter hub loads since high damping is not required for most flight conditions. Comparatively, the maximum field-on equivalent damping (1A) of the MRFE damper is much higher than that of the baseline FE damper. Notably, the equivalent damping of the MRFE damper can be varied dramatically as a function of the applied current, and damping increment of more than three fold could be achieved at the lowest lag motion amplitude. This allows a large controllable damping range such that the required lag damping at certain flight conditions can potentially be achieved.

Having determined that the MRFE can potentially augment damping at the design lag/rev frequency, the next set of results will compare the damping and loss factor of this damper at the 1/rev rotor frequency of 5.8 Hz. Evaluation at 1/rev is important in the development of the MRFE damper because this frequency is seen in the blades during high speed forward flight. Figure 3.9 displays these results. The equivalent damping at 1/rev resembles the response at lag/rev, in that the range of the MRFE damper extends above and below the FE damper performance. The dynamic range of the MRFE damper is observed to decrease at this frequency. This decline in dynamic range will be addressed later in the hydromechanical modeling section. However, turning to the loss factor results in Figure 3.9, it can still be seen that the MRFE damper generally has a much better loss factor than the baseline FE damper.

Helicopter lag dampers encounter multi-frequency excitation, especially in forward flight, where the forced lag motion occurs at the 1/rev rotor frequency. Under such circumstances, the complex modulus of an elastomeric damper at lag/rev frequency

decreases significantly, especially at lower amplitudes. However, in the case of the fluid-elastomeric damper and MRFE damper at zero field, the lag/rev damping available at dual frequency is higher than the damping at single frequency as shown in Figures 3.10a and 3.10b. This can be attributed to the increase in flow rate in valves as damper stroke increases. This issue will also be addressed in the hydromechanical modeling section later. At field on condition, there is an initial drop in damping at lower lag/rev amplitudes as the 1/rev amplitude is increased. However, it is observed that the MRFE damper provides an extended dynamic range between on and off conditions, and a much better loss factor than the FE damper (Figures 3.11a and 3.11b).

3.5 Hydromechanical Modeling of MRFE Damper

Due to the elliptical force-displacement hysteretic behavior of the FE damper and the MRFE damper (zero field), the linear complex modulus model (Kelvin type model) can capture the hysteresis these dampers exhibit. The amplitude dependent in-phase stiffness k' and the equivalent damping C_{eq} determined from the complex modulus method can be applied as the spring stiffness and damping coefficient of the Kelvin model. However, in the baseline FE and MRFE damper systems, this method cannot delineate the stiffness and damping contributions from the elastomer in shear, elastomer compliance and viscous flow. In addition, under the application of a magnetic field, the MRFE damper exhibits a non-linear behavior (Figure 3.6b), and the complex modulus method cannot accurately capture this behavior. In addition, the physical flow dynamics of the fluid or hydraulic based baseline FE and MRFE lag dampers is not well represented. Thus, to accurately describe the flow dynamics and

predict the non-linear hysteretic damping force of the MRFE damper, a hydromechanical model based on hydraulic and mechanical lumped parameters is proposed. The proposed lumped parameter control volumes are shown in Figure 3.12. For clarity, the two MR valves are identified with subscripts *a* and *b*. There are two volume chambers (1 and 5) which are lumped into fluid pressures P_1 and P_5 and compliances S_1 and S_5. Both S_1 and S_5 represent the compliances of the fluid and the chamber. Control volumes *a2*, *a3*, *b2* and *b3* are lumped into fluid inertances I_{a2}, I_{a3} I_{b2} and I_{b3} and passive flow resistances R_{a2}, R_{a3} R_{b2} and R_{b3}. Control volumes *a4* and *b4* are also lumped into fluid inertances I_{a4} and I_{b4} and passive flow resistances R_{a4} and R_{b4} respectively, while ΔP_{a4} and ΔP_{b4} are the pressure drops due to the yield stress of the MR fluid in the corresponding control volumes. A one-dimensional fluid flow is assumed such that the velocity and pressure of a control volume are span wise constant at a particular time, but are time-varying. In addition, incompressible flow is also assumed.

The model is first formulated for a general case where the two MR valves and two chambers are assumed to be different. The Kelvin model is assumed for the shear deformation of the MRFE damper elastomeric body, where it is modeled as a linear spring and linear dashpot combination. The two elastomeric chambers are broken into two semi-circular wall connected at the center, and they are assigned masses m_{r1} and m_{r5}. The shear mode in-phase stiffness and equivalent damping of the MRFE damper elastomeric body from the complex modulus method are utilized as the spring constants k_{r1} and k_{r5} and damping coefficients C_{r1} *and* C_{r5}. These values are estimated

by pouring out the MR fluid from the MRFE device and testing the MRFE damper elastomeric body (i.e. empty MRFE damper).

The proposed lumped parameter model includes three lumped masses (m_A, m_B and m_r) and three dynamic degrees of freedom ($x(t)$, $x_A(t)$ and $x_B(t)$), as will be shown later. From the Kelvin model, the governing equation of motion of the elastomer is given by:

$$F(t) - (k_{r1} + k_{r5})x(t) - (C_{r1} + C_{r5})\dot{x}(t) - A_p(P_5(t) - P_1(1)) = (m_{r1} + m_{r5})\ddot{x}(t) \tag{3.10}$$

Similar to an elastomer deformed in shear, bulging of an elastomer due to volumetric expansion exhibits damping. Colgate *et al* [91] recommend that some improvement could be attained in modeling by considering bulge damping. This bulge or compliant damping is captured by introducing a resistant parameter [89] on the net flow into the compliant chambers resulting in the volumetric expansion. Thus, applying the continuity argument to the volume chambers 1 and 5, the following equations are obtained:

$$A_p\dot{x}(t) - q_a(t) - q_b(t) = S_5(\dot{P}_5(t) - R_5(A_p\ddot{x}(t) - \dot{q}_a(t) - \dot{q}_b(t))) \tag{3.11}$$

$$-A_p\dot{x}(t) + q_a(t) + q_b(t) = S_1(\dot{P}_1(t) - R_1(-A_p\ddot{x}(t) + \dot{q}_a(t) + \dot{q}_b(t))) \tag{3.12}$$

where R_1 and R_5 represent the elastomeric resistances. The flow rates through valves a, and b, in terms of inertance displacements x_{ai} and x_{bi} are given by:

$$q_a(t) = A_{a2}\dot{x}_{a2}(t) = A_{a3}\dot{x}_{a3}(t) = A_{a4}\dot{x}_{a4}(t) \tag{3.13}$$

$$q_b(t) = A_{b2}\dot{x}_{b2}(t) = A_{b3}\dot{x}_{b3}(t) = A_{b4}\dot{x}_{b4}(t) \tag{3.14}$$

where A_{ai} and x_{ai} are the cross sectional area and fluid inertance displacement of the i^{th} lump or control volume. The combined compliances of the fluid chambers for control volume 1 and 5 are given by:

$$S_1 = \frac{A_p^2}{k_{c1}}, \qquad S_5 = \frac{A_p^2}{k_{c5}} \tag{3.15}$$

Here, k_{c1} and k_{c5} represent the bulge stiffness effects of the two volume chambers. Due to the complexity of the damper design, deformation and the absence of a well defined piston, an equivalent piston area A_p is formulated to account for the total displaced fluid volume due to forced elastomer deformation.

Inserting equations 3.13 – 3.15 in equations 3.11 – 3.12, and integrating once and rearranging gives two equations for the chamber pressures as follows:

$$P_5 = \frac{k_{c5}}{A_p^2}\left(A_p x(t) - A_a x_a(t) - A_b x_b(t)\right) + R_5\left(A_p \dot{x}(t) - A_a \dot{x}_a(t) - A_b \dot{x}_b(t)\right) \tag{3.16}$$

$$P_1 = \frac{k_{c1}}{A_p^2}\left(-A_p x(t) + A_a x_a(t) + A_b x_b(t)\right) + R_1\left(-A_p \dot{x}(t) + A_a \dot{x}_a(t) + A_b \dot{x}_b(t)\right) \tag{3.17}$$

Also from the hydraulic model shown in Figure 3.12, the total pressure drop in the two valves *a* and *b* with two passive passages (control volumes 2 and 3) and MR valve annular gap (control volume 4) due to flow of the MR fluid is given by:

$$(P_5(t) - P_1(t)) = I_a \dot{q}_a(t) + R_a q_a(t) + \Delta P_{a4}\, sgn(q_a(t)) \tag{3.18}$$

$$(P_5(t) - P_1(t)) = I_b \dot{q}_b(t) + R_b q_b(t) + \Delta P_{b4}\, sgn(q_b(t)) \tag{3.19}$$

The terms I_a, R_a and ΔP_a (the pressure drop due to MR effect) are given by:

$$I_a = \rho \sum_{i=2}^{4} \frac{l_{ai}}{A_{ai}} \tag{3.20}$$

$$R_a = \frac{128\mu_o}{\pi} \sum_{i=2}^{3} \left(\frac{l_i}{D_i^4} \right)_a + 12\mu_{MR} \left(\frac{l_4}{A_d d_4^2} \right)_a + R_{min\ or\ losses} \tag{3.21}$$

$$\Delta P_{a4} = 2 \frac{l_{a4}}{d_{a4}} \tau_{ya}(H) \tag{3.22}$$

where l is length of control volume, D is diameter, d is MR valve annular gap (lump 4) and A_d is the area of the annular gap in the MR valve. Further, ρ is fluid density and H is the applied field. Under the Bingham assumption, the fluid viscosity μ_o and the post-yield viscosity μ_{MR} are assumed to be equal ($\mu_o = \mu_{MR}$). The Bingham yield stress of the MR fluid at the applied magnetic field is represented by $\tau_{ya}(H)$. The term ΔP can be interpreted as the minimum required differential pressure below which flow is fully restricted. The equation for the resistance is derived from laminar flow analysis. The above equations also hold true for the second flow path by replacing the subscript a with b. Due to laminar flow assumption with low Reynolds number, the minor losses are ignored in this investigation.

By eliminating the internal variables P_1 and P_5 by inserting equations 3.16 – 3.17 in to 3.18 – 3.19, we obtain the following three equations of motions in terms of time varying variables:

$$\begin{aligned}&(m_{r1} + m_{r5})\ddot{x}(t) + (C_{r1} + C_{r2})\dot{x}(t) + (k_{r1} + k_{r2})x(t) \\ &+ (C_{c1} + C_{c5})\left(\dot{x}(t) - \dot{x}_A(t) - \dot{x}_B(t)\right) + (k_{c1} + k_{c5})\left(x(t) - x_A(t) - x_B(t)\right) = F(t)\end{aligned} \tag{3.23}$$

$$\begin{aligned}&m_A\ddot{x}_A(t) + C_A\dot{x}_A(t) - (C_{c1} + C_{c5})\left(\dot{x}(t) - \dot{x}_A(t) - \dot{x}_B(t)\right) \\ &\qquad - (k_{c1} + k_{c5})\left(x(t) - x_A(t) - x_B(t)\right) + F_{yA}sgn(\dot{x}_A(t)) = 0\end{aligned} \tag{3.24}$$

$$m_B\ddot{x}_B(t)+C_B\dot{x}_B(t)-(C_{c1}+C_{c5})\left(\dot{x}(t)-\dot{x}_A(t)-\dot{x}_B(t)\right) \\ -(k_{c1}+k_{c5})\left(x(t)-x_A(t)-x_B(t)\right)+F_{yB}sgn(\dot{x}_B)=0 \tag{3.25}$$

The generalized inertance displacement x_A and mass m_A, and the viscous damping C_A for valve *a* and the bulge damping C_{c1} and C_{c5} are expressed as:

$$\begin{aligned} x_A &= (A_{a4}/A_p)x_{a4}, & m_A &= I_a A_p^2 \\ C_A &= R_a A_p^2, & F_{yA} &= \Delta P_{a4} A_p \\ C_{c1} &= R_1 A_p^2, & C_{c5} &= R_5 A_p^2 \end{aligned} \tag{3.26}$$

Replacing subscripts *A* and *a* with *B* and *b* in the above equations will give the corresponding terms for the second flow valve. Here, F_{yA} and F_{yB} represent the controllable yield forces in each MR valve and are a function of the applied magnetic field.

Equations 3.23 – 3.25 are the basic equations of motions describing the MRFE damper mechanism. However, it is still difficult to formulate a mechanism to describe the systems. This is primarily due to the fact that the input displacement *x*, the generalized inertance displacements x_A and x_B are all coupled to each other through the bulge stiffness and bulge damping components. In addition, in dissimilar valves, which is the initial assumption, there is unequal flow rate in the two valves arising from the difference in head losses. We can define a transfer function relation of the flow rates in equations 3.18 and 3.19 as:

$$q_a(i\omega)=\frac{(P_5-P_1)-\Delta P_{a4}}{\frac{I_a}{R_a}i\omega+1} \tag{3.27}$$

$$q_b(i\omega)=\frac{(P_5-P_1)-\Delta P_{b4}}{\frac{I_b}{R_b}i\omega+1} \tag{3.28}$$

Combining the above equations with parameters defined in equation 3.26, we get the following relation:

$$\frac{x_A}{x_B}(i\omega) = \psi(i\omega) \tag{3.29}$$

where the valve factor $\psi(i\omega)$ is given by:

$$\psi(i\omega) = \frac{x_A}{x_B}(i\omega) = \frac{\left(m_B - \frac{F_{yA} - F_{yB}}{\omega^2 x_B(i\omega)}\right) i\omega + C_B}{m_A i\omega + C_A} \tag{3.30}$$

By plugging equation 3.30 in equations 3.23 – 3.25, we get the following 4 equations of motions:

$$\begin{aligned}&(m_{r1} + m_{r5})\ddot{x}(t) + (C_{r1} + C_{r5})\dot{x}(t) + (k_{r1} + k_{r5})x(t) \\ &+ (C_{c1} + C_{c5})\left(\dot{x}(t) - (1+\psi)\dot{x}_A(t)\right) + (k_{c1} + k_{c5})\left(x(t) - (1+\psi)x_A(t)\right) = F(t)\end{aligned} \tag{3.31}$$

$$\begin{aligned}&m_A\ddot{x}_A(t) + C_A\dot{x}_A(t) - (C_{c1} + C_{c5})\left(\dot{x}(t) - (1+\psi)\dot{x}_A(t)\right) \\ &\qquad - (k_{c1} + k_{c5})\left(x(t) - (1+\psi)x_A(t)\right) + F_{yA}sgn(\dot{x}_A(t)) = 0\end{aligned} \tag{3.32}$$

$$\begin{aligned}&(m_{r1} + m_{r5})\ddot{x}(t) + (C_{r1} + C_{r5})\dot{x}(t) + (k_{r1} + k_{r5})x(t) \\ &+ (C_{c1} + C_{c5})\left(\dot{x}(t) - (1+\psi^{-1})\dot{x}_B(t)\right) + (k_{c1} + k_{c5})\left(x(t) - (1+\psi^{-1})x_B(t)\right) = F(t)\end{aligned} \tag{3.33}$$

$$\begin{aligned}&m_B\ddot{x}_B(t) + C_B\dot{x}_B(t) - (C_{c1} + C_{c5})\left(\dot{x}(t) - (1+\psi^{-1})\dot{x}_B(t)\right) \\ &\qquad - (k_{c1} + k_{c5})\left(x(t) - (1+\psi^{-1})x_B(t)\right) + F_{yb}sgn(\dot{x}_B(t)) = 0\end{aligned} \tag{3.34}$$

Equations 3.31 – 3.32 coupled with equation 3.30 describe damper dynamics in terms of generalized inertance variable x_A and equations 3.33 – 3.34 coupled with equation 3.30 describe in terms of generalized inertance variable x_B. The valve factor, ψ, which relates the generalized inertance variables x_A and x_B, basically varies from zero (no flow in valve *b*) to infinity (no flow in valve *a*). The valve factor is a function of the

head losses encountered in the MR valves as shown in equation 3.30. Bulge damping C_{c1} and C_{c5} represent the damping contribution of the elastomeric body due to volumetric flexing of volume chambers.

Figures 3.13 and 3.14 give the mechanism of the proposed hydromechanical model in terms of generalized inertance variables x_A and x_B respectively. Both systems are composed of parallel and series combinations of linear springs, dashpots, and Coulomb friction elements. The analogous mechanical systems (Figures 3.13 and 14) and governing equations of 3.30 – 3.34 show that in the pre-yield region, the hysteresis behavior is evident in the chamber compliance effects (C_{c1}, C_{c5}, k_{c1}, k_{c5}). The Coulomb elements (F_{yA}, F_{yB}), generalized inertance masses (m_A, m_B) and viscous damping (C_A, C_B) terms represent the post-yield behavior.

In the present snubber type MRFE damper design, since there are two identical MR valves and elastomeric chambers, the following assumptions will hold true: $F_{yA} = F_{yB} = F_y$, $k_{c1} = k_{c5} = k_c$, $C_{c1} = C_{c5} = C_c$, $m_{r1} = m_{r5} = m_r$, $k_{r1} = k_{r5} = k_r$, $C_{r1} = C_{r5} = C_r$ and $\psi = 1$. Thus, equations 3.30 – 3.34 will further reduce to:

$$2m_r\ddot{x}(t) + 2C_r\dot{x}(t) + 2k_r x(t) + 2C_c\left(\dot{x}(t) - 2\dot{x}_A(t)\right) + 2k_c\left(x(t) - 2x_A(t)\right) = F(t) \tag{3.35}$$

$$m_A\ddot{x}_A(t) + C_A\dot{x}_A(t) - 2C_c\left(\dot{x}(t) - 2\dot{x}_A(t)\right) - 2k_c\left(x(t) - 2x_A(t)\right) + F_y sgn(\dot{x}_A(t)) = 0 \tag{3.36}$$

3.6 Parameter Identification and Modeling Results

3.6.1 Single Frequency Performance

To begin the optimization procedure to accurately simulate measured damper dynamics, some parameters were estimated initially to lower the number of optimized

parameters. Table 3.3 outlines the measured and model estimated and dependent parameters. The dependent variables are product of measured and estimated parameters. In order to minimize the squared mean error between the measured and predicted damping force of the MRFE damper, a constrained least-mean-squared (LMS) error minimization technique was employed to estimate and optimize the equivalent piston area A_p, the bulge stiffness k_c, the bulge damping C_c and yield force F_y. The rubber mass is neglected in this optimization. The error function for the hydromechanical model is expressed as:

$$E(A_p, k_c, C_c, F_y) = \sum_{j=1}^{N} \left(F(t_j) - F^*(t_j) \right)^2 \tag{3.37}$$

where $F(t_j)$ is the actual measured force, $F^*(t_j)$ is the calculated force from the hydromechanical modeling, t_j is the time at which the j^{th} sample was measured and N is the number of data per one cycle.

The viscosity and density of the MR fluid is known, so that the fluid resistance and inertance values can be estimated using equations 3.20 and 3.21. These values remain constant since they are not a function of input displacement and applied current. Figures 3.15a and 3.15b show the optimized equivalent piston areas obtained from the error minimization procedure at different amplitudes and frequencies. The shear stiffness and bulge stiffness of the MRFE damper at lag/rev and 1/rev are given in Figures 3.16a and 3.16b respectively. The damping contributions from the hydraulic and mechanical components are given in Figures 3.17a and 3.17b. The plots show that majority of the MRFE device passive damping is provided through viscous damping, while elastomeric shear deformation contributes minimal damping. Figure 3.18 shows the variation of yield force, F_y, as obtained from model optimization. The

yield force increases with increasing applied current, and this trend is similar at both frequencies.

The damping force versus velocity cycles at lag/rev and 1/rev frequencies and different applied fields are given in Figure 3.19. Figure 3.19a shows the force-velocity hysteresis plots at lag/rev frequency and Figure 3.19b shows at 1/rev. The displacement amplitude for each case is 2.286 mm (0.09 in). The figures show that the hydromechanical model is able to capture the non-linear dynamic behavior and closely estimates the actual hysteretic damping force behavior of the MRFE damper from experimental measurements.

To determine how well the lumped parameter model, the average error between the measured and estimated force time histories were calculated. The relative root mean squared (rms) force error per cycle is given by:

$$E_{rms} = \left[\frac{\sum_{j=1}^{N} \left(F(t_j) - F^*(t_j) \right)^2}{\sum_{j=1}^{N} F(t_j)^2} \right]^{1/2} X\ 100\% \tag{3.38}$$

By determining these force errors, we can quantify the measure of how well the model captures the FE damper response. As Figures 3.20a and 3.20b show, the maximum damping force between the estimated and measured force is about 7% at lag/rev and 6% at 1/rev excitation frequencies.

The hydromechanical model is formulated on the basis that it can describe or estimate the physical flow phenomenon that is inherent to the MRFE damper system. Based on this assumption, the MR effect contributed to the damper system is extracted from the model. At both frequencies, the input amplitude was chosen to be

2.286 mm (0.09 in), while the current is varied from 0 A, 0.5 A and 1 A. Ignoring the inertial term, the MR effective force F_{MR} in each valve of the damper system, as extracted from the model, is given by:

$$F_{MR}(t) = C_A \dot{x}_A(t) + F_y \, sgn(\dot{x}_A(t)) \tag{3.39}$$

The first term in the above equation is related to the viscous effect and the second term results from the magnetic effect. These results at field-off condition at lag/rev and 1/rev frequencies are shown in Figures 3.21a and 3.21b. From the figure, it is observed that as the amplitude of excitation increases, the viscous damping, which is the slope of the force versus velocity plot, also increases. This is due to the increment in the effective piston area as amplitude is increased, which results in a higher volume flow rate. This result is consistent with the results shown at single and dual frequency excitation in Figures 3.8 – 3.11. In addition, the MR force-velocity plots at different applied currents are shown in Figures 3.22 at lag/rev and 1/rev frequencies respectively. The model is able to show the Bingham type flow typical of MR fluids, with the y-intercept of the force-velocity plot reflecting the yield force of the MR fluid. It is shown that the active damping of the MRFE is contributed by the MR effect activated through the applied current. As the applied current is increased, the yield force increases, and thus damping is increased. Further, the MRFE damper at 1/rev frequency is operating in a stronger post yield region, reflected in its higher fluid velocity than at lag/rev frequency. The equivalent damping, C_{eq}, can alternatively be computed as:

$$C_{eq} = \frac{E_{dis}}{\pi \omega X^2} \tag{3.40}$$

From this equation, it can be seen that the equivalent damping, C_{eq} is proportional to the energy dissipated, E_{dis}. X is the amplitude of excitation. The energy dissipated is :

$$E_{dis} = \int_{0}^{\frac{2\pi}{\omega}} F(t)dx \tag{3.41}$$

where $F(t)$ is the model estimated damper force. The model estimated equivalent damping at lag/rev and 1/rev are shown in Figure 3.23. The equivalent damping from hydromechanical model shows the same trend as the linear characterization, where during field-on operation, an increase in the input frequency resulted in a lower controllable damping range of the MRFE damper (Figures 3.8 - 3.11), where the damping at maximum applied field tends to approach the zero-field performance.

Further, the total flow rate ($A_p\dot{x}(t)$) and flow rate through MR valves ($2A_p\dot{x}_A(t)$) at lag/rev frequency were plotted and compared at the field-on condition (I = 1 A), at two different input amplitudes. As shown in Figure 3.24a, the MR valve flow rate is less than the total. This is manifested in the "No-flow interval" region in the figure. At this condition, the MR fluid has not yet yielded and volume compensation is attained through bulging of the elastomeric damper body. In addition, as the input amplitude increases, more of the total fluid flow goes through the valves. This is because the MR fluid yields faster at higher velocity, giving the fluid more time to flow through the valves. The portion of the total displaced volume per half cycle that flows through the MR valve ($\%\ Vol_{MR}$) is estimated from the formulated model per the following equation:

$$\%Vol_{MR} = \left.\frac{\int 2A_p\dot{x}_A(t)dt}{\int A_p\dot{x}(t)dt}\right|_{halfcycle} * 100\% \tag{3.42}$$

These results are shown in Figure 3.24b for 3.8 Hz frequency. The plot shows that at field-on condition, $\%Vol_{MR}$ increases with increasing amplitude. It is also observed that, as the current is increased, $\%Vol_{MR}$ decreases due to the increased MR effect.

3.6.2 Performance Prediction Using Hydromechanical Model

It is to be recalled from *Section 3.2* that the MRFE damper is assembled as a sealed unit, so that minimal possibility exists for the fluid to pass from one chamber to the other without traveling through the flow ports of the MR valves. The original FE damper is a hermetically sealed unit which was factory assembled. However, in order to design and retrofit the MR valves, the upper half of the elastomeric center wall was damaged during the disassembly process, as the top plate of the FE damper had to be cut to be removed. A rubber repair kit was used to rebuild the wall and provide a smooth surface for sealing with the new top plate. An epoxy sealant was used to bond existing and rebuilt elastomeric walls. Even though the bond surface adequately sealed the unit, it was not able to maintain the stiffness of the baseline damper. This was evident in the stiffness and loss factor plots shown in Figure 3.8.

The hydromechanical model can thus predict the performance of an MRFE damper, which exhibits the same shear and bulge parameters as the baseline FE damper. This will help understand the MRFE performance had it been factory assembled rather than a retrofit, which future designs are intended to be. To that effect, the following parameters of the FE damper from *Chapter 2*, i.e. shear stiffness k_r, shear damping C_r, bulge stiffness k_c and bulge damping C_c, were applied in the current model, holding all other MRFE parameters constant. These adapted FE damper parameters were parameters determined at 30°C (*Chapter 2*), which was

assumed to give comparable results as the ambient temperature (27.5°C) the MRFE damper was tested under. Figure 3.25 gives the results. Figure 3.25a shows the force vs. displacement plot of the predicted MRFE damper and that of the FE damper. We observe that the peak loads of the predicted MRFE damper at field-off condition and that of the FE damper are similar. At this condition, both show also similar inclination angle, indicating matching stiffness. In addition, the FE damper has a larger enclosed area that the MRFE at zero-field. However, as current is applied, the enclosed area of the MRFE gets bigger. Figure 3.25b gives the in-phase stiffness and loss factor of the predicted MRFE and baseline FE dampers from the complex modulus method. As seen in the plots, the zero field in-phase stiffness of the MRFE is similar to that of the baseline FE damper, which was not the case in the retrofitted MRFE damper case (Refer to Figure 3.8). In addition, due to the increment in in-phase stiffness, the loss factor of the predicted MRFE damper is lower than the retrofitted MRFE damper (Figure 3.8), and it also encloses that of the baseline FE damper.

3.6.3 Dual Frequency Performance

To predict the response of the MRFE damper under dual frequency excitation, it was subjected to various combinations of lag/rev and 1/rev frequency amplitudes under various applied currents, and the force-time history is used to evaluate the model performance. The dual frequency test matrix at all temperatures is given in Table 3.3. Utilizing optimized model parameters, the MRFE damper dual frequency response was predicted by linear superposition of the estimated damper performance at each excitation frequency. The modeling results for two combinations of the lag/rev and 1/rev frequencies at field-off and field-on conditions are given in Figures

3.26 and 3.27. In the figures, X_{lag} represent the amplitude of the harmonic input at the lag/rev frequency while X_{pri} represents the amplitude at 1/rev frequency. The results show that the hydromechanical model was able to predict MRFE damper dual frequency response reasonably well over the amplitudes and frequencies investigated.

3.7 Conclusion

Hingeless and bearingless helicopters are equipped with lag dampers to mitigate instabilities such as air and ground instabilities. Currently, most bearingless helicopters utilize either elastomeric or hybrid fluid-elastomeric dampers, which are proven to be reliable and maintenance free with on-condition visual monitoring requirement. However, elastomeric lag dampers exhibit strong amplitude and frequency dependent damping and stiffness losses. In addition, both elastomeric body and fluid-elastomeric (FE) dampers are adversely affected by temperature. Unlike these passive dampers, an MRFE lag damper has the potential to compensate for damping losses due to inherent material properties or extreme environmental conditions by the application of a controllable magnetic field. A snubber type MRFE damper was developed and investigated to establish its potential in augmenting damping during flight conditions where instabilities are likely to occur, and in compensating for adverse environmental conditions.

To this effect, a snubber type FE lag damper was retrofitted to develop an MRFE lag damper. The MRFE design does not introduce any moving parts to the system in an effort to preserve the proven reliability and maintenance free conditions of the original baseline FE damper. This investigation demonstrated the feasibility of using the MRFE damper to mitigate helicopter rotor instabilities with fixed frame

experiments. The MRFE damper can provide comparable damping force to the baseline FE damper. Moreover, a substantial increase in damping and a wide damping controllable range can be gained by using the MRFE damper. More than a 100% change in damping was obtained over the amplitude range tested. This damping and controllability range of the MRFE damper can be tuned to match actual damping requirements of certain flight conditions where stability margins may deteriorate. Designing the device with reduced field-off damping helps decrease rotor hub loading because higher damping is only required at specific flight conditions. In addition, pairs of MRFE damper can be tuned to match one another, thus, enhancing rotor blade tracking.

To account for the non-linear behavior of the MRFE damper, a lumped parameter based, hydromechanical model was formulated and validated. The model describes the interaction of the mechanical, hydraulic and magnetorheological phenomena within the damper system. The hydromechanical model is a semi-empirical model where parameters are fundamentally dependent on damper geometry and material properties at a given test condition. Thus, physical parameters like fluid inertance and resistance, chamber compliance and yield force are considered. It was observed that the flow dynamics and coupling between the mechanical and hydraulic systems of the MRFE damper were illustrated well by the analogous mechanical system and the corresponding governing equations. This model was shown to accurately estimate the field-dependent hysteretic damping force and illustrate the physical flow dynamics of the MRFE damper, making it valuable for future design and feedback control studies.

Table 3.1 Models for elastomeric, FE, MR and MRFE dampers

		Elastomer		FE damper	MR damper	MRFE damper	
	Model	Linear	Non-linear			De-coupled	Coupled
1	Complex Modulus/ Kelvin model	X		X			
2	Non-linear Complex Modulus [4, 6, 41]		X				
3	Cubic spring + Kelvin model [3, 42]		X				
4	Non-linear Zener model [43]		X				
5	Linear ADF model [44]		X				
6	Non-linear ADF model [45 - 47]		X				
7	Rate-dependent, distributed elasto slide model [5]		X				
8	Lumped parameter model [53, 54]			X			
9	Bingham based models [73 - 78]				X		
10	Viscoelastic-plastic model [10, 72, 78]				X		
11	Function based models [79 - 81]				X		
12	Bouc-Wen model [82, 83]				X		
13	Hydromechanical model [84 - 86]				X		
14	Rate-dependent elasto slide model [87]				X		
15	Model {1} + model {10}					X	
16	Model {7} + model {14}					X	
17	New hydro-mechanical model	X		X			X

Table 3.2 Dual frequency test matrix

$X_{lag/rev}$ [in]	$X_{1/rev}$ [in]	0.03	0.05	0.07	0.09	0.10	0.13
0.03		X	X	X	X	X	X
0.05		X	X	X	X	X	
0.07		X	X	X	X		
0.09		X	X	X			
0.10		X	X				
0.13		X					

Table 3.3 Measured, model estimated and dependent model parameters

Measured Parameters	Model Estimated Parameters	Dependent Parameters
Viscosity, μ	Eqv. Piston area, A_p	Mass, m_A
Resistance, R	Bulge stiffness, k_c	Viscous damping, C_A
Density, ρ	Bulge damping, C_c	
Inertance, I	Yield force, F_y	
Shear stiffness, k_r		
Shear damping, C_r		

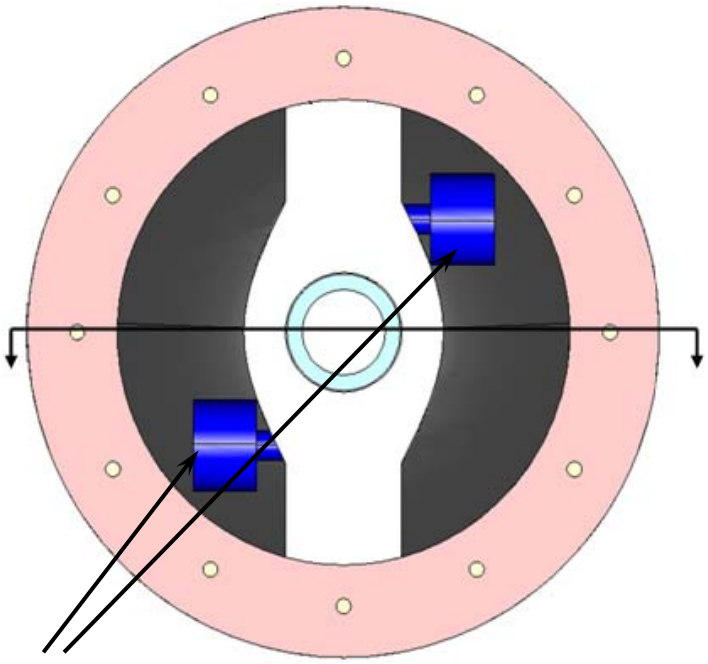

(a) MRFE damper top view

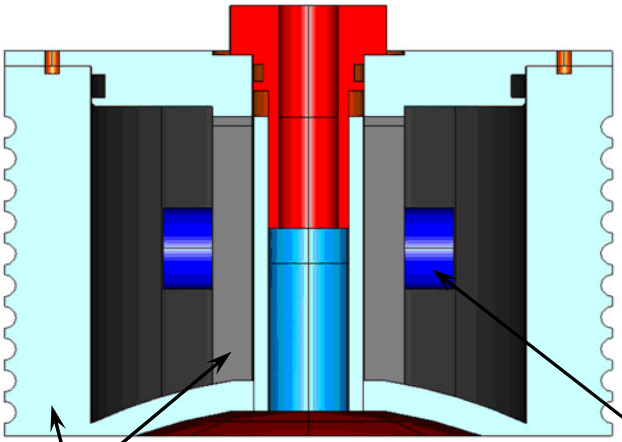

(b) MRFE damper section side view

Figure 3.1: Proposed MRFE damper design configuration

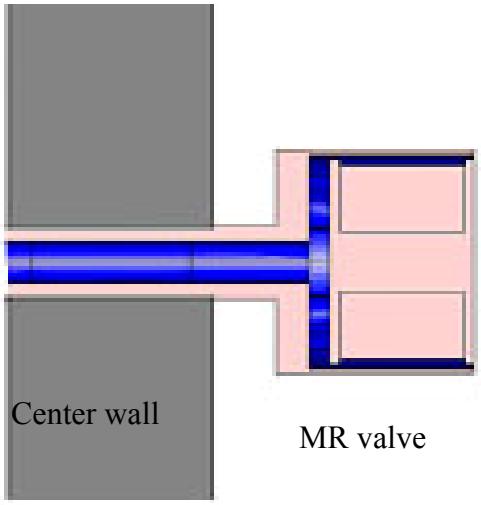

(a) Orientation of MR valve on center wall

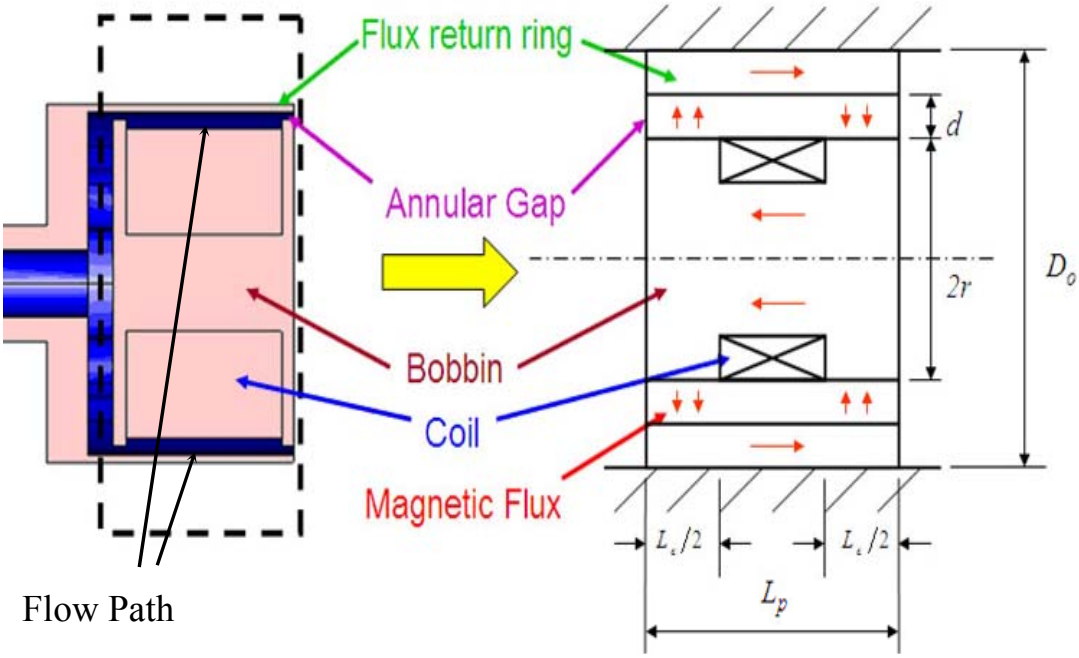

(b) MR valve details

Figure 3.2: MRFE damper design details

Figure 3.3: MR valve components and assembly

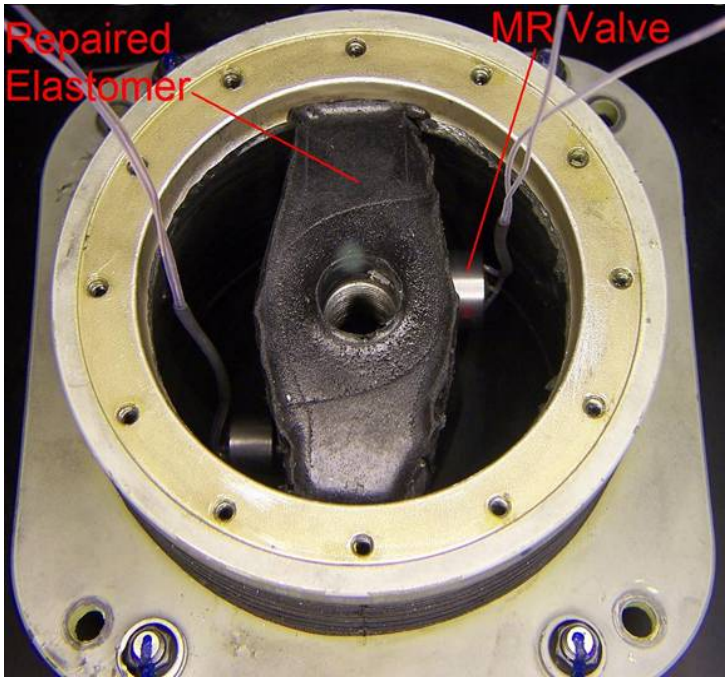

(a) MRFE damper assembly, top plate removed

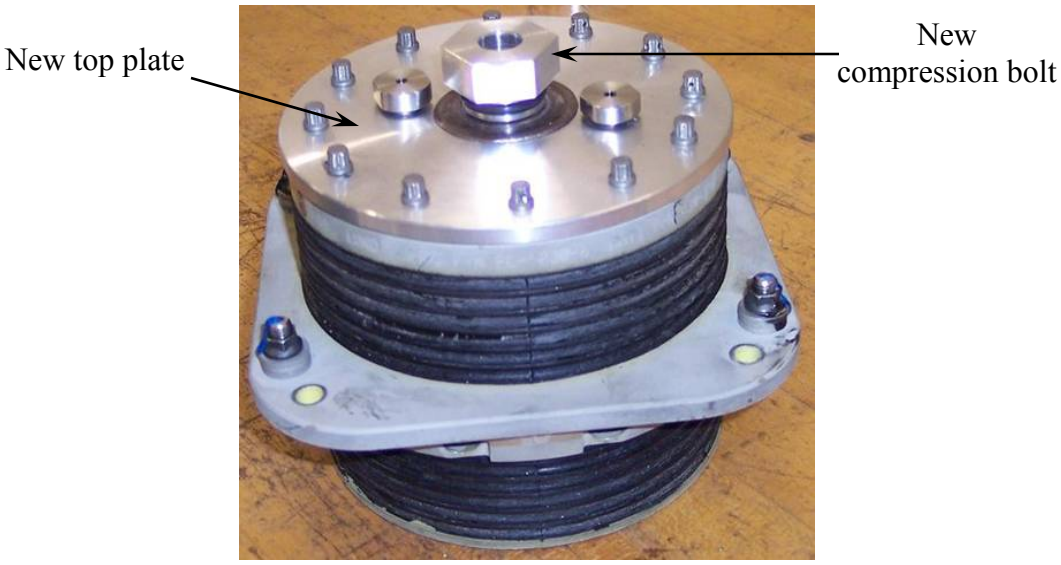

(b) MRFE damper assembly

Figure 3.4: MRFE damper assembly

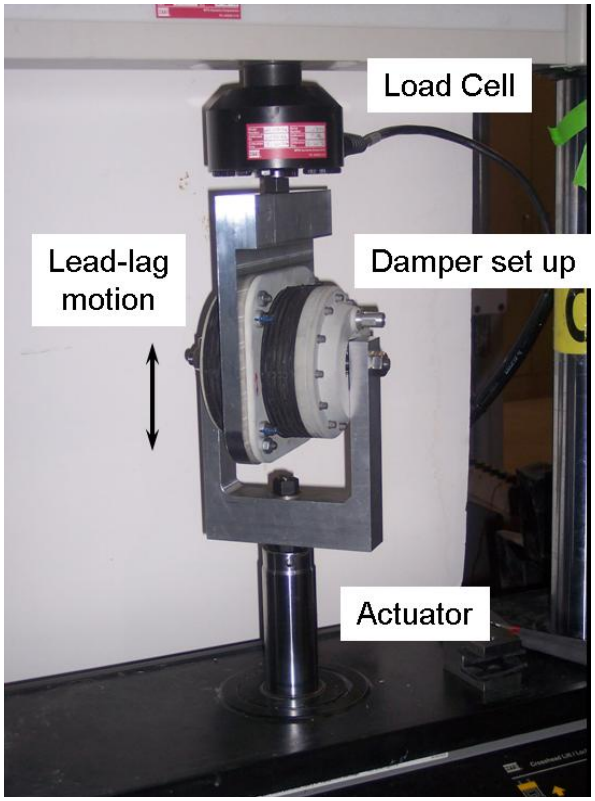

Figure 3.5: FE lag damper test set-up on MTS testing machine

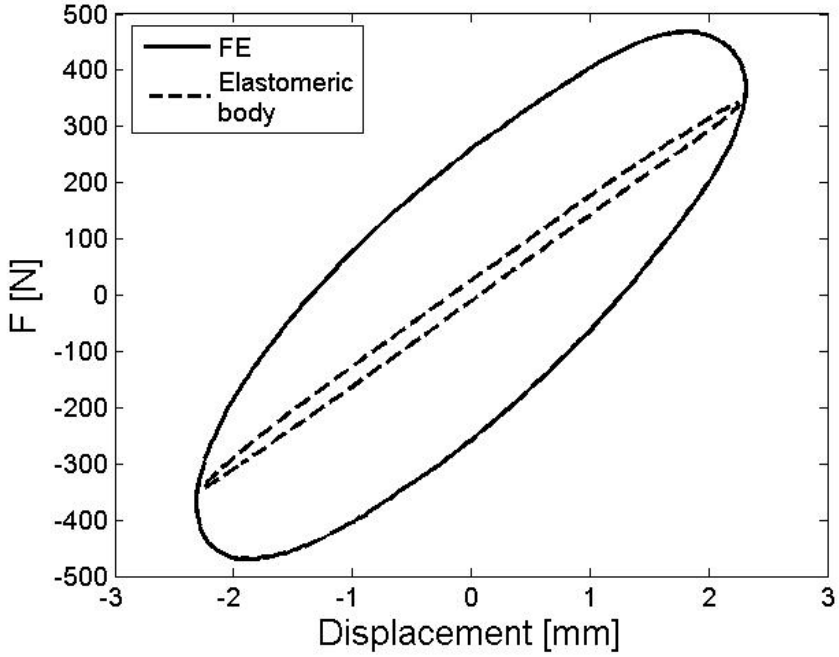

(a) FE damper and FE damper elastomeric body

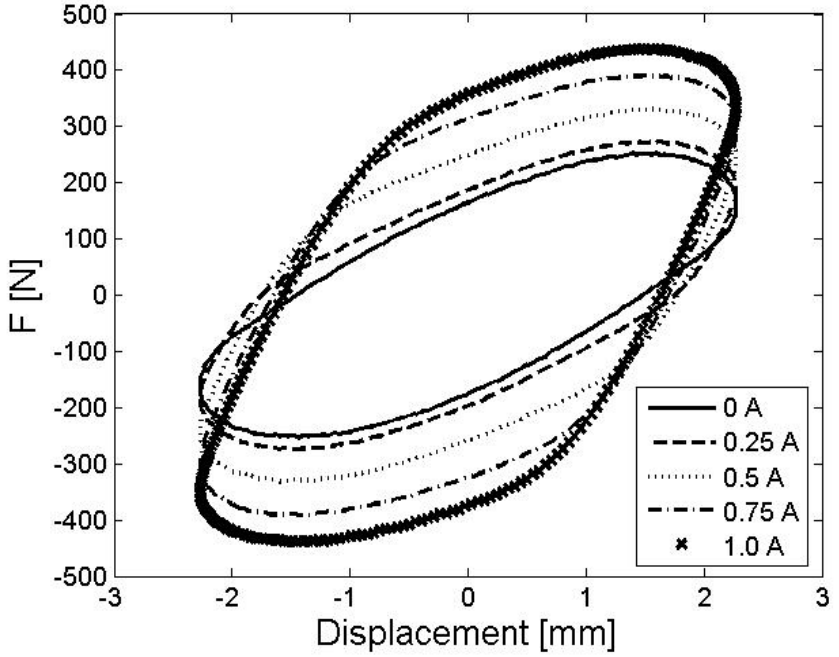

(b) MRFE damper

Figure 3.6: Typical force-displacement hysteresis results at fixed amplitude

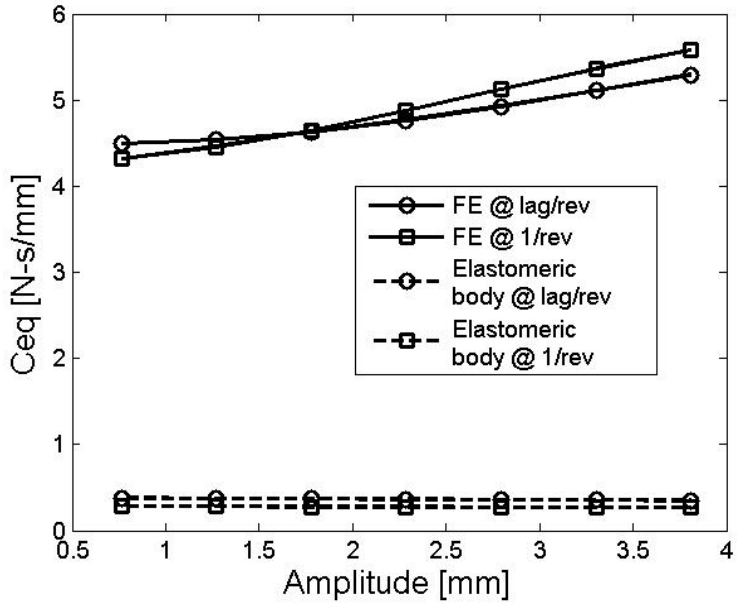

(a) Equivalent damping

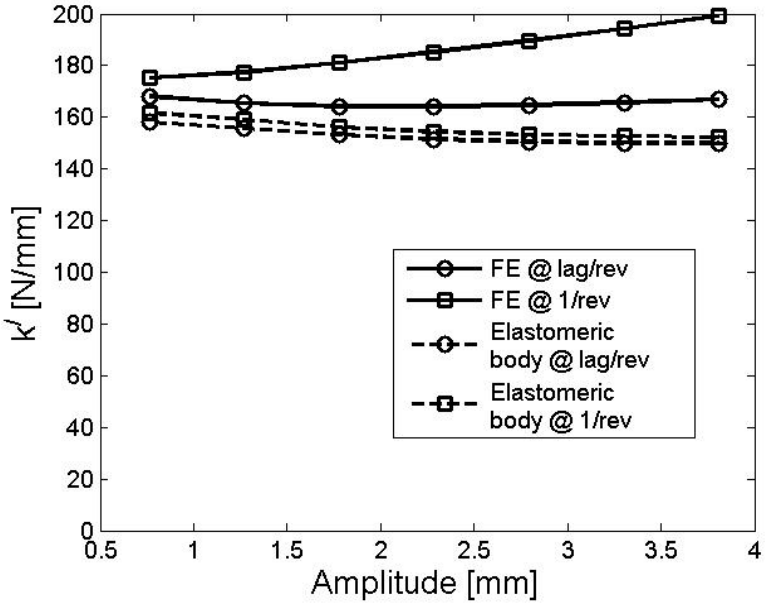

(b) In-phase stiffness

Figure 3.7: Complex modulus characterization of FE damper and FE damper elastomeric body

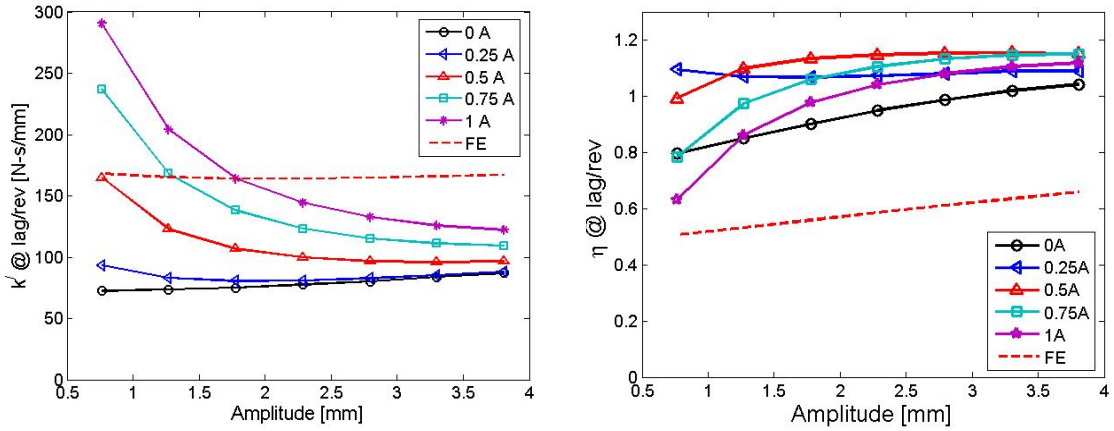

(a) Complex Modulus

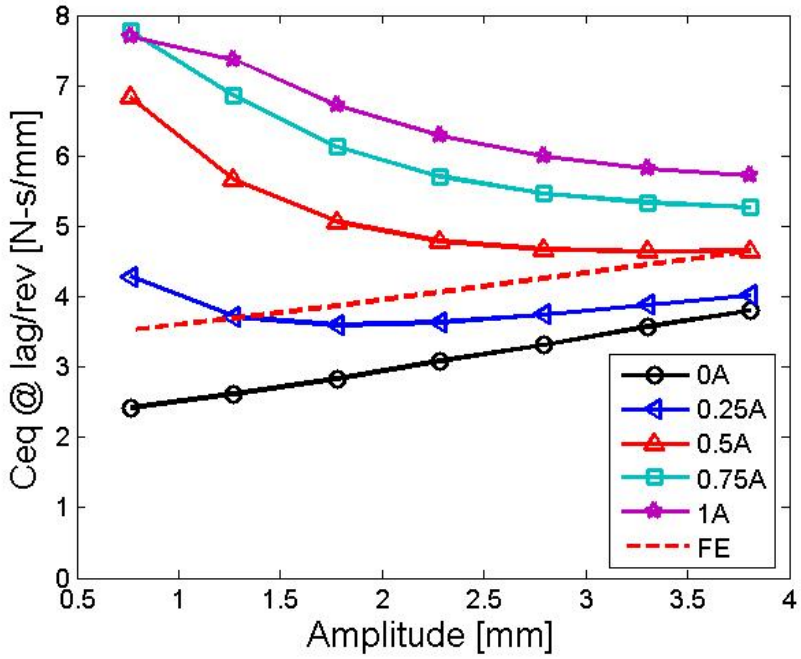

(b) Equivalent Damping

Figure 3.8: Complex modulus characterization of MRFE damper at lag/rev

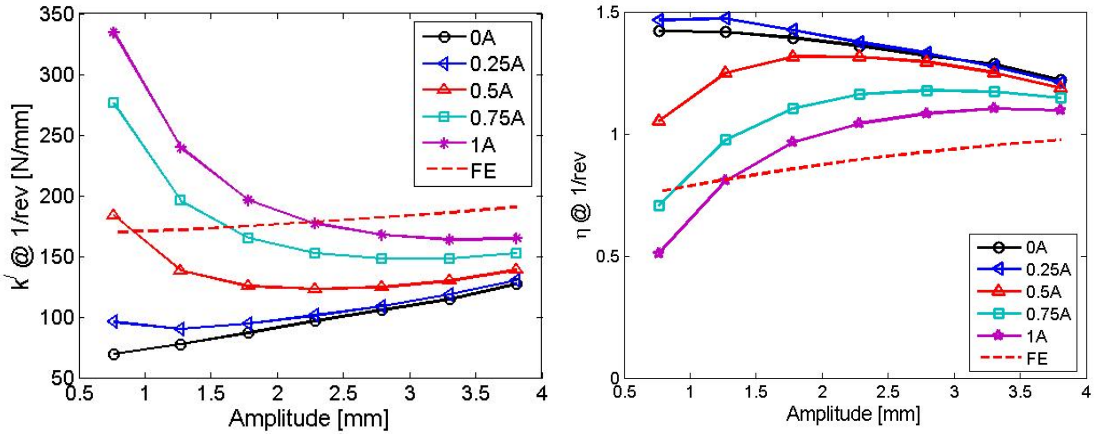

(a) Complex Modulus

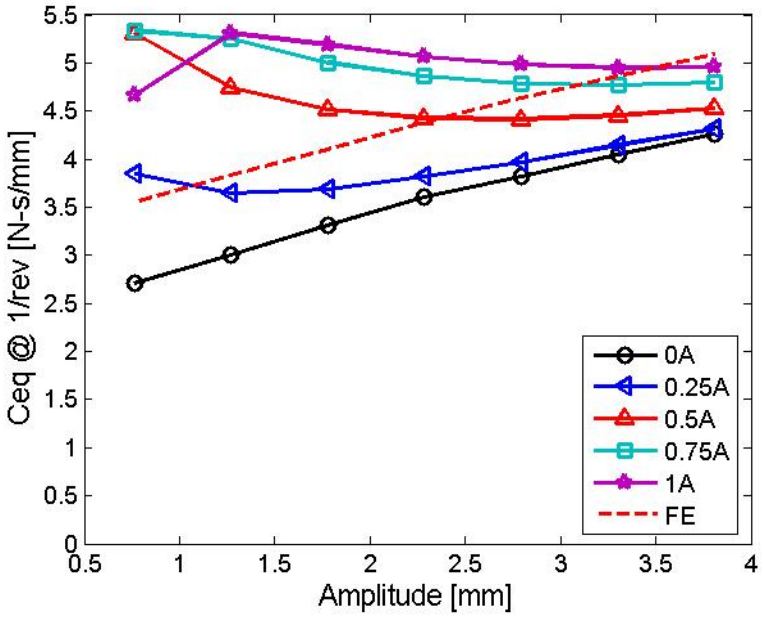

(b) Equivalent Damping

Figure 3.9: Complex modulus characterization of MRFE damper at 1/rev

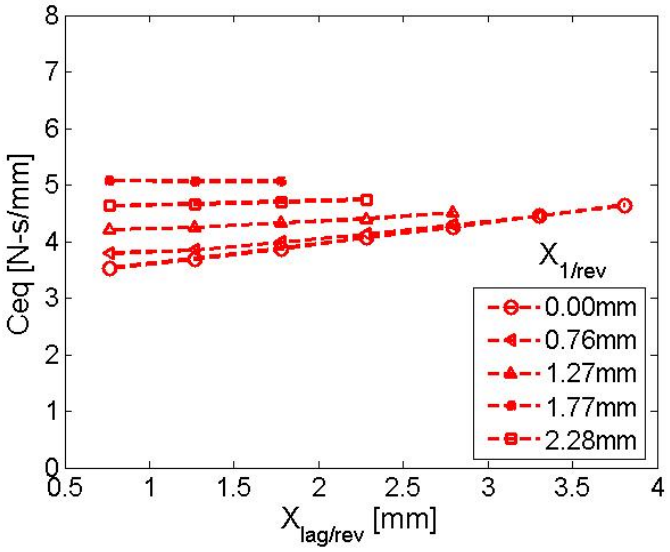

(a) FE, lag/rev equivalent damping

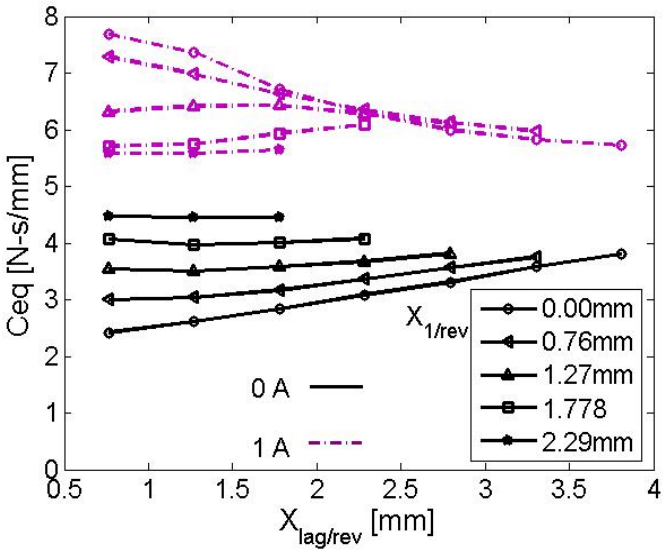

(c) MRFE damper, lag/rev equivalent damping

Figure 3.10: Lag/rev damping of MRFE and FE damper at dual frequency

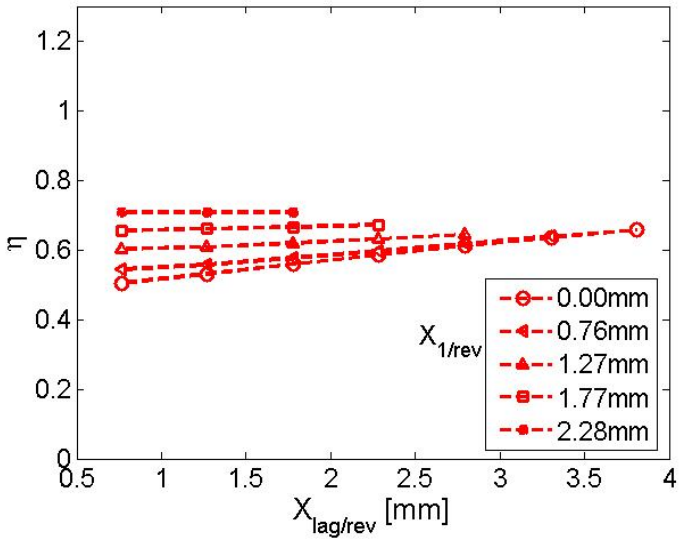

(b) FE, lag/rev loss factor

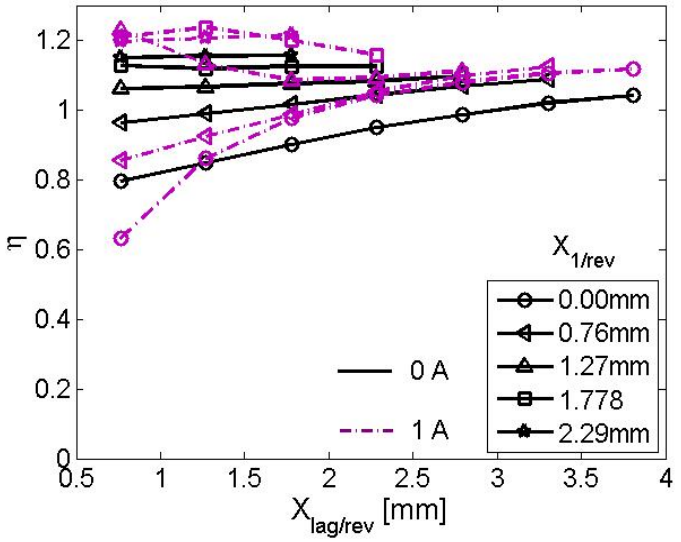

(d) MRFE damper, lag/rev Loss factor

Figure 3.11: Lag/rev loss factor of MRFE and FE damper at dual frequency

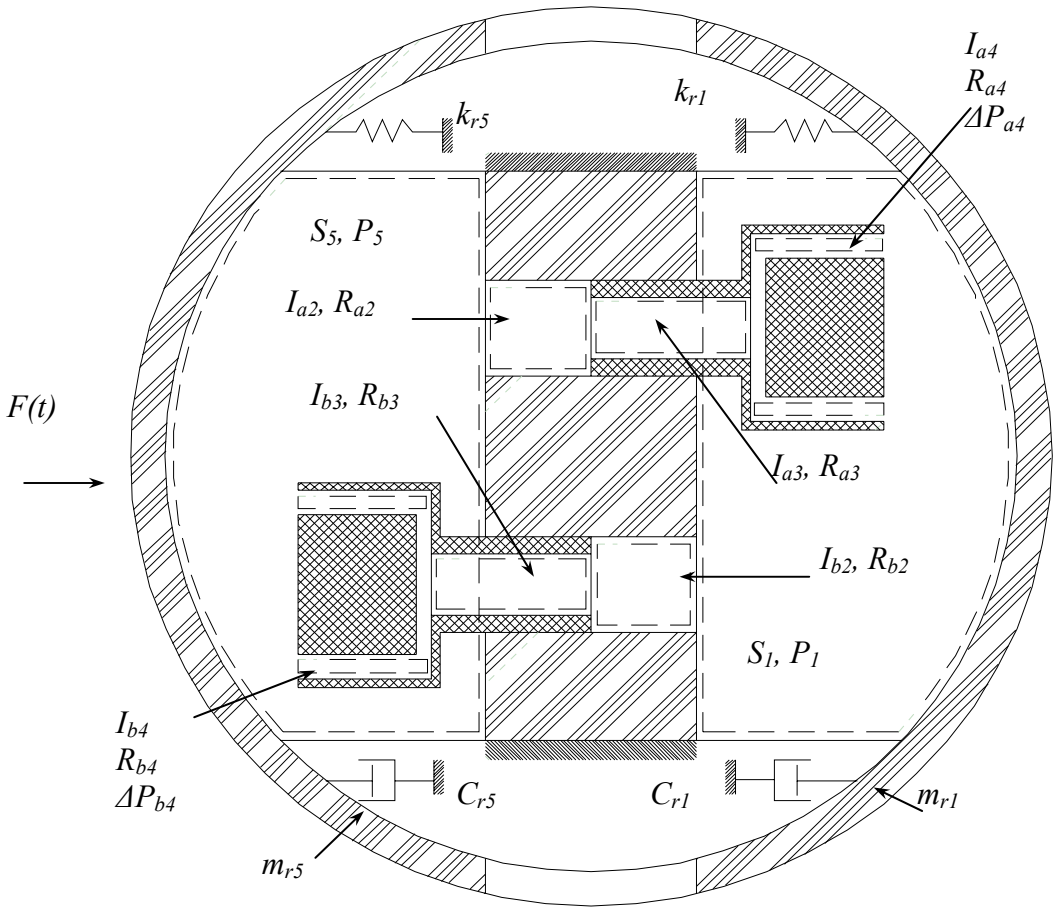

Figure 3.12: Section view of proposed hydromechanical model of MRFE damper

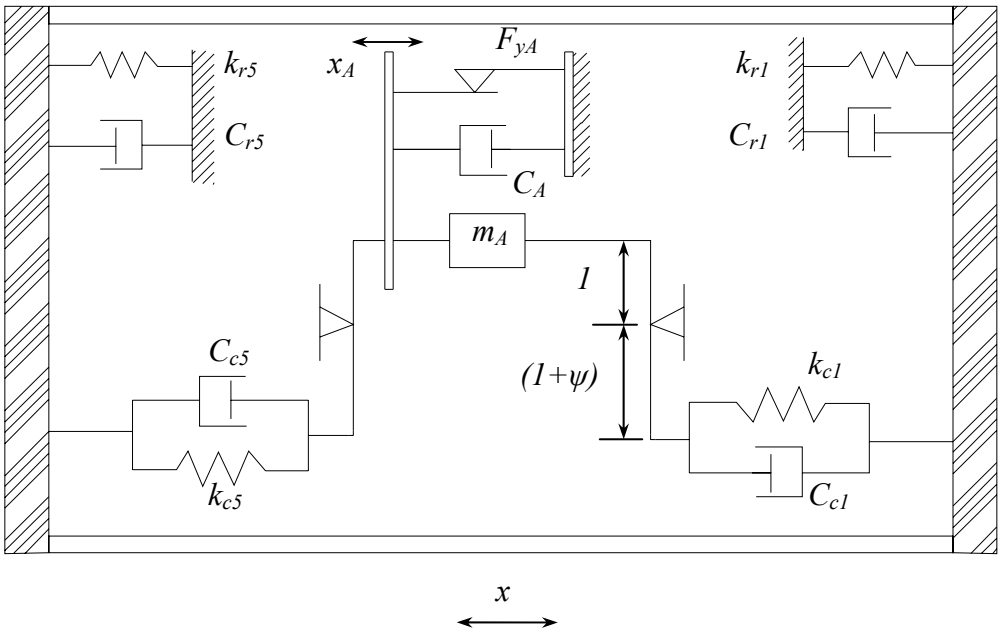

Figure 3.13: Analogous mechanical system of the hydromechanical model of the MRFE damper in terms of x_A

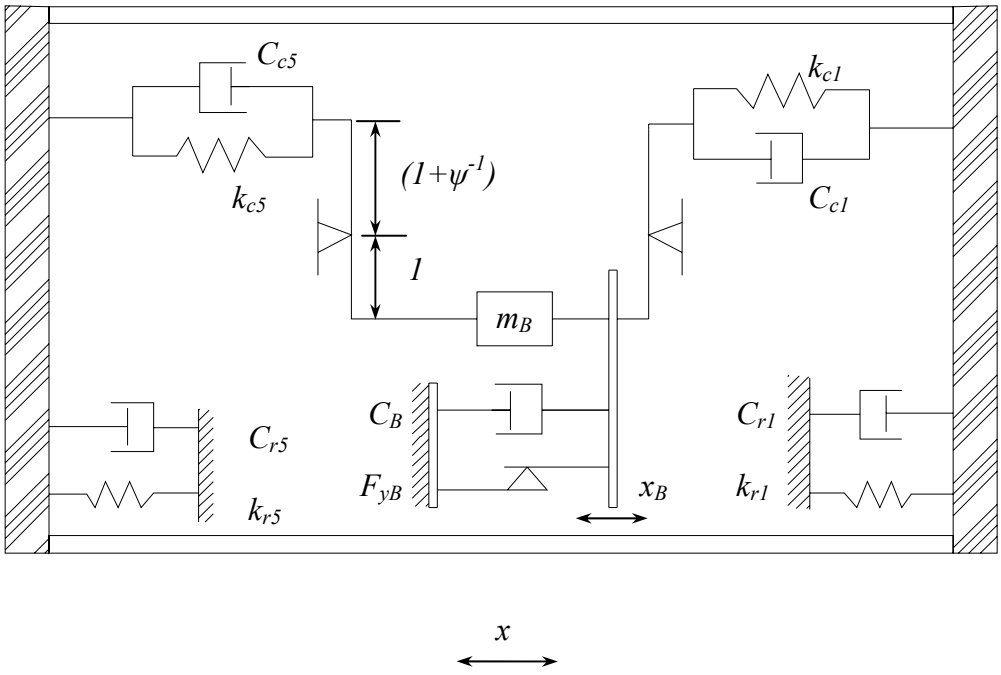

Figure 3.14: Analogous mechanical system of the hydromechanical model of the MRFE damper in terms of x_B

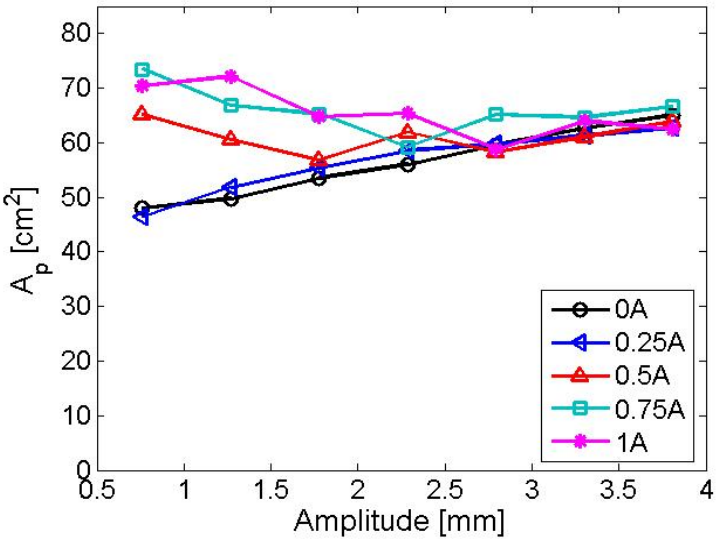

(a) Equivalent piston area at lag/rev, A_p

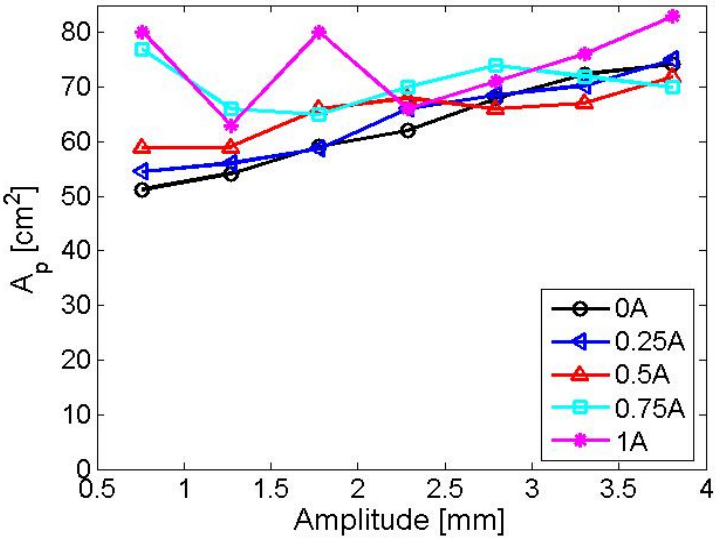

(b) Equivalent piston area at 1/rev,

Figure 3.15: Model estimated equivalent piston area A_p

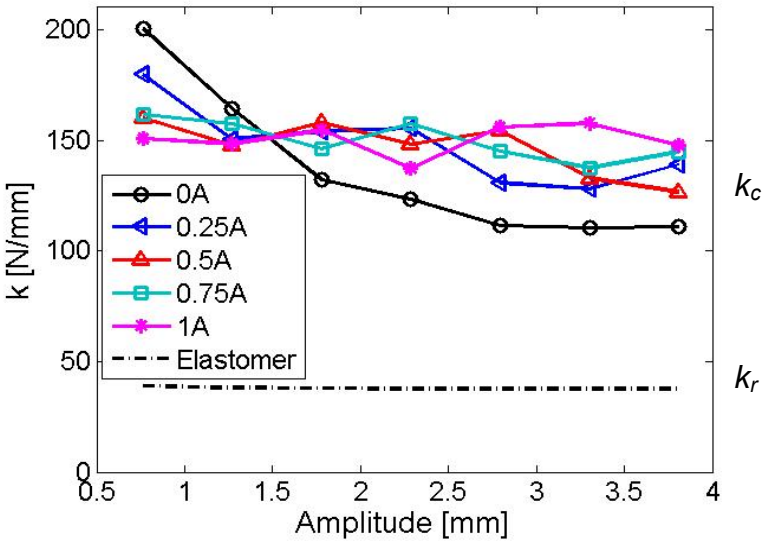

(a) Stiffness at lag/rev

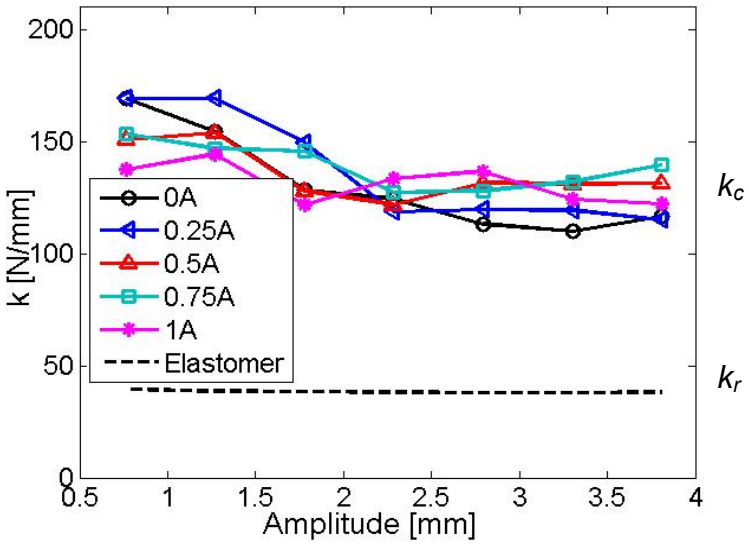

(b) Stiffness at 1/rev

Figure 3.16: Bulge and shear stiffness of MRFE damper

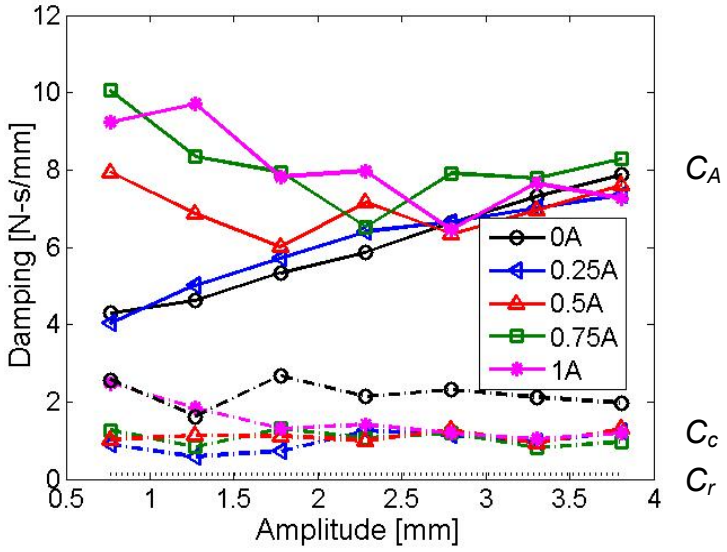

(a) Damping at lag/rev

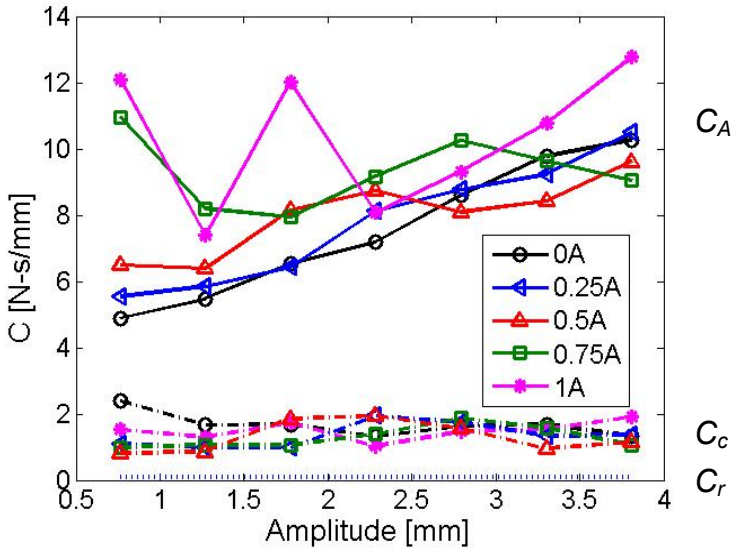

(b) Damping at 1/rev

Figure 3.17: Damping contribution from MRFE damper components

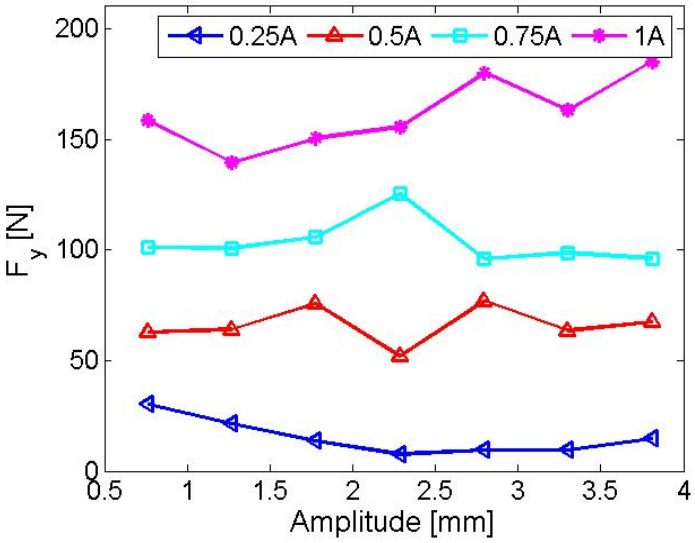

(a) Yield force at lag/rev

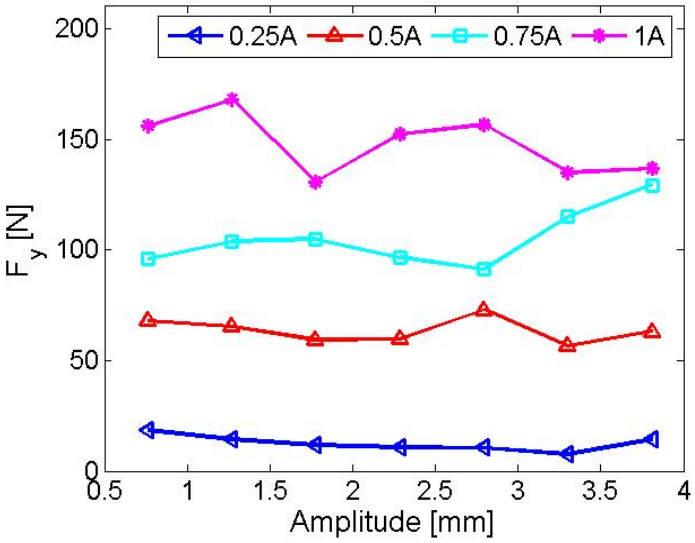

(b) Yield force at 1/rev, F_y

Figure 3.18: Estimated yield force F_y

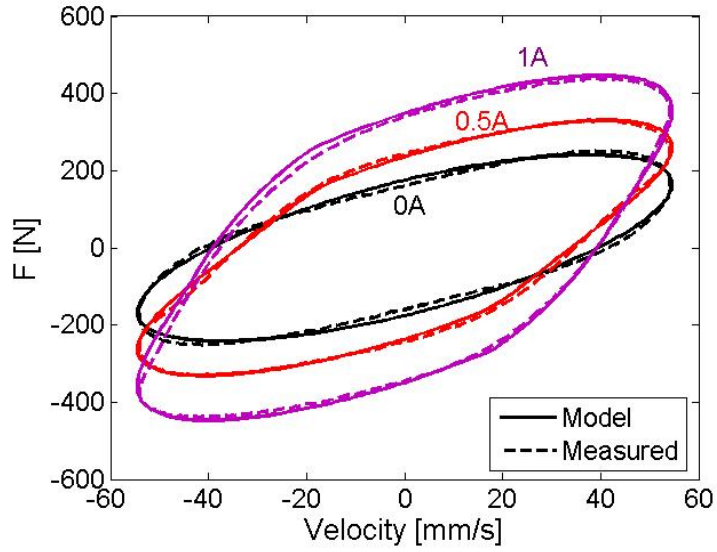

(a) Model performance at lag/rev

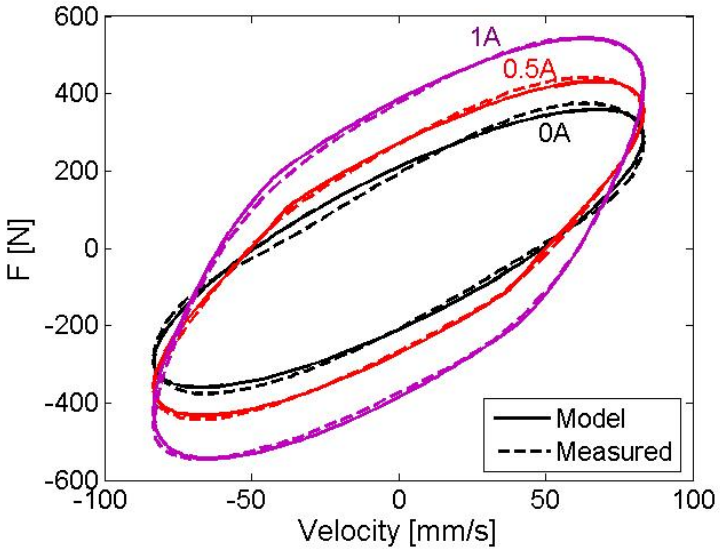

(b) Model performance at 1/rev

Figure 3.19: Experimental and model estimated damping force hysteresis

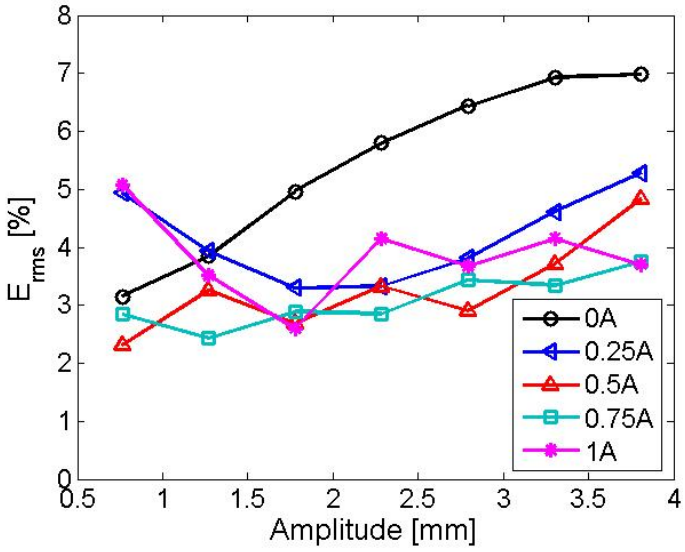

(a) Error at lag/rev frequency

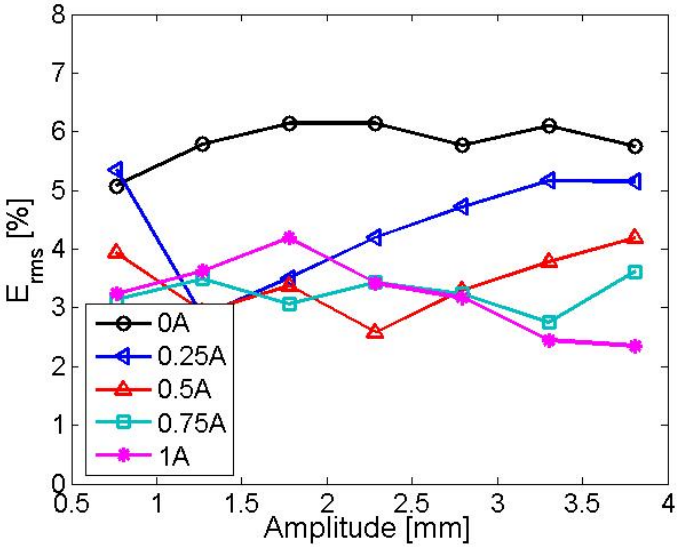

(b) Error at 1/rev frequency

Figure 3.20: Model force error estimation at lag/rev and 1/rev excitation frequencies

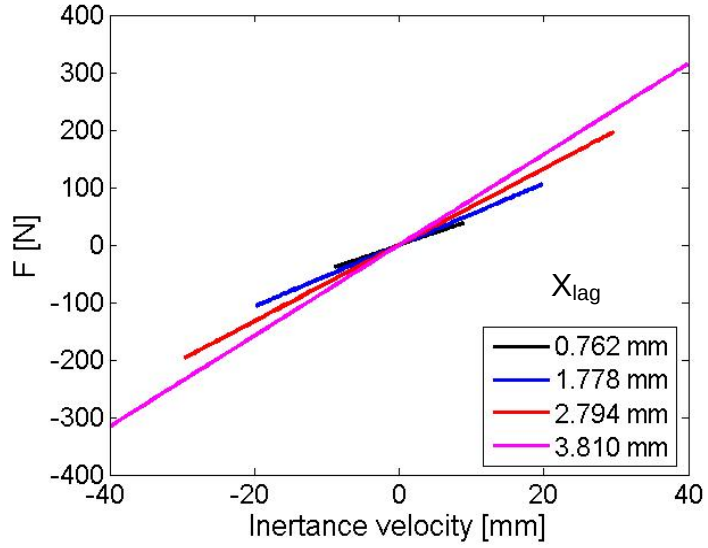

(b) Lag/rev F_{MR} vs generalized inertance velocity, $\dot{x}_A$

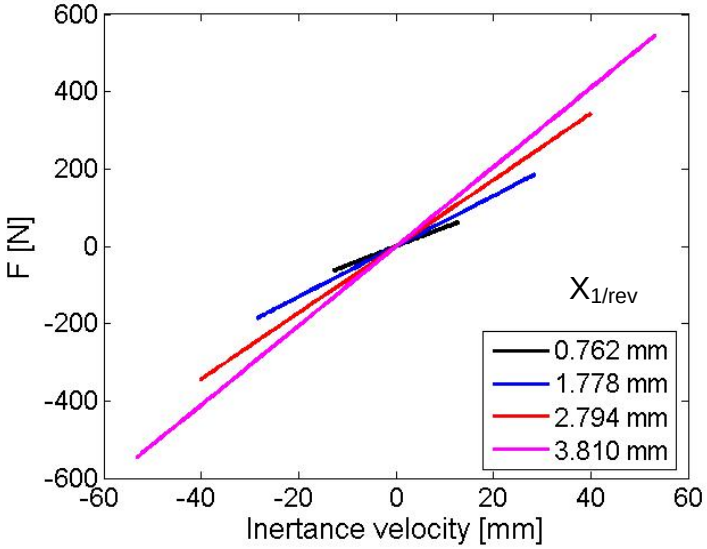

(b) 1/rev F_{MR} vs generalized inertance velocity, $\dot{x}_A$

Figure 3.21: Field-off F_{MR} vs generalized inertance velocity $\dot{x}_A$

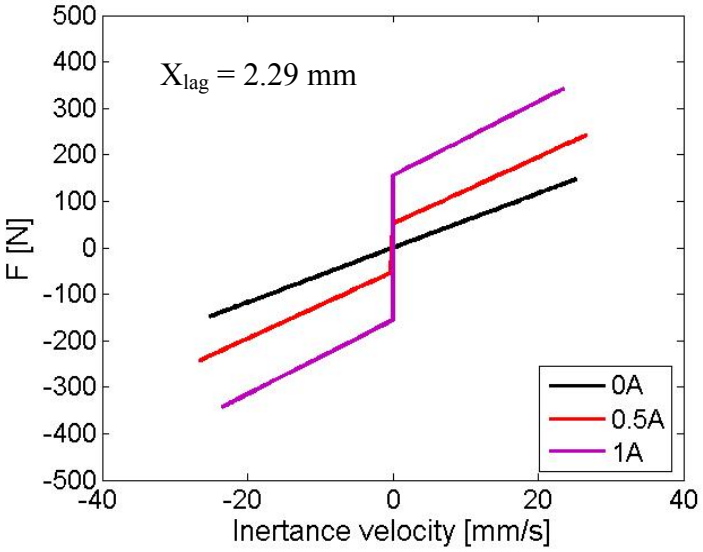

(b) lag/rev F_{MR} vs generalized inertance velocity, $\dot{x}_A$

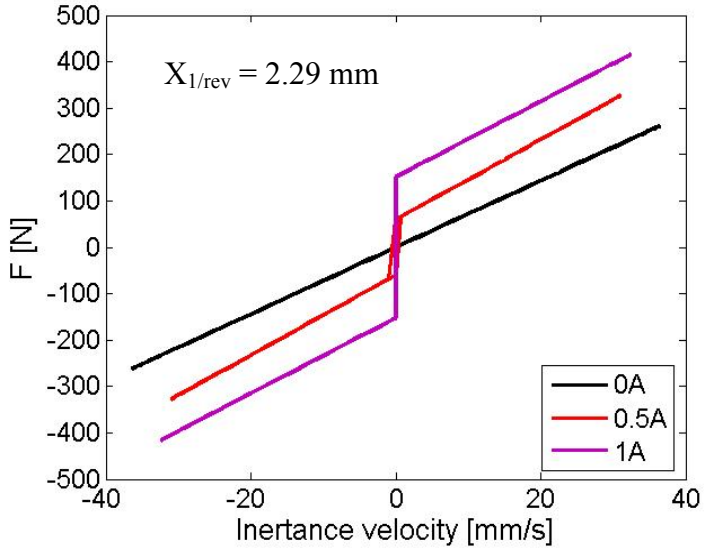

(b) 1/rev F_{MR} vs generalized inertance velocity, $\dot{x}_A$

Figure 3.22: Model estimated MR valve damping force

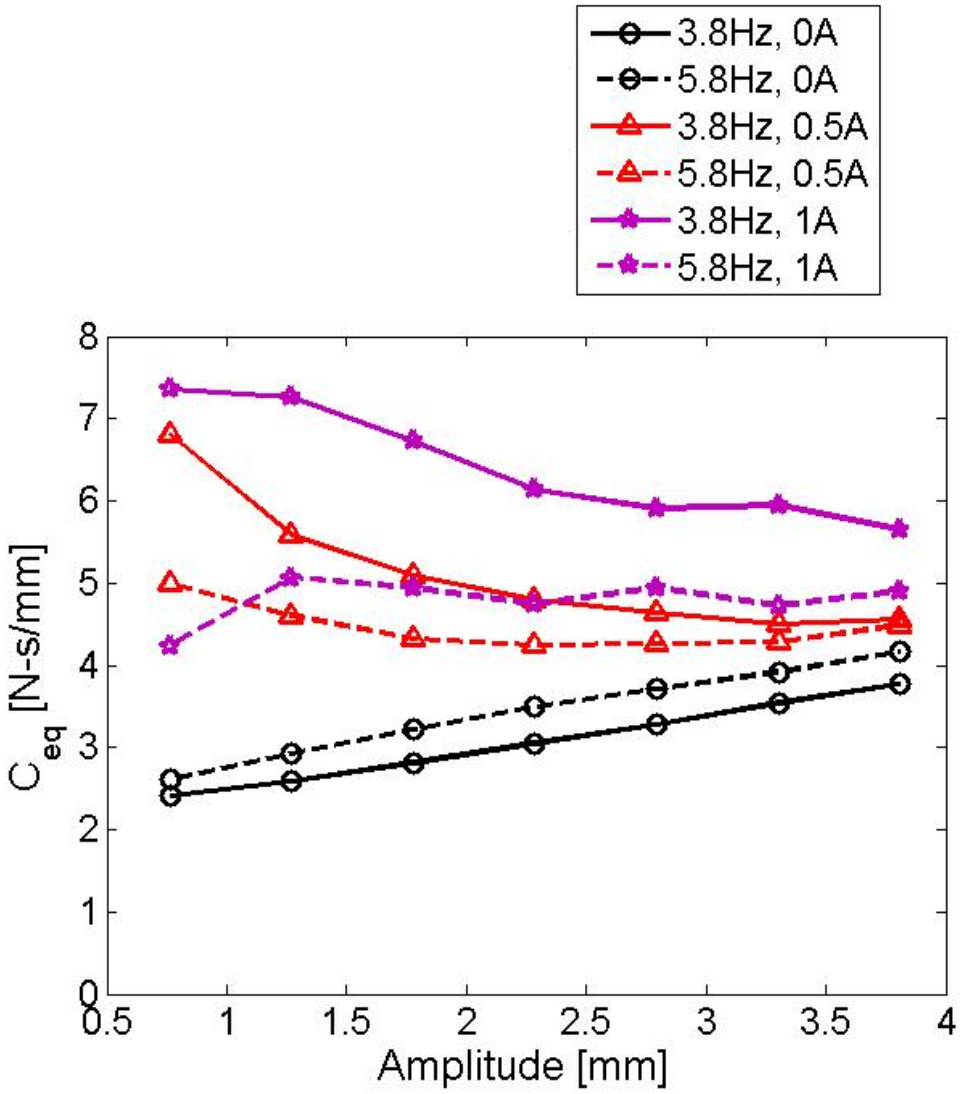

Figure 3.23: Model estimated equivalent damping

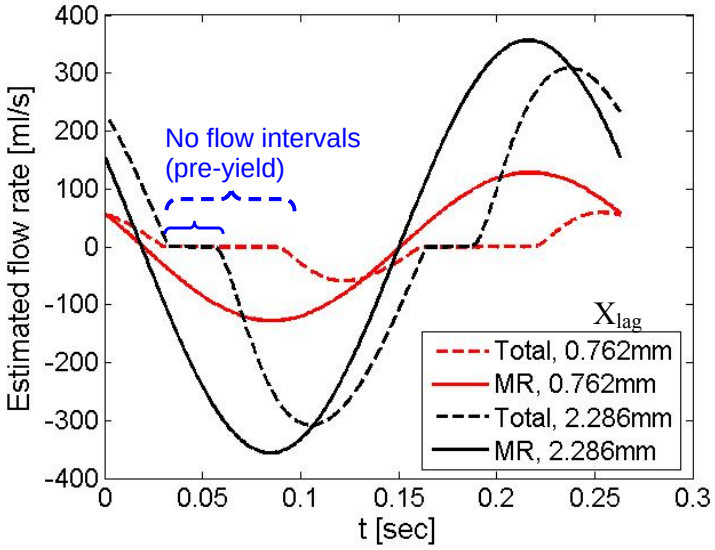

(a) Total and MR valve flow rates at I = 1A, X_{lag} = 2.286 mm and X_{lag} = 0.762 mm

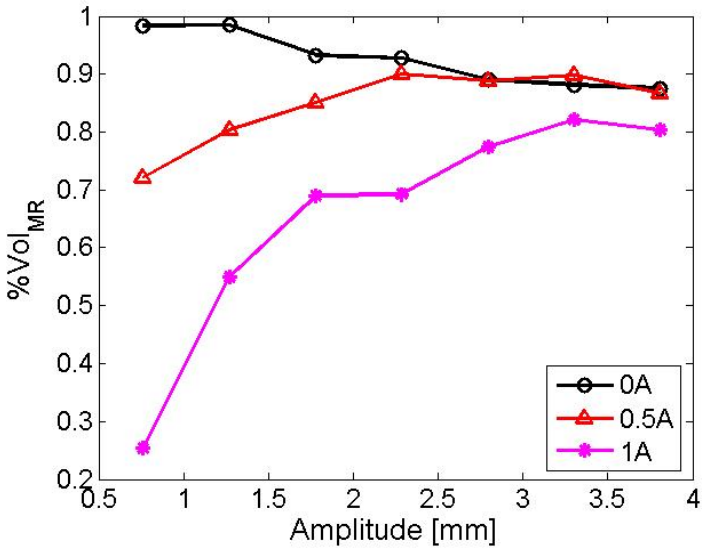

(b) Half-cycle volume flow through MR valve: $\% Vol_{MR}$

Figure 3.24: Model estimated total and MR valve flow rate comparisons at lag/rev

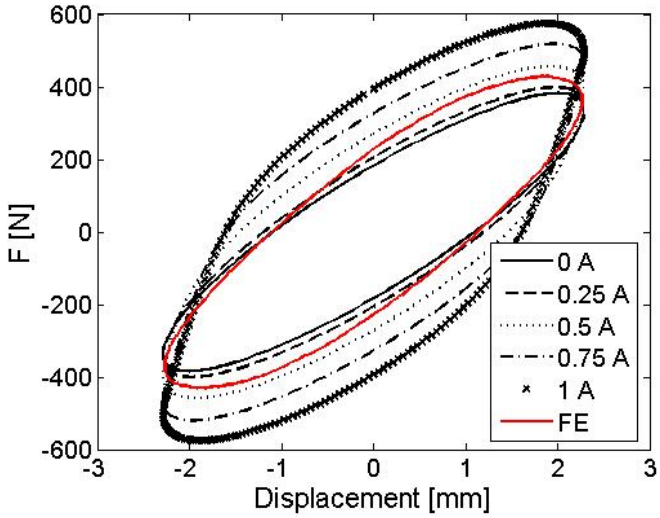

(a) MRFE damper, F vs. displacement plot

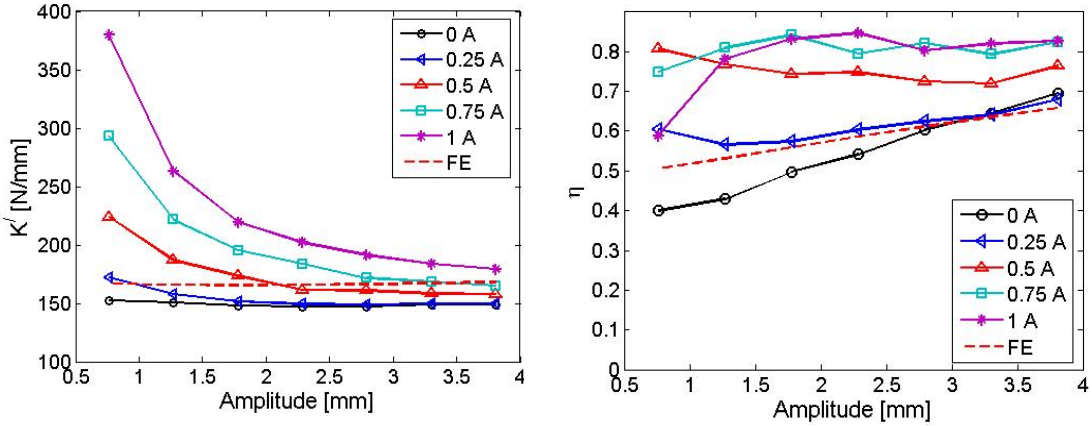

(b) Complex Modulus

Figure 3.25: Lag/rev MRFE damper performance prediction using hydromechanical model

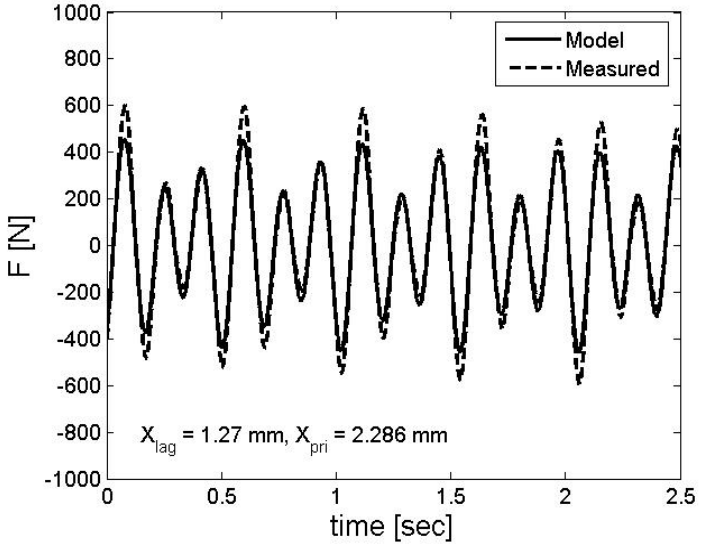

(a) Field-off @ X_{lag} = 1.27 mm, X_{pri} = 1.27 mm

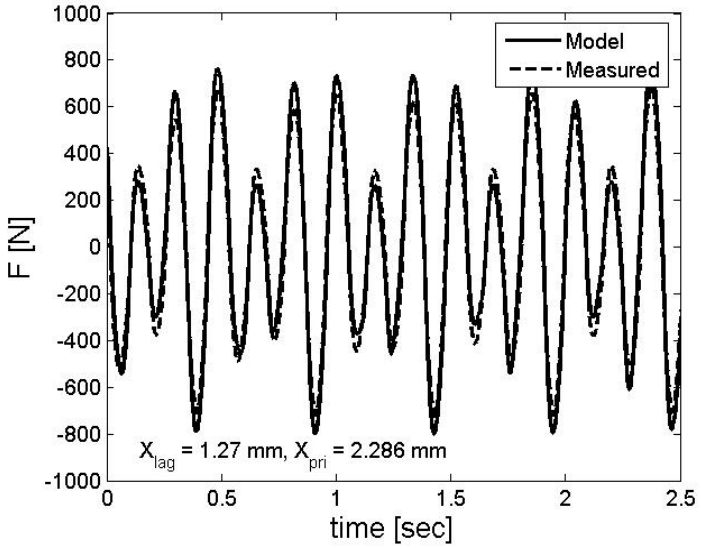

(b) Field-on (0.75 A) @ X_{lag} = 1.27 mm, X_{pri} = 1.27 mm

Figure 3.26: Dual frequency experimental and model estimated damping forces comparison

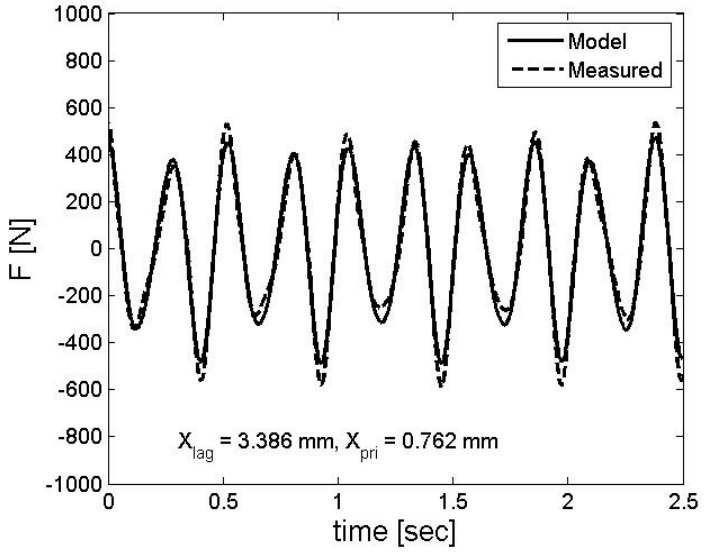

(c) Field-off @ X_{lag} = 3.386 mm, X_{pri} = 0.762 mm

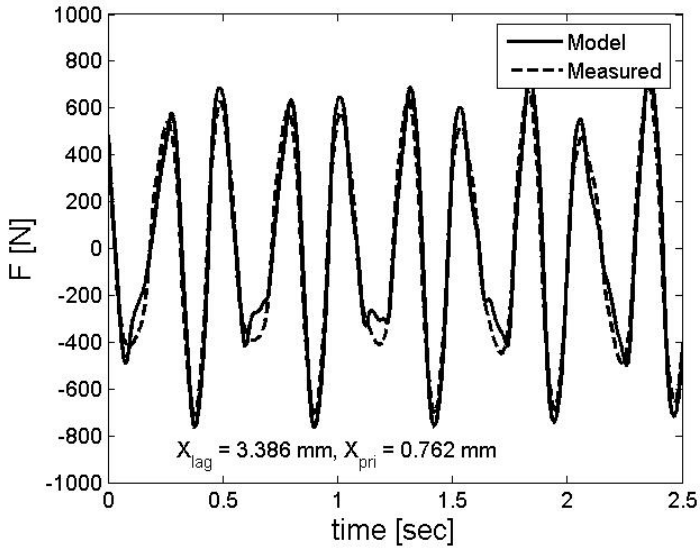

(d) Field-on (0.75 A) @ X_{lag} = 3.386 mm, X_{pri} = 0.762 mm

Figure 3.27: Dual frequency experimental and model estimated damping forces comparison

Chapter 4: Characterization and Modeling of MRFE damper with Temperature Effects

4.1 Introduction

In Chapter 3, a snubber type MRFE lag damper was developed by incorporating two MR valves into a snubber type FE (also known as Fluidlastic®) lag damper as a retrofit. Similar to the baseline FE damper, the retrofitted snubber type MRFE damper did not introduce any moving components, thus it does not require dynamic or sliding seals so that leakage is minimized. At ambient temperature, the investigation demonstrated the feasibility of using the snubber type MRFE damper to mitigate helicopter rotor instabilities with fixed frame experiments. The MRFE damper was able to provide comparable damping force to the baseline FE damper. Moreover, a substantial increase in damping and a wide controllability range was gained by using the MRFE damper. Over a 100% change in damping was obtained over the amplitude range tested. This damping and controllability range of the MRFE damper can be tuned to match actual damping requirements of certain flight conditions where stability margins may deteriorate.

During normal operation, elastomeric, FE and MRFE dampers are exposed to temperature variation from two primary sources: (1) severe ambient atmospheric conditions arising from cold or hot weather operations which tend to decrease or increase damper temperature; and (2) in-service viscous (self-) heating which is

associated with internal energy dissipation. Elastomeric dampers present a temperature dependent softening and stiffening at low and high temperatures respectively [3, 11] which can have an adverse effect on damper performance. Hausmann and Gergely [11] conducted temperature tests that characterized the effects of test temperature and self-heating on damper performance. The hysteresis plots clearly showed the decrease in dissipated energy as elastomer temperature is increased. Experimental results have shown a significant reduction in linearized in-phase and quadrature moduli in elastomeric lag dampers with decreasing temperature [3, 11, 12]. Previous works have shown effects of temperature on fluid based conventional linear stroke MR dampers [68-71]. Experimental results have shown reduction in damping force of an MR damper due to temperature increase, which was attributed to the reduced fluid viscosity [68]. In [71], the main effects of rising temperature are describes as a reduction in yield force, a reduction in fluid post-yield viscosity and a reduction in the force-velocity hysteresis loop. However, since the variation in yield stress of MR fluid between room temperature and 150°C is not more than 5%, it was assumed to be independent of the temperature and a function of the applied field only [38, 69]. Thus, MR dampers have the potential to compensate damping degradation due to a rise in temperature by increasing the applied magnetic field until the required damping is attained. Chapter 2 outlined temperature effects on FE lag damper. The damping losses with temperature increment are significant, where as high as a 50% damping loss is observed at excitation frequency of 3.8 Hz as the temperature was varied from 10°C to 50°C. The reduction in damping was caused mainly due to reduced fluid viscosity with a lesser contribution from elastomer

softening. The elastomer and MR fluid components of the snubber type MRFE damper from Chapter 3 are also expected to be affected by temperature. Nevertheless, the MRFE damper developed in this research has the potential to offset these adverse effects by varying the applied field as required.

In the present study, the MRFE damper developed in Chapter 3 is tested at different temperatures ranging from 20°C to 50°C to characterize and compare its performance as test temperature is varied. The upper temperature bound was chosen to be close enough to the maximum ambient operating range of the FE damper, which is 125ºF (51.67ºC). The lower temperature bound was the minimum temperature at which the MRFE damper provided a significant controllable damping range. The retrofit MRFE damper was developed by threading the two MR valves into the existing flow ports of the FE damper. Due to the small space envelope inside the damper, the valve sizing had to be checked against the operating stroke range of the damper to avoid contact with the outer cylindrical wall. Further, threading the MR valves into the flow ports created additional viscous losses due to unnecessary passive flow passages in the valves. These small diameter passages created flow chocking at temperatures below 20ºC due to the rise in viscosity of the MR fluid. Thus, 20ºC was chosen to be the lower bound of the temperature test range.

Temperature experiments were conducted by placing the MRFE damper in an environmental chamber and adjusting the ambient temperature surrounding the damper. The MRFE damper performance at each test temperature is compared with the baseline FE lag damper tested under same temperature conditions. The complex modulus linearization technique was used to characterize damper performance. At

each test temperature, a significant damping control range was provided by the MRFE damper that also encloses the FE damper performance at the specified temperature. Even though the complex modulus linearization technique is used to characterize the MRFE damper, this technique is not adequate to the tasks of reconstructing non-linear dynamic behavior of the MRFE damper, especially when current is applied. A hydromechanical model that accurately describes the hysteretic behavior of the MRFE damper at ambient temperature was developed and validated in the previous chapter. In the current chapter, this model is extended to account for damper performance variation with temperature. Since model parameters are functions of damper geometry and material property, temperature effects will only cause the latter to change. Thus, most material properties at each temperature are initially estimated, which later are reasonably scaled to accurately simulate the measured hysteretic force-displacement and force-velocity histories of the MRFE damper under single and dual frequency excitations.

4.2 Temperature Testing of MRFE Damper

The flexible body of the baseline FE damper is made of metallic shims interspersed with elastomeric layers, or a multiple lamination of metallic and elastomeric ring layers. These laminates are bonded to metallic plates at both ends. At center height, a circumferential middle plate is attached to the elastomeric cylinder wall. A flexible center wall made of rubber runs along the diameter of the flexible cylinder, completely molded at both ends to the elastomeric damper body. This creates two distinct volume chambers into which a viscous fluid is poured and completely sealed. The only way the two chambers communicate is through two flow

ports that are incorporated in the center wall. There are four threaded holes for filling and draining fluid, two on each side of the damper. Once fluid is injected into the chambers, the holes are bolted and a compression bolt is mounted through the vertical center hole of the damper assembly.

The design of the MRFE damper requires the development and retrofit of two MR valves inside the existing baseline FE damper body and exchanging the existing passive, hydraulic fluid with field-controllable, MR fluid (provided by LORD Corp.). The development of the MR valves involves fitting the existing two port holes located in the center wall with two flow mode MR valves (Refer to Figure 3.3). These internal MR valves are placed at the two existing flow ports located in the center wall, one in each hole on each of the fluid chambers. The new MR retrofit design only adds the MR valves, thus, introducing no moving part to the system. In addition, this helps minimize the weight penalty incurred due to addition of components. Detail discussions of the MRFE lag damper development are given in Chapter 3. The original FE damper is assembled as a factory sealed unit and is preloaded in compression. However, because the damper was produced as a molded unit, the top layer of the center elastomer wall was significantly damaged during the disassembly process, as the top plate had to be cut to get access to damper inner body. A rubber repair kit was used to rebuild the wall and provide a smooth surface for sealing with a new top plate. Initially, a new elastomeric wall was rebuilt on top of the existing wall, however, the bond surface kept failing after a few test runs. Thus, to create a sufficiently strong bond between the existing elastomer wall and the rebuilt elastomer material, an epoxy method suggested by LORD Corp. was ultimately determined to

suffice. In addition, the high pre-compression applied during MRFE assembly (18%, see Chapter 3) contributed to the frequent failure of the built rubber and bond surface. Thus, during assembly of the prototype MRFE parts for temperature testing, the MR fluid was injected and sealed and the elastomer was then approximately 14% pre-compressed. This pre-compression was also less than the 20% pre-compression of the baseline FE damper. This lower pre-compression was necessary to avoid damaging the rebuilt elastomer wall and bond surface. The 14% pre-compression was assumed to create sufficient positive pressure in the damper.

The MRFE damper dynamics and the associated deformation have already been discussed in *Section 3.3, paragraph 1*, and will not be repeated here. To mimic the lead-lag motion of helicopter blades as applied to the MRFE lag damper, a test fixture was fabricated to hold dampers in a 24.5 kN MTS servo-hydraulic testing machine. Figure 4.1 shows the MRFE lag damper test set-up where the mid-plate is connected to the load cell by means of the test jig via an extension rod. The lower mounting bracket is attached to the lag damper through a mounting rod that is slotted in at the mounting hole, located at the center of the lag damper assembly. The lower mounting bracket is attached to the MTS actuator through an extension rod. The center wall is oriented horizontally such that the motion of the MTS actuator connected to the lower bracket forces fluid to flow from one chamber to the other, by deforming the elastomeric outer wall, and emulating the lead-lag motion. The displacement and force were measured by the LVDT sensor and load cell of the MTS machine. The frequencies of excitations were chosen to be 3.8 Hz and 5.8 Hz, which correspond to an actual rotor system lag/rev and 1/rev or rotor RPM frequency. The damper

excitation amplitudes ranged from 0.762 mm (30 mil) to 3.81 mm (150 mil) in increments of 0.50 mm (20 mil) at both lag/rev and 1/rev frequencies.

To evaluate MRFE damper performance at varying temperatures, the damper was placed in an ATS environmental heating chamber or test oven as shown in Figure 4.1. The test oven is capable of generating temperatures as high as 425°C. It is also designed for cryogenic cooling, and liquid nitrogen (LN2) tanks were used for stabilizing lower temperature testing (20ºC). The oven is designed to be mounted on the MTS machine (Figure 4.1) using mounting brackets. The environmental heating chamber is equipped with a temperature control system, which regulates and maintains the desired temperature as measured by the control thermocouple. An external thermocouple was also submerged in the MR fluid to provide a measurement of the temperature inside the damper before and during testing. The readings from the heating chamber control thermocouple and the external thermocouple were matched before each temperature test was conducted. In addition, during testing, the real time readings from the external thermocouple were used to make sure the MR fluid temperature was kept within acceptable range.

During each test, the sampling frequencies were 1024 Hz and 512 Hz for the single and dual frequency tests respectively, which are considerably higher than the required Nyquist frequency. Nominally, ten cycles of force and displacement data were collected at each test set up. To reduce the noise of the input sinusoidal displacement signal, a Fourier series was used to reconstruct the input displacement. The reconstructed displacement signal was then differentiated to obtain the velocity signal. The Fourier series expansion of the input displacement signal is given by:

$$x(t) = \frac{x_o}{2} + \sum_{k=1}^{\infty} \left(X_{c,k} \cos(k\omega t) + X_{s,k} \sin(k\omega t) \right) \tag{4.1}$$

where

$$X_{c,k} = \frac{\omega}{\pi k} \int_0^{\frac{2\pi}{k\omega}} x(t) \cos(k\omega t) dt$$

$$X_{s,k} = \frac{\omega}{\pi k} \int_0^{\frac{2\pi}{k\omega}} x(t) \sin(k\omega t) dt \tag{4.2}$$

Any bias and higher harmonics at single frequency tests were filtered, so as only the frequencies of interest, i.e. $\omega = \omega_{lag}$ and $\omega = \omega_{pri}$, remained. Then the displacement and velocity data were reconstructed using the first harmonics only as

$$x(t) = X_s \sin(\omega t) + X_c \cos(\omega t)$$

$$\dot{x}(t) = \omega X_s \cos(\omega t) - \omega X_c \sin(\omega t) \tag{4.3}$$

For dual frequency evaluation, an HP8904A function generator was used to create and sum the two sinusoidal signals in order to attain an accurate dual frequency excitation. The general equation for the input dual displacement signal is:

$$x(t) = X_{lag} \sin(\omega_{lag} t) + X_{pri} \sin(\omega_{pri} t) \tag{4.4}$$

where ω_{lag} and X_{lag} represent the lag/rev (lag) frequency and the corresponding input amplitude while ω_{pri} and X_{pri} represent the 1/rev frequency (rotor) and the corresponding amplitude. The signal is periodic with a period equal to the frequency corresponding to the highest common factor of the two harmonics, which is 0.2 Hz. Thus, the displacement input signal was filtered using the Fourier expansion at 0.2 Hz as the base frequency. The first twenty-nine harmonics were required to reconstruct

the dual frequency displacement signal. The measured force data at all frequencies and temperatures was not filtered and was used in the developed model as recorded.

At a selected amplitude of 2.286 mm, Figures 4.2a and 4.2b show the force versus displacement plots of the MRFE damper at lag/rev frequency and varying applied currents at two different temperatures, 20°C and 50°C respectively. In each force-displacement plot, the area enclosed by the hysteresis loop is proportional to the amount of energy dissipated per cycle. And the damping available is in turn proportional to the energy dissipated per cycle. In both cases, as control current is applied, the dissipated energy per cycle, thus the available damping in the MRFE device, increases significantly. And at both field-on and –off conditions, the peak load at 20°C is higher that at 50°C. This is well illustrated in Figure 4.3, which shows the force-displacement plot at field-off (0A) and field-on conditions (1A).

4.3 Linear Temperature Characterization of MRFE Damper

A typical approach for characterization of damper performance quantitatively is the complex modulus method. It is a linear characterization technique of damper properties which treats the complex stiffness k^* as a combination of the in-phase stiffness k' and the loss stiffness k'', given as:

$$k^* = k' + ik'' = k'(1 + i\eta) \tag{4.5}$$

where the loss factor η is defined as the ratio of the loss stiffness to the in-phase stiffness. This technique has been extensively used in characterizing elastomeric, fluid-elastomeric and MRFE dampers. The damper force is estimated by the first Fourier sine and cosine components at the excitation frequency:

$$F(t) = F_s \sin(\omega t) + F_c \cos(\omega t)$$
$$= k'x(t) + \frac{k''}{\omega}\dot{x}(t) \tag{4.6}$$

The stiffness k' and k'' are determined by substituting the displacement function and its derivative from equation 4.3 into the force equation:

$$k' = \frac{F_c X_c + F_s X_s}{X_c^2 + X_s^2} \tag{4.7}$$

$$k'' = \frac{F_c X_s - F_s X_c}{X_c^2 + X_s^2} \tag{4.8}$$

The equivalent damping C_{eq} is approximated by:

$$C_{eq} \cong \frac{k''}{\omega} \tag{4.9}$$

This linearization technique is an approximation method in non-linear systems because the complex stiffness assumes steady state harmonics at the excitation frequency. However, it gives an acceptable representation of the linearized in-phase stiffness and equivalent damping of the FE and MRFE dampers for comparing overall damping performance under different loading conditions.

The lag/rev loss and in-phase stiffness of the MRFE lag damper at 20°C and varying applied currents are shown in Figures 4.4a and 4.4b. Figures 4.5a and 4.5b show the same data at 50°C. From Figure 4.4, the field-off loss stiffness, thus available damping, is the minimum damping that can be provided by the MRFE damper at the corresponding temperatures. As the applied current increases, the loss stiffness, thus damping, increases significantly. This implies that the MRFE damper can provide a substantial damping control range that can be tailored in an optimal manner. The magnitude of increment in damping is higher at lower amplitudes. At

20°C, there is an approximately 140% and 40% quadrature stiffness increment at the lowest and highest amplitudes respectively. Similarly, at 50°C, the increments are about 420% and 55% at the lowest and highest amplitudes. The in-phase stiffness at both temperatures also increases with increasing applied field (Figures 4.4b and 45b). In addition, at field-on condition, there is an increase in in-phase stiffness as the amplitude of excitation decreases. It is also observed that the magnitude of the stiffness at 50°C is always lower than that of the 20°C results. There is a minimum of 25% decrement in in-phase stiffness as the temperature is increased from 20°C to 50°C. Due to the lower in-phase modulus and relatively higher loss modulus at 50°C, its loss factor is expected to be higher. This is reflected in Figure 4.6a.

The maximum (1A) and minimum (0A) damping available from the MRFE damper at lag/rev and different temperatures and the corresponding passive damping from the FE damper are shown in Figure 4.6b. The dotted lines in the figure represent the equivalent damping of the baseline FE damper at different temperature. As the operating temperature is increasing, the available damping from the FE damper is substantially reduced. There is an average drop of 35% in FE damping as temperature is varied from 20°C to 50°C. There is a similar drop in the field-off damping of the MRFE device as temperature is increased. However, since the variation in the field-on damping (1A) is relatively small, especially at higher amplitudes, the associated drop in field-off damping at higher temperatures will result in an improved controllable dynamic damping range of the MRFE device. This suggests that, in the future, the MR valve could be designed for a lower temperature limit, which automatically makes high temperature performance accounted for. It is also observed

that, at all temperatures, a controllable dynamic range is provided by the MRFE device, and the FE damper performance is enclosed within this controllable damping range at the corresponding temperatures. In addition, at lower amplitude, a drop in damping is observed as the temperature is goes down. The hydromechanical analysis in the later section will address these issues.

Helicopter lag dampers encounter multi-frequency excitation, especially in forward flight, where the forced lag motion occurs at the 1/rev rotor frequency. The dual frequency performance of the MRFE damper at 20°C and 50°C are shown in Figures 4.7a and 4.7b. Under such circumstances, the field-off lag/rev damping available at dual frequency is higher than the damping at single frequency at both temperature conditions. This increment is due to the rise in volume flow rate in the MR valves, and the logic behind it has been addressed in *section 3.6*.

4.4 Hydromechanical Modeling of MRFE Damper

Figure 4.8 gives the mechanism of the hydromechanical model of the MRFE damper developed in Chapter 3, which is composed of parallel and series combinations of linear springs, dashpots, and Coulomb friction elements. The corresponding governing equations are given by:

$$2C_r\dot{x}(t) + 2k_r x(t) + 2C_c\left(\dot{x}(t) - 2\dot{x}_A(t)\right) + 2k_c\left(x(t) - 2x_A(t)\right) = F(t) \tag{4.10}$$

$$m_A\ddot{x}_A(t) + C_A\dot{x}_A(t) - 2C_c\left(\dot{x}(t) - 2\dot{x}_A(t)\right) - 2k_c\left(x(t) - 2x_A(t)\right) + F_y sgn(\dot{x}_A(t)) = 0 \tag{4.11}$$

The terms k_r and C_r represent the shear stiffness and damping of the MRFE damper elastomeric body (i.e. empty MRFE damper). Bulge damping C_c and bulge stiffness k_c resulted from the volumetric expansion or bulging of the elastomeric body due to

forced deformation and ensuing fluid flow. The rubber mass, m_r, is small and its effects are negligible without loss of generality. m_A accounts for the inertial effect of the MR fluid in the MR valve and C_A represents the passive viscous damping due to flow resistance in the MR valves. Controllable damping enters into the system through F_y, which represents the field-controllable yield force of the MR fluid in each valve. The snubber type MRFE damper does not have a well defined piston, and fluid flow is generated through a complex deformation of the elastomer body. Elastomer deformation is only known and recorded at damper center, where the input displacement *x(t)* from the MTS machine is applied. Detail descriptions of the model are given in Chapter 3. The analogous mechanical system (Figure 4.8) and the corresponding governing equations 4.10 – 4.11 show that in the pre-yield region, the hysteresis behavior is evident in the chamber compliance effects (bulge damping C_c and bulge stiffness k_c). The coulomb element (F_y), generalized inertance mass (m_A) and viscous damping (C_A) terms represent the post-yield behavior.

4.5 Temperature Dependent Parameter Estimation and Adjustment

In order to minimize the squared mean error between the measured and predicted damping force of the MRFE damper at each, a constrained least-mean-squared (LMS) error minimization technique was utilized. To begin the optimization procedure to accurately simulate measured damper dynamics, all model parameters except the equivalent piston area A_p were measured or estimated before the MRFE damper was assembled and tested. Table 4.1 outlines the measured, model estimated and dependent parameters. The dependent variables are product of measured and estimated parameters. Model parameters are functions of valve geometry and material

properties. Valve geometry is assumed to be independent of temperature. However, temperature will alter material properties, which in turn will alter the MRFE damper dynamic response. In the following sub-sections, an initial measurement or estimation procedure of material dependent model parameters is outlined. Some of these parameters are later adjusted appropriately to best fit the model to actual MRFE damper data. The need for the adjustment is also discussed. The other important point is that the discussion in this chapter will show the potential of the hydromechanical model in determining model parameters *a priori*, and predict expected damper performance.

4.5.1 Fluid Inertance and Resistance

The hydromechanical model developed takes into consideration the inertia of the MR fluid mass and the viscous losses of the transient fluid flow through the passive and active passages. The pre-existing flow ports accounts for the passive passages and the retrofitted MR valve accounts for the active losses. The fluid inertance, which represents the inertia of the MR fluid in both active and passive passages, is given by:

$$I_a = \rho \sum_i \frac{l_{ai}}{A_{ai}} \tag{4.12}$$

In the above equation, l and A are the length and cross-sectional area of each lump or section of the flow passages. Neglecting the small density variation with temperature, fluid density ρ, thus the fluid inertance, is assumed to remain constant. Using equation 3.21, the viscous resistance in the circular passive and annular active flow passages of the MR valve as a function of temperature can be expressed as:

$$R_a = \mu(T)\left(\frac{128}{\pi}\sum_i \frac{l_i}{D_i^4} + 12\frac{l_4}{A_d d_4^2}\right)_a \tag{4.13}$$

where T is the damper temperature. The first term in brackets is the resistance in the circular sections and the second term is the resistance of the annular section. Using the input velocity, the Reynolds number for the flow through the active and passive passages was within the laminar flow range (Re < 400). Thus, the viscous flow resistance was calculated based on the Hagen-Poiseuille solutions for laminar flow in circular and annular passage ways. In addition, based on Bingham-Plastic flow analysis, the field-off viscosity and the post-yield viscosity of the MR fluid are assumed equal. Due to the low velocity and low Reynolds number flow, minor losses were also neglected. Since all geometric parameters are constant, temperature variation results in viscosity changes in the above resistance equation, which will directly affects the passive viscous damping. The viscosity variation with temperature of MR fluids can be estimated using the following empirical equation (Lord Corp.):

$$\mu(T) = \mu_{40}\, exp\left(\frac{(1+2.43\phi)(40-T)}{(48+T)}\right) \tag{4.15}$$

In the above equation, μ_{40} is the fluid viscosity at 40°C and ϕ is the volume fraction of magnetic particles in the MR fluid. Using equations 4.14 and 4.15, the viscous resistances of the MR fluid at different temperatures are shown in Figure 4.9. As expected, the resistance decreases significantly with increasing temperature, primarily due to reduction in viscosity with temperature.

4.5.2 Yield Force

The yield force is a function of the applied field, which increases with increasing applied current. The relationship between the yield stress and the applied current for the MR fluid can be obtained by an empirical equation as [92]:

$$\tau_y = 271700\phi^{1.5239} \tanh(6.33 \times 10^{-6} H) \tag{4.16}$$

A Gauss meter was used to determine the relation between applied current and the corresponding field generated. For the range of applied current *i*, the applied field is proportional to the current as bellow:

$$H = 0.1076I \tag{4.17}$$

Using equations 3.26, 4.19 and 4.20, the empirical yield force F_y was estimated, and is shown in Table 4.2. Here, the actual center wall area (~ 80 cm^2) was utilized to estimate the yield force. The yield stress of MR fluids has been proven to show a stable performance over a wide temperature range, from -40ºC to 150ºC [38, 69]. Since the test temperature array selected falls within this temperature range, the yield force from the empirical equation was utilized in model simulation at all temperatures.

4.5.3 Estimated Shear Stiffness k_r^* and Damping C_r^*

The MRFE damper elastomeric body basically undergoes two types of deformations. One is the shear deformation of the elastomer due to input displacement, and the second one is the corresponding volumetric expansion due to the ensuing fluid flow. The shear stiffness and damping are initially estimated by

testing the MRFE damper elastomeric body after pouring out the MR fluid from the MRFE device. In this condition, equation 4.10 reduces to:

$$2C_r^*\dot{x}(t) + 2k_r^*x(t) = F(t) \tag{4.18}$$

where C_r^* and k_r^* are the estimated shear damping and stiffness of the MRFE damper elastomeric body. The above equation represents a Kelvin-type model, where the system is represented by a parallel combination of a dash-pot and spring. Recalling that the elastomer in the MRFE damper behaves linearly under a specific dynamic test condition, the shear damping C_r^* and stiffness k_r^* can be estimated by applying equations 4.6 – 4.9 on the measured displacement and force data. These results are shown in Figure 4.10. Both parameters decrease with increasing temperature. However, they are weakly dependent on amplitude.

4.5.4 Estimated Bulge Stiffness k_c^* and Bulge damping C_c^*

The elastomeric chambers of the MRFE damper act as both pumping chambers and accumulators. Thus, the elastomer undergoes a volumetric expansion and contraction while pumping fluid from one chamber to the other as a result of flexing or deformation. This will create stiffness and damping effects. To estimate these effects, the MR valves were first removed from the MRFE damper and the port holes were plugged and sealed so that no fluid can transfer from chamber to the other under applied load. Then the MRFE damper with plugged valves was re-filled with MR fluid and dynamic tests were carried out at different temperature conditions. The governing equation can be derived from equation 4.10 as follows:

$$F_c(t) = F(t) - 2k_r x(t) - 2C_r \dot{x}(t)$$
$$= 2k_c^* x(t) + 2C_c^* \dot{x}(t) \tag{4.19}$$

where F_c is the compliance force, C_c^* and k_c^* are the estimated bulge damping and bulge stiffness of the MRFE damper with plugged valves. Again, the last expression in the above equation represents a Kelvin-type model, where the system is represented by a parallel combination of a dash-pot and spring. The bulge stiffness k_c^* and bulge damping C_c^* can initially be estimated by applying equations 4.6 – 4.9 on the measured displacement and force data. These results are shown in Figure 4.11. The parameters are plotted against peak compliance force $(F_c)_{max}$. The figure shows that the bulge stiffness increases (due to elastomer stiffening) as the temperature goes down. However, this trend is not seen in the bulge damping. Here, the damping shows an increasing trend with increasing temperature. However, the variation in bulge damping is generally less than 20% except at two displacements points (1.778 mm, 2.286 mm).

To estimate the bulge stiffness k_c^* and bulge damping C_c^* of the MRFE damper, first equation 4.10 is applied to determine the maximum or peak compliance force of the MRFE damper as follows:

$$F_c(t) = F(t) - 2k_c^* x(t) - 2C_r^* \dot{x}(t)$$
$$= 2k_c^* (x(t) - 2x_A(t)) + 2C_c^* (\dot{x}(t) - 2\dot{x}_A(t)) \tag{4.20}$$

where F_c is the compliance force. Once the peak compliance force $(F_c)_{max}$ of the MRFE damper at each test temperature is determined, the corresponding bulge stiffness, and bulge damping are estimated by interpolating or extrapolating using Figure 4.11 at the corresponding test temperature.

4.5.5 Parameter Adjustments

Before beginning the optimization routine, some factors affecting the MRFE damper behavior are briefly discussed. These factors were either assumed negligible or difficult to account for in the hydromechanical model formulation. However, they still have some major and minor impacts on the model performance as discussed in the proceeding sections. There are two major factors that influenced the performance of the MRFE damper model:

- Temperature variation during bare elastomer testing

The shear stiffness k_r and damping C_r employed in the hydromechanical model simulation are determined from the estimated shear stiffness k_r^* and damping C_r^* using the following scaling factors:

$$\left.\begin{aligned} k_r &= \varphi\, k_r^* \\ C_r &= \varphi\, C_r^* \end{aligned}\right\} \quad where \;\; \varphi = \begin{cases} 0.85 & if\; T = 50^o C \\ 0.95 & if\; T = 40^o C \\ 1 & if\; T = 30^o C \\ 1 & if\; T = 20^o C \end{cases} \tag{4.21}$$

During temperature testing of the MRFE damper elastomeric body (empty MRFE damper) using the ATS heating chamber, material temperature was controlled by attaching a thermocouple on the surface of the elastomeric material. However, the thermocouple was not sufficiently insulated from its surroundings, which could have resulted in an inaccurate temperature reading. Thus, to account for this effect and to better fit the model to the experimental data, the initial shear stiffness and damping parameters estimated in *section 4.5.3*, were scaled by a factor within a reasonable

limit, as shown in equation 4.21. The scaling factors were determined through trial and error at selected test conditions.

- System bulk modulus

The compliance model parameters (bulge stiffness k_c and bulge damping C_c) employed in the model simulation are given as:

$$\left.\begin{aligned} k_c &= \delta\, k_c^* \\ C_c &= \delta\, C_c^* \end{aligned}\right\} \quad where\ the\ scaling\ factor\ \ \delta = \begin{cases} 1.12 & if\ T = 50^o C \\ 1.08 & if\ T = 40^o C \\ 1.00 & if\ T = 30^o C \\ 0.80 & if\ T = 20^o C \end{cases} \tag{4.28}$$

In a hydromechanical system, such as the current MRFE damper, the stiffness characteristics of the MRFE device are influenced by the interaction of the bulk modulus of the MR fluid and compliance of the elastomeric volume chamber. However, entrapped air adversely affects the bulk modulus, thus stiffness, of the fluid due to its higher compliant property. Further, the isothermal bulk modulus of air is simply the fluid pressure itself, and from ideal gas law, the air pressure is directly proportional to the fluid temperature at a constant volume [93]. Thus, increasing the air temperature will increase pressure, which will in tern increase the air bulk modulus.

In all MRFE damper testing performed, it is to be recalled that the MR fluid was simply poured into the damper and sealed and compressed to create positive pressure. This is expected to entrap air in the fluid and the viscosity of the fluid will prevent the air bubbles from escaping. Since it is very difficult to extract air completely, creating

a high internal pressure will compensate the bulk modulus loss associated with entrapped air, and as the pressure is increased, the entrapped air will dissolve into the liquid and will not further affect the bulk modulus [94]. This was well achieved when the MRFE damper was tested with the valves plugged to estimate the bulge stiffness. This is shown in Figure 4.11 where the stiffness is predominantly a function of MR fluid and volume chamber stiffness. However, in the actual MRFE damper testing, the damper was not sufficiently pressurized and thus leaving a higher percentage of the air bubbles suspended in the fluid. As a result, the bulk modulus of the MRFE is significantly affected by the bulk modulus of entrapped air, which tends to increase with an increase in temperature. This behavior is reflected in Figure 4.3b. In the figure, the left and right sides of the plot follow a similar trend as the bulge stiffness of the MRFE damper. As the temperature is increased, the slopes of these lines increase, indicating an increase in stiffness. Thus, to account for these effects and to better fit the model to the experimental data, the initial compliance parameters estimated in *section 4.5.4*, were scaled by a factor to emulate the actual compliance property of the MRFE damper. The scaling factors were determined through trial and error at selected test conditions.

4.6 Model Performance

In order to minimize the squared mean error between the measured and predicted damping force of the MRFE damper at each, a constrained least-mean-squared (LMS) error minimization technique was employed to estimate and optimize the equivalent piston area A_p only. The rubber mass is neglected in this optimization without loss of generality. The error function for the hydromechanical model is expressed as:

$$E(A_p) = \sum_{j=1}^{N} \left(F(t_j) - F^*(t_j) \right)^2 \tag{4.29}$$

where $F(t_j)$ is the actual measured force, $F^*(t_j)$ is the calculated force from the hydromechanical modeling, t_j is the time at which the j^{th} sample was measured and N is the number of data per one cycle.

Figure 4.12 and 4.13 shows the optimized equivalent piston areas at lag/rev obtained from the error minimization procedure at different temperatures. The figures show the equivalent piston area exhibits similar trends at all temperatures. There is also a small increment as the temperature is increased. The equivalent piston area is observed to increase with increasing current, especially at lower amplitudes. However, as the displacement amplitude increases, the variation in piston area diminishes, tending to approach a similar value in the limit.

The field-off and field-on damping force versus velocity cycles at lag/rev frequency and different temperatures are given in Figures 4.14 and 4.15. The displacement amplitude for each case is 2.286 mm (0.09 in). The figures show that the hydromechanical model is able to capture the non-linear dynamic behavior and closely estimates the actual hysteretic damping force behavior of the MRFE damper from experimental measurements.

The MR effective force F_{MR} in each valve of the damper system, as extracted from the model, is given by:

$$F_{MR}(t) = C_A \dot{x}_A(t) + F_y \, sgn(\dot{x}_A(t)) \tag{3.39}$$

The first term in the above equation is related to the viscous effect and the second term results from the magnetic effect. These results at field-on condition at lag/rev frequencies are shown in Figures 4.16 and 4.17 for the minimum and maximum

displacement inputs respectively. From Figure 4.16, it is observed that at minimum displacement (0.0762 mm), the field-on damping at 20ºC is less than at 50ºC, which is consistent with the previous result (Figure 4.6b). This increasing damping at 50ºC is reflected in the force-displacement plot by its larger enclosed loop area. Even though at 20ºC the apparent post-yield viscosity is larger, due to smaller fluid displacement, thus reduced flow rate, the total available damping will be lower. However, as the input amplitude increases, the damping variation between the two temperatures gets narrower. From Figure 4.17, it is observed that at the maximum input displacement, the damping available at both temperatures is quite similar.

To predict the response of the MRFE damper under dual frequency excitation, it was subjected to various combinations of lag/rev and 1/rev frequency amplitudes under various applied currents, and the force-time history is used to evaluate the model performance. The dual frequency test matrix at all temperatures is given in Table 4.3. Utilizing optimized model parameters, the MRFE damper dual frequency response was predicted by linear superposition of the estimated damper performance at each excitation frequency. The modeling results for two combinations of the lag/rev and 1/rev frequencies at field-off and field-on conditions are given in Figures 4.18 and 4.19. In the figures, X_{lag} represent the amplitude of the harmonic input at the lag/rev frequency while X_{pri} represents the amplitude at 1/rev frequency. The results show that the hydromechanical model was able to predict MRFE damper dual frequency performance reasonably well over the amplitudes and frequencies investigated.

4.7 Conclusion

The investigation in this chapter demonstrated the feasibility of using the snubber type MRFE damper in mitigating helicopter rotor instabilities under varying operating temperatures. Currently, most hingeless and bearingless helicopters utilize either elastomeric or hybrid fluid-elastomeric (FE) lag dampers. However, these advanced lead-lag dampers are passive devices and can only operate with a single damping profile. Additionally, the elastomeric materials used in these devices exhibit temperature-dependent behavior that causes their stiffness and damping properties to deviate. In addition, the hydraulic fluid viscosity in FE dampers change with temperature and this significantly alters the viscous damping available in the device. The MRFE lag damper has been proven to provide controllable damping profile that can be optimal tuned to specific requirements. Thus, the MRFE damper has the potential to compensate temperature related performance degradation by varying the applied current to the MR valve. In the current chapter, the MRFE is shown to provide comparable damping force as compared with a baseline FE damper for all temperature cases. Moreover, at all temperature conditions, a significant increase in damping and a wide controllability range can be gained by using the MRFE damper. For example, at lower displacement amplitudes, more than a 100% change in damping was obtained at all temperatures. As a result, the damping and controllability spectrum of the MRFE can potentially be tuned to match actual damping requirements of certain flight conditions where instabilities tend to be instigated.

To account for the non-linear hysteretic behavior of the MRFE damper, a lumped parameter based model was formulated in Chapter 3. In this chapter, the model was

employed to characterize MRFE damper performance at varying temperatures. Since model parameters are fundamentally dependent on damper geometry and material properties, temperature variation will only cause the later to vary. To that effect, most material properties (seven out of eight) at different temperatures were estimated or measured *a priori*, which later were reasonably scaled to simulate damper data accurately. The model was shown to accurately reconstruct the force-velocity and force-time histories at single and dual frequencies at all temperature conditions.

Table 4.1 Measured, model estimated and dependent model parameters

Measured Parameters	Model Estimated Parameters	Dependent Parameters
Viscosity, μ	Eqv. Piston area, A_p	Mass, m_A
Resistance, R		Viscous damping, C_A
Density, ρ		
Inertance, I		
Shear stiffness, k_r		
Shear damping, C_r		
Bulge stiffness, k_c		
Bulge damping, C_c		
Yield force, F_y		

Table 4.2 Estimated yield force

Current [A]	Fy [N]
0.00	0.00
0.25	31.30
0.50	62.50
0.75	93.63
1.00	124.63

Table 4.3 Dual frequency test matrix

$X_{lag/rev}$ [in]	$X_{1/rev}$ [in]	0.03	0.05	0.07	0.09	0.10	0.13
0.03		X	X	X	X	X	X
0.05		X	X	X	X	X	
0.07		X	X	X	X		
0.09		X	X	X			
0.10		X	X				
0.13		X					

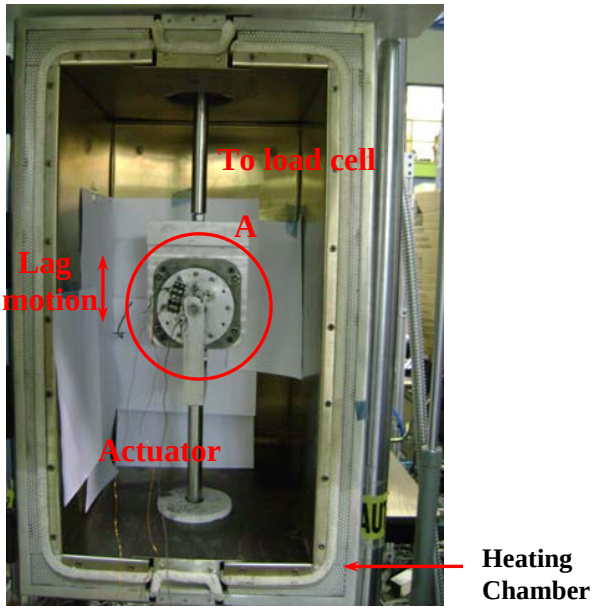

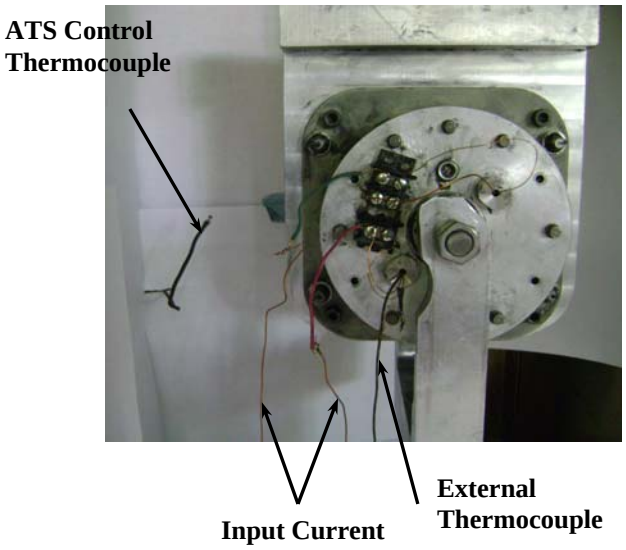

Detail A

Figure 4.1: MRFE lag damper test set-up on MTS testing machine and ATS environmental heating chamber

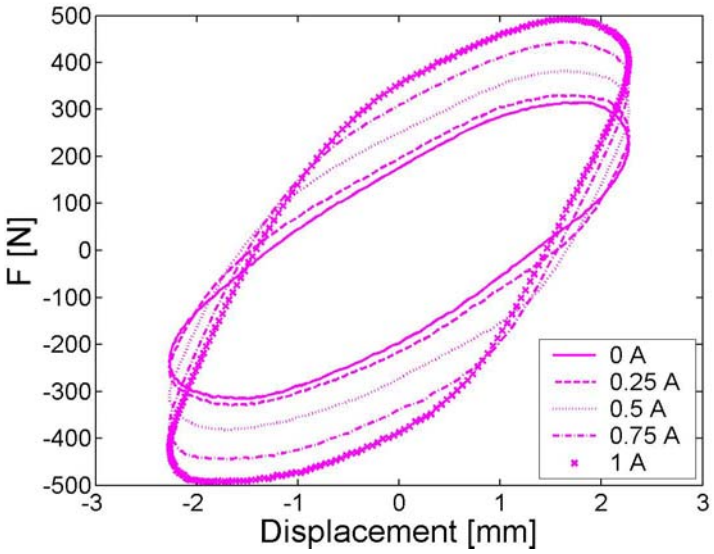

(a) T = 20ºC

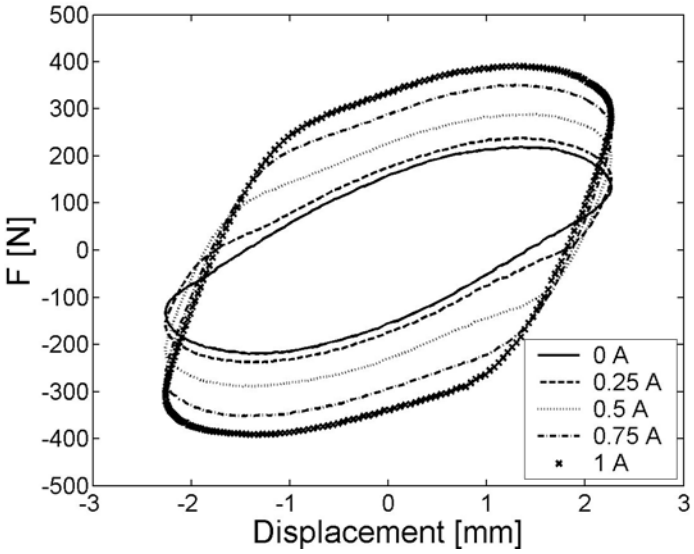

(b) T = 50ºC

Figure 4.2: MRFE lag damper typical test results

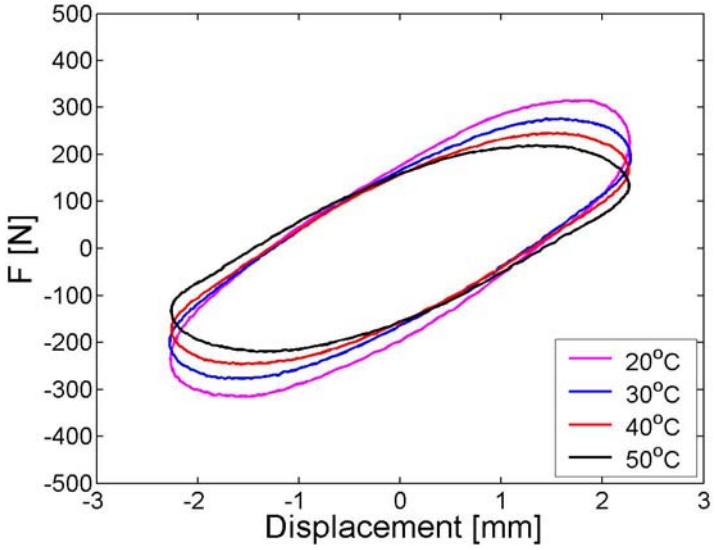

(a) Field-off

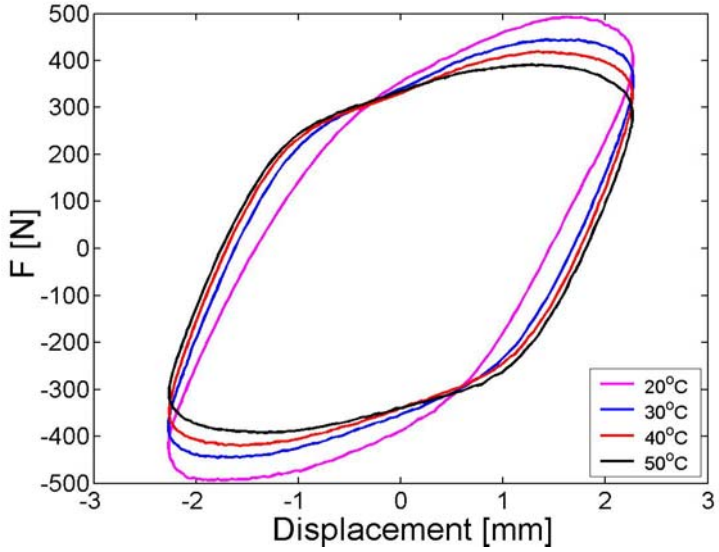

(b) Field-on @ 1A

Figure 4.3: MRFE lag damper typical test results

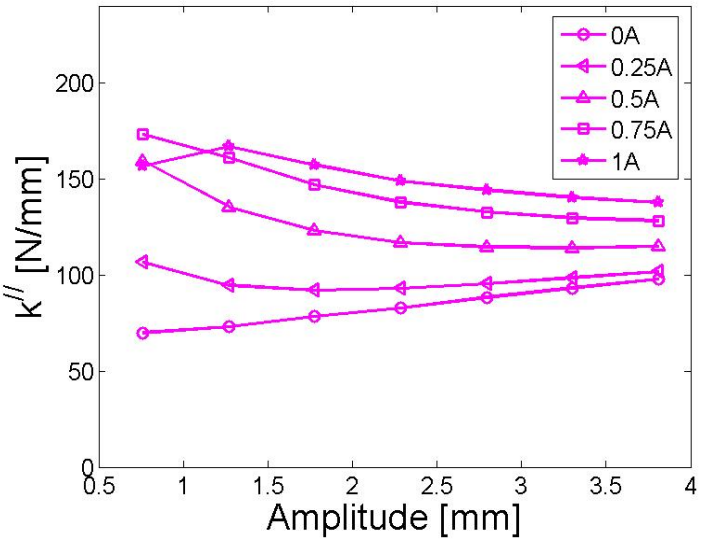

(a) Loss stiffness @ 20°C

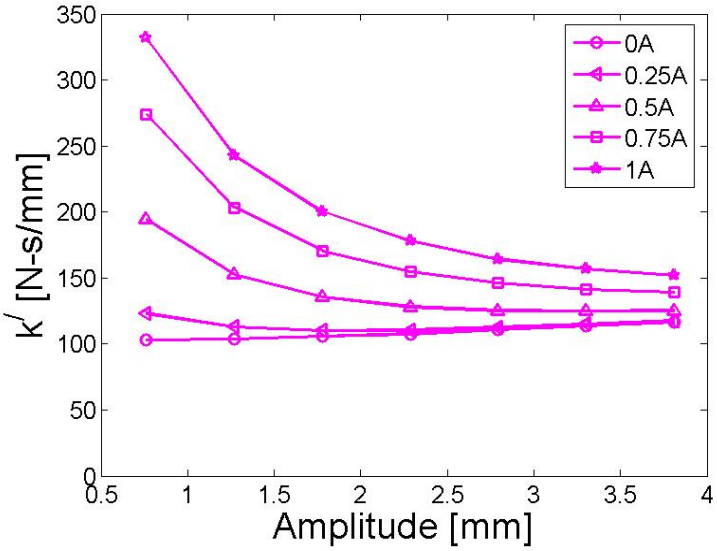

(b) In-phase stiffness @ 20°C

Figure 4.4: MRFE damper lag/rev performance at 20°C

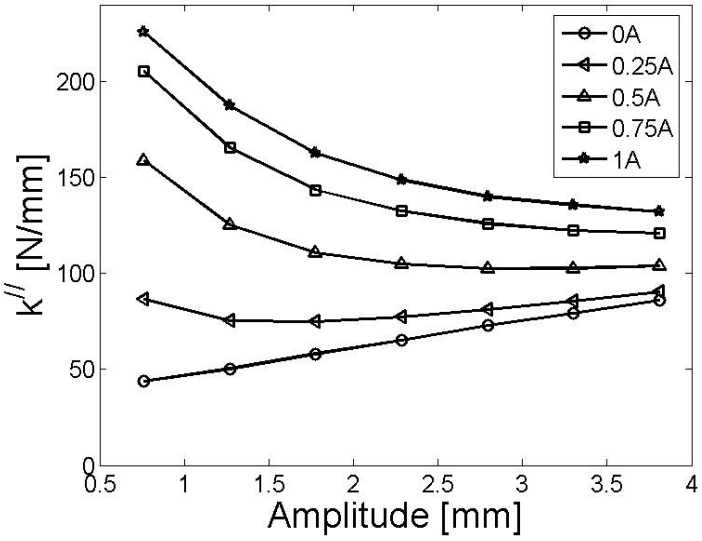

(c) Loss stiffness @ 50°C

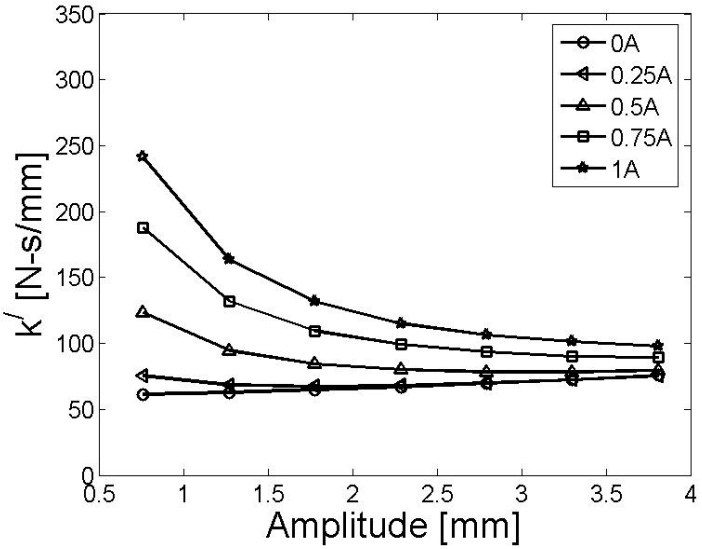

(d) In-phase stiffness @ 50°C

Figure 4.5: MRFE damper lag/rev performance at 50°C

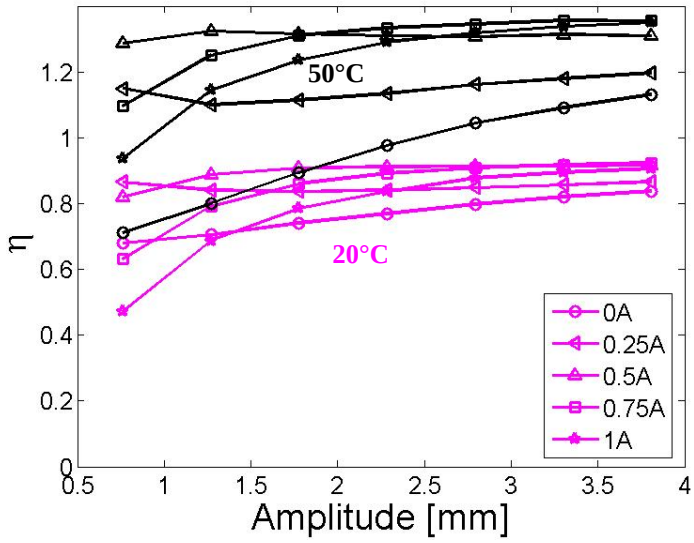

(a) MRFE damper lag/rev loss factor

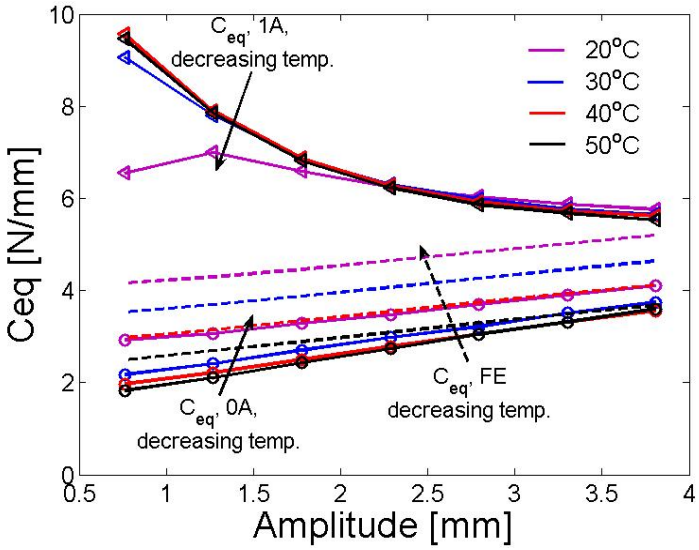

(b) MRFE damper lag/rev equivalent damping

Figure 4.6: MRFE damper lag/rev performance at varying temperatures

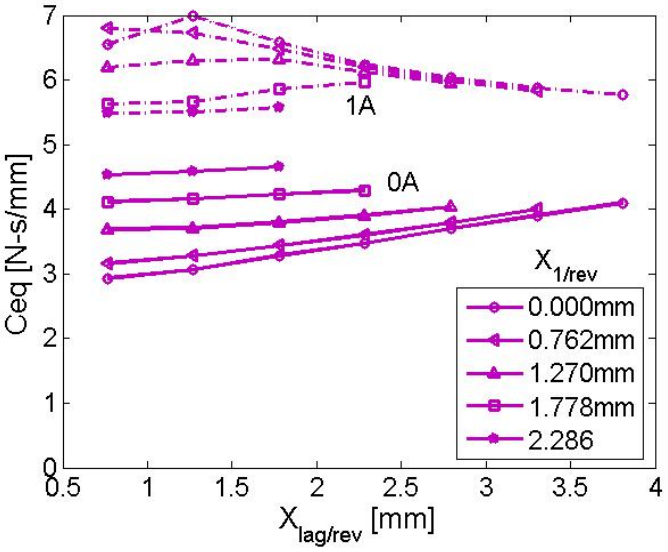

(a) MRFE damper, lag/rev damping at 20°C

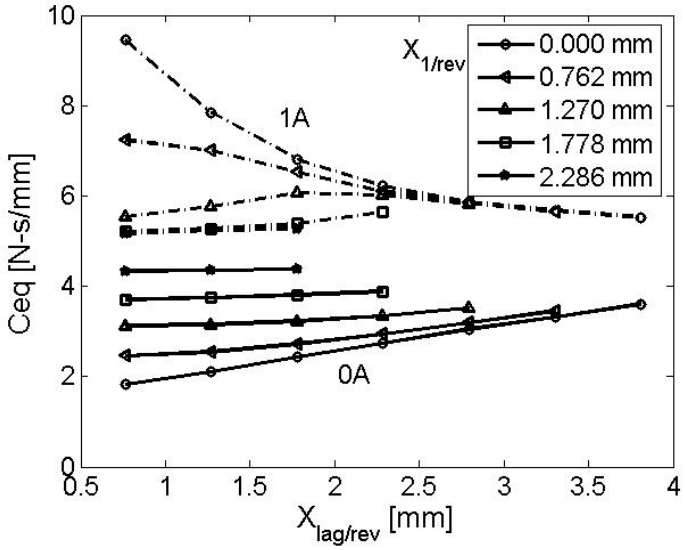

(b) MRFE damper, lag/rev damping at 50°C

Figure 4.7: Lag/rev damping of MRFE damper at dual frequency

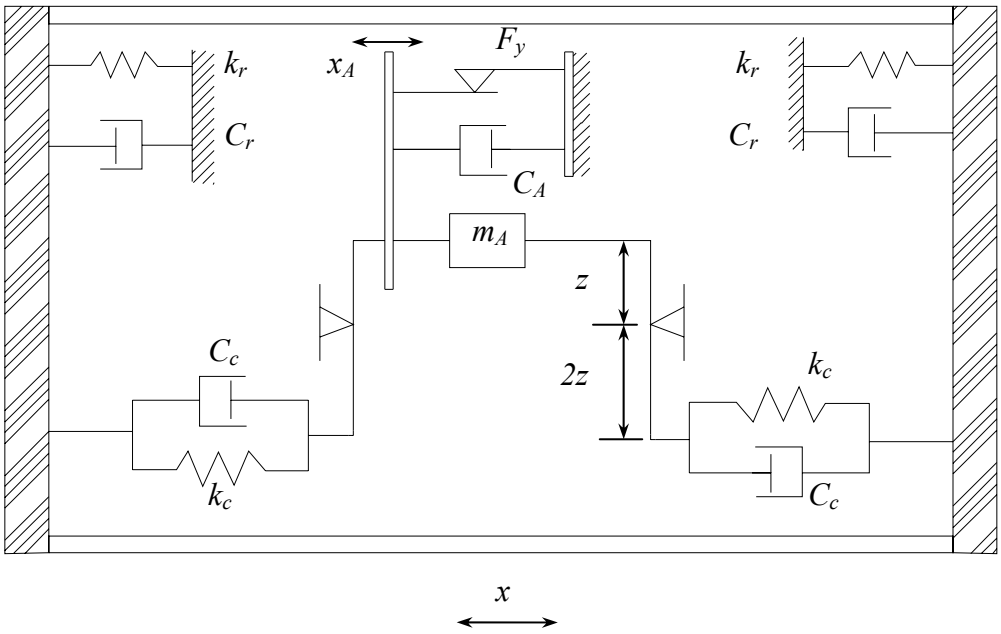

Figure 4.8: Analogous mechanical system of the hydromechanical model of the MRFE damper in terms of x_A

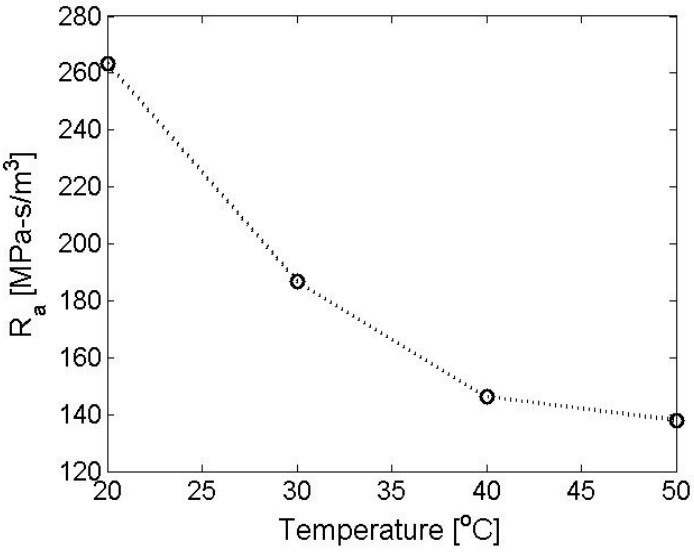

Figure 4.9: Resistance due to viscous flow in port holes

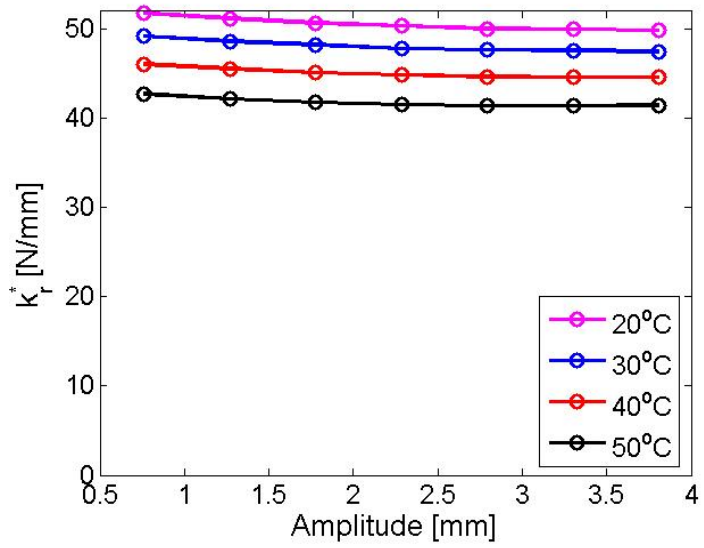

(a) Shear stiffness k_r^*

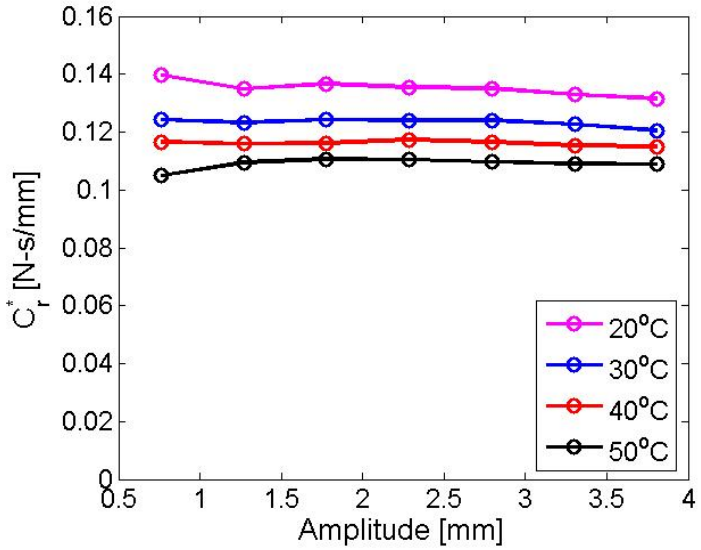

(b) Shear damping C_r^*

Figure 4.10: Estimated shear damping C_r^* and stiffness k_r^*

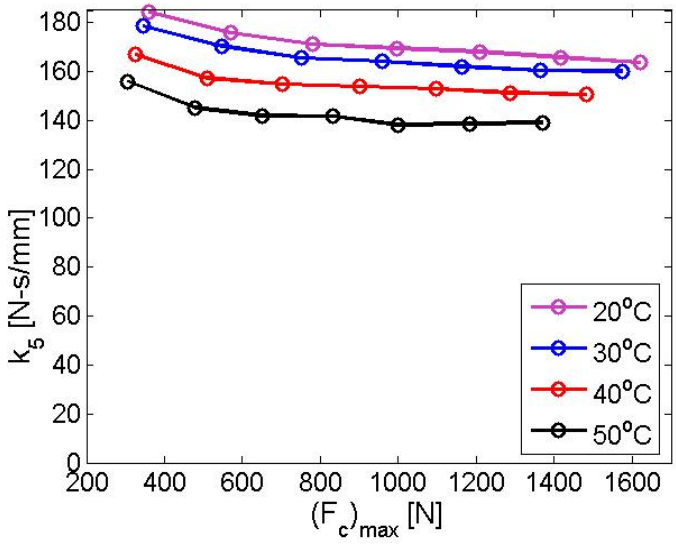

(a) Bulge stiffness k_c^*

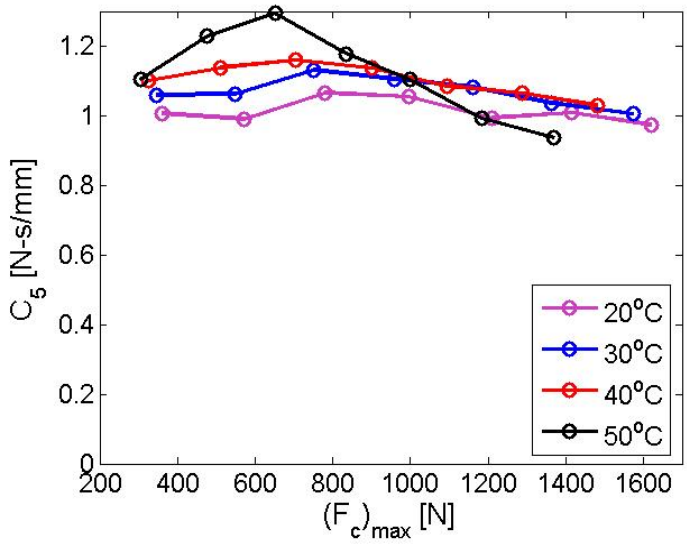

(b) Bulge damping C_c^*

Figure 4.11: Estimated bulge damping C_c^* and bulge stiffness k_c^*

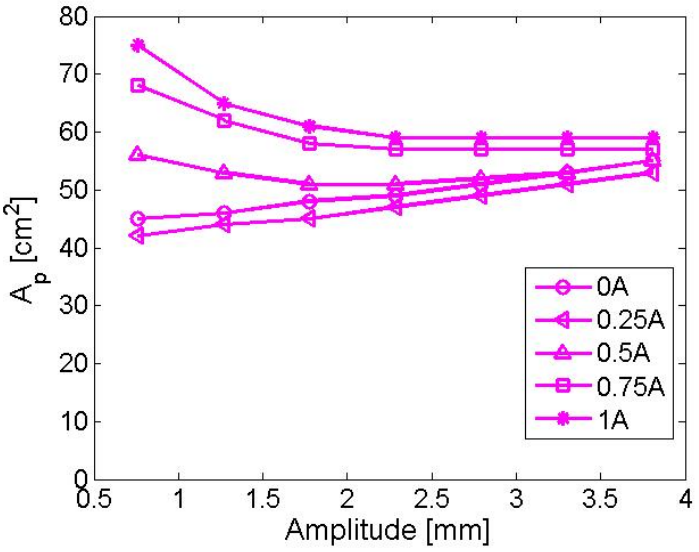

(a) T = 20ºC

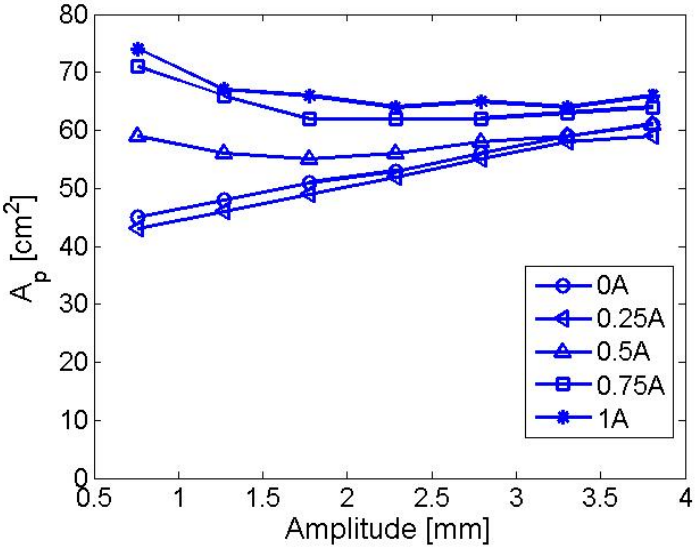

(b) T = 30ºC

Figure 4.12: Model estimated equivalent piston area A_p

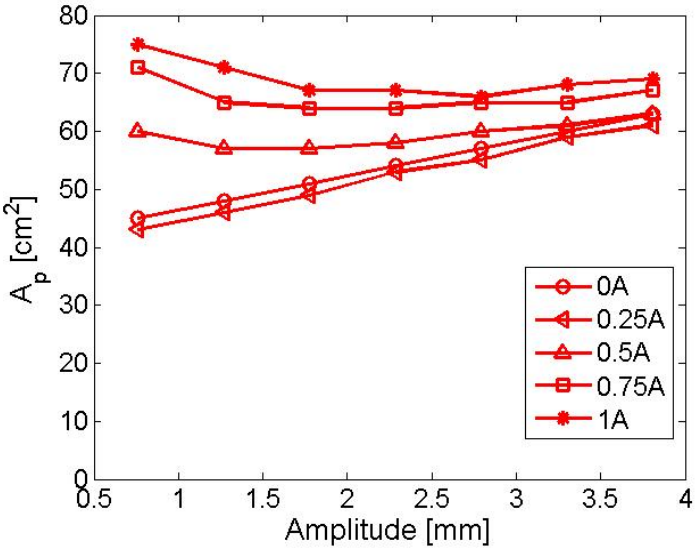

(a) T = 40ºC

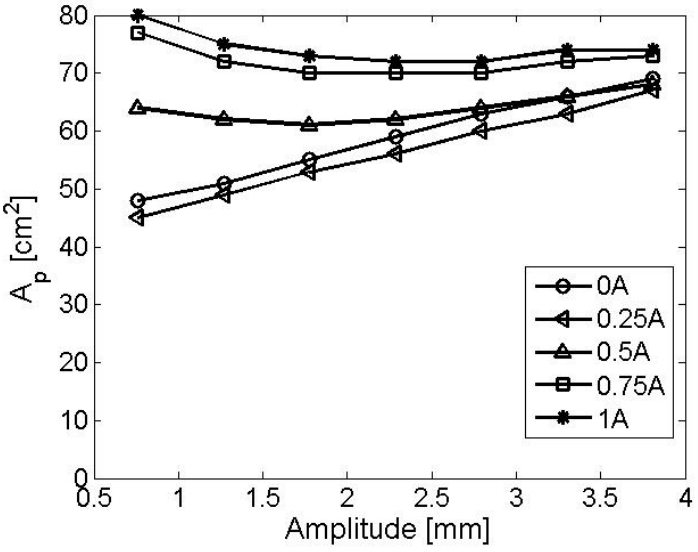

(b) T = 50ºC

Figure 4.13: Model estimated equivalent piston area A_p

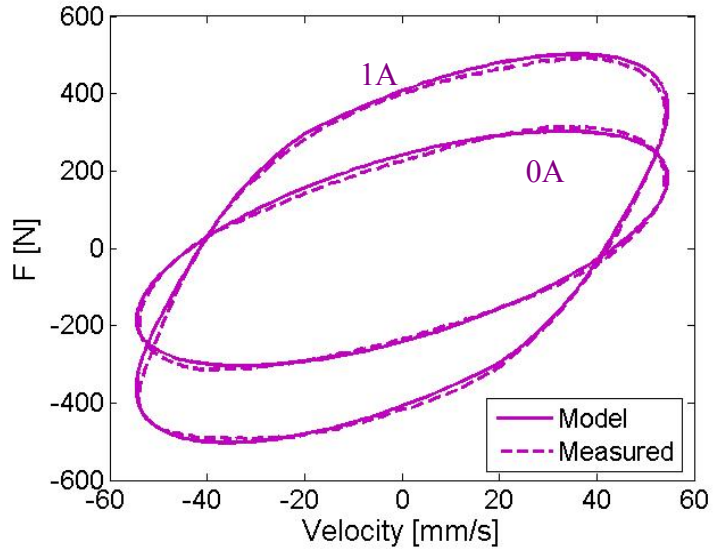

(a) T= 20ºC

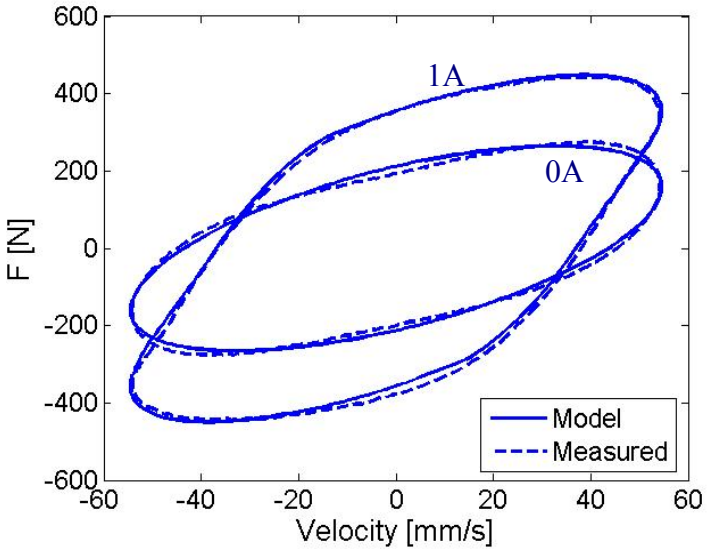

(b) T= 30ºC

Figure 4.14: Experimental and model estimated damping force hysteresis

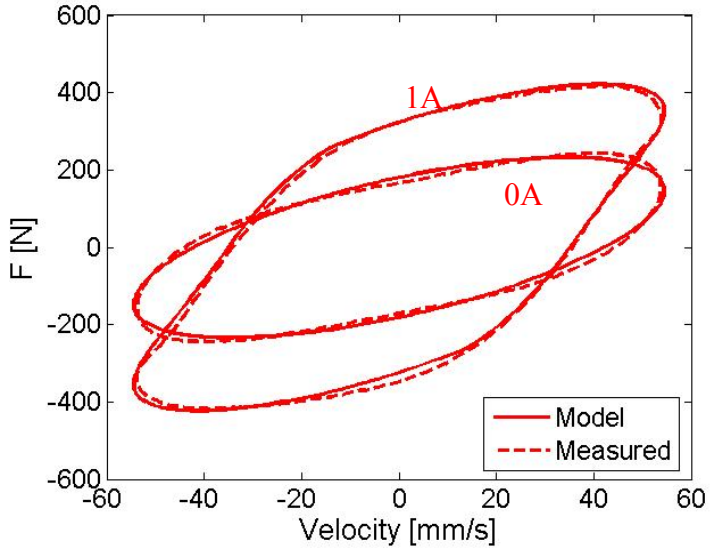

(a) T= 40ºC

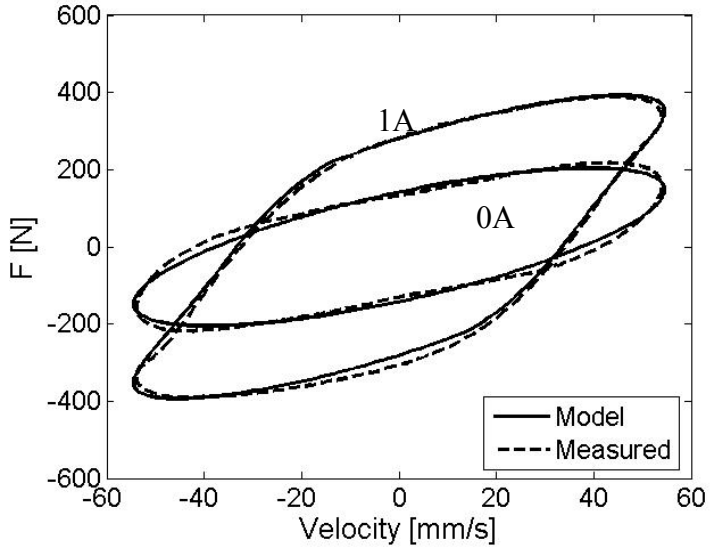

(b) T= 50ºC

Figure 4.15: Experimental and model estimated damping force hysteresis

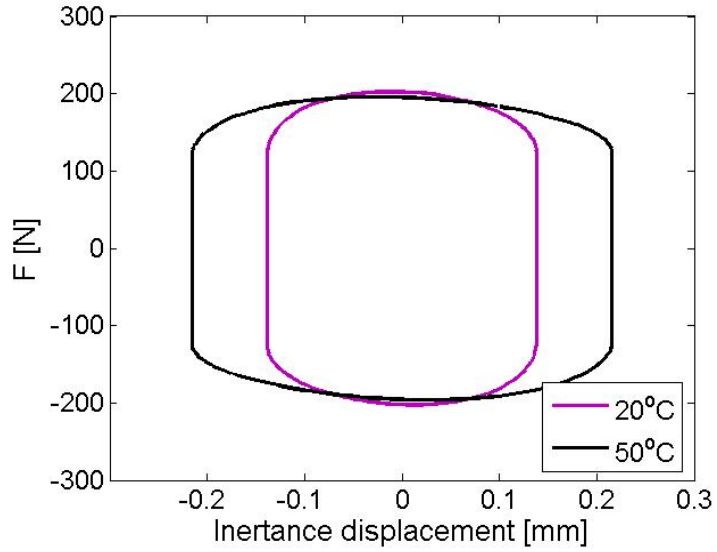

(a) F_{MR} vs generalized inertance displacement, x_A

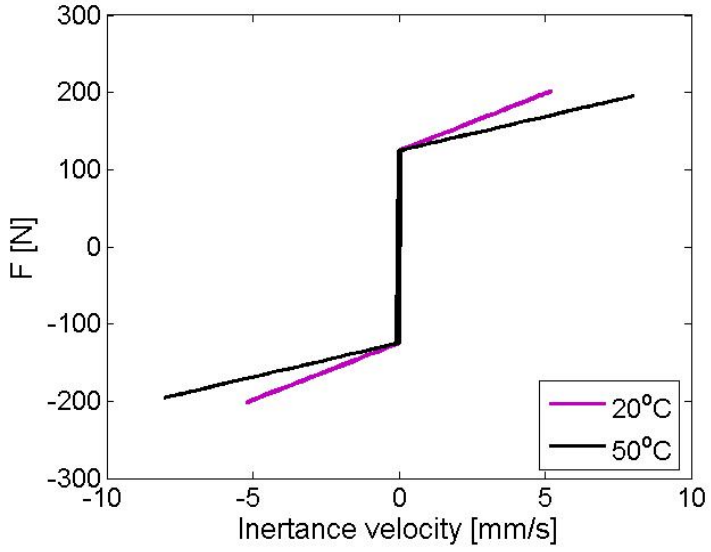

(b) F_{MR} vs generalized inertance velocity, $\dot{x}_A$

Figure 4.16: Model estimated MR damping force hysteresis at X_{lag} = 0.762 mm

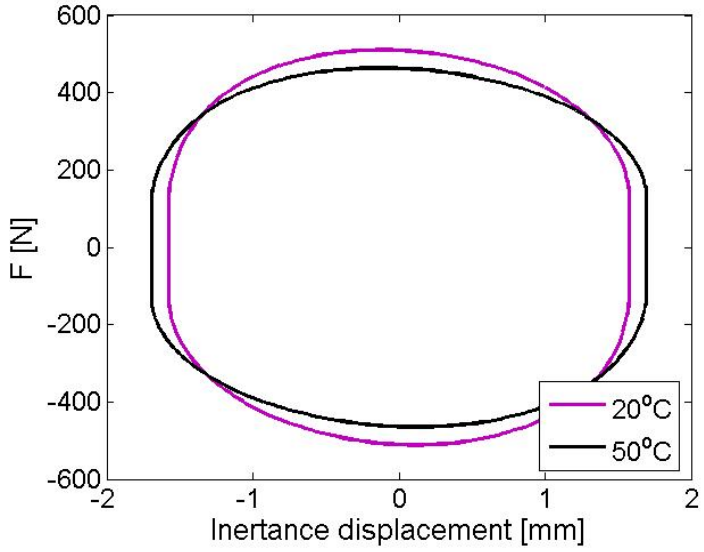

(a) F_{MR} vs generalized inertance displacement, x_A

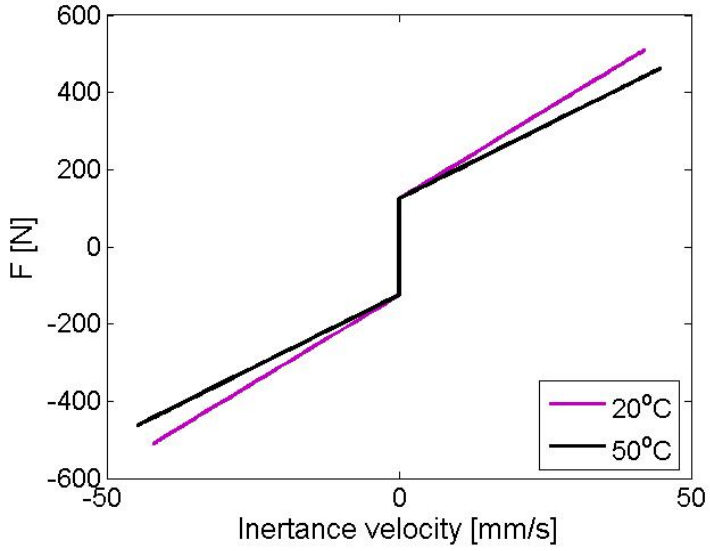

(b) F_{MR} vs generalized inertance velocity, $\dot{x}_A$

Figure 4.17: Model estimated MR damping force hysteresis at X_{lag} = 3.38 mm

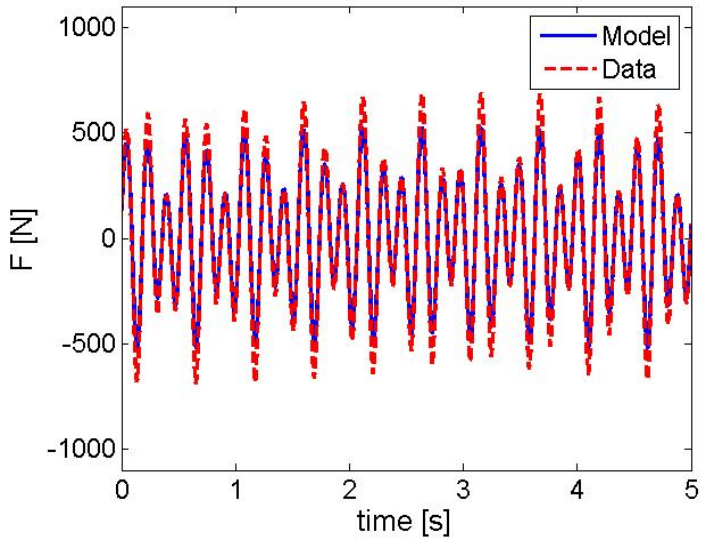

(a) T = 20°C, X_{lag} = 1.27 mm, $X_{1/rev}$ = 2.29 mm @ 0A

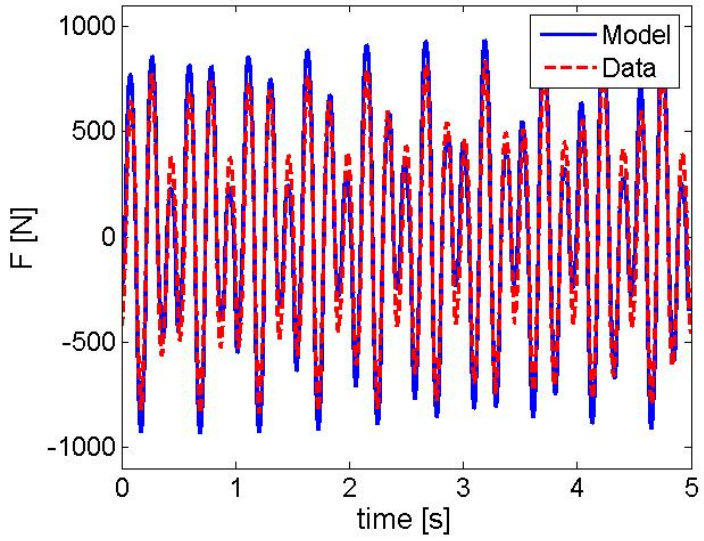

(b) T = 20°C, X_{lag} = 1.27 mm, $X_{1/rev}$ = 2.29 mm @ 1A

Figure 4.18: Dual frequency comparison between measured and predicted damper forces at 20ºC

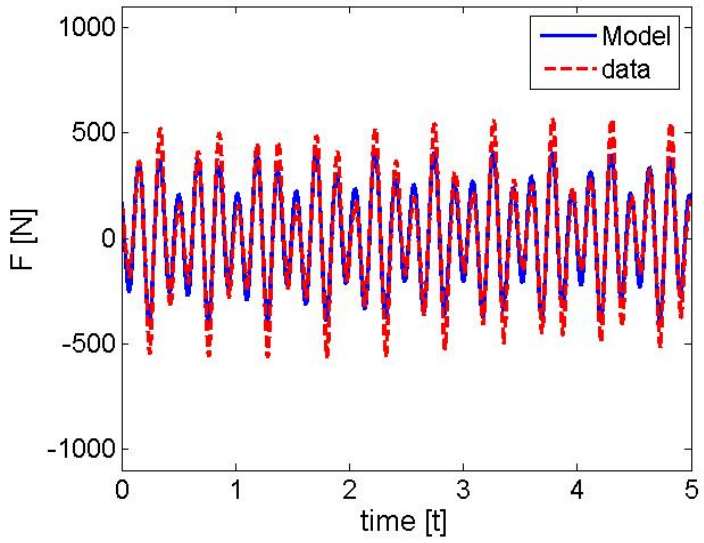

(a) T = 50°C, X_{lag} = 1.27 mm, $X_{1/rev}$ = 2.29 mm @ 0A

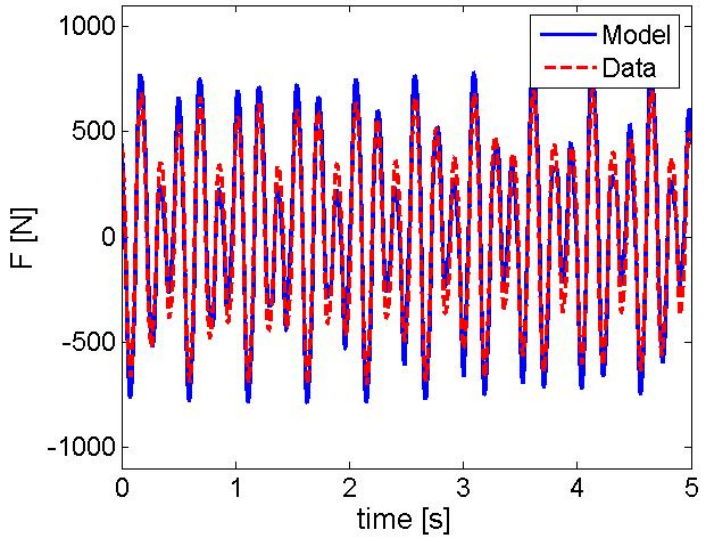

(b) T = 50°C, X_{lag} = 1.27 mm, $X_{1/rev}$ = 2.29 mm @ 1A

Figure 4.19: Dual frequency comparison between measured and predicted damper forces at 50ºC

Chapter 5: Temperature Compensation for an MRFE lag Damper

5.1 Introduction

Semi-active lead-lag dampers employing field-controllable fluids, such as Magneto-Rheological (MR) fluids, have demonstrated the potential to greatly improve damper performance by providing a means by which to augment damping in real-time [7, 10, 14]. By employing magnetorheological technology with advanced fluid elastomeric devices to create a magnetorheological fluid elastomeric (MRFE) lag damper, the ability to augment or optimize damping in flight can be achieved [7]. Adjusting stability margins in flight for optimal characteristics could potentially increase forward speed, maneuverability, and payload capacity in a broadened operational environment.

Control studies have taken place to explore the potential that semi-active dampers have for advanced rotor systems. Marathe *et al* [59] combined an MR damper model into a rotor aeromechanical model and investigated the effects of two different control schemes on rotor stability. The two control schemes were the On-Off scheme and the Feedback Linearization scheme, and they were compared for lag transient responses in ground resonance and their ability to reduce periodic damper loads in forward flight. The results implied that using a shear mode MR damper of size comparable to an elastomeric lag damper can provide sufficient damping for ground resonance

stabilization and can significantly reduce periodic damper loads with a judicious choice of operation scheme. The On-Off scheme is simple and easy to apply, but it is not optimal in reducing hub loads. Feedback linearization control was more versatile, however it was recognized that since such algorithm is developed based on the MR damper model, its performance is sensitive to model error or uncertainties [67]. Gandhi *et al* [67] explored the effects of MR fluid damper model uncertainties on helicopter rotor system stability when feedback control law was utilized. The study showed that by increasing control gain, hence increasing the prescribed damping ratio, to a sufficiently high value, limit cycle instability can eventually be eliminated, for given uncertainty bound. However, large prescribed damping ratios would result in high periodic damper loads in forward flight. The study suggested that the periodic damper loads can be substantially reduced, while maintaining stability, if a band-rejecting filter is used which eliminates the 1/rev periodic component of velocity and leaves only the perturbation velocity in the feedback signal. Zhao *et al* [60] developed a different linearization feedback control strategy to integrate the MR damper into classic linear ground resonance analysis, and be applied to the ground resonance problem to stabilize an unstable rotor system assuming an isotropic rotor hub (all damper and blades similar), and to control undamaged dampers to recover rotor stability in case of an anisotropic rotor hub due to damper damage and/or degradation. The study showed that using MR dampers and a semi-active controller can stabilize an unstable rotor and maintain the design stability margin in the rotor system. In addition, the robustness study showed that the MR dampers, actuated with a properly

designed controller, can recover stability when the rotor system loses stability due to damper degradation, except in the case where 100% damping was lost on one blade.

These investigations have all considered linear stroke MR dampers, in their control evaluations. In addition, the control studies outlined above did not account for temperature uncertainties that could arise due to self-heating and/or atmospheric conditions. Due to damper temperature variation, the available damping from the dampers might not match the lag mode damping required to augment rotor stability. The yield stress of an MR fluid shows little variation for a wide temperature range (-40ºC to 150ºC). However, the viscosity of the MR fluid is a function of temperature. Since the viscosity of the MR fluid increases exponentially with decreasing temperature, the viscous or passive damping force of the MR lag damper at low temperatures could become very high, making the lag mode very stiff. This might lead to increased rotor hub loads. Further, at high damper temperatures, the viscosity, thus the damping available, from the MR lag damper decreases. This reduced available damping could present a limit cycle instability in the rotor system.

Hence, the focus of this chapter is to explore the temperature compensating potential of the snubber type MRFE lag damper in terms of tracking a target damping profile at the lag/rev frequency in the presence of temperature and displacement amplitude variations. The target damping profile in lag mode for the rotor system for various combinations of single (lag/rev) and dual (lag/rev and 1/rev) frequencies and displacements can be formulated using the actual rotor lag mode stability analysis. However, in this research, the available damping of a new and unmodified snubber type FE damper at ambient conditions is set as the target damping profile to evaluate

the MRFE damper in its temperature compensating property. Once the target or required damping is set, it is imperative that the MRFE damper is intended to provide that damping regardless of damper operational temperature. To that effect, the temperature compensating capability of the MRFE lag damper at and above room temperatures is evaluated in this chapter. The lag/rev frequency of excitation was utilized for this investigation. Three control techniques will be designed, implemented, experimentally evaluated, and compared for steady-state error and response time over the amplitude and temperature ranges tested.

5.2 Hydromechanical Modeling Summary

Chapter 2 and 3 outlined the effort placed on establishing a predictive design tool that can be used in future design revision of the present retro-fit device. Thus, the lumped parameter, hydromechanical model was derived fundamentally based on damper geometry and material properties. Effects of parameter variation due to temperature have also been included in the model for both the existing FE device (Chapter 2) and the MRFE damper (Chapter 4). The resulting model was used to aid in the design of the control systems and will be briefly introduced here.

The analogous mechanical system of the MRFE damper developed in Chapter 3 is shown in Figure 5.1. Note that the original model derivation was for the general case where the valves and flow ports were not necessarily the same, but these are identical for the prototype MRFE damper, causing the equivalences and reduced form shown. Given an input displacement to the damper of *x(t)*, the force response can be computed according to:

$$2C_r\dot{x}(t) + 2k_r x(t) + 2C_c\left(\dot{x}(t) - 2\dot{x}_A(t)\right) + 2k_c\left(x(t) - 2x_A(t)\right) = F(t) \qquad (5.1)$$

$$m_A\ddot{x}_A(t) + C_A\dot{x}_A(t) - 2C_c\left(\dot{x}(t) - 2\dot{x}_A(t)\right) - 2k_c\left(x(t) - 2x_A(t)\right) + F_y sgn(\dot{x}_A(t)) = 0 \tag{5.2}$$

For the MRFE damper, the pre-yield behavior is a function of C_c and k_c, implying that the pre-yield stiffness is dominated by the fluid chamber compliance properties, while the post-yield behavior is governed primarily by m_A, C_A and F_y. This set of equations does illustrate MRFE damper behavior, and it must be noted that for a constant excitation frequency, the key parameters involved have the following dependencies on displacement amplitude, X, temperature, T, and applied current, i:

$$\begin{aligned} C_r &= C_r(X,T) \\ k_r &= k_r(X,T) \\ C_c &= C_c(X,T) \\ k_c &= k_c(X,T) \\ m_A &= m_A(X,T) \\ C_A &= C_A(X,T) \\ F_y &= F_y(i). \end{aligned} \tag{5.3}$$

These parameter dependencies imply that the MRFE lag damper has three inputs, two of which cannot be directly controlled (displacement and temperature). However, it is the applied current that can be adjusted to compensate for force level variations due to these two inputs, giving the possibility of multiple operating points. Hence, this prospect of obtaining optimal damping profiles motivates the exploration of control techniques with the MRFE damper.

5.3 Control Design

The utility of three different control schemes was evaluated in terms of tracking a reference damping profile that was a function of only displacement amplitude, though

temperature was also varied from 30ºC to 55ºC. In this fixed-frame, feasibility study, the unmodified FE damper performance at ambient temperature (~27.5ºC) and rotor lag/rev (3.8 Hz) was selected as the target profile over an amplitude range of 0.8 mm to 3.4 mm. Recall that this is the dashed line in Figure 3.8a. In each of the three control techniques employed, two real-time measurements are required, though they are not necessarily the same for each technique.

5.3.1 Computation of Performance Metric

The performance metric discussed previously was the equivalent damping. This works well for characterizing damper performance and in designing an gain scheduled controller, but it does require extra computations and more knowledge of the signals, which could increase complexity of a control system. The equivalent damping, C_{eq}, can alternatively be computed as:

$$C_{eq} = \frac{E_{dis}}{\pi \omega X^2} \tag{5.4}$$

From this equation, it can be seen that the equivalent damping, C_{eq} is proportional to the energy dissipated, E_{dis}, but requires frequency and amplitude information. Hence, using the energy dissipated as the performance metric would certainly reduce the number of computations that must be performed, and it is given by:

$$E_{dis} = \int_0^{\frac{2\pi}{\omega}} F(t)dx \tag{5.5}$$

The integration occurs over one period, for the lag/rev frequency of 3.8 Hz, this is 0.26 seconds. Based on the target damping profile at the rotor lag/rev frequency, the target energy dissipation profile can be calculated directly from the C_{eq} equation

above. Figures 5.2a and 5.2b show the target damping profile and its associated target energy dissipation profile respectively. There is very little (near zero) energy dissipation at the lowest amplitude and this increases nonlinearly to 4 Nm or 4 J at the high end of the displacement amplitude range.

A secondary advantage of using energy dissipation as the performance metric of choice for the MRFE lag damper, though still following along the justification for a reduction in computational intensity, is that it will be directly applicable to a closed-loop control system that uses damping (energy dissipated) as a feedback variable. Details of this approach will be discussed later.

It was shown that two measurement signals (force and displacement) are integrated over one period to calculate energy dissipation. To implement this in a digital control system, a series of discrete transfer functions can be assembled to perform the base operations. Two discrete transfer functions that perform a difference operation of the form:

$$B(z) = \frac{z-1}{z} \tag{5.6}$$

and a unit delay

$$A(z) = \frac{1}{z} \tag{5.7}$$

all having zero initial conditions, can be used to calculate the elements of a trapezoidal integral estimate over one time step. The change in displacement can be given as:

$$\Delta x_j = x[j] - x[j-1] \tag{5.8}$$

where j is the current time step, and the change in force is

$$f_j = \frac{1}{2}\left(F[j] - F[j-1]\right) + F[j-1]. \tag{5.9}$$

Having these two elements, integration over one period can be performed

$$E_{dis} = \sum_{j=1}^{N} f_j \Delta x_j \tag{5.10}$$

which essentially adds a pre-selected number of values together. Since the sample rate of the controller would be known prior to implementation, the number of data samples that occur over one period can easily be calculated. It has been assumed here that the period of interest is the lag/rev period, though this could be changed without consequence to the method. Knowing the number of samples per period, n^*, a finite impulse response (FIR) filter can be designed. The general form is [95]:

$$y[j] = \sum_{m=0}^{N} b_m w[j-m], \tag{5.11}$$

where $y[j]$ is the output (in this case, E_{dis}), $w[j-m]$ are the inputs (in this case, $f_m \Delta x_m$), and b_m are the coefficients. Using a FIR filter simply for addition (integration) of previous points, the coefficients are specified by $b_m = 1$, for $m = 0, 1, \ldots, N$. This filter remembers only the previous N samples and adds them together with equal weighting for each. Each new time step, the filter will basically forget the oldest sample and replaces it with the new input value before performing the windowed summation. Note that this does have an initial one cycle delay until there are N measurement samples available, however. Substituting the δ function for the input of the filter gives the impulse response function form:

$$h[j] = \sum_{m=0}^{N} b_m \delta[j-m] = b_j \tag{5.12}$$

From here, the z-transform can be taken to arrive in the discrete domain form of the filter as:

$$H(z) = Z\{h[j]\} = \sum_{j=-\infty}^{j=\infty} h[j]z^{-j} = \sum_{j=0}^{N} b_j z^{-j} \tag{5.13}$$

5.3.2 Gain Scheduled Control Design

A simplified ground resonance stability approach is shown in Figure 5.3a. In this approach, there are two inputs to the rotor stability analysis. The input parameters *IP* accounts for all inputs required to compute the rotor stability margins. These include, but not limited to, rotor frequency, blade mass, blade mass moment of inertia, hub mass, hub spring, and fuselage support frequencies. The ζ represents lag mode deformation of the rotor blade. The stability analysis provides the damping required at a certain flight condition, which is fed into the Temperature Compensating MRFE Damper system, which in turn provides the required damping to the rotor system. Two control schemes were studied in designing the temperature compensator. The first one is the gain scheduled control design. This system has two inputs to a controller with one output, as shown in Figure 5.3b. A look-up table database was assembled based on MRFE damper characterization data at a number of control currents and temperatures. For each of four temperatures (20°C, 30°C, 40°C, 50°C), similar damper characterization data displayed in Figure 3.8 was collected. Recall that the unmodified FE damper performance at ambient temperature (~27.5ºC) and rotor lag/rev (3.8 Hz) was selected as the target damping profile, $C_{eq,r}$, over an amplitude range of 0.8 mm to 3.4 mm. Thus, with two inputs (estimation of displacement amplitude and measured internal damper temperature) and using the

hydromechanical damper model, the gain scheduled controller was designed to select the appropriate gain scheduled control current, i_{OLC}, to match the target damping profile, $C_{eq,r}$, by two-dimensional interpolation or extrapolation:

$$i_{OLC}(X,T) = \min_{i}\left\{C_{eq}(X,T,i) - C_{eq,r}(X)\right\} \tag{5.14}$$

Note that the displacement amplitude was calculated with a discrete FIR filter similar to that described previously for calculation of the dissipated energy, except that the filter coefficients were redefined for a moving average, rather than the former windowed sum, as:

$$b_m = \frac{1}{N+1}, \tag{5.15}$$

and the input to the filter was:

$$w[j] = \left(x[j]\right)^2, \tag{5.16}$$

which, along with a square root operation (yielding an RMS value) and multiplication by $\sqrt{2}$, gives the amplitude estimation of the past N samples. A root-means-square estimation could have been employed similarly with no consequence, but since the database was already organized in terms of amplitudes, this approach was adopted. Note that $C_{eq,a}$ represents the actual equivalent damping that is fed to the rotor system.

Parameterization of the gain scheduled controller with the experimental database gives the corresponding control currents that are displayed in Figure 5.4. Here in Figure 5.4a, the entire range of the database is shown for the temperatures and displacement amplitudes used in the experimental damper characterization, while Figure 5.4b shows a couple discrete segments taken from the control currents to more clearly illustrate the general trends. It is seen here that the control current increases

with amplitude and temperature in order to maintain the target damping profile. Note that the damping properties of the MRFE device decrease with increasing temperature primarily due to reduction in viscosity, which justifies the need to increase control current at higher temperatures in an effort to increase the yield force in the MR fluid. Looking over the entire range of inputs, the minimum current level (0.14 A) occurs at the smallest displacement amplitude (0.76 mm) and lowest temperature (20^{o}C). Conversely, the maximum current level (0.86 A) occurs at the largest displacement amplitude (3.38 mm) and the highest temperature (50^{o}C). Since the minimum current required was nonzero, this does imply that the presently designed prototype MRFE lag damper could match the target damping profile, defined as the ambient temperature performance of the FE damper, at temperatures colder than 20^{o}C. In the ideal case for the valve design approach taken here (low off-state damping), the damper performance with no current (0 A) would match the target damping profile at the coldest temperature of interest.

With this form of the controller parameterized from the experimental database, the gain scheduled control system (damper model included) was simulated at a few off-design points to show that the interpolation functions were performing properly. These simulations were performed with constant stroke amplitude and constant temperature for the duration of each simulation, and at the rotor lag/rev frequency of 3.8 Hz. Figure 5.5 displays the results at 25^{o}C, 35^{o}C , and 45^{o}C over the range of stroke amplitudes tested. The energy dissipation of the controlled MRFE lag damper model is shown in relation to the target profile (black dashed line). As it can be seen, the gain scheduled controller has the ability to maintain the desired damping level,

regardless of changes in stroke amplitude or temperature. There are two locations at the 25°C condition where deviation from the target profile is noticeable (near 1 mm and near 2.8 mm), but these deviations are all less than 10% error. Hence, the gain scheduled controller form has been validated.

5.3.3 Closed-Loop Control Design

While the gain scheduled controller was shown to accurately track a reference damping profile, one disadvantage of the technique is that there is no measurement of accuracy or self-adjustment. With this in mind, a second approach, i.e., a closed-loop control, was considered as an alternative strategy. The general diagram of the negative feedback system employed on the snubber type MRFE damper is shown in Figure 5.6. *Ref* E_{dis} is the reference energy dissipation (function of displacement amplitude only), e is the error signal or the difference between the desired energy dissipation and the actual (measured) energy dissipation (input to controller), i is the control current (output of controller), T and x are the respective temperature and displacement (inputs to damper), and F is the force (output of damper).

The control problem of interest in this investigation is reference tracking. As such, integral control is most appropriate of the standard techniques. The hydromechanical damper model was modified to incorporate an integral controller and a series of simulations was performed to optimize the control gain. Parameters varied in the optimization routine were displacement amplitude (7 total, ranging from 0.8 mm to 3.4 mm) and temperature (3 total, ranging from 30°C to 50°C). The integral gain was adjusted between 0 and 15 at each of the (amplitude, temperature) combinations. An error metric was computed at the end of each simulation according to:

$$J = \int_0^{T_f} e^2(t)dt \tag{5.17}$$

where J is a cumulative error metric and T_f is the final time of the simulation (3 seconds). Therefore, the control gain that produces the minimum value of the cumulative error metric, *J,* will be the ideal parameter for each case. Figure 5.7 shows the simulation results at the minimum (Figure 5.7a) and maximum (Figure 5.7b) displacement amplitudes. As seen in these figures, the temperature appears to have little effect on the optimal control gain at either of the amplitudes shown. For example, at X = 0.8 mm, $8.6 < k_I < 9.8$, and at X = 3.4 mm, $1.0 < k_I < 1.2$ over the temperature range simulated. There is a large variation in the optimal gain (minimum *J*) over the displacement amplitude range, however, varying nearly an order of magnitude from Figure 5.7a to Figure 5.7b.

The error metric J gives an estimate for the optimal integral control gain based on overall error, but the time in which the closed-loop system can respond and begin to follow the desired energy dissipation level is also important. Accordingly, a response time metric, t_R, was also considered in the design. This value represents the time it takes for the closed-loop system to come within 10% of the desired level, based on the squared error computation. Figure 5.8 displays the response time simulation results, again with the minimum amplitude in Figure 5.8a and the maximum amplitude in Figure 5.8b. Note that the plateau regions seen at 3 s imply that the closed-loop system did not come settle with those corresponding gains during the simulation. Also, as with the cumulative error, the response time metric is minimally dependent on temperature, with $7.8 < k_I < 8.6$ at 0.8 mm and $0.8 < k_I < 1.0$ at 3.4 mm, but it does show a large dependence on displacement amplitude. Conveniently, the

optimal control gain from these two metrics nearly coincides at each of the amplitude and temperature settings. Figure 5.9a illustrates this at 30°C and 3.4 mm.

To more closely examine the amplitude dependency of the control gains, the optimal values from each of the two metrics are shown overlaying each other in Figure 5.9b for the 30°C condition. Each point in this figure represents the minimum value of the associated metric, as shown in the previous set of figures. It is clear here that the optimal integral gains follow the same trend of high gain at small amplitude and low gain at large amplitude, and the gain values are nearly equivalent at each amplitude. Based on this similarity, an average value of k_I could be used between J and t_R. This does not consider the large variation with amplitude, however, which could potentially cause a decrease in performance for a controller with a fixed gain. Hence, at this point, the decision was made to consider two closed-loop systems. The first was a simple integral controller with a single gain, that being the average value over the amplitude range of interest, and the second was a gain scheduling integral controller, where the value of the gain would change using the real-time amplitude estimate as the scheduling variable

$$k_I = k_I(X) \tag{5.18}$$

Recall that there is little variation in the optimal gains in the temperature range of interest. Figure 5.10 has been included to show how the controller will be modified to account for an amplitude-dependent gain.

Simulations were performed to assess the performance of the closed-loop systems. Both were able to track the target energy dissipation profile with negligible error, which is an improvement over the gain scheduled system that had a maximum

error near 10%. The difference between these two systems was the response time, and this is portrayed in Figure 5.11 at an amplitude of 0.8 mm and 30ºC. The fixed gain value in these simulations is k_I = 2.8 A/Js and the scheduled gain is k_I(0.8 mm) = 8.3 A/Js. As expected, the figure shows that the scheduled gain controller allows the damper system to settle at the reference dissipation level faster (~264 ms) than the fixed gain controller (~1.41 s). This provides justification for the consideration of a gain scheduling controller. Also, note that the oscillations seen in the response are periodic with the damper excitation frequency (3.8 Hz) and are artifacts of the averaging that takes place to estimate the energy dissipation and amplitude. The oscillation amplitude shown here is approximately 4% of the target dissipation value.

5.4 Experimental Set up

Displacement and force measurements were collected from an MTS machine through its analog readout ports and then passed through analog-to-digital converters of a dSPACE DS1103 board. One thermocouple was installed inside the MRFE damper, submerged in the fluid, and was conditioned by an Omega CNi3253 temperature/process controller to produce another signal that was recorded with dSPACE. The thermal input to the damper was supplied by an Applied Test Systems, Inc. temperature control system and an environmental chamber around the damper. The control signal became the output from a digital-to-analog dSPACE DS1103 board and fed an AE Techron LVC 623 linear amplifier, which generated the desired current signal to the MRFE damper. A proportional voltage signal was also an output of the amplifier that allowed real-time monitoring of the current in dSPACE and ControlDesk. The key components of the test setup are shown in Figure 5.12.

While the control simulations were performed at constant displacement amplitudes and temperatures, it is not likely that this is a close approximation to what a typical lag damper would experience during a mission. Accordingly, a varying displacement amplitude profile was designed that spanned the range of tested amplitudes. Figure 5.13 shows the amplitude variations. Seven sinusoidal amplitudes were selected to provide an adequate measure of the control system performance at the Lag/rev frequency of 3.8 Hz, with the transition between each occurring as a step change. Note that the relative increase or decrease is varied, as well. Each amplitude completes 50 cycles before making a step change to the next amplitude level, giving a total of 350 cycles per test (approximately 90 second duration). Since the temperature cannot vary substantially over this length of time, a number of tests were conducted in succession while the temperature slowly increased from ambient (~27ºC) to 55ºC, using the same amplitude profile for each.

5.5 Control Evaluation Results

5.5.1 Gain Scheduled Controller Performance

Figure 5.14a shows the ability of the gain scheduled control system to restore performance losses in the passive damper at high temperature. It is observed that for the field-off test, the current simply remains at 0 A for the entire test, but when the controller is active, it follows the designed profile based on amplitude estimates. There are also spikes in the current signals here, but this is due to the testing machine, which must momentarily stop before switching excitation amplitudes. However, the controller computations continue to take place with the result shown.

Figure 5.14b shows how the gain scheduled controller performs over the tested temperature range. In the field-off (no control) condition, there is a clear trend in the damper of decreasing energy dissipation as the temperature increases, and this has been noted previously in temperature characterization data (see Chapter 4). The controlled results show that damping loss compensation was achieved with the MRFE damper using gain scheduled control. The maximum error for the controlled results over the entire amplitude range and temperature range is only 11.8%, occurring at 53^{o}C with an amplitude of 0.8 mm. Note that the field-off energy dissipation at this test condition is below the desired point by 62.6%. The overall average deviation from the target profile for the gain scheduled controlled case is only 3.3%.

5.5.2 Closed-Loop Performance

Prior to beginning the closed-loop control evaluations, a number of individual tests were run to verify that the gains chosen from the simulations corresponded well with the experiment. While the simulation study could easily vary a number of parameters in a short time, performing the same optimization manually in the experiment would require a substantial amount of time and effort, so only the ambient temperature (30^{o}C) was used here, and only three amplitudes were considered (0.8, 1.4, 3.4 mm).

Sample results collected at 3.4 mm displacement amplitude are shown in Figure 5.15a. Considering first the value of J, it can be seen that the minimum occurs when k_I = 3, which is higher than that predicted (k_I = 1.0). The gain at which the response time metric t_R is minimum (k_I = 1.5) is closer to the predicted value (k_I = 1.0), however. Recall that the optimal value of the two performance metrics coincided

during the design simulations, which is not the case here. Since J does not vary substantially between $k_I = 1.5$ and $k_I = 3$, the decision was made to use the response time value as the ideal gain at this test condition.

It should also be mentioned that the magnitude of the performance metrics vary somewhat from the design case. While this is likely attributable to measurement noise present in the experiment and the minor discrepancies between the mathematical model and the prototype MRFE lag damper, a term was added to the controller to increase performance. The added term was a proportional gain, k_P. Accordingly, the integral gain was fixed at $k_I = 1.5$ A/Js and a number of tests were run with varying k_P values. These results are shown in Figure 5.15b for 3.4 mm and 30^{o}C. Again, the minimums of the two metrics do not coincide, but response time was given priority, so the "best" proportional gain was determined to be $k_P = 0.03$ A/J at this test condition. Important to note is the response time metric values between this figure and the last. With $k_P = 0$ (Figure 5.15b), the fastest time achieved is 0.8 s, but when $k_P = 0.03$, this response time metric drops to 0.6 s. This shows that nearly a 25% reduction was possible by adding a proportional gain to the closed-loop system.

Similar experiments were also conducted at the other two amplitudes mentioned, and the final selected gain values are displayed in Figure 5.16. The same trends are seen in both gain values, that being larger amplitudes require smaller control gains. This is also the general trend that was predicted in the closed-loop control simulations, but it appears to be more linear here. Since the gain values do appear to vary linearly with amplitude, the average values were the designated closed-loop control gains for the first experimental evaluation. A loss in performance is certainly

expected (being more pronounced at the extremes), but this is one of the trade-offs that must be made to maintain a simpler control strategy. The fixed gain control parameters are hence, k_P = 0.31 A/J and k_I = 4.75 A/Js. For the gain scheduling version, the values in Figure 5.16 were used in interpolation tables and were selected with the FIR filter that estimates displacement amplitude.

An example data set from the experimental closed-loop evaluations is shown in Figure 5.17 for 51^{o}C. This data is for the gain scheduling controller, though the fixed gain controller performed quite similarly. The controlled response overlays the reference signal for the majority of the time at each amplitude level, with the exception of the transition periods. Although the amplitude changes are pre-programmed into the test machine, recall that there is a momentary stop between changes that causes a spike in the estimates. The closed-loop design indicated that less than 1 A would be needed for proper tracking, so it should be noted here that the current was limited to 1.5 A during these experiments to provide some margin.

Figure 5.18a highlights the performance of the closed-loop systems. Since the energy dissipated data points represent time and temperature averaged values at each amplitude, it should be noted that the largest time-averaged or steady-state error calculated at any amplitude or temperature condition was less than 0.2%. This is to be expected with the control technique used here, however. The PI controller will continuously adjust the control signal until the error (input to controller) becomes zero. This means that the error will vanish eventually, but this brings up the issue of response time and was ultimately why two closed-loop systems were tested.

Figure 5.18b provides a picture of how the two closed-loop techniques compare in terms of response time across the amplitude range tested. Each data point shown represents the average across all temperatures at its corresponding amplitude, where it can be seen that all are around 1 s. There are two amplitudes where the scheduled gains actually cause a slower system response (1.4 mm and 2.8 mm). This was unexpected, but when looking back at the time history data, it is these two amplitudes that correspond to the largest two amplitude decreases. With the test machine used in the experiments, its inability to smoothly transition from one amplitude to the next without first momentarily stopping, and the control system's continuous calculations, this leads to impulsive estimates of the amplitude and damping, which also cause control current saturation. This effect was largest in both gain scheduled and closed-loop at these two amplitudes, as well. The gain scheduling technique was employed after completing the fixed gain experiments in an attempt to increase the speed of response in bringing the energy dissipation of the prototype MRFE damper to a desired level. While this was successful at 5 of the 7 amplitudes tested, the margin of the speed increase (settling time decrease) was relatively small.

5.6 Conclusion

A semi-active, fluid-elastomeric lag damper with field-controllable magnetorheological fluid was evaluated for its capability to track a reference damping profile and restore performance losses due to increasing temperatures. Gain scheduled and closed-loop control techniques were investigated in this fixed-frame study using a modified Bell 430 lag damper (manufactured by Lord). A hydromechanical model of the damper behavior was used in designing the controllers, and this proved effective

in preparing for experimental evaluations. Measured results indicated that the gain scheduled (look-up table) and closed-loop (PI and gain scheduled PI) control schemes had the ability to compensate for changes in displacement amplitude and temperature, with the two closed-loop systems demonstrating superior tracking capability over the gain scheduled system. Additionally, the ability of the control systems, designed using the hydromechanical model, to perform well experimentally offers validation of the model form. Thus, the chapter demonstrated the feasibility or potential of the MRFE damper in tracking damping requirements in the fixed frame, as amplitude and temperature were varied.

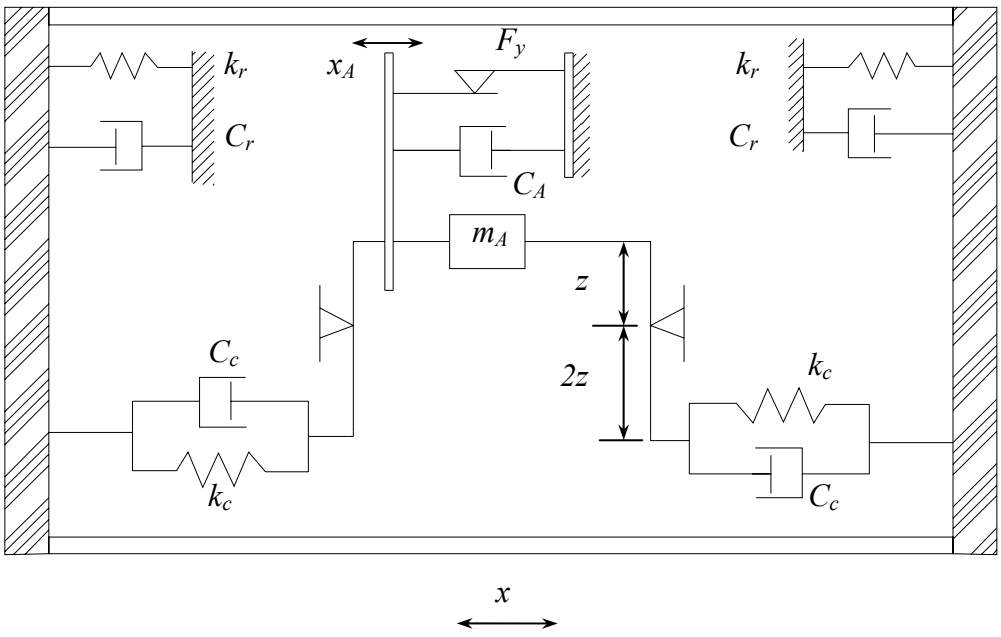

Figure 5.1: Analogous mechanical system of the hydromechanical model of the MRFE damper

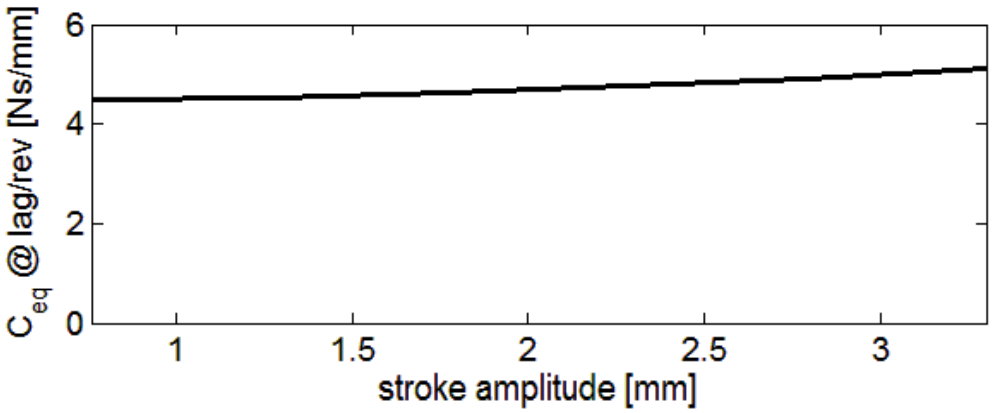

(a) Target equivalent damping

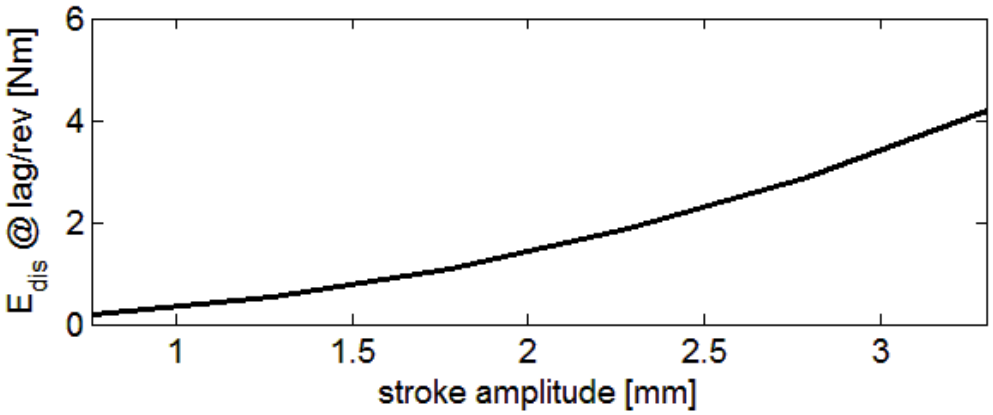

(b) Target energy dissipation per cycle

Figure 5.2: Target equivalent damping and energy dissipation per cycle

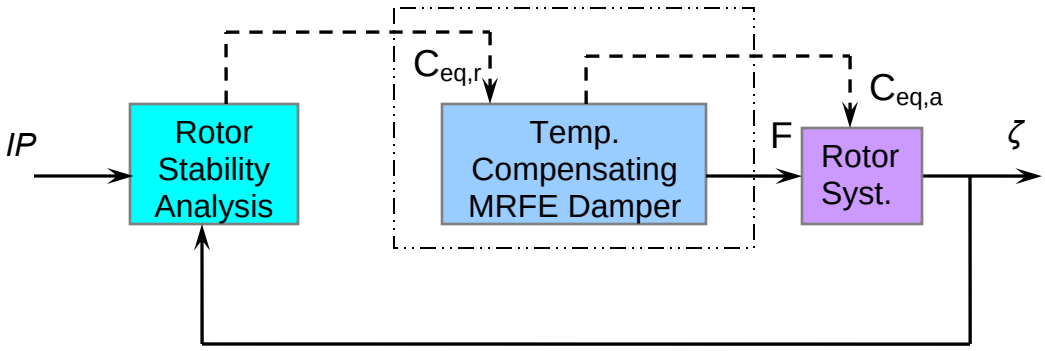

(a) Simplified lag mode stability approach for gain scheduled control

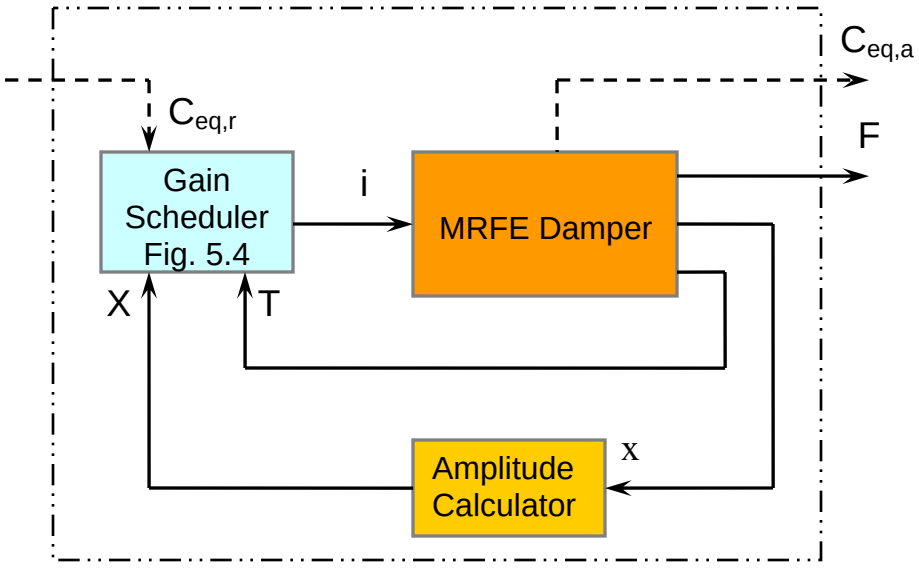

(b) Temperature compensating MRFE damper: gain scheduled

Figure 5.3: Gain scheduled control approach

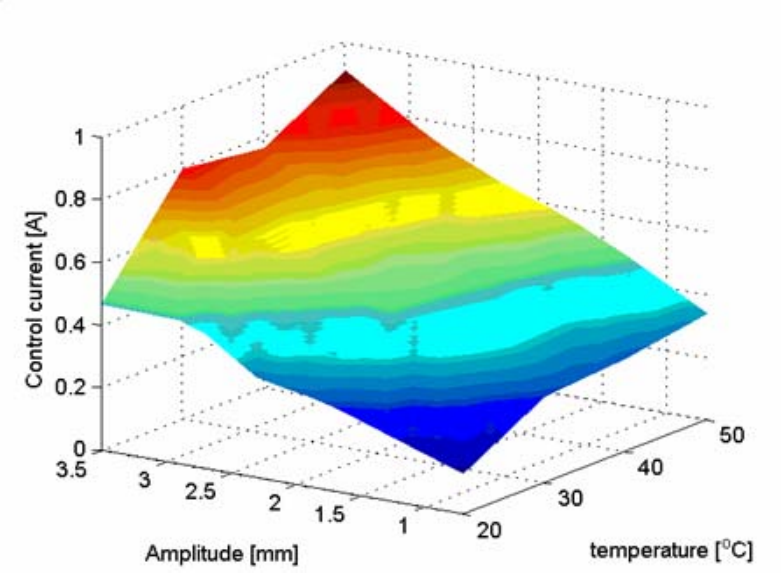

(a) Range of database

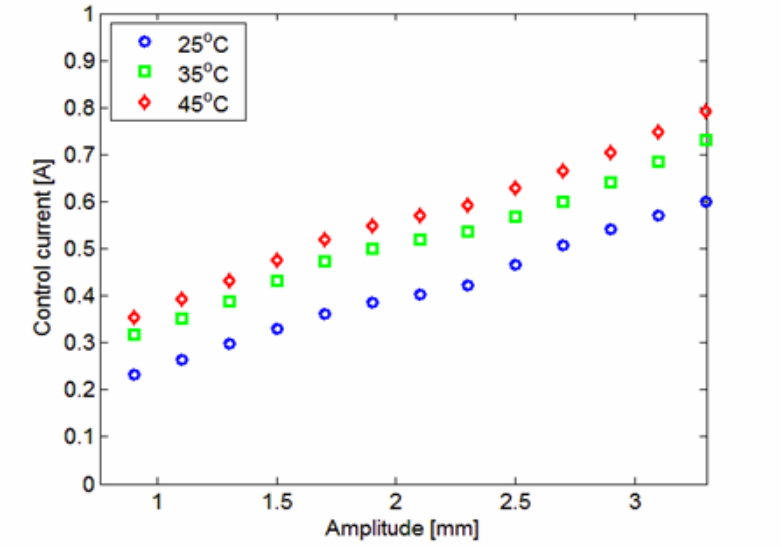

(b) Distinct temperature profile

Figure 5.4: Gain scheduled control parameterization

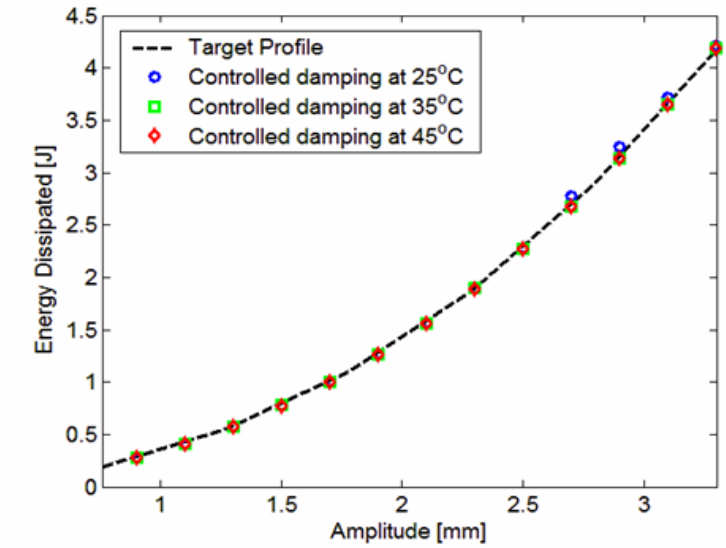

Figure 5.5: Gain scheduled control simulation results at lag/rev

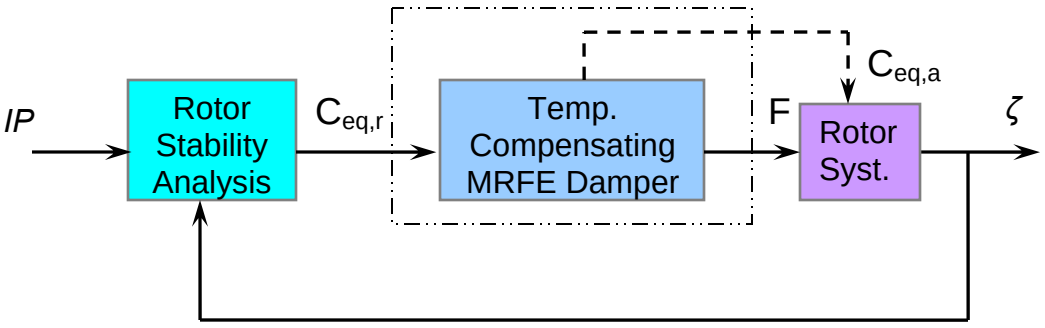

(a) Simplified lag mode stability approach for close loop control

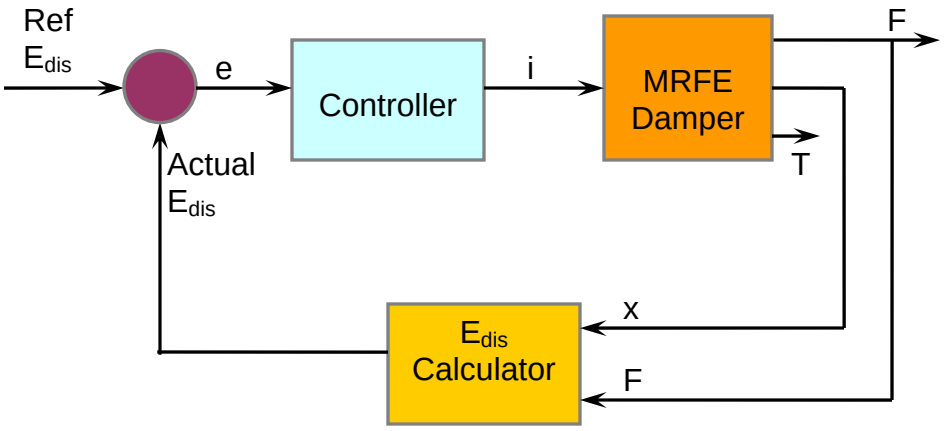

(b) Temperature compensating MRFE damper: Closed loop

Figure 5.6: Closed-loop control approach

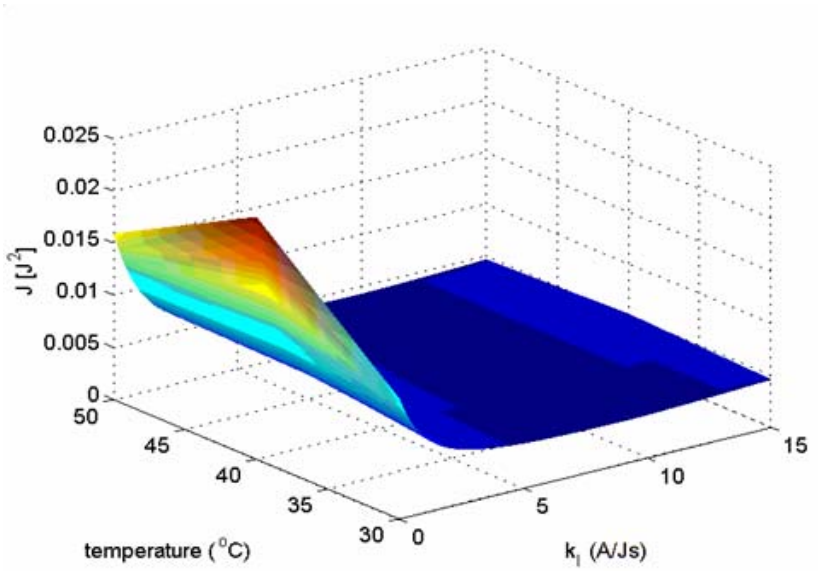

(a) Amplitude 0.80 mm

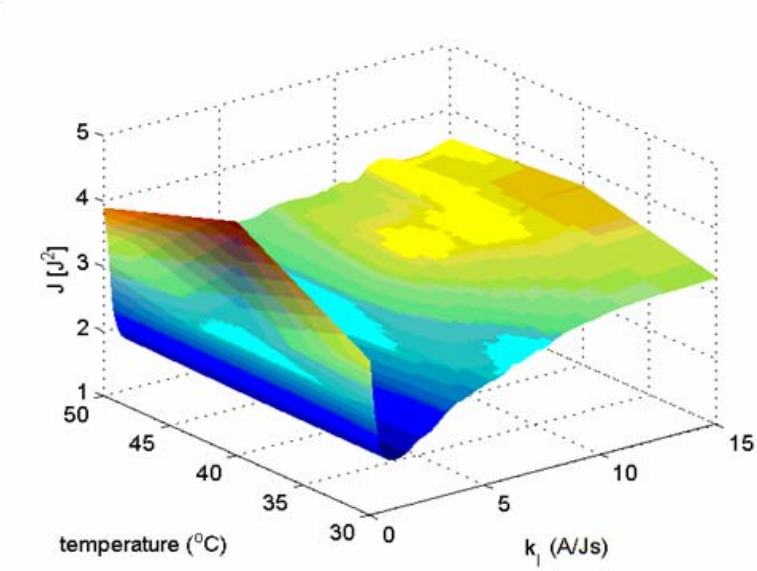

(b) Amplitude 3.4 mm

Figure 5.7: Integral gain tuning using error metric

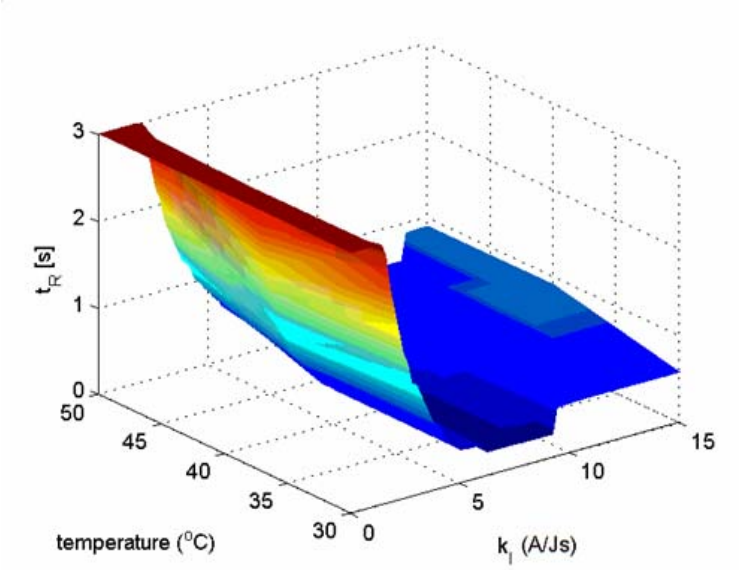

(a) Amplitude 0.80 mm

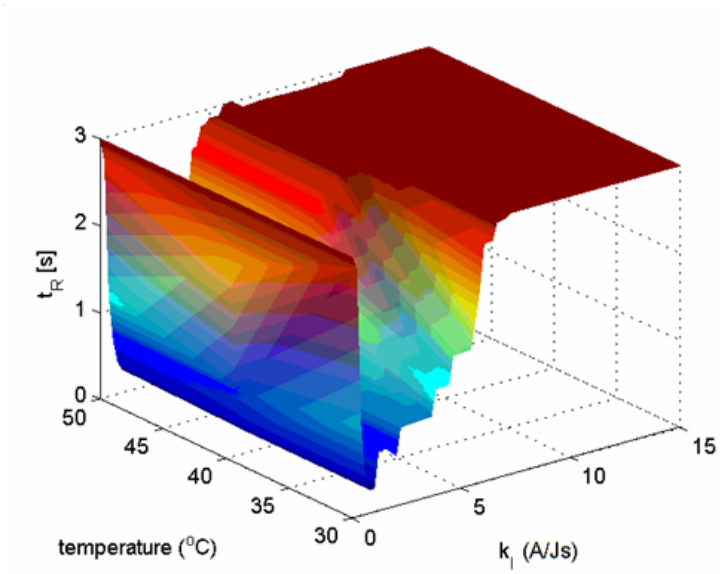

(b) Amplitude 3.4 mm

Figure 5.8: Integral gain tuning using response time

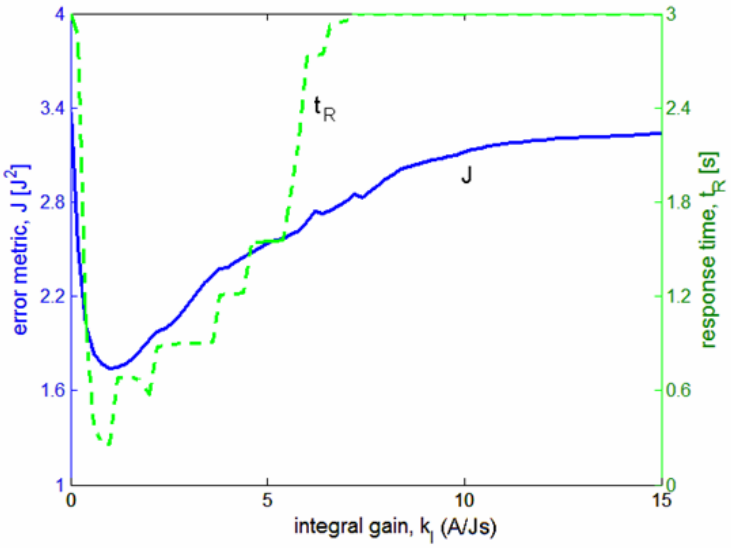

(a) At 30ºC and 3.4 mm

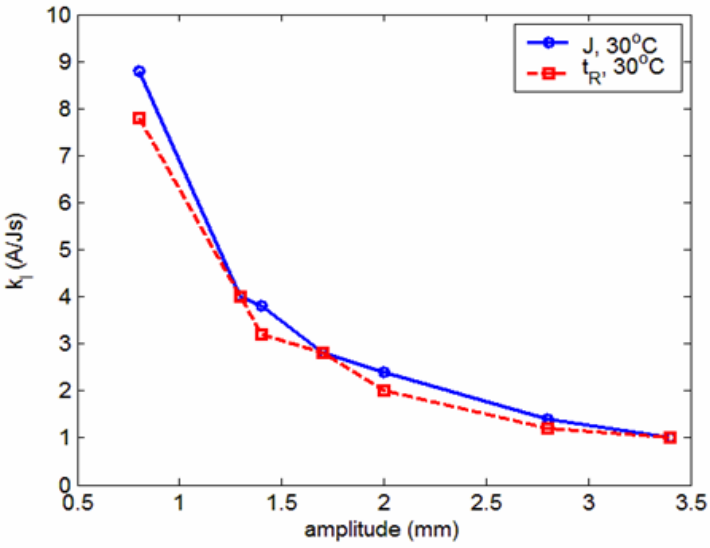

(b) As a function of amplitude

Figure 5.9: Integral gain tuning results

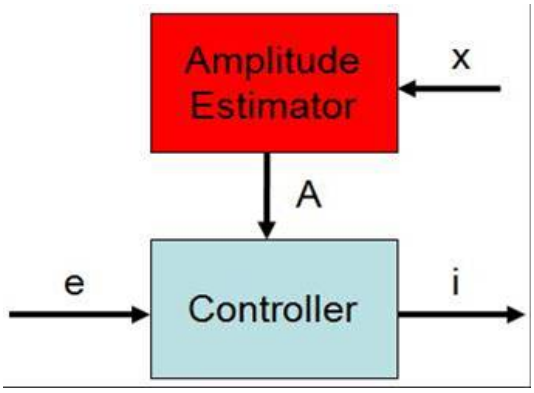

Figure 5.10: Gain scheduling closed-loop controller approach

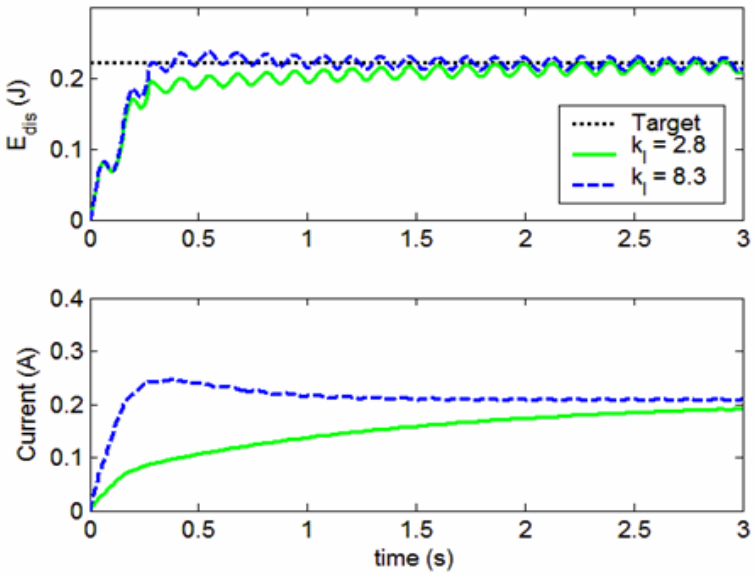

Figure 5.11: Performance comparison of closed-loop systems, 0.8 mm and 30ºC

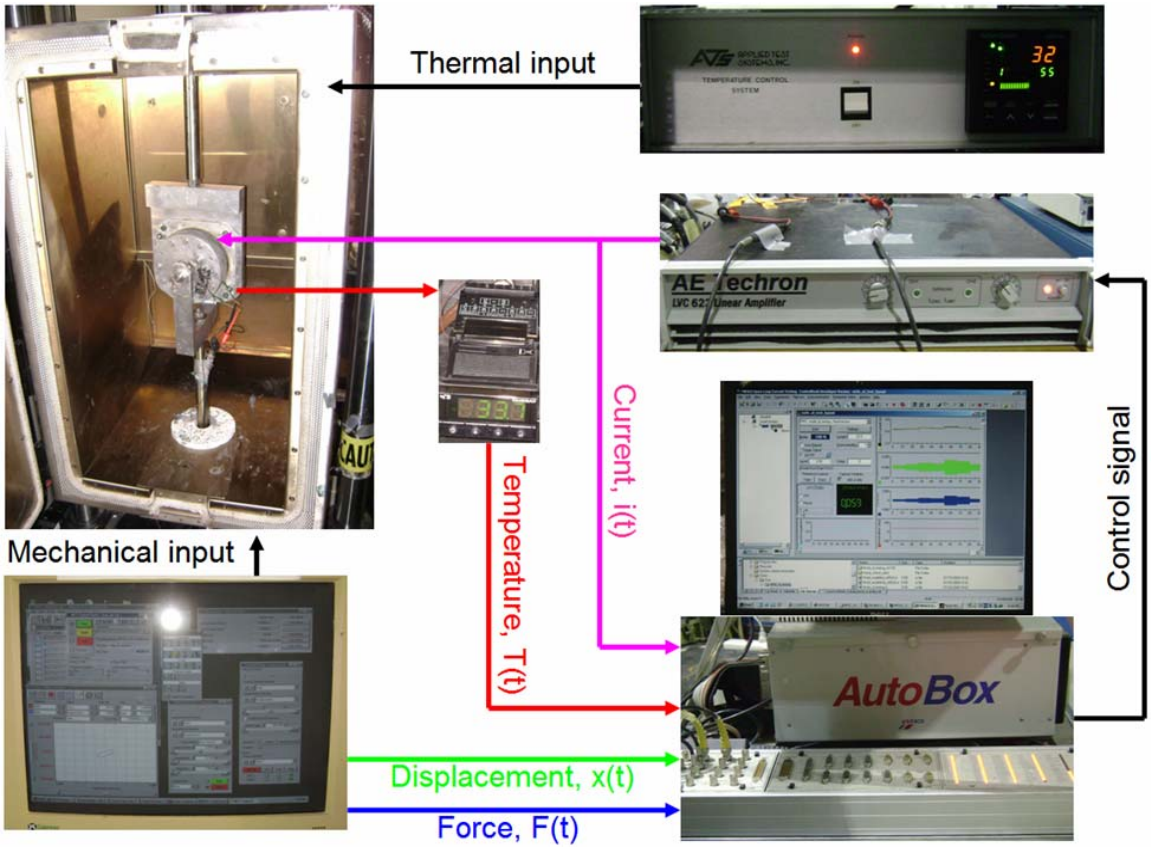

Figure 5.12: Experimental setup for MRFE damper control evaluations

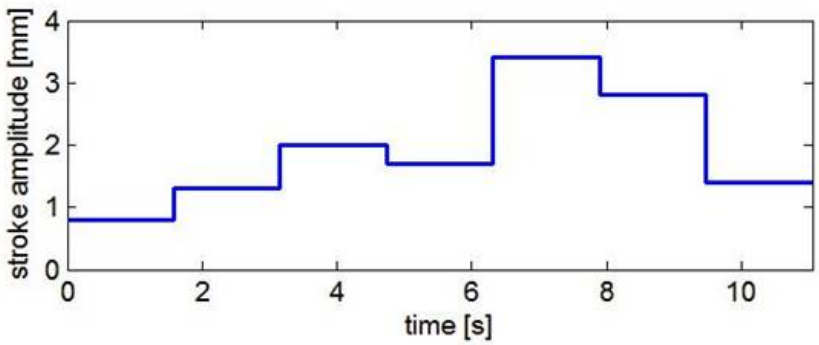

Figure 5.13: Designed displacement amplitude variation

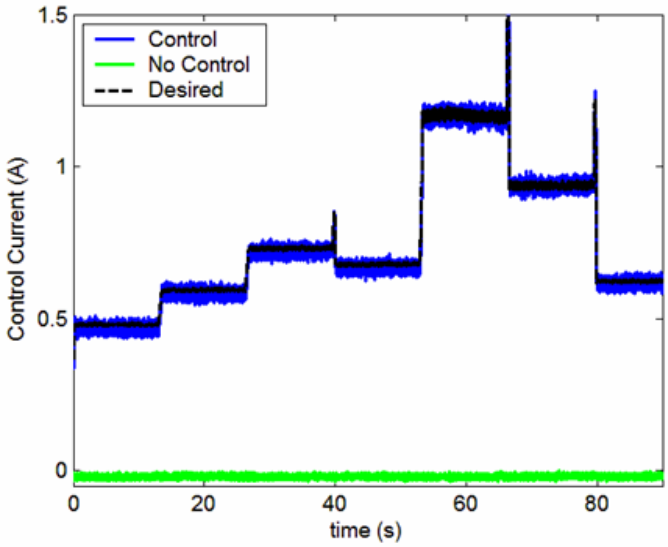

(a) Control current at 53ºC

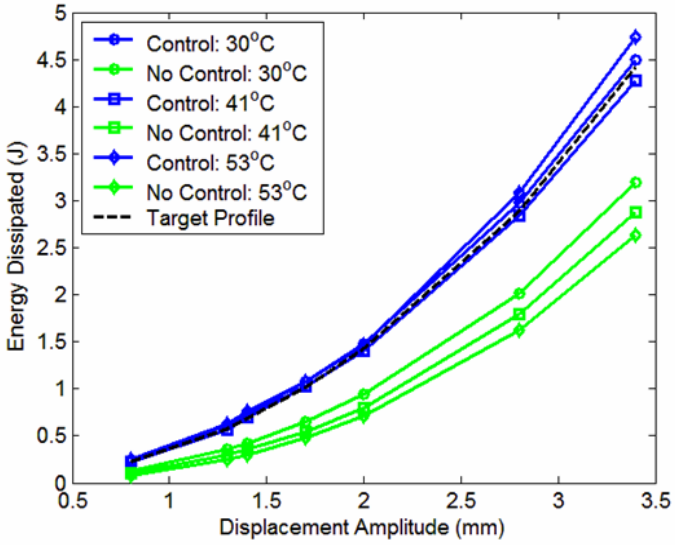

(b) Energy dissipation profile

Figure 5.14: Experimental results from gain scheduled control test

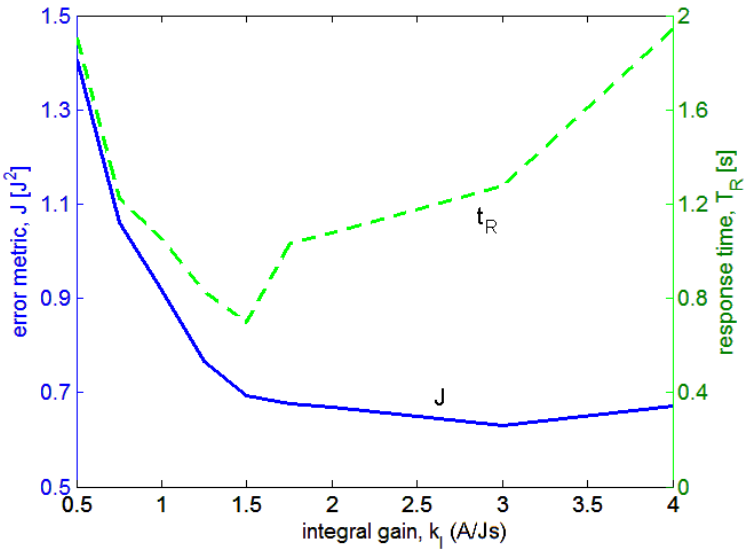

(a) Integral gain

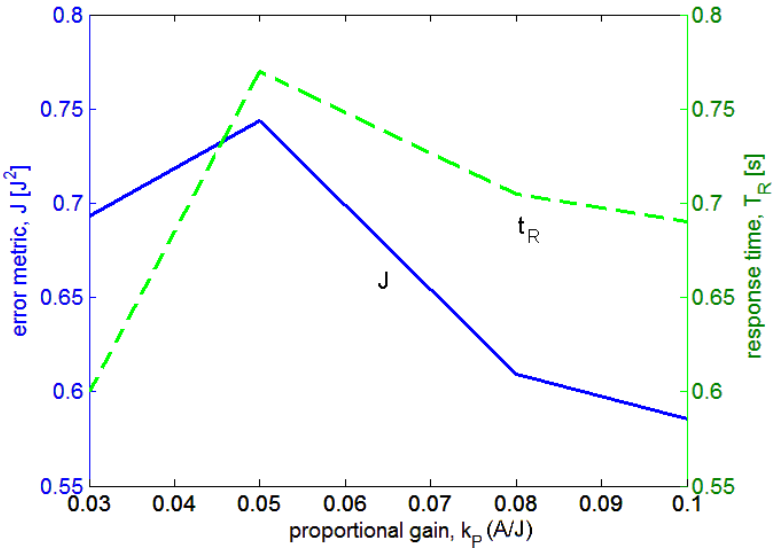

(b) Proportional gain

Figure 5.15: Experimental gain tuning, 3.4 mm and 30^{o}C

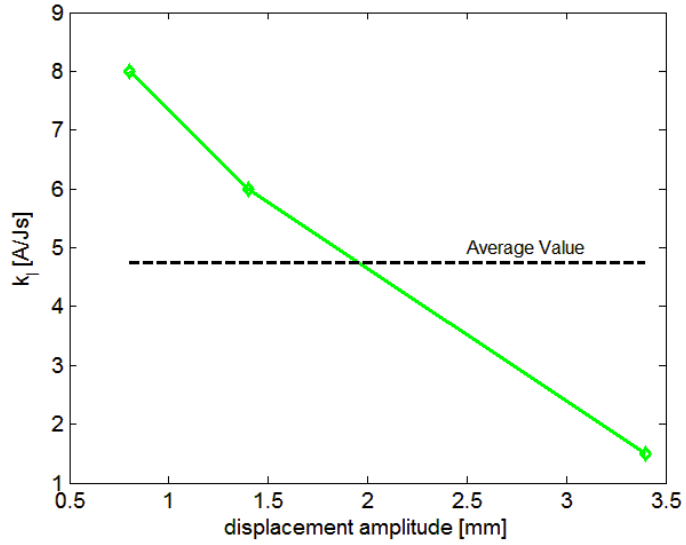

(a) Integral gain

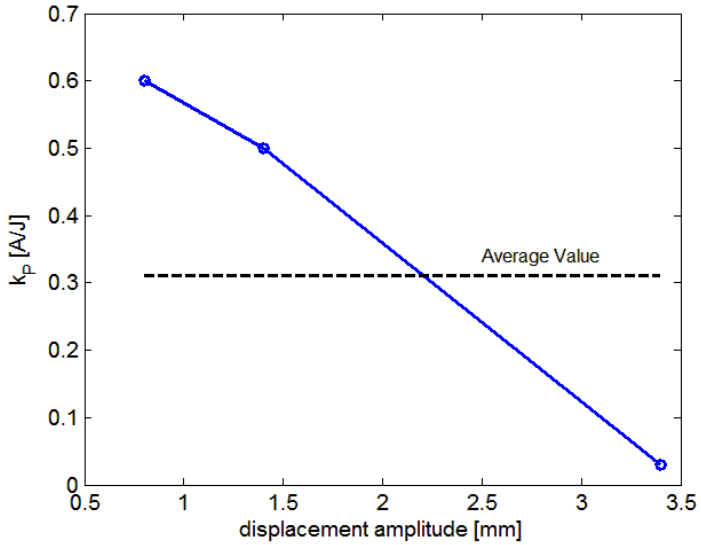

(b) Proportional gain

Figure 5.16: Experimental closed-loop gain tuning at 30ºC

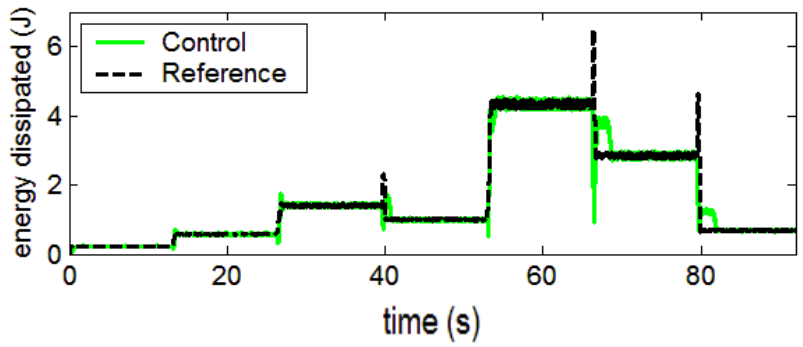

(a) Energy dissipated

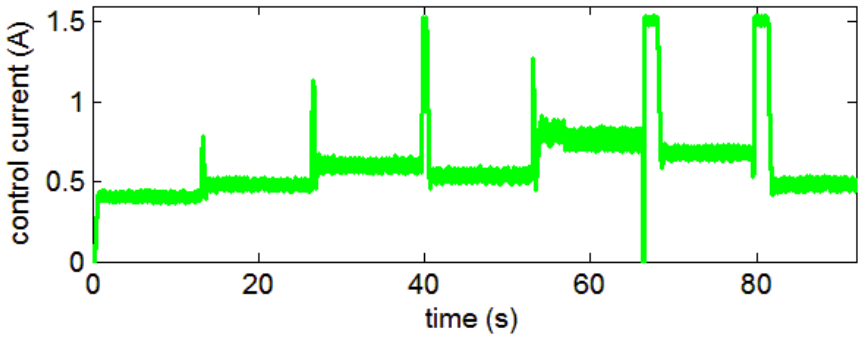

(b) Control Current

Figure 5.17: Experimental closed-loop gain scheduling results at 51ºC

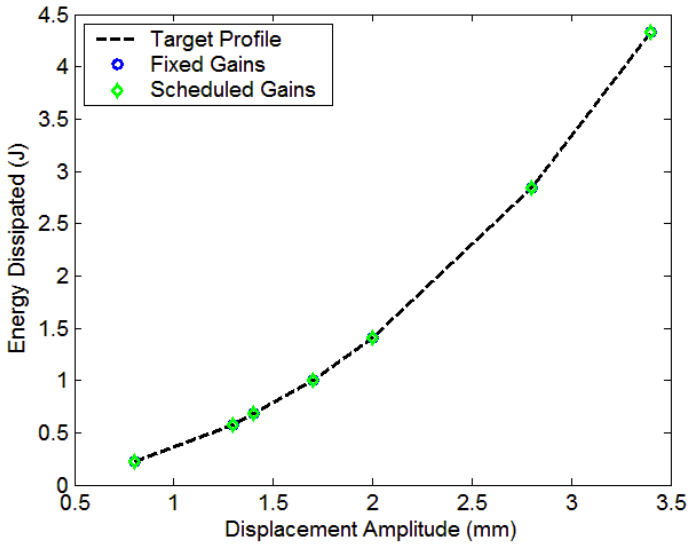

(a) Energy dissipation

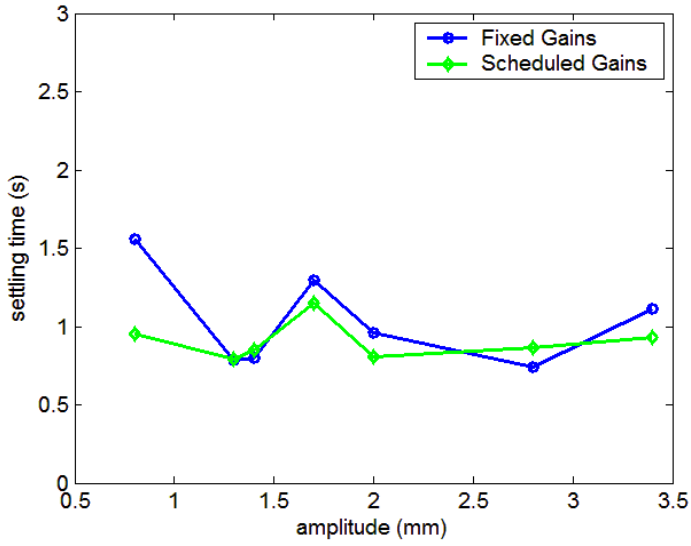

(b) Settling time

Figure 5.18: Experimental results from closed-loop MRFE control tests

Chapter 6: Summary and Conclusions

This research focused on the development and evaluation of an adaptive MRFE lag damper technology and its potential to augment helicopter rotor stability by providing adjustable and controlled damping. The two main objectives accomplished in this research include the experimental evaluation of the snubber type MRFE lag damper and modeling of damper response. Initially, MRFE damper configuration and design parameters were evaluated in the potential application of the MRFE damper in lead-lag damping augmentation. The prototype MRFE damper was able to demonstrate that a fail safe lag damping, control of single and double frequency losses and control of temperature related damping degradation. The specific contribution in developing and evaluating MRFE dampers are:

1) Design, development and fabrication of a round-stack or snubber type magnetorheological fluid elastomeric lag damper
2) Experimental evaluation of the MRFE damper in its potential to provide controllable damping augmentation at different lag mode excitations
3) Experimental investigation of the MRFE damper in its capability in providing required damping augmentation at different operating temperatures.

Second, an extensive MRFE damper characterization was performed, and a new modeling strategy was developed to provide significant contribution in modeling coupled MR fluid elastomeric systems, which previous models did not address. In

addition, the model was able to describe the dependence of damper performance on amplitude, frequency and temperature. Using this model, response modeling of a passive fluid-elastomeric (FE) and MRFE dampers were conducted and model's fidelity evaluated. These original contributions can be described as:

1) Development of a hydromechanical model to describe hysteretic behavior demonstrated by the passive baseline FE damper. This time domain model is developed based on lumped parameter approach, which takes into account the physical hydraulic and mechanical phenomenon taking place in each lump or section. Model parameters are fundamentally dependent on damper geometry and material properties, which employ physical parameters such as inertia, damping, and compliances. Using the hydromechanical approach, the damper model can describe amplitude, frequency and temperature dependent behavior of the MRFE damper.
2) Development of a hydromechanical model to describe the non-linear hysteretic behavior demonstrated by the MRFE damper. This time domain model is developed by expanding the hydromechanical model developed in 1 to include the magnetorheological effects demonstrated by the MRFE damper. Thus, this lumped parameter approach takes also into account the physical hydraulic and mechanical, and plus magnetorheological phenomenon taking place in each lump or section. Model parameters are also fundamentally dependent on damper geometry and material properties, which employ physical parameters such as inertia, damping, yield force and compliances. Using the hydromechanical approach, the damper model can describe

amplitude, frequency and temperature dependent behavior of the MRFE damper.

3) Evaluation of the hydromechanical model in predicting damper dynamic behavior under single and dual frequency excitations and varying operating temperature conditions.
4) The potential determination of model parameters *a priori,* which will help in designing and predicting the expected damper performance beforehand.

In the proceeding sections, the significant modeling contributions made through this research as outlined above are briefly discussed and summarized. Then, some future work that would help in the advancement of the state-of-the-art MRFE damping technology is outlined.

6.1 FE and MRFE Damper Modeling

In Chapters 2 and 3, a hydromechanical model for the snubber type FE and MRFE dampers was developed. The hydromechanical model is a lumped parameter approach. The hydromechanical model is a convenient modeling approach that deals with time-varying behavior of connected components or lumps of a system, assuming no span-wise variation within each component or lump. The hydromechanical model can delineate the physical flow motion of the system and accurately describe the non-linear hysteretic behavior of the FE and MRFE dampers. The model is a design based model which portrays the damper system with a series of lumped hydraulic, mechanical and magnetorheological (MRFE damper only) components. In the current FE and MRFE lag damper configuration, the hydromechanical model is able to account for the coupling between the elastomeric material and the hydraulic (FE

damper) or hydraulic+MR (MRFE damper) system, which is manifested through chamber compliances. The model employs physical parameters such as inertia, damping, yield force and compliances that are dependent on damper geometry and material properties of components.

The model was derived using simplified conservation of mass and momentum equations. Certain simplifying assumptions regarding the nature of the flow, such as incompressible flow assumption, were made. Three fundamental sets of equations were formulated: 1) expression for the interaction between elastomer shear deformation and pressure in volume chambers, 2) an equation for the losses in passages between the volume chambers and, 3) a continuity equation relating volume flow rates between volume chambers. The model was able to introduce a Bingham-type Coulomb friction element to account for the MR effect. In addition to the compliance, the model was able to account for the elastomeric damping due to the volumetric expansion of the elastomeric volume chambers under pressure. Further, the model was able to relate, through a transfer function, the losses incurred in the two flow passages present in the damper, which essentially simplified the mechanical analogy of the system from a 3DOF system into a 2DOF system.

The model has eight independent (seven for FE) variables and two dependent parameter, which basically are a combination of the independent variables. Initially at varying FE temperature and ambient MRFE temperature condition, most of these parameters were model estimated through an optimization routine. The model reconstructed forced response correlated very well with the single and dual frequency experimental results.

6.2 MRFE Modeling with Temperature Effects

In Chapters 2 and 3, a hydromechanical model was formulated to characterized the performances of FE and MRFE dampers. The model, which has eight independent and two dependent parameters, was able to simulate damper performance accurately. However, more than one independent parameter (three for FE and four for MRFE) was model estimated through an optimization routine. Due to the high number and the non-linear nature of optimized variables, the optimization task was cumbersome and time consuming. In addition, optimized parameters could result in values that are not the true or realistic values, since the routine is searching for a local minimum. To address this situation, a simulated annealing optimization was also incorporated; however, this made the optimization routine more arduous and plus it also does not also guarantee the real values parameters. In order to minimize model optimized parameters, separate tests and analysis were conducted to determine material property dependent parameters. Since model parameters are fundamentally functions of damper geometry and material property, temperature effects will only cause the latter to change. Thus, in Chapter 4, most material properties at each test temperature are initially estimated either through manufacturer's data or material testing. Some of these parameters are reasonably scaled to accurately simulate the measured hysteretic force-displacement and force-velocity histories of the MRFE damper under single and dual frequency excitations. The reasoning behind the scaling was also discussed. Thus, all except one model parameter was estimated beforehand and plugged into the model to simulate damper performance. The results have shown that the model was able to accurately predict the damper response for the range of amplitude, frequency

and temperature tested. The important point is that the model was able to show the potential in determining model parameters *a priori*, and predict expected damper performance and make sure damping requirements are met before development and production.

6.3 Temperature Compensation of MRFE Damper

The semi-active Magneto-Rheological Fluid-Elastic (MRFE) device has been assembled and evaluated in control experiments to demonstrate its utility to compensate for measured changes as a helicopter lag damper. The baseline FE damper used in this study was a Fluidlastic® FL-1030-8 damper manufactured by Lord Corporation for the Bell 430 helicopter. This damper was disassembled and modified to include two internal magnetorheological control valves, and the existing hydraulic fluid was replaced with magnetorheological fluid. Hence, the resulting prototype damper is a retro-fit design that can easily be installed in a test rotor in future evaluations. The MRFE damper was subject to extensive performance characterization at displacement amplitudes ranging from 0.8 mm to 3.4 mm, temperatures ranging from 20ºC to 55ºC, and control currents up to 1.0 A. Using this database and a hydromechanical model of the damper, control systems were designed to track a reference damping profile, which is a function of amplitude only, in the presence of measured amplitude and temperature variations at the rotor lag/rev frequency (3.8 Hz). Both gain scheduled (interpolating look-up table) and closed-loop (proportional-integral and gain scheduling) techniques were employed in simulations and experiments. The results demonstrated that all of the control schemes were effective, though minimum tracking error was achieved with the

closed-loop systems. Comparing the two closed-loop systems, the gain scheduling controller provided a faster response overall, but the improvement was marginal.

6.4 Future Work

6.4.1 Hydromechanical Modeling of MRFE Damper

In this study, the hydromechanical model has shown great promise in modeling the coupled system of the MRFE lag damper. The model can very well capture the non-linear hysteretic behavior of the damper over the amplitude, frequency and temperature range tested. Model parameters are shown to be fundamentally dependent on damper geometry and material property, which can be known from manufacturer's data sheet or simple material testing. However, the capability of the model over a broader frequency range, and for different scale factors, has not been studied. The geometric deformation of the elastomer and its effect of the equivalent piston area was not also investigated in detail. In addition, the model was formulated for low speed, laminar flow analysis. To conduct a more detailed evaluation of the model performance, and improve the model performance, the following task should be undertaken in the future:

1) The hydromechanical MRFE damper model is expected to be employed in predicting damper performance from wind tunnel rotor speed condition to full scale rotor speed condition, the fidelity of the model over a broader frequency range should be evaluated. Thus, high frequency (i.e. > 10 Hz) sinusoidal excitation should be applied to the MRFE damper the experimental data should be compared to the modeling results.

2) A helicopter lag damper is exposed to a wider temperature variation than that was covered in this research. So, the MRFE damper should also be tested over a wider temperature range (i.e. -55ºF to 220ºF) and its performance evaluated. The model should also be evaluated in its ability to capture the performance variation in such a wide temperature range. A thermal shift function to account for model parameter variation due to temperature dependent material properties should also be formulated.
3) The coupling effect of elastomeric compliance, hydraulic and MR effect should also be further investigated. Especially due attention should be given to the coupling of bulge stiffness and MR yield force in designing the MR valves. Due to the in-series nature of the two systems, one parameter will affect the other. For instance, a too high yield force could completely block flow passages and could only result in a volumetric expansion of elastomeric wall, there by significantly dimensioning the damping of the system.
4) The geometric deformation of the elastomeric body of the MRFE damper based on input amplitude, internal pressure and flow resistance should further be investigated to be able to determine *a priori* the equivalent piston area, which was the only parameter that was determined through model optimization routine.
5) The model should also account for minor losses in the flow passages in a more accurate way. Minor losses involve pressure lost in the working fluid due to sudden expansion and contractions and leakage through repair edges. In addition, as flow approaches transient and turbulent flow regions, the friction

factors and the losses associated are also expected to increase, and the model should also be able to account for these added losses. These losses will be critical in predicting the damper performance at very high pumping frequencies.

6) Since future dampers will vary in size and performance depending on different rotor hub designs, the variation of the model parameters with the damper scale should be investigated such that the model can be expanded to be utilized in predicting the behavior of the MRFE damper at any given scale and configuration.
7) A comprehensive control analysis should be conducted by integrating the formulated hydromechanical model into the actual rotor stability equation and asses its controllable capability in augmenting lad damping.

6.4.2 Future Development of MRFE Damper

This preliminary research on the snubber type MRFE damper has shown a promising result in helicopter rotor damping augmentation. However, there remains a great challenge in integrating the MRFE damper system in an actual full scale rotor system. A key issue the future work should address is the refinement and improvement of damper ruggedness while operating at high centrifugal loading conditions and wide operating temperature ranges. Further, the MRFE damper should be able to provide a fail-safe operational damping by behaving as a passive damper in the event of reduced or lost power. The passive damping from the hydraulic and elastomeric components can be designed in such a way that they provide the minimum required damping that ensures rotor stability.

Based upon the database and analysis of Magnetorheological (MR) fluids and design and development of the MRFE damper, damper refinement together with a comprehensive design tool should be carried out to meet the operating conditions of a helicopter lead-lag damper system. System parameters such as magnetic field dependent yield force, viscosity, MR valve and damper geometries, mechanical and hydraulic characteristics, and power and control electronics should be examined to the first order. The damper refinement should include:

1) Devise a comprehensive MRFE design tool based on full-scale rotor system
2) Investigate different types of off-the-shelf MR fluids and elastomeric materials
3) Minimize passive or friction losses due to unnecessary and complex passage ways. In the current MRFE damper, the MR valves were threaded into the existing port holes (Figure 6.1a), which created unnecessary viscous losses. Future MR valve can be integrated into the center rubber wall, which will significantly reduce friction losses (Figure 6.1b). This, in addition, will help to design an optimal MR valve which will not be limited in dimensions due to the very small space available in volume chambers. This will make sure that the MR vale will have the optimal active valve length and diameter.
4) Minimize leakage through repair edges. Improve the quality of the center wall by having it completely molded, similar to the original FE damper.
5) Maximize internal pressure to avoid the detrimental effects of entrapped air. This could be achieved through an installation tool design which can be mounted on an MTS machine to compress elastomer and create required inner

pressure without the need of manual torque application, which can be very difficult and in addition damages components.

6) Conduct single and dual frequency harmonic excitation in a rotating plane (eg. vacuum chamber) and wind tunnel to evaluate damper performance and validate design tools.
7) Assessment of long term fatigue, in-service MR fluid thickening, erosion of internal parts, thermal dissipation and operating temperature effects.

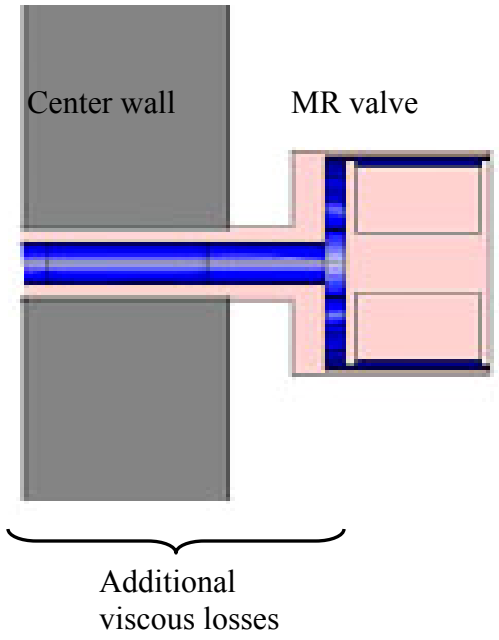

(a) Current threaded type MR valve design

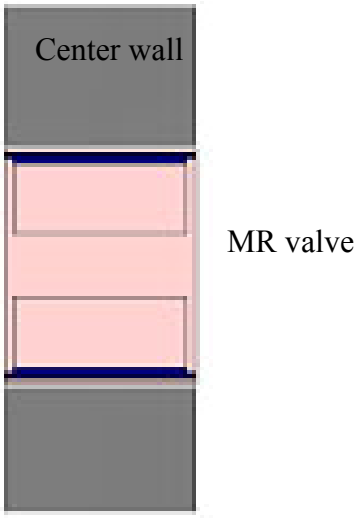

(b) Conceptual embedded type MR valve design

Figure 6.1: Current and future MRFE damper design details

Appendix A: Dimorphic Magnetorheological Fluids: Exploiting Partial Substitution of Microspheres by Nanowires

A.1 Introduction

Magnetorheological fluids typically consist of spherical micron-sized magnetic particles (microspheres) suspended in a liquid medium such as silicone or hydraulic oil [A1-A2]. Their rheological properties, and thus their yield stresses and viscosities, can be rapidly and continuously controlled by varying the applied magnetic field. Conventional MR fluids utilize spherical micron-sized iron particles at high weight fractions and are shown to exhibit high yield stresses, up to 100 KPa [A1, A3-A5]. The fast response and controllability of MR fluids [A6] make them very attractive for implementation in semi-active smart vibration-absorption systems [A7], primary vehicle suspension systems [A8], landing gear for aircraft [A9-A11], adaptive crew seats for vibration [A12-A14] and shock isolation [A15-A16].

Under a magnetic field, the suspended iron particles position themselves nearly parallel with the magnetic field lines, causing them to form a series of chain structures. A finite stress must be applied to break these chained structures and initiate flow, thus giving rise to the apparent yield stress characteristic of MR fluids. Even though conventional MR fluids with spherical microparticles at high weight fractions exhibit high yield stresses, they are very prone to particle sedimentation under no- or low-magnetic field conditions and in the absence of constant or frequent mixing. This behavior arises from the dominance of gravitational forces on larger

particles as a result of their higher density compared to the carrier fluid [A17]. The iron particles sediment and agglomerate at the bottom of the container, making the suspension no longer effective. Once particles sediment, remnant magnetism that is present in particles results in undesired tightly bound particle clusters, which makes re-dispersion very difficult [A17-A18]. In addition, particles could also be subjected to van de Waals forces, which further increases interparticle attraction [A5, A17]. Different additives and coatings have been studied to mitigate sedimentation of particles in MR fluids. Some of these include adding thixotropic agents such as silica nanoparticles [A18-A19], nanoscale additives [A20], sub-micron sized filler organo-clay additives [A21-A22] and organic poly (vinyl butyral) (PVB) coating [A23-A24].

Nano-sized particles have also been utilized to overcome particle sedimentation while maintaining the magnetorheological properties of MR fluids [A4-A5, A25-A28]. Nanoparticles tend to settle slowly, or remain suspended indefinitely (ferrofluids), by Brownian motion [A28-A30]. Ferrofluids utilize nanoparticles of less than 10 nm, and do not exhibit a significant yield stress [A28-A29, A31]. Nanoparticles based MR fluids have been formulated from three perspectives: MR fluids employing nanoparticles [A25, A28], extremely bimodal MR fluids [A27, A32-A33] and bidesperse MR fluids [A4-A5, A34]. In the first group, nanoparticles (10 nm – 100 nm) were mixed in a fluid medium to alleviate particle sedimentation while maintaining functional level of yield stress. The resulting yield stress of these fluids was significantly reduced when compared with MR fluids made of micron-sized particles at same volume fraction. Extreme bimodal MR fluids are suspensions of iron microparticles in a ferrofluid with nanoparticles less or equal to 10 nm. Ginder *et al*

[A26] dispersed 2-10 μm iron microparticles in a ferrofluid (< 10 nm magnetic particles) to obtain extremely bimodal MR fluids. These MR fluids are shown to have yield stresses as high as 200 KPa and the nominal volume fraction of iron powder was 50 vol% (>90 wt%). Viota *et al* [A33] utilized iron microparticles (~1.45 μm), nanoparticles (~9 nm) and water as carrier fluid. The study found that the addition of increasing concentration of nano-magnetite to suspensions containing micrometer sized magnetite provokes a substantial increase in weak-field susceptibility, coercivity of the suspension and saturation magnetization of the extremely bimodal MR fluids. Lopez-Lopez *et al* [A27] investigated bimodal MR fluids containing iron microparticles (~0.93 nm) dispersed in ferrofluids composed of nanoparticles (~7.8 nm) in kerosene. This study demonstrated that as the concentration of nanoparticles in kerosene based ferrofluids increases, the settling rate of microparticles suspended in the ferrofluid was reduced. Partial substitution of micronparticles with nanoparticles (>>10 nm) leads to bidisperse MR fluids [A4-A5, A34]. Our prior work on bidisperse MR fluids utilized nanoparticles of average sizes 28 nm [A4] and 40 nm [A34]. By substituting a portion of microparticles with nanoparticles, sedimentation of suspended particles was effectively mitigated by the re-dispersive behavior of nanoparticles in the suspension due to thermal convection (Brownian motion) [A4, A30]. But, as the nanoparticle concentration is increased, the apparent yield stress of the MR fluids declined by as much as 50% [A34].

Previous studies suggest that MR fluids utilizing non-spherical iron particles exhibit enhanced rheological properties as well as greater stability [A29, A35]. MR fluids composed strictly of iron nanowires have displayed better performance in terms

of magnetoreology and stability than corresponding fluids containing only spherical particles at similar volume fractions [A29]. Suspensions of cobalt wires have also shown a notable increase in yield stress when compared to cobalt microspheres at same volume percentage [A36]. However, these studies were limited to low particle volume fractions of 10 vol% (48 wt%) or less, thus producing small yield stresses that are largely insufficient for most dynamic applications. Due to their high wetted area and wire-to-wire interactions, it is difficult to produce and handle an all nanowire MR fluid at high vol% iron loading. As the aspect ratio of particles is increased at constant volume concentration, the viscosity of the suspension will also rise [A37]. In addition, as the concentration of particles keeps on increasing, there will no longer be enough fluid to lubricate the relative motion of particles, thus increasing viscosity to infinity [A38]. In a viscous dominated suspension, the packing density of smooth spheres is 0.68 while it drops to 0.18 for ellipsoids with an aspect ratio of 27 that are randomly aligned and no outside influences present, such as, sheer or magnetic field [A38]. In concentrated suspensions of long slender particles, the rotational, end-over-end motion of each rod is severely restricted as well as the translational motion perpendicular to the rod axis due to entanglement [A39]. This suggests that the settling velocity hindering factor is greatly increased in concentrated suspensions due to particle-particle and particle-fluid interactions. This sedimentation stability has been demonstrated for MR suspensions that contain 6 vol% of iron nanowires only, which produced fluids that did not settle even after 2 months [A29]. Thus, by replacing part of the microsphere particles of a high wt% loaded MR fluid with nanowires similar to those used in [A29], it was possible to produce dimorphic MR

fluids. These fluids were created with the aim of improving the settling properties of MR fluids while maintaining a higher vol% of ferromagnetic particles and, thus, a greater workable yield stress than fluids using strictly nanowires. In this study, we report the effect of substituting a portion of the microspheres with nanowires on the magnetorheological (yield stress and viscosity) and stability (sedimentation rate, sedimentation percentage and ease of re-dispersion) properties of MR fluids.

A.2 Magnetorheological Fluid Generation

Spherical iron particles ranging from 6 to 10 μm in diameter (Alfa Aesar) were used in this study. The iron nanowires were generated using template-based electrodeposition with commercially available anodized alumina membranes (Whatman) as templates. Iron nanowires can typically have a wire diameter ranging from 5 nm to 250 nm [A40]. The electrolytic solution consisted of 0.9 M FeSO4, 0.03 M FeCl2, 0.10 M NH4Cl, 0.01 M C6H8O6, 0.5 M H3BO3 at a pH of 3. High purity iron electrodes (99.995%) were suspended approximately 2 cm above the alumina template in the iron solutions. The nanowires were electrodeposited at a current density of 5.7 mA-cm^2 under ambient conditions without agitation. The wires were recovered by dissolving the template in a 1 M sodium hydroxide solution. Dimensional information and size distribution of the nanowires were obtained using a Hitachi S570 scanning electron microscope (SEM). These nanowires have a mean diameter of 230 nm and a length distribution of 7.6 ± 5.1 μm. Silicone oil (GE SF96-200) with a viscosity of 0.175 Pa-s was used as the carrier fluid to prepare both conventional and dimorphic MR fluids. Lecithin (2 wt% of the total metal content) was utilized to produce stable dispersions. The lecithin was thoroughly mixed with

the silicone oil before the addition of the iron particles. The MR fluids were generated according to Table A.1.

A.3 Rheological Characterization

Flow curves of the MR fluids were determined using an Anton-Paar MCR300 parallel disc rheometer equipped with an MRD180 MR cell capable of generating a controllable magnetic field up to 1 T. The magnetic field is oriented perpendicular to the parallel plates. The plates are held at a standard gap of 1 mm, and a sample of nominally 3 mL was injected into this gap. Rotational tests were carried out to establish the flow curves (shear stress vs shear rate) at specified magnetic fields. The Bingham-Plastic (BP) constitutive model was then fitted to the flow curves to determine the apparent yield stresses and viscosities of the samples. In the BP model, the total shear stress is given by:

$$\tau = \tau_y + \mu\dot{\gamma} \tag{A.1}$$

where is τ_y the yield stress, is μ the post yield viscosity and $\dot{\gamma}$ is the shear rate. The BP model predicts that in the pre-yield region, where stress is below the apparent yield stress, the fluid exhibits a rigid behavior. And in the post-yield region, the fluid exhibits a viscous flow behavior. To ensure homogeneity of the mixture, the samples were continuously mixed for 6-8 hours before testing. This technique was also employed to ensure a uniform dispersion for sedimentation testing.

A.4 Sedimentation Characterization

The magnetic properties of MR fluid particles can be exploited to characterize and quantify sedimentation velocity of these suspensions. During settling, particles

sediment towards the bottom of the container, creating a volume of supernatant fluid (the clarified carrier fluid above the sediment mudline) as seen in Figure A.1a. To quantify and compare the sedimentation velocity of conventional sphere-based MR fluids with those containing nanowires, an inductance-based solenoid sensor was constructed to track the mudline location of the settling fluid [A34, A41]. The sedimentation velocity is defined as the rate at which the mudline descends due to particle settling. As the MR fluid sediments, the mudline travels downwards, until all the iron particles fully deposit at the bottom of the container and little or no further compacting is possible. The magnetic permeability of the MR fluid enclosed by the inductive sensor solenoid is highly dependent on the volume fraction of fluid within this region. The permeability of the MR fluid enclosed within the sensor is related to the sensor inductance L by:

$$L = \frac{N^2 A \mu_0}{l} \mu_r \tag{A.2}$$

where N is the number of turns, A is cross-sectional area of the wire of the solenoid, l is solenoid length, μ_0 is magnetic permeability of vacuum and μ_r is relative permeability of the enclosed MR fluid. Thus, by measuring the rate of change of magnetic inductance of the sensor, the rate of change of the mudline position can be estimated as it traverses through the sensor height. The inductance measuring instrument is comprised of an inductance meter, the sensor assembly and a stand to mount the apparatus as shown in Figure A.1b [A34]. Using this instrument, the change in sedimentation velocity as a function of change in fluid composition was examined.

To perform these tests, the linear range between inductance and mudline location within the sensor was determined and a vertically moving reference frame was assigned, with the origin fixed at the top of the sensor and positive downwards (Figure A.1b) [A34]. With these parameters set, the sedimentation test is run between any two initial and final mudline locations x_s and x_t ($x_s < x_t$) within sensor where inductance is linear. The sedimentation velocity can then be estimated using the pre-determined inductances L_t and L_s at points x_t and x_s and continuously measured inductance $L(t)$. The sensor was moved up by x_s amount and held fixed there after and the fluid was allowed to sediment in time until inductance $L(t)$ reached L_t [A34]. At this point, the total settling height of the mudline equals (x_t - x_s). Thus, the mudline location at any measured inductance $L(t)$ is:

$$x(t) = (x_t - x_s)\frac{L_s - L(t)}{L_s - L_t} \tag{A.3}$$

where x_s and L_s are initial mudline height and corresponding inductance and x_t and L_t are final mudline height and corresponding inductance. The data is then plotted as mudline location, x, versus time and is linearly fitted with a straight line. The slope of the fitted line gives the sedimentation velocity.

A.5 Rheological Results

Using the Anton-Paar parallel disc rheometer, the flow curve (shear stress vs shear rate) of each MR fluid was determined. The BP model was fitted to the data using a weighted-least-squares error minimization procedure by selecting the yield stress and post-yield viscosity of the MR fluids. Since shear rates are used as weights, shear stress values at high shear rates were selected to better match the BP model

asymptotically and estimate the apparent yield stress value of the MR fluid. The yield stress is given by the intercept of the high shear rate asymptote with the shear stress axis. Refer to Figures A.2a and A.2b.

Figures A.3a and A.3b show the apparent yield stresses versus magnetic flux density of the applied field for fluids with iron loading of 50 and 60 wt% containing strictly spheres and those with 6 and 8 wt% substitution of microspheres with nanowires, respectively. For these samples, there is no significant difference in yield stress between the all microsphere and dimorphic MR fluids at the same total iron loading. Figure A.4a shows the yield stress variation for samples with 80 wt% total iron loading. The results indicate that the yield stresses in the low magnetic flux region are quite similar for the increasing substitution of wires for spheres. In contrast, at higher magnetic flux densities, there is an initial increase in the yield stress with 2 wt% substitution followed by a steady decline in the yield stress as the wt% of the nanowire substitution is increased.

The SEM micrograph of the dimorphic MR fluid particles under no magnetic field clearly indicate that the nanowires are uniformly dispersed and randomly oriented throughout the fluid as seen in Figure A.5a and was similarly observed for all fluid compositions. These samples were prepared by suspending the particles in ethanol at the desired concentrations and then allowing the ethanol to evaporate locking in the structure of the suspended particles. Application of a magnetic field causes the nanowires and microspheres to arrange themselves quite differently. Figures A.5b, A.6a and A.6b show SEM micrographs of dimorphic MR fluids (at concentrations representative of samples 8, 10 and 11) within a magnetic field. These samples were

generated in a similar fashion as before accept that the ethanol was allowed to evaporate in a planar magnetic field of 0.26 T. The SEM image in Figure A.5b shows that at low nanowire loadings the microspheres still form chained clusters and that the wires are arranged very sparsely in the voids between and alongside these chain structures. As the nanowire concentration increases (Figures A.6a and A.6b), they not only fill the gaps between the microsphere chain structures, but begin to interfere with the chain structure formed by the spherical particles as a larger number of nanowires become lodged between the microspheres (long axis perpendicular to the field lines). We believe that this interference of the nanowires in the chain structure of the microspheres is the cause of the decrease in maximum achievable yield stress. Further experimental and theoretical studies will need to be performed to confirm this hypothesis.

The maximum apparent yield stress for the aforementioned samples as a function of magnetic flux density is shown in Figure A.4b. The samples display an initial increase in the maximum yield stress followed by a steady drop as the nanowire loading is increased. This represents a less than 10% difference in the yield stress of fluids with nanowires compared to those not containing nanowires. At this stage, even though we observe some variation in yield stress among the dimorphic fluids, the presence of nanowires at this level of concentration does not degrade the apparent yield strength of the MR fluids as is the case for many others additives aimed at reducing sedimentation.

The off-state viscosity of the above samples is given in Table A.2. These dimorphic MR fluids tend to have a higher off-state viscosities as compared with the

MR fluids composed of only microspheres. The maximum viscosity increase of the dimorphic MR fluid is more than threefold that of the microsphere-based fluid.

A.6 Sedimentation Results

The sedimentation rates of samples 3 though 8 were tested in order to compare conventional MR fluid settling rates to that of the dimorphic fluids. Two methods were used to estimate and compare the stability of MR fluids. First, the sedimentation velocity was determined as outlined in Section 4. Figures A.7a and A.7b show sample sedimentation plots as obtained from inductance measurements for MR fluid samples 7 and 8. A linear least-squares fitting was used to determine the sedimentation velocity. These figures show that there is a twofold improvement in the sedimentation rate with only a small substitution of spheres with nanowires dropping from 0.0254 μm/s for the 80 wt% iron sphere loading to 0.0122 μm/s with only 2 wt% substitution with nanowires. The estimated sedimentation velocity of the MR fluid with 50 wt% microsphere particles is 1.90 μm/s while for the dimorphic MR fluid with 44 wt% microspheres and 6 wt% nanowires the sedimentation velocity drops to 0.036 μm/s. For the fluid compositions studied here, a maximum drop in sedimentation velocity of almost two orders of magnitude is observed as seen in Table A.3.

The second method used to characterize stability was to determine sedimentation percentage of the fluids as given by [A29]

$$\text{Sedimentation Percentage} = \frac{\text{Volume of supernatent fluid}}{\text{Total volume of MR fluid}} \times 100\% \tag{A.4}$$

This ratio was determined after the fluids were allowed to settle undisturbed, for a minimum of 1 month. These results are shown in Table A.4. It is seen that all

dimorphic fluids have a lower sedimentation ratio, implying a smaller magnitude of sedimentation than conventional microsphere-based MR fluids. This reduction in sedimentation ratio results in a more porous agglomeration of particles at the container bottom, making re-dispersion much easier and providing a homogenous mixture more quickly.

Referring again to Figure A3.a which shows a dimorphic MR fluid under no magnetic field, we observe that the wires are uniformly dispersed and randomly oriented throughout the fluid. The wires arrange themselves randomly between neighboring spherical particles. Also, the addition of the nanowires appears to enhance the interaction of neighboring particles and with the fluid flow, as well as creating entanglement due to their limited rotational and translational motions [A39]. Naturally, these types of interparticle interactions would increase considerably as the percentage of the nanowires increases. Therefore, the presence of the nanowires tends to increase the viscosity of the dimorphic suspensions generating fluids with an increased sedimentation hindrance factor. All these effects are expected to account for the reduction in the average particle settling velocity, and considerably reducing overall sedimentation making re-dispersion much easier.

A.7 Conclusions

This study investigated and quantified the changes in yield stress, off-state viscosity, sedimentation velocity and sedimentation percentage of MR fluids as nanowires were substituted for the spherical particles in dimorphic MR fluids. These substitutions significantly reduced the rate of particle settling, enabling the MR fluid to maintain a uniform dispersion without marked sedimentation for an extended

period of time. Even after the onset of sedimentation, the presence of the nanowires tended to produce a more porous particle sediment which suggests ease of re-dispersion. In addition, at the level of nanowire concentration and geometry studied, it was possible to maintain the high level of yield stress observed in conventional microsphere-based MR fluids.

A.8 References

[A1] Genc, S. and Phule, P., "Rheological Properties of Magnetorheological Fluids," *Smart Materials and Structures*, Vol. 11, 2002, pp. 140-146.

[A2] Jolly, M., Bender, J. and Carlson, J., "Properties and Application of Commercial Magnetorheological Fluids," *Journal of Intelligent Material Systems and Structures*, Vol. 10, 1999, pp. 5-13.

[A3] Ginder, J. and Davis, L., "Shear Stress in Magnetorheological Fluids: Role of Magnetic Saturation," *Applied Physics Letters,* Vol.65, 1994, pp. 3410-3412.

[A4] Trihan, J., Yoo, J-H., Wereley, N., Kotha, S., Suggs, A., Radhakrishnan, R., Sudarshan, T. and Love, B., "Impact of Varying Concentration of Nanometer-sized Particles in a Bidisperse Magnetorheological Fluid *Proceedings of the SPIE*, Vol. *5052*, 2003, pp. 175-185.

[A5] Chaudhuri, A., Yoo, J-H., John, S., Wereley, N., Kotha, S., Suggs, A., Radhakrishna, R., Sudarshan, T. and Love, B., "Bidisperse MR Fluids Using Fe Particles at Nanometer and Micron Scale," *Journal of Intelligent Material Systems and Structures*, Vol.17, 2006, pp 393-401.

[A6] Carlson, J., "Critical Factors for MR Fluids in Vehicle Systems," *International Journal of Vehicle Design*, Vol. 33, Nos. 1-3, 2003, pp. 207-217.

[A7] Choi, Y-T., Wereley, N. and Jeon, Y-S., "Semi-active Vibration Isolation Using Magnetorheological Isolators," *AIAA Journal of Aircraft,* Vol. 42, 2005, pp. 1244-1251.

[A8] Sahin, H., Liu, Y., Wang, X., Gordaninejad, F., Evrensel, C., and Fuchs, A., "Full-scale Magnetorheological Fluid Dampers for Heavy Vehicle Rollover," *Journal of Intelligent Material Systems and Structures*, Vol. 18, No. 12, 2007, pp. 1161-1167.

[A9] Choi, Y. T., and Wereley, N. M., "Vibration Control of a Landing Gear System Featuring Electrorheological/Magnetorheological Fluids," *AIAA Journal of Aircraft*, Vol. 40, No. 3, 2003, pp. 432-439.

[A10] Batterbee, D., Sims, N., Stanway, R., and Wolejsza, Z., "Magnetorheological Landing Gear: 1. A Design Methdology," *Smart Materials and Structures,* Vol. 16, 2007, pp. 2429-2440.

[A11] Batterbee, D. C., Sims, N. D., Stanway, R., and Rennison, M., "Magnetorheological Landing Gear: 2. A Design Methdology," *Smart Materials and Structures*, Vol. 16, No. 6, 2007, pp. 2441-2452.

[A12] McManus, S. J., St. Clair, K. A., Boileau, P. E., Boutin, J., and Rakheja, S., "Evaluation of Vibration and Shock Attenuation Performance of a Suspension Seat with a Semi-active Magnetorheological Fluid Damper," *Journal of Sound and Vibration*, Vol. 253, No. 1, 2002, pp. 313-327.

[A13] Choi, S. B., Nam, M. H., and Lee, B. K., "Vibration Control of a MR Seat Damper for Commercial Vehicles," *Journal of Intelligent Material Systems and Structures*, Vol. 11, No. 12, 2000, pp. 936-944.

[A14] Hiemenz, G. J., Hu, W., and Wereley N.M.,"Semi-active Magnetorheological Helicopter Crew Seat Suspension for Vibration Isolation," *AIAA Journal of Aircraft*, Vol. 45, No. 3, 2008, pp. 945-953.

[A15] Choi, Y. T., and Wereley, N. M., "Mitigation of Biodynamic Response to Vibratory and Blast-induced Shock Loads Using Magnetorheological Seat Suspensions," *Journal Automobile Engineering*, Vol. 219, No. D6, 2005, pp. 741-754.

[A16] Hiemenz, G. J., Choi, Y. T., and Wereley, N. M., "Semi-active Control of a Vertical Stroking Helicopter Crew Seat for Enhanced Crashworthiness," *AIAA Journal of Aircraft*, Vol. 44, No. 3, 2007, pp. 1031-1034.

[A17] Phule, P., Mihalcin, M. and Genc, S., "The Role of the Dispersed-Phase Remnant Magnetization on the Redispersibility of Magnetorheological Fluids," *Journal of Material Research,* Vol. 14, 1999, pp. 3037-3041.

[A18] Lopez-Lopez, M., Zugaldia, A., Gonzalez-Caballero, F. and Duran, J., "Sedimentation and Redispersion Phenomena in Iron-Based Magnetorheological Fluids," *Journal of Rheology,* Vol. 50, 2006, pp 543-560.

[A19] de Vicente, J., Lopez-Lopez, M. and Gonzalez-Caballero, F., "Rheological Study of the Stabilization of Magnetizable Colloidal Suspensions by Addition of Silica Nanoparticles," *Journal of Rheology,* Vol. 47, 2003, pp. 1093-1109.

[A20] Phule, P., "Synthesis and Properties of Novel Magnetorheological Fluids Having Improved Stability and Redispersibility," *International Journal of Modern Physics B*, Vol. 13, 1999, pp. 2019-2027.

[A21] Lim, S., Cho, M. and Choi, H., "Magnetorheological Characterization of Organoclay Added Carbonyl-Iron Suspensions," *International Journal of Modern Physics B*, Vol. 19, 2005, pp. 1142-1148.

[A22] Lim, S., Hoi, H-J. and Jhon, M., "Magnetorheological Characterization of Carbonyl Iron-Organoclay Suspensions," *IEEE Transactions*, Vol. 41, 2005, pp 3745-3747.

[A23] You, J., Park, B. and Choi, H., "Preparation and Magnetorheological Characterization of CI/PVB Core/Shell Particle Suspended MR Fluids," *International Journal of Modern Physics B*, Vol. 21, 2007, pp. 4996-5002.

[A24] Jang, I., Kim, H., Lee, J., You, J. and Choi, H., "Role of Organic Coating on Carbonyl Iron Suspended Particles in Magnetorheological Fluids," *Journal of Applied Physics,* Vol. 97, 2005, 10Q912.

[A25] Kormann, C., Laun, H. and Ritcher, H., "MR Fluids with Nanosized Magnetic Particles," *International Journal of Modern Physics B*, Vol. 10, 1996, pp. 3167-3172.

[A26] Ginder, J., Elie, L. and Davis, L., Magnetic Fluid Based MR Fluids, *US Patent 5,549,837, 1996.*

[A27] Lopez-Lopez, M. and de Vicente, J., "Preparation of Stable Magnetorheological Fluids Based on Extremely Bimodal Iron-Magnetite Suspensions," *Journal of Material Research,* Vol. 20, 2005, pp. 874-882.

[A28] Rosenfeld, N., Wereley, N., Radakrishnan, R. and Sudarshan, T., "Behavior of Magnetorheological Fluids Utilizing Nanopowder Iron," *International Journal of Modern Physics B*, Vol. 16, 2002, pp. 2392–2398.

[A29] Bell, R., Karli, J., Vavreck, A., Zimmerman, D., Ngatu, G., and Wereley, N., "Magnetorheology of Submicron Diameter Iron Microwires Dispersed in Silicone Oil," *Smart Materials and Structures*, Vol. 17, 2008, 015028.

[A30] Rosenweig R E 1997 Ferrohydro-Dynamics *Dover Publication.*

[A31] Odenbach, S., "2000 Magnetoviscous and Viscoelastic Effects in Ferrofluids," *International Journal of Modern Physics B*, Vol. 14, 2000, pp. 1615-1631.

[A32] Lopez-Lopez, M., Kuzhir, P., Lacis, S., Bossis, G., Gonzalez-Caballero, F. and Duran, J., "Magnetorheology for Suspensions of Solid Particles Dispersed in Ferrofluids," *Journal of Physics: Condensed Matter*, Vol. 18, 2006, S2803-S2813.

[A33] Viota, J., Duran, J., Gonzalez-Caballero, F. and Delgado, A., "Magnetic Properties of Extremely Bimodal Magnetic Suspensions," *Journal of Magnetism and Magnetic Materials,* Vol. 314, 2007, pp. 80-86.

[A34] Ngatu, G. and Wereley, N., "Viscometric and Sedimentation Characterization of Bidisperse MR Fluids," *IEEE Transactions*, Vol. 43, 2007, pp. 2474-2476.

[A35] Levin, M. and Polesskii, D., "Some Features of the Magnetorheological Effect," *Journal of Engineering Physics and Thermophysics*, Vol. 70, 1997, pp. 769-772.

[A36] Lopez-Lopez, M., Vertelov, G., Bossis, G., Kuzhir, P. and Duran, D., "New Magnetorheological Fluid Based on Magnetic Fibers," *Journal of Materials Chemistry*, Vol. 17, 2007, pp. 3839-3844.

[A37] Ferguson J and Kemblowski Z 1991 Applied Fluid Rheology *Elsevier Science Publication.*

[A38] Metzner, A., "Rheology of Suspensions in Polymeric Liquids," *Journal of Rheology,* V0l. 29, 1985, pp. 739-775.

[A39] Doi, M. and Edwards, S., "1978 Dynamics of Rod-like Macromolecules in Concentrated Solution," *Journal of the Chemical Society, Faraday Transactions II,* Vol. 74, 1978, pp. 560-570.

[A40] Kroll, M., Blau, W., Grandjean, D., Benfield, R., Lui, F., Paulus, P. and de Jongh, L., "Magnetic Properties of Ferromagnetic Nanowires Embedded in Nanoporous Alumina Membranes," *Journal of Magnetism and Magnetic Materials,* Vol. 249, 2002, pp. 241-245.

[A41] Gorodkin, S., Kordonski, W., Medvedeva, E., Novikova, Z., Shorey, A. and Jacobs, S., "A Method and Device for Measurement of a Sedimentation Constant of MR Fluids," *Review of Scientific Instruments*, Vol. 71, 2000, pp. 2476-2480.

Table A.1: MR Fluid samples

Sample ID		3	4	5	6	7	8	9	10	11
Total Iron Loading	Wt%	50	50	60	60	80	80	80	80	80
	Vol%	11.5	11.5	16	16	33	33	33	33	33
Microspheres	Wt%	50	44	60	52	80	78	76	74	72
	Vol%	11.5	10	16	13.5	33	32.1	31.4	30.4	29.6
Nanowires	Wt%	0	7	0	8	0	2	4	6	8
	Vol%	0	1.5	0	2.5	0	0.9	1.6	2.6	3.4

Table A.2: Off-state viscosities of MR Fluid samples

Sample ID	Sample Description	Off-state viscosity [Pa s]
7	80wt% sphere	1.3
8	78wt% sphere 2wt% wire	2.1
9	76wt% sphere 4wt% wire	3.5
10	74wt% sphere 6wt% wire	3.5
11	72wt% sphere 8wt% wire	4.4

Table A.3: Sedimentation Velocities of Conventional and Dimorphic MR Fluid Samples

Sample ID	Sample Description	Sedimentation Velocity [μm/s]
3	50wt% sphere	1.9
4	44wt% sphere 6wt% wire	0.036
5	60wt% sphere	0.86
6	52wt% sphere 8wt% wire	0.017
7	80wt% sphere	0.0254
8	78wt% sphere 2wt% wire	0.0122
9	76wt% sphere 4wt% wire	0.0021

Table A.4: Sedimentation Percentages of Samples

Sample ID	Composition	Sedimentation Percentage (%)
3	50wt% spheres	72.9
4	44wt% spheres 6wt% wires	23.4
5	60wt% spheres	66.7
6	52wt% spheres 8wt% wires	14.0
7	80wt% spheres	14.8
8	78wt% spheres 2wt% wires	8.8
9	76wt% spheres 4wt% wires	5.7

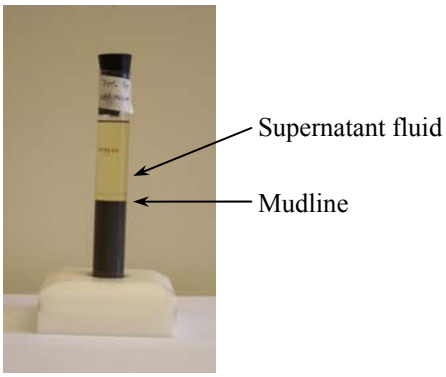

(a) A settling MR fluid

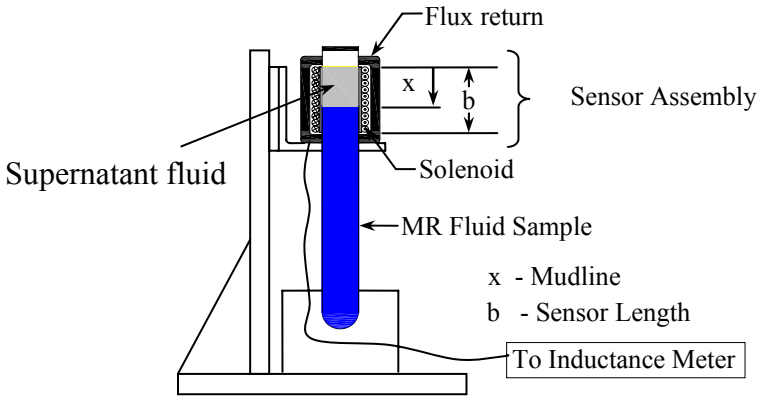

(b) Sedimentation measurement

Figure A.1: A settling MR fluid and test set-up for sedimentation measurement

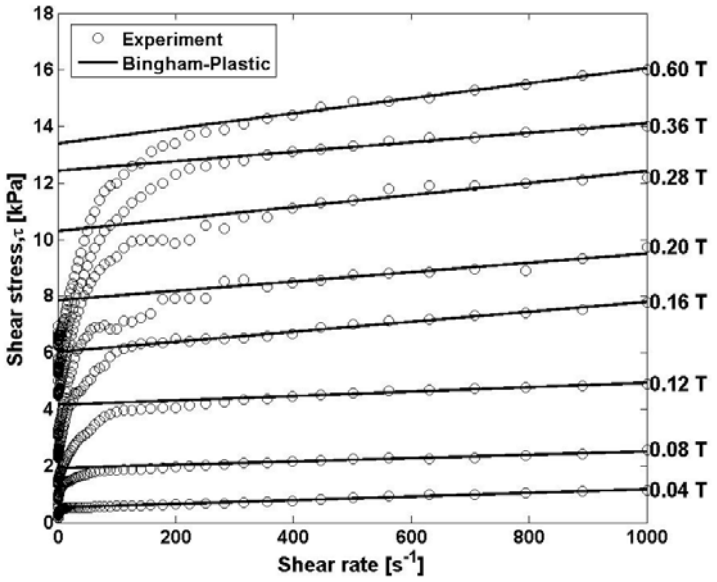

(a) Sample 3 containing 50 wt% microspheres only

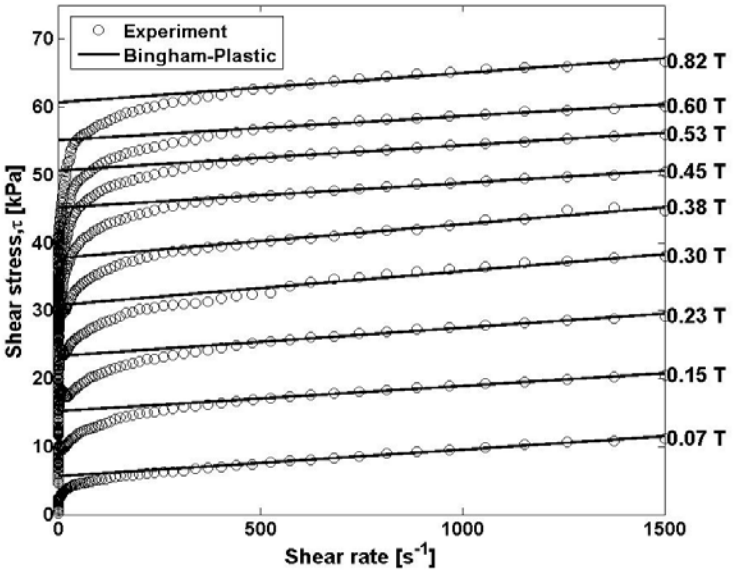

(b) Sample 9 containing 76 wt% microspheres and 4 wt% nanowires

Figure A.2: MR fluid experimental flow curves

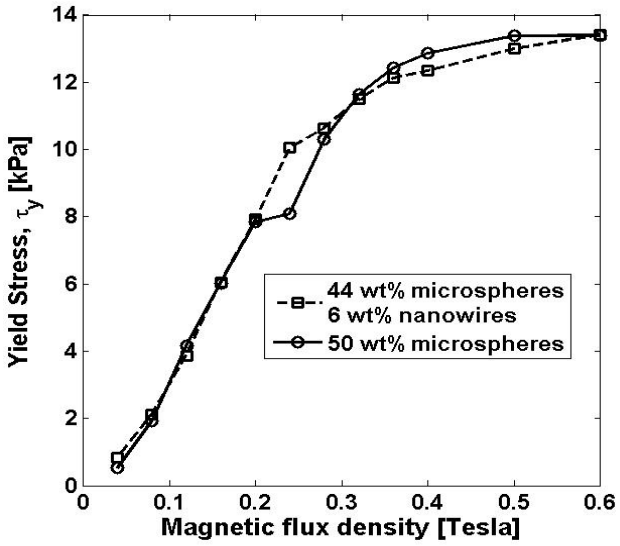

(a) MR fluids containing total 50 wt% iron particles

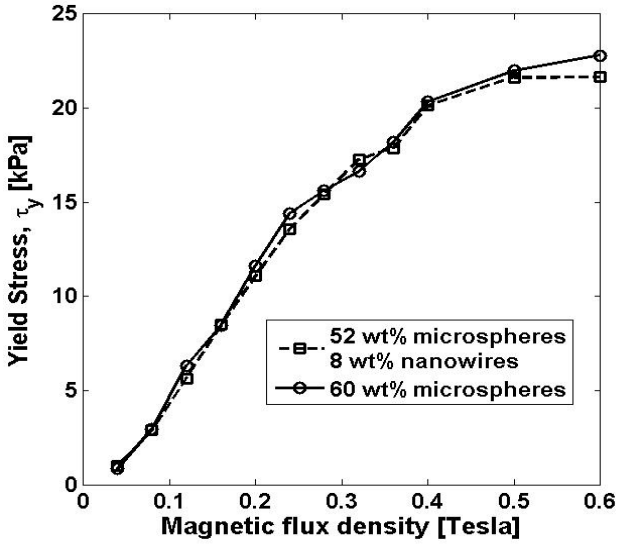

(b) MR fluids containing total 50 wt% iron particles

Figure A.3: Yield stress vs magnetic field

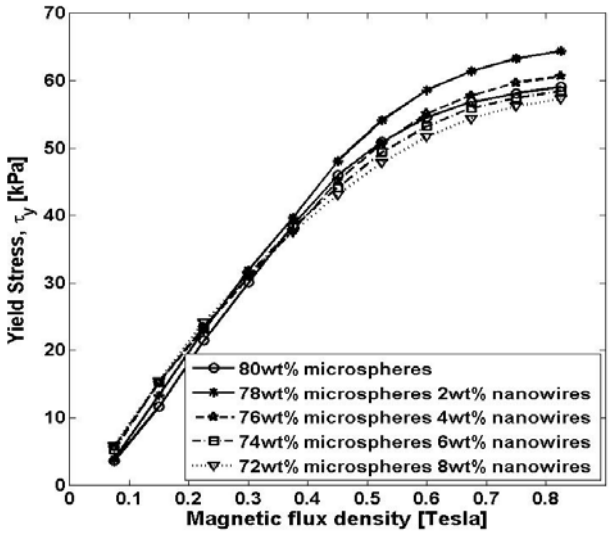

(a) MR fluids containing total 80 wt% iron particles

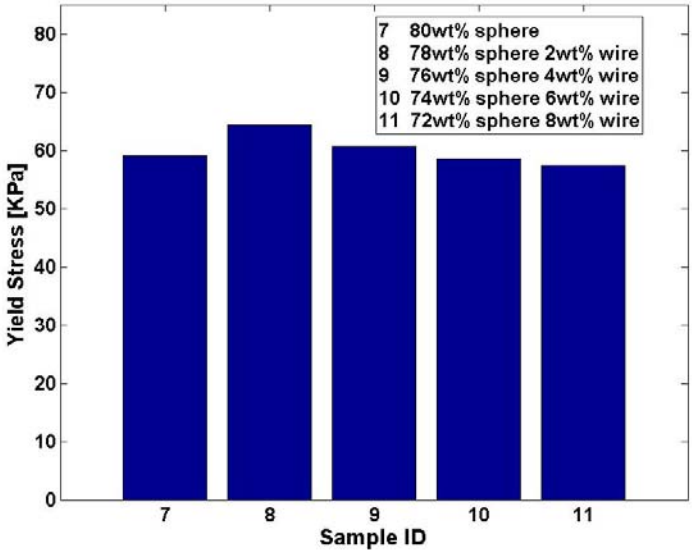

(b) Maximum measured yield stress for 80 wt%

Figure A.4: Yield stress vs magnetic field and maximum measured yield stress at 80 wt% iron particles

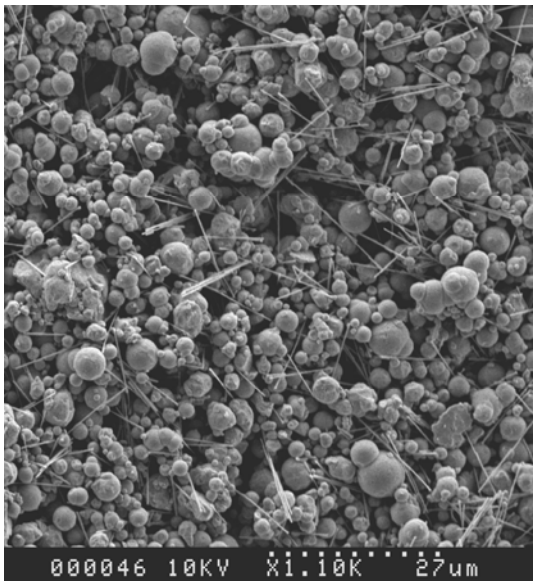

(a) MR fluid with 76 wt% microspheres and 4 wt% nanowires under no magnetic field

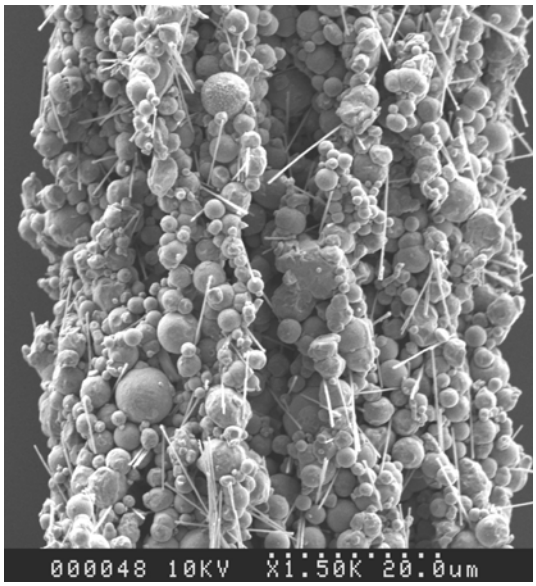

(b) MR fluid with 78 wt% microspheres and 2 wt% nanowires under 0.26T magnetic field

Figure A.5: SEM micrograph of MR fluids

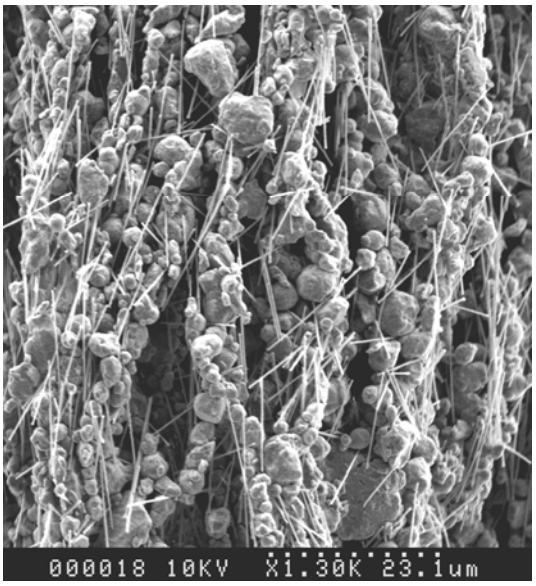

(a) MR fluid with 74 wt% microspheres and 6 wt% nanowires under 0.26T magnetic field

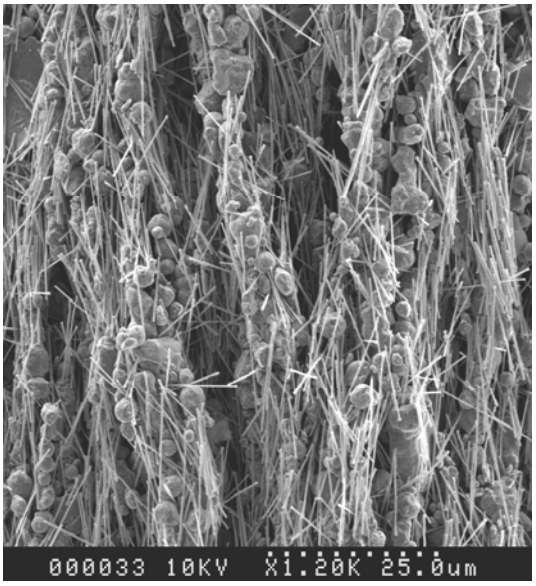

(b) MR fluid with 72 wt% microspheres and 8 wt% nanowires under 0.26T magnetic field

Figure A.6: SEM micrograph of MR fluids

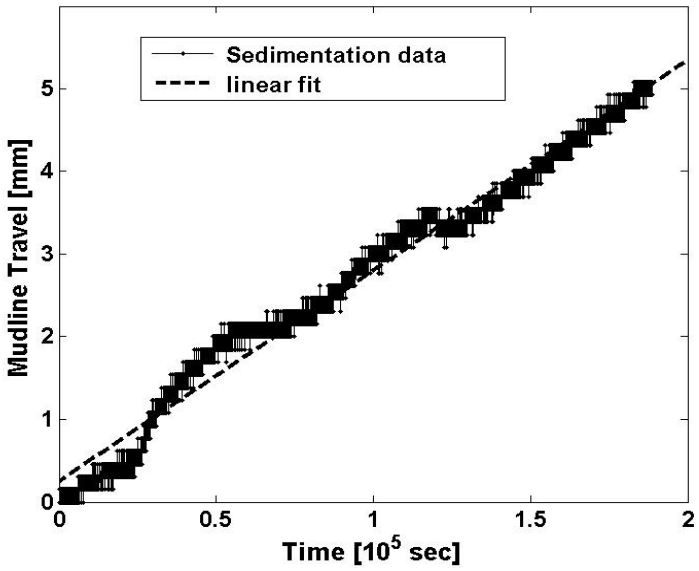

(a) MR fluid with 80wt% microspheres

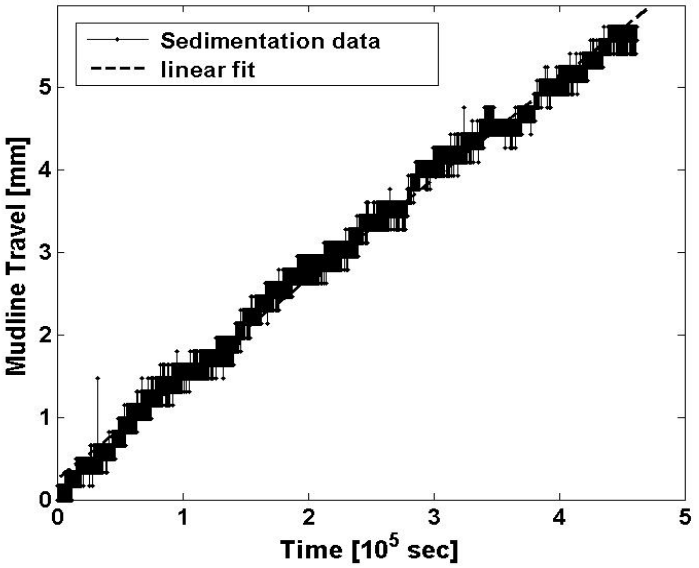

(b) MR fluid with 78 wt% microspheres and 2 wt% nanowires

Figure A.7: Mudline travel vs time plot under gravitational field

Bibliography

[1] Chopra, I., "Perspectives in Aeromechanical Stability of Helicopter Rotors," *Vertica*, Vol. 14, No. 4, 1990, pp. 457-508.

[2] Jones, P., Russell, D., and McGuire, P., "Latest Development in Fluidlastic® Lead-Lag Dampers for Vibration Control in Helicopters," *Proceedings of the American Helicopter Society 59th Annual Forum*, Phoenix, Arizona, May 6 – 8, 2003.

[3] Snyder, R., Krishnan, R., Wereley, N.M., and Seig, T., "Mechanisms Based Analysis of Elastomeric Lag Damper Behavior Under Single and Dual Frequency Excitation Including Temperature Effects," *Proceedings of the American Helicopter Society 57th Annual Forum*, Washington, DC, 2001.

[4] Panda, B., Mychalowycz, E., and Tarzanin, F., "Application of Passive Dampers to Modern Helicopters," *Smart Materials and Structures*, Vol. 5, No. 5, 1996, pp. 509-516.

[5] Hu, W., and Wereley, N.M., "Distributed Rate-Dependent Elastoslide Model for Elastomeric Lag Dampers," *AIAA Journal of Aircraft*, Vol. 44, No. 6, 2007, pp. 1972-1984.

[6] Felker, F., Lau, B., McLaughlin, S., and Johnson, W., 1987, "Nonlinear Behavior of an Elastomeric Lag Damper Undergoing Dual-Frequency Motion and its Effect on Rotor Dynamics," *Journal of the American Helicopter Society*, Vol. 32, No. 4, 1987, pp. 45-53.

[7] Hu, W. and Wereley, N.M., "Hybrid Magnetorheological Fluid-Elastomeric Lag Dampers for Helicopter Stability Augmentation," *Smart Materials and Structures*, Vol. 17, No. 4, 2008, 045021.

[8] McGuire, D.P., "Fluidlastic® Dampers and Isolators for Vibration Control in Helicopters," *American Helicopter Society 50th Annual Forum*, Washington, DC, May 1994.

[9] Panda, B., and Mychalowycz, E., "Aeroelastic Stability Wind Tunnel Testing with Analytical Correlation of the Comanche Bearingless Main Rotor," *Journal of the American Helicopter Society*, Vol. 42, No. 3, 1997, pp. 207-217.

[10] Kamath, G.M., Wereley, N.M., and Jolly, M.R., "Characterization of Magnetorheological Helicopter Lag Dampers," *Journal of the American Helicopter Society*, Vol. 44, No. 3, 1999, pp. 234-248.

[11] Hausmann, G., and Gergely, P., "Approximate Methods for Thermoviscoelastic Characterization and Analysis of Elastomeric Lead-lag Dampers," *Proceedings of the 18th European Rotorcraft Forum*, Avignon, France,1992.

[12] Brackbill, R., Lesieutre, G., Smith, E., and Govindswamy, K., "Thermomechanical Modeling of Elastomeric Materials," *Smart Materials and Structures*, Vol. 5, 1996, pp. 529-539.

[13] Hu, Wei, "Development of Magnetorheological Fluid Elastomeric Dampers for Helicopter Stability Augmentation," *Ph.D. Thesis*, Aerospace Engineering, University of Maryland, 2005.

[14] Hu, W., Wereley, N.M., Chemouni, L. and Chen, P.C., "Semi-active Linear Stroke Magnetorheological Fluid-Elastic (MRFE) Damper for Helicopter Main Rotor Blades," *AIAA Journal of Guidance, Control, and Dynamics*, Vol. 30, No. 2, 2007, pp. 565-575.

[15] Genç, S. and Phulé, P., "Rheological Properties of Magnetorheological Fluids," *Smart Materials and Structures*, Vol. 11, 2002, pp. 140–146.

[16] Bell, R., Karli, J., Vavreck, A., Zimmerman, D., Ngatu, G., and Wereley, N., "Magnetorheology of Submicron Diameter Iron Microwires Dispersed in Silicone Oil," *Smart Materials and Structures*, Vol. 17, 2008, 015028.

[17] Choi, Y. T., Wereley, N. M., and Jeon, Y. S., "Semi-active Vibration Isolation Using Magnetorheological Isolators," *AIAA Journal of. Aircraft*, Vol. 42, No. 5, 2005, pp. 1244-1251.

[18] Carlson, J., "Critical Factors for MR Fluids in Vehicle Systems," *International Journal of Vehicle Design*, Vol. 33, Nos. 1-3, 2003, pp. 207-217.

[19] Sahin, H., Liu, Y., Wang, X., Gordaninejad, F., Evrensel, C., and Fuchs, A., "Full-scale Magnetorheological Fluid Dampers for Heavy Vehicle Rollover," *Journal of Intelligent Material Systems and Structures*, Vol. 18, No. 12, 2007, pp. 1161-1167.

[20] Choi, Y. T., and Wereley, N. M., "Vibration Control of a Landing Gear System Featuring Electrorheological/Magnetorheological Fluids," *AIAA Journal of Aircraft*, Vol. 40, No. 3, 2003, pp. 432-439.

[21] Batterbee, D. C., Sims, N. D., Stanway, R., and Wolejsza, Z., "Magnetorheological Landing Gear: 1. A Design Methdology," *Smart Materials and Structures*, Vol. 16, No. 6, 2007, pp. 2429-2440.

[22] Batterbee, D. C., Sims, N. D., Stanway, R., Rennison, M., "Magnetorheological Landing Gear: 2. Validation Using Experimental Data," *Smart Materials and Structures,* Vol. 16, No. 6, 2007, pp. 2441-2452.

[23] McManus, S. J., St. Clair, K. A., Boileau, P. E., Boutin, J., and Rakheja, S., "Evaluation of Vibration and Shock Attenuation Performance of a Suspension Seat with a Semi-active Magnetorheological Fluid Damper," *Journal of Sound and Vibration*, Vol. 253, No. 1, 2002, pp. 313-327.

[24] Choi, S. B., Nam, M. H., and Lee, B. K., "Vibration Control of a MR Seat Damper for Commercial Vehicles," *Journal of Intelligent Material Systems and Structures*, Vol. 11, No. 12, 2000, pp. 936-944.

[25] Hiemenz, G. J., Hu, W., and Wereley N.M.,"Semi-active Magnetorheological Helicopter Crew Seat Suspension for Vibration Isolation," *AIAA Journal of Aircraft*, Vol. 45, No. 3, 2008, pp. 945-953.

[26] Choi, Y. T., and Wereley, N. M., "Mitigation of Biodynamic Response to Vibratory and Blast-induced Shock Loads Using Magnetorheological Seat Suspensions," *Journal Automobile Engineering*, Vol. 219, No. D6, 2005, pp. 741-754.

[27] Hiemenz, G. J., Choi, Y. T., and Wereley, N. M., "Semi-active Control of a Vertical Stroking Helicopter Crew Seat for Enhanced Crashworthiness," *AIAA Journal of Aircraft*, Vol. 44, No. 3, 2007, pp. 1031-1034.

[28] Jones, T., and Saha, B., "Nonlinear Interactions of Particles in Chains," *Journal of Applied Physics,* Vol. 68, 1990, pp. 404–410.

[29] Rosenfeld, N., Wereley, N., Radakrishnan, R. and Sudarshan, T., "Behavior of Magnetorheological Fluids Utilizing Nanopowder Iron," *International Journal of Modern Physics B*, Vol. 16, 2002, pp. 2392–2398.

[30] Poddar, P., Wilson, J., Srikanth, H., Yoo, J., Wereley, N., Kotha, S., Barghouty, L. and Radhakrishnan, R., "Nanocomposite Magneto-Rheological Fluids with Uniformly Dispersed Fe Nanoparticles," *Journal of Nanoscience and Nanotechnology,* Vol. 4, 2004, pp. 192–196.

[31] Chaudhuri, A., Wereley, N.M., Kotha, S., Radhakrishnan, R. and Sudarshan, T., "Viscometric Characterization of Cobalt Nanoparticle-based Magnetorheological Fluids Using Genetic Algorithms," *Journal of Magnetism and Magnetic Materials,* Vol. 293, 2005, pp. 206–214.

[32] Ngatu, G. and Wereley, N., "Viscometric and Sedimentation Characterization of Bidisperse MR Fluids," *IEEE Transactions*, Vol. 43, 2007, pp. 2474-2476.

[33] Phulé, P. and Ginder, J., "The Materials Science of Field-Responsive Fluids," *MRS Bulletin*, Vol. 23, 1998, pp. 19–21.

[34] Chin, B., Park, J., Kwon, M. and Park, O., "Rheological Properties and Dispersion Stability of Magnetorheological (MR) Suspensions," *Rheologica Acta*, Vol. 40, 2001, pp. 211–219.

[35] Weiss, K., Nixon, D., Carlson, J. and Margida, A., "Thixotropic Magnetorheological Materials," US Patent 5 645 754, 1997.

[36] Wereley, N.M., Chaudhuri, A., Yoo, J., John, S., Kotha, S., Suggs, A., Radhakrishnan, R., Love, B. and Sudarshan, T., "2006 Bidisperse Magnetorheological Fluids Using Fe Particles at Nanometer and Micro Scale," *Journal of Intelligent Material Systems and Structures*, Vol. 17, 2006, pp. 393–401.

[37] Levin, M. and Polesskii, D., "Some Features of the Magnetorheological Effect," *Journal of Engineering Physics and Thermophysics*, Vol. 70, 1997, pp. 769-772.

[38] Weiss, D. and Duclos, T., "Controllable Fluids: Temperature Dependence of Post-yield Properties," *International Journal of Modern Physics B*, Vol. 8, 1994, pp. 3015-3032.

[39] Kunz, D., "Influence of Elastomeric Damper Modeling on the Dynamic Response of Helicopter Rotors," *AIAA Journal*, Vol. 35, 1997, pp. 349-354.

[40] Payne, A. and Whittaker, R., "Strain Dynamic Properties of Filled Rubbers," *Rubber Chemistry and Technology*, Vol. 44, 1971, pp. 440-478.

[41] Tarzanin F.J., and Panda, B., "Development and Application of Nonlinear Elastomeric and Hydraulic Lag Damper Models," *Proceedings of the 36th AIAA/ASME/ASCE/AHS/ASC Structures, Structural Dynamics, and Materials Conference*, New Orleans, Louisiana, April 1995.

[42] Krishnan, R., "Mechanisms-based Analysis and Modeling of Elastomeric Lag Damper Behavior," *Master of Science*, University of Maryland, Aerospace Engineering, 2000.

[43] Gandhi, F., and Chopra, I., "A Time-domain Non-linear Viscoelastic Damper Model," *Smart Materials and Structures*, Vol. 5, No. 5, 1996, pp. 517-528.

[44] Lesieutre, G. and Bianchini, E., "Time Domain Modeling of Linear Viscoelasticity Using Anelastic Displacement Fields," *Transactions of the ASME*, Vol. 117, 1995, pp. 424-430.

[45] Govindswamy, K., Lesieutre, G.A., Smith, E.C., and Beale, M.R., "Characterization and Modeling of Strain-Dependent Dynamics Behavior of Viscoelastic Elastomers in Simple Shear," *Proceedings of the 36th AIAA/ASME/ASCE/AHS/ASC Structures, Structural Dynamics, and Materials Conference*, New Orleans, LA, April 1996.

[46] Brackbill, C.R., Lesieutre, G.A., Smith, E.C., Ruhl, L.E., "Characterization and Modeling of Low Strain Amplitude and Frequency Dependent Behavior of Elastomeric Damper Materials," *Journal of the American Helicopter Society*, Vol. 45, 2000, pp.

[47] Ramrakhyani, D., Lesieutre, G. and Smith E., "Modeling of elastomeric materials using nonlinear fractional derivative and continuously yielding friction elements," *International Journal of Solids and Structures*, Vol. 41, 2004, pp. 3929–3948.

[48] Coveney, V.A., Johnson D.E., and Turner D.M., "A Triboelastic Model for the Cyclic Mechanical Behavior of Filled Vulcanizates," *Rubber Chemistry and Technology*, Vol. 68, 1995, pp. 660-670.

[49] Turner, D.M., "A Triboelastic Model for the Mechanical Behavior of Rubber," *Plastics and Rubber, Processing and Applications*, No.9, 1988, pp. 197-201.

[50] Hausmann, G. and Gergely, P., "Approximation Methods for Thermoviscoelastic Characterization and Analysis of Elastomeric Lead-Lag Dampers," *Proceedings of the 18th Annual European Rotorcraft Forum*, Avignon, France, 1992.

[51] Gobel, E., "Rubber Springs Design," *Butterworth & Co. Publication*, 1974.

[52] Brackbill, R., Lesieutre, G., Smith, E. and Govindswamy, K., "Thermomechanical Modeling of Elastomeric Materials," *Smart Materials and Structures*, 5, 1996, pp. 529-539.

[53] Smith, E., Lesieutre, G., Szefi T. and Marr, C., "Time Domain Fluidlastic® Lag Damper Modeling," *Proceedings of the American Helicopter Society 62nd Annual Forum*, Phoenix, AZ, 2006.

[54] Marr, C., Lesieutre, G. and Smith, E., "Non-Linear, Temperature Dependent, Fluidlastic Lead-Lag Damper Modeling," *Proceedings of the American Helicopter Society 64th Annual Forum*, Montreal, Canada, 2008.

[55] White, F., "Viscous Fluid Flow," McGraw Hill International Edition, 2006.

[56] Brackbill, C., Lesieutre, G., Smith, E. and Ruhl, L., "Characterization and Modeling of the Low Strain Amplitude and Frequency Dependent Behavior of Elastomeric Damper Materials," *Journal of the American Helicopter Society*, Vol. 45, No. 1, 2000, pp. 34-42.

[57] Jolly, M., Bender, J., and Carlson, J., "Properties and Applications of Commercial Magnetorheological Fluids," *Journal of Intelligent Material Systems and Structures*, Vol. 10, No. 1, 1999, pp. 5-13.

[58] Ngatu, G., and Wereley, N.M., "High Versus Low Field Viscometric Characterization of Bidisperse MR Fluids," *International Journal of Modern Physics B*, Vol. 21, Nos. 28 & 29, 2007, pp. 4922-4928.

[59] Marathe, S., Gandhi, F., and Wang, K.W., "Helicopter Blade Response and Aeromechanical Stability with a Magnetorheological Fluid Based Lag Damper," *Journal of Intelligent Material Systems and Structures*, Vol. 9, No. 4, 1998, pp. 272-282.

[60] Zhao, Y.S., Choi, Y.T. and Wereley, N.M., 2004, "Semi-active Damping of Ground Resonance in Helicopters Using Magnetorheological Dampers," *Journal of the American Helicopter Society*, Vol. 49, No. 4, 2004, pp. 468-482.

[61] Hurt, M. and Wereley, N.M., "Controllable fluid dampers for helicopter rotor stability augmentation," *AIAA/ASME/AHS Adaptive Structures Forum*, Salt Lake City, UT, Apr., 1996.

[62] Wang, K.W., Kim, Y.S. and Shea, D.B., "Structural Vibration Control via Electrorheological-Fluid Based Actuators with Adaptive Viscous and Frictional Damping," *Journal of Sound and Vibration*, Vol. 177, No. 2, pp. 227-237.

[63] Sims, N., Stanway, R., Peel, D., Bullough, W. and Johnson, A., "Controllable Viscous Damping: An Experimental Study of An

Electrorheological Long-Stroke Damper Under Proportional Feedback Control," *Smart Materials and Structures*, Vol. 8, No. 5, pp.601-615.

[64] Dyke, S.J., Spencer Jr., B.F., Sain, M.K. and Carlson, J.D., "Modeling and Control of Magnetorheological Dampers for Seismic Response Reduction," *Smart Materials and Structures*, Vol. 5, pp. 565-575.

[65] Marathe, S., Wang, K. and Gandhi, F., "Feedback Linearization Control of Magnetorheological Fluid Damper Based Systems with Model Uncertainty," *Smart Materials and Structures*, Vol. 13, 2004, pp. 1006–1016.

[66] Lee, H.-S. and Choi, S.-B., ''Control and Response Characteristics of a Magneto-rheological Fluid Damper for Passenger Vehicles,'' *Journal of Intelligent Material Systems and Structures*, Vol. 11, 2000, pp. 80–87.

[67] Gandhi, F., Wang, K.W. and Xia, L., "Magnetorheological Fluid Damper Feedback Linearization Control for Helicopter Rotor Application," *Smart Materials and Structures*, Vol. 10, 2001, pp. 96-103.

[68] Gordaninejad, F. and Breese, D., ''Heating of Magnetorheological Fluid Dampers,' *Journal of Intelligent Material Systems and Structures*, Vol. 10, No. 8, 1999, pp. 634–645.

[69] Dogruoz, M., Wang, E., Gordaninejad, F. and Stipanovic, A., ''Augmenting Heat Transfer from Fail-safe Magnetorheological Fluid Dampers using Fins,'' *Journal of Intelligent Material Systems and Structures*, Vol. 14, 2003, pp. 79–86.

[70] Liu, Y., Gordaninejad, F., Evrensel, C., Dogruer, U., Yeo, M.-S., Karakas, E. and Fuchs, A., ''Temperature Dependent Skyhook Control of HMMWV

Suspension using a Failsafe Magneto-rheological Damper,'' *SPIE Annual International Symposium on Smart Structures and Materials*, Vol. 5054, pp. 332–340.

[71] Batterbee, D. and Sims, N., "Temperature Sensitive Controller Performance of MR Dampers." *Journal of Intelligent Material Systems and Structures*, Vol. 20, 2009, pp. 297–309.

[72] Kamath, G., Wereley, N.M., and Madhavan, V., "Hysteresis Modeling of Semi-Active Magnetorheological Helicopter Dampers," *Journal of Intelligent Material Systems and Structures*, Vol. 10, No. 8, 1999, pp. 624-633.

[73] Stanway, R., Sproston, J. and Stevens, N., "Nonlinear Modeling of an Electrorheological Vibration Damper," *Journal of Electrostatics*, Vol. 20, 1987, pp. 167-184.

[74] Kamath, G., Hurt, M. and Wereley, N.M., "Analysis and Testing of Bingham Plastic Behavior in Semi-Active Electrorheological Fluid Dampers," *Smart Materterials and Structures*, Vol. 5, No. 5, 1996, pp. 576-590.

[75] Wereley, N.M., "Non-Dimensional Herschel-Builkley Analysis of Magnetorheological and Electroreological Dampers," *Journal of Intelligent Material Systems and Structures*, Vol. 19, No. 3, 2008, pp. 257-268.

[76] Pang, L., Kamath, G. and Wereley, N.M., "Idealized Hysteresis Modeling of Electrorheological and Magnetorheological Dampers," *Journal of Intelligent Material Systems and Structures*, Vol. 9, No. 8, 1998, pp. 642-649.

[77] Stanway, R., Sproston, J. and El-Wahed, A., "Application of Electro-rheological Fluids in Vibration Control: A Survey," *Smart Materterials and Structures*, Vol. 5, No. 5, 1996, pp.464-482.

[78] Gamota, D. and Filisko, F., "Dynamic Mechanical Studies of Electrorheological Materials: Moderate Frequency," *Journal of Rheology*, Vol. 35, 1991, pp. 399-425.

[79] Choi, S.B., Lee, S.K. and Park, Y.P., "A Hysteresis Model for the Field-Dependent Damping Force of a Magnetorheological Damper," *Journal of Sound and Vibration*, Vol. 245, No. 2, 2001, pp. 375-383.

[80] Ma, X., Wang, E., Rakhela, S. and Su, C., "Modeling Hysteretic Characteristics of MR-Fluid Damper and Model Validation," *Proceeding of the 41st IEEE Conference on Decision and Control*, Las Vegas, NV, 2002.

[81] Wang, E., Ma, X., Rakhela, S. and Su, C., "Modelling the Hysteretic Characteristics of a Magnetorheological Fluid Damper," *Proceedings of the Institution of Mechanical Engineers, Part D: Journal of Automobile Engineering*, Vol. 217, 2005.

[82] Wen, Y., "Method for Random Vibration of Hysteretic System," *Journal of Engineering Mechanics Division*, Vol. 102, 1976, pp. 249-263.

[83] Spencer (Jr.), B.F., Dyke, S.J., Sain, M.K. and Carlson, J.D., "Phenomenological Model of a Magnetorheological Damper," *Journal of Engineering Mechanics*, Vol. 123, No. 3, 1997, pp. 230-238.

[84] Hong, S.R., Choi, S.B., Choi, Y.T. and Wereley, N.M., "A Hydromechanical Model for Hysteretic Damping Force Prediction of ER Damper:

Experimental Verification," *Journal of Sound and Vibration*, Vol. 285, No. 4&5, 2005, pp. 1180-1188.

[85] Hong, S.R., Wang, G., Hu W., and Wereley, N.M., "Hydromechanical Analysis of a Magnetorheological Bypass Damper," *Proceedings of the 10th International Conference on Electrorheological Fluids and Magnetorheological Suspensions*, Lake Tahoe, USA, June 18-22, 2006.

[86] Min Mao, M., Hu, W., Wereley, N.M., Browne, A. and Ulicny, J., "Shock Load Mitigation Using Magnetorheological Energy Absorber with Bifold Valves," *Proceedings of the SPIE*, Volume 6527, 2007, pp. 652-710.

[87] Hu, W. and Wereley, N.M., "Rate-Dependent Elasto-Slide Model for Single and Dual Frequency MR Lag Damper Behavior," *International Journal of Modern Physics B*, Vol. 19, No. 7-9, 2005, pp. 1527-1533.

[88] Singh, R., Kim, G. and Ravindra, P.V., "Linear Analysis of Automotive Hydromechanical Mount with Emphasis on De-coupler Characteristics," *Journal of Sound and Vibration*, Vol. 158, No. 2, 1992, pp. 219-243.

[89] Geisberger, A., Khajepour A. and Golnaraghi, F., "Non-linear Modelling of Hydraulic Mounts: Theory and Experiment," *Journal of Sound and Vibration*, Vol. 249, No. 2, 2002, pp. 371-397.

[90] Doebelin, E., "System Dynamics: Modeling, Analysis, Simulation, Design," *Marcel Dekker, Inc. Publication*, 1998.

[91] Colgate, J., Chang, T., Chiou, C., Liu, K. and Kerr, M., "Modeling of a Hydraulic Engine Mount Focusing on Response to Sinusoidal and

Composite Excitations," *Journal of Sound and Vibration*, Vol. 184, No. 2, 1995, pp. 503-528.

[92] Carlson, J., "MR Fluids and devices in the Real World," *International Journal of Modern Physics B*, Vol. 19, No. 7-9, 2005, pp. 1463-1470.

[93] Manring, N., "Hydraulic Control Systems," *John Wiley & Sons, Inc. Publication*, 2005.

[94] Merrit, H., "Hydraulic Control Systems," *John Wiley & Sons, Inc. Publication*, 1967.

[95] Mitra, S.K., 2001, "Digital Signal Processing: A Computer-Based Approach," *McGraw-Hill Publication*, 2001.